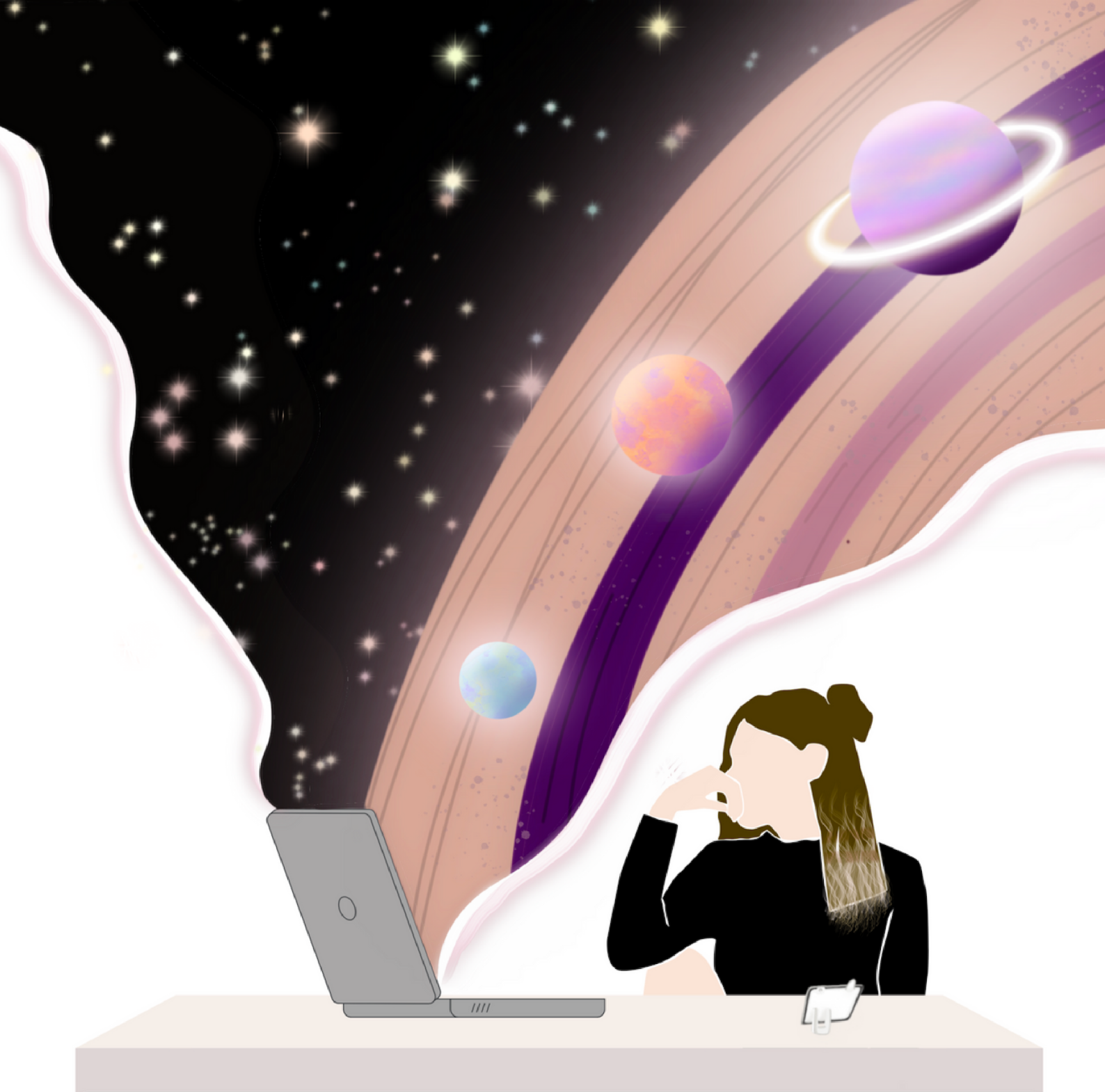

How dust shapes protoplanetary discs and the implications to planet formation

Sofia Savvidou

Dissertation

submitted to the

Combined Faculty of Natural Sciences and Mathematics

of Heidelberg University, Germany

for the degree of

Doctor of Natural Sciences

Put forward by

Sofia Savvidou

born in: Marousi (Athens), Greece

Oral examination: May 24th, 2023

How dust shapes protoplanetary discs and the implications to planet formation

Referees: Dr. Bertram Bitsch

Prof. Dr. Cornellis Dullemond

Abstract

Protoplanetary discs are the natal environments of planets and contain the building blocks from which planets form. It is therefore of crucial importance to understand how the dust growth and evolution shapes discs and what the implications are for planet formation. At the same time, our observational capabilities have improved in the recent years, providing us with more constraints that need to be considered in our theoretical studies. The goal of this thesis is to determine through numerical simulations how the dust shapes the (thermal) structure of the protoplanetary disc, how the conditions within the disc affect the growth of planets and how the forming planets affect the dust mass itself. We find that opacity models based only on micrometer-sized dust grains might not be a good approximation to simulate the disc's structure, especially for discs with significant viscous heating. There is a trade-off between the pebble isolation mass and the planetary growth timescale, which is important for the modeling of the growth of super-Earths via pebble accretion. We also find that the most favorable conditions for giant planet formation are high disc mass, early formation, and a large enough disc, however we conclude that their formation is mainly the outcome of a combination of beneficial factors or lack of adverse ones. Our findings strengthen the hypothesis that planet formation has already happened or is ongoing in Class II discs and we show that the assumption of an optically thin emission significantly underestimates the total dust mass in discs, if a giant planet is present that traps dust exterior to its orbit. We conclude that we should use the ever-increasing and improved observational data to better constrain the protoplanetary disc properties and connect the dots better to the observed exoplanets, based on our more sophisticated theoretical models.

Zusammenfassung

Protoplanetare Scheiben sind die Geburtsumgebung von Planeten und enthalten die Bausteine, aus denen sie sich bilden. Daher ist es von entscheidender Bedeutung zu verstehen, wie das Wachstum und die Entwicklung von Staub die Scheiben formen und welche Auswirkungen dies auf die Entstehung von Planeten hat. Gleichzeitig haben sich unsere Beobachtungsmöglichkeiten in den letzten Jahren verbessert, sodass wir mehr Einschränkungen haben, die wir in unseren theoretischen Modellen berücksichtigen müssen. Ziel dieser Arbeit ist es, anhand numerischer Simulationen zu bestimmen, wie der Staub die (thermische) Struktur der protoplanetaren Scheibe ausbildet, wie die Bedingungen innerhalb der Scheibe das Wachstum von Planeten beeinflussen und wie die sich bildenden Planeten die Staubmasse selbst beeinflussen. Unsere Analyse zeigt, dass Opazitätsmodelle, die nur auf mikrometergroßen Staubkörnern basieren, möglicherweise keine gute Annäherung sind, um die Struktur der Scheibe zu simulieren, insbesondere bei Scheiben mit erheblicher viskositätsbedingter Erwärmung. Es existiert einen Ausgleich zwischen der Isolationsmasse der Kieselsteinen und der Zeitskala für das Planetenwachstum, was für die Modellierung des Wachstums von Supererden durch die Akkretion von Kieselsteinen wichtig ist. Außerdem stellen wir fest, dass die günstigsten Bedingungen für die Entstehung von Riesenplaneten eine hohe Scheibenmasse, eine frühe Entstehung, und eine ausreichend große Scheibe sind. Jedoch kommen wir zu dem Schluss, dass ihre Entstehung hauptsächlich das Ergebnis einer Kombination von günstigen Faktoren oder dem Fehlen von ungünstigen Faktoren ist. Unsere Ergebnisse bestärken die Hypothese, dass die Planetenentstehung in Scheiben der Klasse II bereits stattgefunden hat oder noch andauert, und wir zeigen, dass die Annahme einer optisch dünnen Emission die Gesamtstaubmasse in den Scheiben deutlich unterschätzt, wenn ein Riesenplanet vorhanden ist, der außerhalb seiner Umlaufbahn Staub einfängt. Daher kommen wir zu dem Schluss, dass man die ständig zunehmenden und verbesserten Beobachtungsdaten nutzen sollte, um die Eigenschaften der protoplanetaren Scheiben stärker eingrenzen und die Punkte besser mit den beobachteten Exoplaneten verbinden zu können, basierend auf unseren fortgeschrittenen theoretischen Modellen.

Σύνοψη

Οι πρωτοπλανητικοί δίσκοι είναι το γενεσιουργό περιβάλλον των πλανητών και περιέχουν τα δομικά στοιχεία από τα οποία σχηματίζονται οι πλανήτες. Είναι, επομένως, ζωτικής σημασίας να κατανοήσουμε πώς η ανάπτυξη και η εξέλιξη της σκόνης διαμορφώνει τους δίσκους και ποιες είναι οι συνέπειες για το σχηματισμό των πλανητών. Ταυτόχρονα, τα τελευταία χρόνια οι παρατηρησιακές μας δυνατότητες έχουν βελτιωθεί, παρέχοντάς μας περισσότερους περιορισμούς που πρέπει να ληφθούν υπόψη στις θεωρητικές μας μελέτες. Ο στόχος αυτής της διατριβής είναι να προσδιορίσουμε μέσω αριθμητικών προσομοιώσεων πώς η σκόνη διαμορφώνει τη (θερμική) δομή του πρωτοπλανητικού δίσκου, πώς οι συνθήκες εντός του δίσκου επηρεάζουν την ανάπτυξη των πλανητών και πώς οι σχηματιζόμενοι πλανήτες επηρεάζουν την ίδια τη μάζα της σκόνης. Συμπεραίνουμε πως τα μοντέλα αδιαφάνειας που βασίζονται μόνο σε κόκκους σκόνης μεγέθους μικρομέτρων μπορεί να μην είναι μια καλή προσέγγιση για την προσομοίωση της δομής του δίσκου, ειδικά για δίσκους με σημαντική θέρμανση λόγω τυρβώδους ιξώδους. Υπάρχει μια αντιστάθμιση μεταξύ της μάζας απομόνωσης των βότσαλων και της χρονικής κλίμακας ανάπτυξης των πλανητών, η οποία είναι σημαντική για τη μοντελοποίηση του σχηματισμού των υπερ-Γαιών μέσω της προσαύξησης των βότσαλων. Διαπιστώνουμε επίσης ότι οι πιο ευνοϊκές συνθήκες για το σχηματισμό γιγάντιων πλανητών είναι η υψηλή μάζα του δίσκου, ο πρώιμος σχηματισμός και ένας αρκετά μεγάλος δίσκος, ωστόσο καταλήγουμε στο συμπέρασμα ότι ο σχηματισμός τους είναι κυρίως αποτέλεσμα ενός συνδυασμού ευεργετικών παραγόντων ή της έλλειψης δυσμενών. Τα ευρήματά μας ενισχύουν την υπόθεση ότι ο σχηματισμός πλανητών έχει ήδη συμβεί ή βρίσκεται σε εξέλιξη στους δίσκους κλάσης II και δείχνουμε ότι η υπόθεση της οπτικά αραιής εκπομπής υποτιμά σημαντικά τη συνολική μάζα σκόνης στους δίσκους, αν υπάρχει ένας γιγάντιος πλανήτης που παγιδεύει σκόνη εξωτερικά της τροχιάς του. Καταλήγουμε στο συμπέρασμα ότι θα πρέπει να χρησιμοποιήσουμε τα συνεχώς αυξανόμενα και βελτιωμένα παρατηρησιακά δεδομένα για να προσδιορίσουμε καλύτερα τις ιδιότητες των πρωτοπλανητικών δίσκων και να τις συνδέσουμε καλύτερα με τους παρατηρούμενους εξωπλανήτες, με βάση τα πιο εξελιγμένα θεωρητικά μας μοντέλα.

Contents

Abstract v

Zusammenfassung vii

Σύνοψη ix

1 Motivation 1
- 1.0.1 The hunt for the exoplanets . . . 2
- 1.0.2 Taking a look at the protoplanetary discs . . . 6
- 1.0.3 But first, there was theory . . . 7
- 1.0.4 Where does this thesis stand in all these? . . . 8

2 Foundations 11
- 2.1 Protoplanetary disc structure . . . 11
  - 2.1.1 Disc formation as a by-product of star formation . . . 11
  - 2.1.2 Classification of young stellar objects . . . 12
  - 2.1.3 Disc substructures . . . 14
  - 2.1.4 Vertical and radial structure . . . 16
- 2.2 From dust to pebbles, planetesimals and planetary embryos . . . 17
  - 2.2.1 Dust dynamics . . . 17
  - 2.2.2 Barriers . . . 21
  - 2.2.3 Forming the first embryos . . . 22
- 2.3 Radiative transfer . . . 23
  - 2.3.1 The formal radiative transfer equation . . . 23
  - 2.3.2 Solutions of the radiative transfer equation . . . 24
  - 2.3.3 Opacity . . . 24
- 2.4 Planet formation within the core accretion scenario . . . 26
  - 2.4.1 Pebble accretion . . . 27
  - 2.4.2 Gas accretion . . . 28
  - 2.4.3 Gap formation . . . 29
  - 2.4.4 Planet migration . . . 30

3 Thermal structures of protoplanetary discs 31
- 3.1 Context . . . 32
  - 3.1.1 Relative velocities and grain size distribution . . . 33
  - 3.1.2 Opacity . . . 34
  - 3.1.3 Disc structure and grain size distribution. . . . 34
  - 3.1.4 Disc structure, opacity, and cooling rate . . . 35
  - 3.1.5 Disc structure, grain size distribution, and opacity . . . 35
  - 3.1.6 Motivation . . . 36

3.2 Methods . . . 37
3.2.1 Hydrodynamical simulations . . . 37
3.2.2 Opacity-Temperature module . . . 37
3.2.3 Grain size distributions . . . 40
3.2.4 Vertical distribution of grains . . . 44
3.2.5 Simulations setup . . . 45
3.3 Grain size distributions . . . 47
3.3.1 Comparison between the two grain size distributions . . . 47
3.3.2 Opacities and temperature . . . 50
3.3.3 Dust surface densities . . . 51
3.3.4 Dominant grain sizes . . . 52
3.4 Dependence on viscosity, gas surface density and dust-to-gas ratio . 54
3.5 Implications . . . 56
3.5.1 Iceline . . . 56
3.5.2 Planet migration . . . 59
3.5.3 Implications for planet formation and protoplanetary disc simulations . . . 61
3.6 Summary . . . 62

4 The growth of super-Earths. 65
4.1 Context . . . 65
4.2 Methods . . . 67
4.2.1 Opacities . . . 67
4.2.2 Hydrodynamical simulations . . . 69
4.2.3 Pebble accretion . . . 70
4.2.4 Pebble isolation mass . . . 70
4.2.5 Advantages and limitations of our model . . . 71
4.3 disc structure . . . 72
4.3.1 Dependence on viscosity, gas surface density, and fragmentation velocity . . . 72
4.3.2 Disc evolution . . . 77
4.4 Planet formation . . . 78
4.4.1 Pebble isolation mass . . . 79
4.4.2 Planet growth until pebble isolation mass . . . 79
4.4.3 Testing higher dust-to-gas ratio, gas surface density, and initial planetary seed mass . . . 80
4.5 Discussion . . . 82
4.5.1 Planet growth . . . 82
4.5.2 Comparison to the Kepler data . . . 83
4.5.3 Disc parameters . . . 84
4.6 Summary . . . 85

5 The growth of giant planets. 87
5.1 Context . . . 88
5.2 Methods . . . 89
5.2.1 Model description . . . 89

5.2.2 Initial conditions . . . 91
5.3 Growth tracks . . . 92
5.4 Favorable conditions for giant planet formation . . . 100
5.4.1 Dependence on the initial conditions . . . 101
5.5 Discussion . . . 106
5.6 Summary . . . 110

6 How planet formation affects the dust mass evolution of protoplanetary discs 113
6.1 Context . . . 113
6.2 Methods . . . 115
6.2.1 Model and parameters used . . . 115
6.2.2 Optically thin dust mass estimates . . . 116
6.3 Dust mass evolution after the gas giant formation . . . 116
6.4 The mass budget problem . . . 120
6.5 Summary . . . 123

7 Summary and outlook 125

A Additional material to Chapter 3 129
A.1 Dust surface densities for different α-viscosity values . . . 129
A.2 Iceline position as a function of α-viscosity, initial gas surface density and dust-to-gas ratio . . . 134
A.3 The effect of settling . . . 134

B Additional material to Chapter 4 139

List of Figures 141

List of Tables 145

List of own publications 147

Bibliography 149

Acknowledgements 171

1

Motivation

Before I introduce you to the motivation that binds this thesis together, I would like to take you on a journey through the history of our field. I know, I know... These seem to be found quite often in theses and it may seem repetitive and out-of-touch at times, but I promise there is a point to be made, relevant to this thesis and hopefully I will manage to make it an interesting journey. The eager reader can already see the specific motivation of this PhD journey summarized in the box at the end of this chapter. At the same time, and given that this is *my* thesis, I would like to grab the opportunity and firstly share a few of my thoughts that will help you understand why *I* find this field so intriguing and mesmerizing.

Planet formation is inevitably linked to our existence as living organisms on a terrestrial planet within our Solar System. Meteorite composition measurements point to an age for our planet of around 4.57 billion years (Amelin et al. 2002; Baker et al. 2005; Connelly et al. 2012; Patterson 1956) and life is believed to have emerged 3.7 to 4.5 billion years ago (Pearce et al. 2018). Jumping several million years, going through the first multi-cellular life (El Albani et al. 2014), and the five massive extinctions (Racki 2021), we arrive to the Cenozoic Era (the age of Mammals), the evolution of hominids, and ultimately, to *homo sapiens*, the present day (researching) human beings.

How amazing and statistically puzzling does it sound that one species, us humans, have evolved into sentient beings observing the world (what we call Universe) around them and trying to understand it. So in a sense, us, a minor part of the Universe, have evolved to be observing and studying the Universe itself. To make a long story short, my ambition as an astrophysicist is not merely a desire to investigate what is out there, wonder what we are-still and perhaps always will be-missing and get a sense out of what we experience but rather an inability to not think about it. And planet formation as a field allows us to zoom out of ourselves and our experiences as a species on Earth but not so much as to lose touch completely of how we connect to the Cosmos.

There are two sides to the coin that is planet formation. On one side, we have the protoplanetary discs, the by-products of star formation, within which the na-

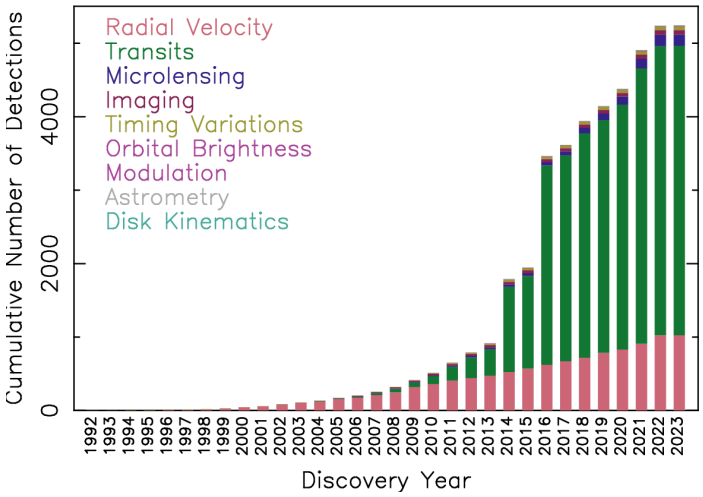

Figure 1.1. Cumulative number of confirmed exoplanets per year for different observational techniques.

tal environment and the building blocks of planets are shaped. On the other side, we have exoplanets themselves, with their individual characteristics and dynamical evolution. One might think, *surely studying the planets themselves must be easier given that we currently reside on one.* Of course, a lot of valuable information about planet formation comes from our own neighborhood, from the (isotopic) compositions of Solar System meteorites/asteroid belt (e.g. DeMeo & Carry 2014; Kruijer et al. 2014; Leya et al. 2008; Nomura et al. 2022; Warren 2011, and references therein) or planets (Allègre et al. 2001; Braukmüller et al. 2019; Nimmo & Kleine 2007; Palme et al. 2014, etc.), the interior structure or atmospheric characterization of the planets (Helled et al. 2022; Miguel & Vazan 2023) and the observed architecture of our system (see here for a basic overview on the "discoveries" of the Solar System objects) to the Minimum Mass Solar Nebula approximation (Hayashi 1981a; Weidenschilling 1977c) and the potential scenarios to explain our system's formation (summarized in Raymond & Morbidelli 2022). But as it turns out, our Solar System is a weird one (Raymond et al. 2020). And this makes it not a great example of how planets form in general, therefore we need to point our antennas elsewhere, too.

1.0.1 The hunt for the exoplanets

Humanity's journey in exoplanet hunting began with a bang, given that the first exoplanets to be observed questioned the knowledge of the scientific community of the time and some of them can be considered extreme cases even with our current understanding. Deciding which was the very first exoplanet observation is not a simple matter and is left to the interested reader to decide. In 1988, Campbell et al. used the radial velocities technique (RV)[1] and detected the signal of a Jupiter mass planet orbiting γCep but the authors backed away from the claim in 1992 (Walker et al. 1992). The signal was, however, confirmed to be caused by an exoplanet by Hatzes et al. (2003).

[1] A review of the current observational techniques is beyond the scope of this thesis, but remains quite interesting, therefore I refer any interested reader to this webpage for more information on the methods and how succesfull they have been so far, or see a brief review of the connection to the stellar hosts in Rojas-Ayala (2023).

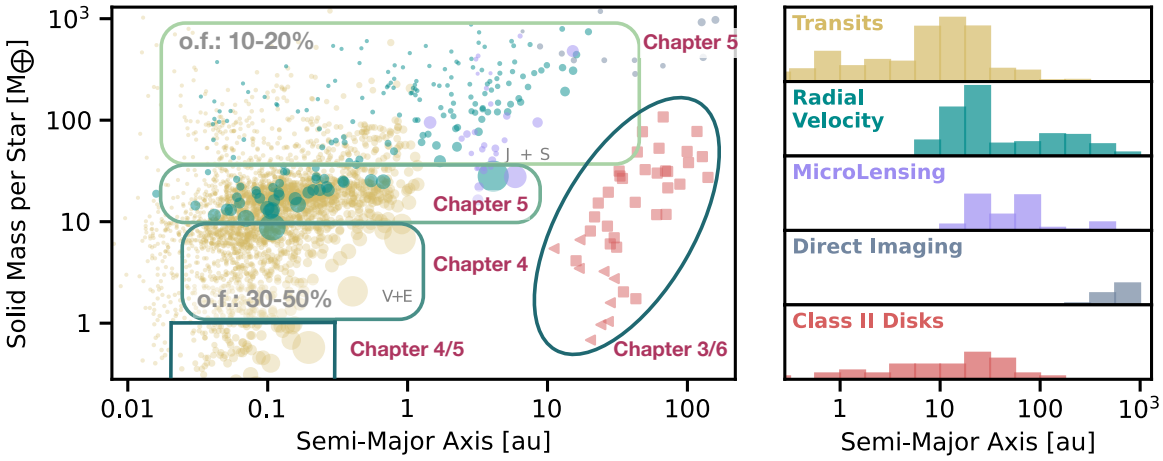

Figure 1.2. Inferred solid mass as a function of semi-major axis for the confirmed exoplanets up to date orbiting solar-type stars (circles, color-coded by the observational method) and the Class II protoplanetary disc masses obtained via mm observations (red squares or triangles). The solid masses are estimated from observed masses and radii following the relations on Thorngren et al. (2016) and Chen & Kipping (2017). To correct for detection bias, each detected planet has a circle area proportional to the intrinsic occurrence of that planetary system, following **?**. The different objects (type of planet or disc) are encircled with different colors (see Fig. 1.3 for the color-coding) and the relevant chapters of this thesis are marked in red. In gray, I note the occurence fractions for gas giant planets and super-Earths. Figure adapted from Drążkowska et al. (2022).

The next dip in the exoplanet waters happened less than a year later, again via RV. Latham et al. (1989) reported the detection of a companion around HD114762 that could have a mass as low as 11 M_{Jup} and while they speculated it could be a planet, they mainly suggested that it was a brown dwarf. A couple of years later, Wolszczan & Frail (1992) not only observed evidence of two Earth-mass planets outside our own Solar System but the host of this system is a pulsar (PSR1257+12 or Lich) and the discovery was made via pulsar timing. This technique interestingly accounts to only 0.13% of exoplanet discoveries up to date and the formation mechanisms of such planets are still not well constrained. In Fig. 1.1, we see the cumulative number of confirmed exoplanets per year of discovery, however the dates start from 1992 because the detections prior to this year where confirmed as planets years later, with follow-up data. In 1995, M.Mayor and D.Queloz discovered 51 Peg b (again via RV), the first giant planet orbiting a Solar-like star and for this discovery they won half of the Nobel prize in Physics (Mayor & Queloz 1995).

There are, in general, several possible ways to observe exoplanets, however the most successful one is by far (at least to the present day) the transit method (75.2% exoplanets found via transits), with the second main one being radial velocities (RV, 19.5%), which is the one that provided the first ground-based discoveries. My journey in the world of planet formation began with my M.Sc. thesis project in 2017-2018 and 31% of the total confirmed exoplanets, to date, have been discovered within the short span of these 5-6 years until today. This rapid increase in the discovery

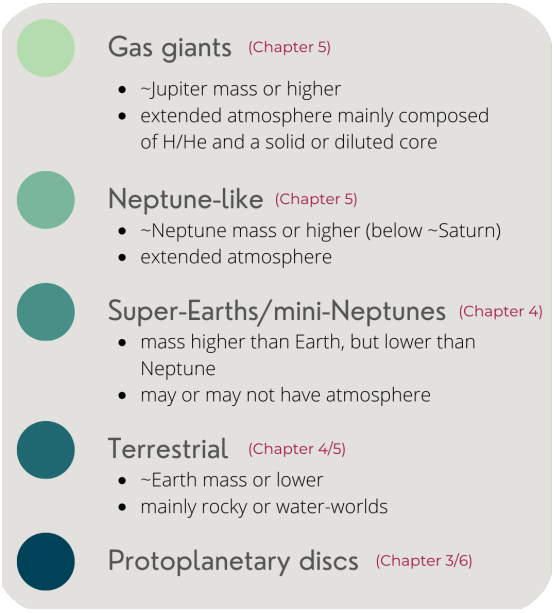

Figure 1.3. Types of objects discussed in this thesis. The classification of the planets is based mainly on the observed exoplanets and the different types are defined by the planetary masses.

rate can be attributed mainly to the dedicated space-based missions, namely the Kepler mission and, to a smaller extend, the TESS mission. To this day, there are still many more candidates from multiple missions in line to be confirmed and the number of the discoveries will keep increasing.

In Fig. 1.2, we see the inferred solid mass as a function of semi-major axis for the confirmed candidates (circles, color-coded by the observational method) around solar type stars and the Class II protoplanetary disc masses (red squares or triangles). The size of the circles is inversely proportional to the survey completeness for each exoplanet, following (Mulders et al. 2021). In the right panel, we see the occurence-weighted histogram of the solid-mass distributions. It is obvious that each technique has its own biases and is mainly able to detect a specific range of planets. Some parts of this plot remain largely unexplored, such as the lower-mass planets (terrestrials) and this leaves a lot of open questions about the nature of such planets and their comparison to the terrestrial planets in our Solar System. At the same time, the detections extend into regions which are not necessarily easily predicted and fully explained by our current theoretical planet formation models, such as the population of ultra-short-period planets (orbital periods < 1 day Winn et al. 2018) or the radius and density gaps (e.g. Fulton et al. 2017; Luque & Pallé 2022; Van Eylen et al. 2021).

One may wonder how the observed numbers compare to the intrinsic fractions of planets of a certain type but such fractions are difficult to estimate with the limited data that we have and the uncertainties that accompany them. However, a lot of work is being done in calculating the occurrence fractions of planets per star (reviews by Winn & Fabrycky 2015; Zhu & Dong 2021) and I show the current estimates for super-Earths and gas giants on the plot (following the estimates discussed in Drążkowska et al. (2022)). It is not necessarily straightforward to compare the occurrence fraction estimates to the fractions of planets we have observed, however it is an indication of the observational biases and it points towards the fact that a lot of planets remain unknown or unseen, therefore we cannot be certain about

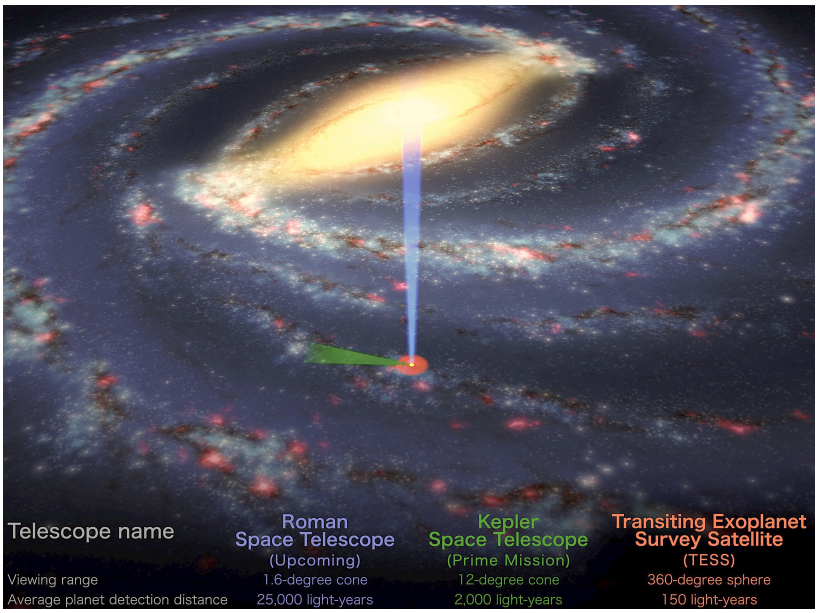

Figure 1.4. Field of view for current (Kepler and TESS) and future (Nancy Grace Roman Telescope) exoplanet hunting surveys.

the expected (intrinsic) fractions of each type of planet. Or whether this taxonomy of planets, as defined in the right of Fig. 1.3, is an accurate representation of the actual population.

Currently, we are almost entirely confined to the Milky Way and specifically the detected exoplanets are located within the field of view (FOV) of Kepler, the area that TESS spans around our Sun and the direction of the Galactic bulge for microlensing (see Fig. 1.4 for the Kepler, TESS and future Nancy Grace Roman Telescope FOV). To a small degree, some exoplanets have already been detected in various galactic disc locations (mainly via microlensing) and even non-detections can lead to an adjustment of the occurence rates (e.g. Bashi & Zucker 2022). Some general estimates can be also done considering the different stellar metallicities, masses and ages of our currently accessible populations, however, expanding our horizons might either bring new interesting samples that require previous unexplored formation pathways or establish the conditions under which planet formation is challenged.

This past January, the JWST confirmed its first exoplanet, LHS 475 b, an Earth-sized exoplanet that orbits a red dwarf star within 2 days only (Stevenson 2023). Just two months ago, a circumbinary planet was detected for the first time by RV only. It was also only the second confirmed multiplanetary circumbinary system to date and the innermost planet of that system is the only one currently, for which an atmospheric characterisation can be carried out by the JWST (Standing et al. 2023). This showcases how much progress is happening at very short intervals and also an exciting prospect of the field; to gain even more information about the bulk or atmospheric composition of the exoplanets, so that we can define the different types more accurately. As our range of possible systems to discover will broaden, our formation models could be challenged more but the more information we get about what is possible out there, the better our theory will explain what we find.

1.0.2 Taking a look at the protoplanetary discs

The first protoplanetary disc was observed around β Pic by Smith & Terrile, in 1984. Already in the late 1970s, it was suggested in the seminal paper of Lynden-Bell & Pringle (1974) that the infrared excess emission in the spectral energy distributions (SEDs) of certain protostars was due to the presence of a viscous accretion disc surrounding them and this would explain the observations of T Tauri stars. At the moment, there are three possible ways to study protoplanetary discs observationally: scattered light, thermal continuum emission, and molecular spectral line emission (see Andrews 2020, for a review). Given that each tracer probes different regions and properies of the disc, a combination of multiple traces would provide the most information about a disc, however this is not always done or even feasible. Measurements at millimeter wavelengths have been historically considered particularly desirable, as the thermal continuum emission from dust grains is assumed to be optically thin and therefore probing the full disc volume (Beckwith & Sargent 1991; Beckwith et al. 1990). Several hundreds of disk masses were initially estimated from single-dish millimeter photometry surveys (e.g. Andre & Montmerle 1994; Andrews & Williams 2005a; Osterloh & Beckwith 1995) and early interferometric studies (e.g. Lay et al. 1997, 1994; Mundy et al. 1996). However, the further back we go, the more limited we have been by the low resolution of the observations.

In the recent years, our view into the star-forming regions has significantly cleared up, mainly owing to the Spectro-Polarimetric High-contrast Exoplanet REsearch (SPHERE) instrument installed in the Very Large Telescope (VLT) and the Atacama Large Millimetre/submillimetre Array (ALMA) interferometer, both located in Chile, probing the scattered light and the dust continuumm, respectively. Several surveys have been conducted with these facilites, some of which at very high resolution (3-5 AU or 0.02" to 0.035") such as D-SHARP (Disk Substructures at High Angular Resolution Project Andrews et al. 2018) and part of the ODISEA (Ophiuchus DIsc Survey Employing ALMA Cieza et al. 2019), revealing a wide variety of substructures (see also Sect. 2.1.3). The use of polarimetric differential imaging[2] had already offered a glimpse into the morphological variety of protoplanetary discs within the first years of SPHERE but recently efforts have been made to generalize high-contrast-imaging observations on a population level with comparable resolution to ALMA with the DARTTS-S survey (Disks around T Tauri Stars with SPHERE Avenhaus et al. 2018). SPHERE also provided the first glimpse into forming planets, within their natal disc (Haffert et al. 2019; Keppler et al. 2018; Müller et al. 2018a).

One of the eye-opening discoveries of the ALMA observations was how common substructures are in protoplanetary discs, with not only rings-cavities (Long et al. 2018; Pinilla et al. 2017; Tsukagoshi et al. 2019; van der Marel et al. 2018a; van der Plas et al. 2017) and rings-gaps (ALMA Partnership et al. 2015; Andrews et al. 2018; Guzmán et al. 2018; van Terwisga et al. 2018), but even spirals (Huang et al. 2018; Pérez et al. 2016), and arcs (Casassus et al. 2013; Dong et al. 2018; Isella

[2]PDI takes into advantage the different nature of the stellar light, which is mainly unpolarised, and the scattered light from the disc surface, which is strongly polarised, in order to separate these two light components

et al. 2013; Marino et al. 2015). I refer the interested reader to Andrews (2020) for a nice illustration of the various physical mechanisms creating such substructures. I will discuss more our current understanding of the causing mechanisms behind such substructures in Sect. 2.1.3 but the point to be made here is that this next step, studying the potential physical mechanisms, requires extensive theoretical models often including the interplay of dust evolution.

Our ability to study protoplanetary discs at a population level has led to significant statistics about their bulk properties, such as their masses. In Fig. 1.2, we can see a comparison between the inferred solid masses of the observed planetary systems around solar-type stars and the observed Class II protoplanetary discs and we find that the estimated disc masses are equal or lower to the exoplanet masses. This poses the question of how can planets form within such discs if their natal environments do not have enough mass for their formation (see Chapter 6 for a detailed discussion). It should be noted, however, that comparing the observed exoplanets and the observed protoplanetary discs might be misleading, especially considering that the natal protoplanetary discs from which the observed exoplanets formed and the observed protoplanetary discs could be fundamentally different populations. There are different observational biases affecting exoplanet and disc surveys and even if we account for the time evolution of the K and M type stars, around which discs are mainly observed with ALMA and even pre-ALMA (Pascucci et al. 2016; Testi et al. 2014), we cannot be sure that a direct comparison is possible.

1.0.3 But first, there was theory

Theoretical models of protoplanetary disc structures are an ongoing and relatively young field of study (Chiang & Goldreich 1997; Dullemond et al. 2001, 2007; Dullemond & Monnier 2010; Hueso & Guillot 2005a; Lynden-Bell & Pringle 1974; Pringle 1981, etc.), even though the *Nebula Hypothesis*[3], dates back to the eighteenth century, partially proposed by Swedenborg (1734, discussed here), further developed and published by Kant (1755) and then independently by Laplace (1797) (discussion in Woolfson 1993). A lot of work has been done to understand the disc dynamics in detail, in regards to the dust-gas interplay (e.g. Brauer et al. 2008a), the turbulence and how angular momentum is transported (e.g. Shakura & Sunyaev 1973), the hydrodynamical instabilities, the role of magnetic fields and winds (see Lesur et al. 2022; Pascucci et al. 2022, for the recent developments). Such elaborate studies are imperative for the interpretation of observations or to shape our expectations before them.

At a similar time (and before there was a clear idea on how protoplanetary discs were formed), planet formation models were developed (Goldreich & Ward 1973; Safronov 1969), discussing that planets were forming from the aggregation of solids and particles into large bodies, but mainly disregarded the dust evolution and assumed that the larger bodies, planetesimals or planetary embryos formed quickly and then further collided to create a planet.

Theoretical work has, evidently, long preceded the observations of extra-solar

[3]the idea that our Solar System formed from a rotating disc of gas and dust

planets and protoplanetary discs as the main driver of the scientific exploration, even though the most common ancestors of our present days theories were formed in a similar time with the dawn of the observational era. Undeniably, the continuous improvement and the increasing number of observations has been and will continue being a valuable tool in our toolbox, putting constraints, challenging our understanding, testing theories and validating models, as we work towards a self-consistent theory encompassing all stages from dust to planets. Given that this thesis is a product of theoretical work, the theoretical groundwork of protoplanetary discs and planet formation will be discussed in more detail in Chapter 2.

1.0.4 Where does this thesis stand in all these?

The processes within (what we perceive as) the Universe seem to be universal, from the Cosmic Web, to the galaxies, the stars forming withing them and the planetary systems orbiting around them. At the same time, the diversity that we observe is astonishing: from lava worlds (55 Cancri e) and planets hotter than our Sun (KOI-55 b), to water-worlds (Kepler-22 b), a hot Jupiter torn apart by its star (WASP-12 b) and a gas giant with the density of a marshmallow (TOI-3757 b). The field of planet formation aims to understand and explain the processes that the material within a protoplanetary disc undergoes until it forms various types of planets.

To introduce the motivation for this thesis let's come back to the two-faced problem that is planet formation. As mentioned above, we have on one hand the protoplanetary discs and on the other hand the exoplanets. The goal of the planet formation field is to connect the dots between these two populations and fortunately we have already gone a long way since the first idea that a spherical molecular cloud collapses, an accretion disc forms around the protostar and planets form by sweeping up the large boulders around them. Several questions remain unanswered, though, and by the nature of science itself, the more questions we are able to answer, the better questions we are able to formulate for future quests. The theoretical foundations of protoplanetary discs and planet formation existed way before we were able to observe the discs and exoplanets in detail but we are fortunate to live in an era where actual celestial objects can be used to constrain the material of our virtual labs. The more our observational capabilities advance, the more data we will collect to unravel how we get from protoplanetary discs to planetary systems.

It has already been established with the help of the observational data we have obtained, that dust grows and evolves in protoplanetary discs and discs are often heavily substructured, therefore, it is for crucial importance to understand the relevant processes, the interplay with the (thermal) structure of the disc and study the implications for planet formation, as dust will grow into the building blocks of planets. Additionally, the ever-increasing number of detected exoplanets serves as a copious sample of varying properties which are in need of elaborate formation pathways. This thesis stands in the middle of all these, building upon the theoretical knowledge of the field, while considering the new insights brought by the state-of-the-art observations, making the effort to connect the dots between them. For this purposes, we lay the groundwork for the interplay between dust and the thermal structure of protoplanetary discs in Chapter 3, we discuss in Chapter 4, the

formation of super-Earths (the presented pathway could lead to terrestrial planet formation, though, or mini-Neptunes if we considered gas accretion), in Chapter 5, the formation of gas giants (discussing ice giants as well and presenting the results for all planetary masses produced by our model) and finally in Chapter 6 we discuss how the disc (dust) mass evolves after a planet forms and how/if we can compare the estimated disc masses from observations to the observed exoplanet masses.

Before moving forward to Chapter 2 and the theoretical background of this thesis, I believe it is important to stress that this is a very active and young field of research that still has many unknowns or uncertainties. For reasons of clarity, I may refer, here, to something as a fact but we should keep in mind that this is our current understanding of the physics behind the astrophysical objects discussed here and several aspects of them could be adapted in the future when more detailed and accurate information has been acquired. I can only smile already with the idea of re-reading this thesis in a couple of decades and pointing out the improvements in our knowledge.

In a nutshell...

Our observational capabilities are ever-increasing and improving, both in regards to protoplanetary discs around young stars and in regards to exoplanets or exoplanetary systems around older stars. However, as it usually happens with science, the more information we get, the more advanced questions we are able and forced to formulate. Protoplanetary disc are the birth environments and contain the building blocks from which planets can eventually form. Planet formation is happening between these two observables (disc populations and exoplanets) and multiple processes are expected to be underway from the time a disc forms until a planetary system exists. This thesis strives to connect these pieces and addresses the following questions:

- ⋆ How do the dust grains and their corresponding opacities influence the thermal structure of the disc and vice versa? (Chapter 3)
- ⋆ How does the thermal structure of the inner disc influence the pebble isolation mass and the time to reach it and thus the growth of super-Earths? (Chapter 4)
- ⋆ How do the initial disc conditions affect the growth of giant planets? (Chapter 5)
- ⋆ How is the disc dust mass affected by the growth of a (giant) planet and how does this connect to the estimated disc masses from (ALMA) observations? (Chapter 6)

2

Foundations

In this chapter I introduce the relevant theoretical background for protoplanetary discs as the birthing environments of planets and for the planet formation mechanisms. While it aims to be as broad as possible to encompass the various aspects of planet formation, it mainly introduces the topics which are directly related to the work presented in the next chapters.

2.1 Protoplanetary disc structure

2.1.1 Disc formation as a by-product of star formation

The life of a protoplanetary disc begins with the formation of a protostar inside the "stellar nurseries" of molecular clouds (MCs), which can be observationally defined as overdensities or bright, compact features with molecular gas (in comparison to the ISM) (Chevance et al. 2022). In the classical picture, these "stellar nurseries" are regions or cores within a MC of dense, cool gas and dust that undergo gravitational collapse when their self-gravity exceeds thermal, kinetic (turbulent) and magnetic support (Hunter 1977; Larson 1969; Penston 1969; Shu 1977). During this collapse, material falls towards the center of the core or towards multiple centers, forming one or more protostars. More recent work, motivated initially by *Herschel* observations has shown that star formation is more complicated than this (André et al. 2014). MCs feature a lot of sub-structures and most dense cores are formed as clumps within filaments because of shock-compression, therefore core collapse and star formation are deeply intertwined with the molecular clouds properties and cannot be studied as spherical, isolated systems in most cases (Pineda et al. 2022). This tension between what we thought and what current data point towards is shown in Fig. 2.1.

The rotation of the star forming cores has been estimated via velocity gradients to be small (Goodman et al. 1993) and the clumps are supported by magnetic fields and turbulent motions (McKee & Tan 2003), however how much angular momentum can be carried away this way is still an active field of research (Li et al. 2014).

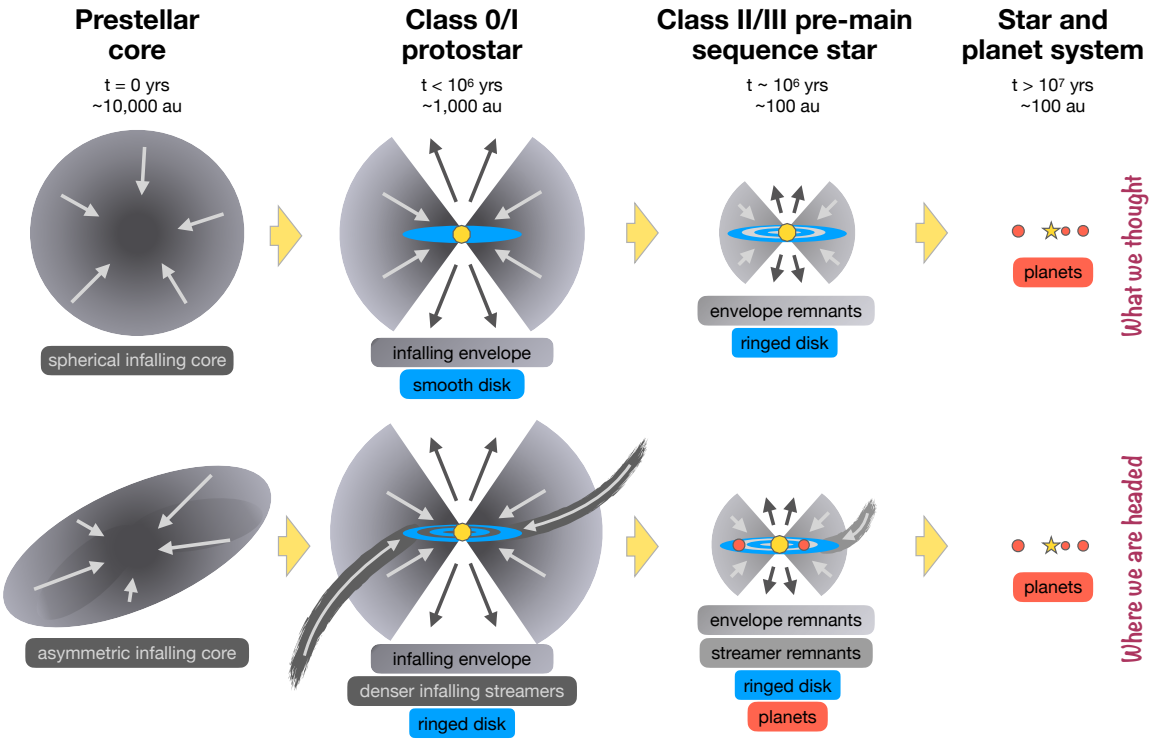

Figure 2.1. Evolutionary stages of star formation in the classical scenario (top row) and the picture painted by the recent developments in the field (bottom row). Figure adapted from D.Segura-Cox.

Nevertheless, the angular momentum is not possible to be contained by the protostar alone and this can also be concluded by comparing the masses of molecular clouds to the masses of protostars (Hartmann et al. 2016). Observations of forming stars in relatively late evolutionary stages suggest that the angular momentum tends to a constant value, as expected from conservation of angular momentum under infall. As a natural consequence, a rotationally-supported, circumstellar disc is expected to form eventually, the so-called protoplanetary disc.

The accretion to the star continues through this disc, but in order for matter to be transported inwards, angular momentum has to be transported outwards through the disc (Lynden-Bell & Pringle 1974). These discs surround the young stellar objects (YSOs) at their first few million years and since planet formation is expected to take place there, they are called protoplanetary discs. The structure of a protoplanetary disc determines several stages of formation and growth of planets, from the growth of dust particles to pebbles (Sect. 2.2.1), the movement of pebbles because of gas drag (Sect. 2.2.2), the formation of planetesimals or planetary cores (Sect. 2.2.3), to gas accretion (Sect. 2.4.2) and planet migration (Sect. 2.4.4).

2.1.2 Classification of young stellar objects

Throughout the years, a classification scheme has been established for the evolutionary stages of YSOs, based on the IR-excess in their spectral energy distribution (SED) (Adams et al. 1987; Andre et al. 1993; Greene et al. 1994; Lada & Wilking

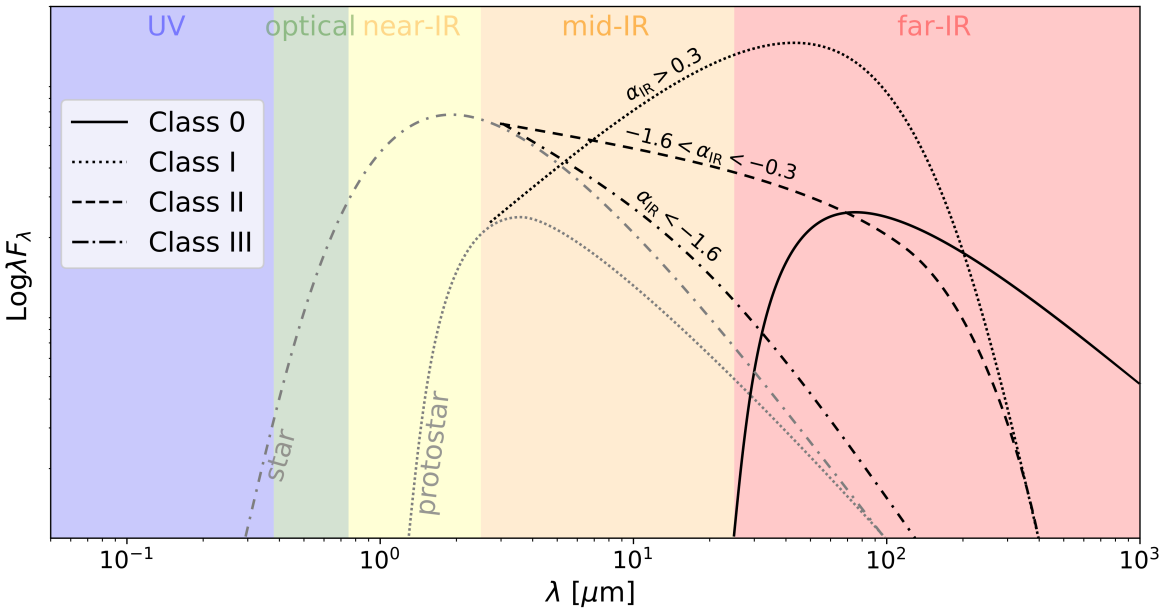

Figure 2.2. Sketch of the SED shapes and IR-excess slopes for Classes 0-III (following the spectral indices of Greene et al. (1994)). Figure from L.Eriksson.

1984), and quantified through the spectral index (Lada 1987)

$$\alpha_{IR} = \frac{d\log(\lambda F_\lambda)}{d\log\lambda} \ , \tag{2.1}$$

compared to the slope of the SED at mid-IR wavelengths. The rough shapes of the SEDs and the corresponding slopes of the IR-excess for the four main classes is illustrated in Fig. 2.2.

Class 0 corresponds to the first evolutionary step after the collapse of the prestellar core (Andre et al. 1993, 2000), while the protostar is still surrounded by a dense, massive, rotating, and infalling envelope. This is the main accretion phase and by the end of it, the young star has accreted most of its mass. There has been evidence that rotating discs are already forming around the protostars at this primitive stage (Codella et al. 2014; Gaudel et al. 2020; Murillo et al. 2013; Tobin et al. 2012), however these sources are heavily extincted by the thick, dusty, molecular gas envelope surrounding them, making it very hard to observe them.

Moving on to the **Class I** stage, most of the system's mass is now in the young star and the envelope starts dispersing, so that the disc is easier to be observed (e.g. Harsono et al. 2014). However, the duration of the Class 0 phase is quite short for potential observability, even though it is longer than the one for Class I (0.4 Myr in comparison to 0.2 Myr). Interestingly, rings and gaps have been observed in Class I discs, suggesting that any sort of mechanism responsible for substructures starts operating early on (see Sect. 2.1.3). At the same time, there has also been evidence for grain growth in Class I or even Class 0 but I will discuss this more in Sect. 2.2.1.

In the **Class II** stage, the envelope is completely dispersed, leaving behind a pre-main-sequence star and a protoplanetary disc. Given that the lifetimes of Class II sources are on the order of a few million years and that the disc is optically visible, they are significantly more common to observe. Greene et al. (1994), introduced,

Class	SED slope	Physical properties	Observational characteristics
0	–	$M_{\rm env} > M_{\rm star} > M_{\rm disk}$	No optical or near-IR emission
I	$\alpha_{\rm IR} > 0.3$	$M_{\rm star} > M_{\rm env} \sim M_{\rm disk}$	Generally optically obscured
FS	$-0.3 < \alpha_{\rm IR} < 0.3$		Intermediate between Class I and II
II	$-1.6 < \alpha_{\rm IR} < -0.3$	$M_{\rm disk}/M_{\rm star} \sim 1\%$, $M_{\rm env} \sim 0$	Accreting disk; strong Hα and UV
III	$\alpha_{\rm IR} < -1.6$	$M_{\rm disk}/M_{\rm star} \ll 1\%$, $M_{\rm env} \sim 0$	Passive disk; no or very weak accretion

Figure 2.3. Classification of YSOs with numerical boundaries for α_{IR} from Greene et al. (1994). Table from Williams & Cieza (2011).

also, the flat spectrum sources (**FS**) as intermediates between Class I and Class II.

Finally, **Class III** corresponds to the evolutionary stage where the disc has dispersed (with the exception of debris discs), and the SED is again dominated by the star, even though it can, normally, be distinguished from a main-sequence star. These different classes also feature different physical properties and to some extend distinct observational characteristics (Fig. 2.3).

Even though this classification is a useful tool when interpreting observations, it is prone to misclassifications due to the geometric orientation relative to the line of sight (Crapsi et al. 2008) and its multiplicity (either born as a binary system or part of a cluster). Another classification can also be used based on the mass of the YSO. Protostars, still embedded within their envelopes and with masses less than 2 $M_\odot$ are called **T-Tauri stars**[1] (Joy 1945). Pre-main sequence stars with masses between 2 and 8 $M_\odot$ are called **Herbig Ae/Be stars**. Their spectral types are A and B, while the ones for T Tauri protostars are F, G, K, M.

Both of the aforementioned classifications refer to low-mass star formation. The formation of massive stars (M $>$ 8 $M_\odot$) is more complicated to study (and obtain observational data), given that these stars evolve quickly and become main-sequence stars while deeply embedded in the envelope. Additionally, massive stars are found to be rare, with a frequency sharply decreasing with mass (Kroupa 2001).

In this thesis, what we call protoplanetary disc and consider as the birthing environment of planets is assumed to be a Class II disc around a solar mass star, however there has been increasing evidence that planet formation might begin earlier, during the Class I or even the Class 0 stage. I will discuss this in more detail in Chapter 6.

2.1.3 Disc substructures

High resolution (dust) observations have made it clear that protoplanetary discs sometimes feature substructures, posing the questions of how common these substructures are, how long do they last and how do they form. The various substructures are mainly observed in the millimeter continuum emission, however some features have also been observed in scattered light (e.g. Avenhaus et al. 2018, 2014; Benisty et al. 2015; Follette et al. 2015; Stolker et al. 2017). As mentioned in the previous chapter, the observed substructures are inner cavities, rings and gaps, spirals and azimuthal asymmetries or arcs and in some discs were multiple tracers have been

[1] After T-Tauri, the first star of this type to be observed.

compared, the type of substructure is different in each tracer. For example, MWC 758 and HD 135344 B, show spirals in the scattered light observations (Benisty et al. 2015; Stolker et al. 2017) and rings at sub-millimeter wavelengths (Cazzoletti et al. 2018; Dong et al. 2018). This could be due to different mechanisms but it could also be the same mechanism affecting various dust grain sizes in distinctive ways.

A very exciting prospect for the field of planet formation is that substructures are caused by planet-disc interactions (e.g. Dipierro et al. 2015; Pinilla et al. 2012a; Rosotti et al. 2016) and hopefully in the future, more observations will be able to confirm the formation of planets directly in the birthing environments.

Another (personally exciting) prospect for the formation of rings and gaps is the concentration near evaporation fronts (Ros & Johansen 2013; Saito & Sirono 2011; Zhang et al. 2015), however directly linking the features with icelines is complicated (van der Marel et al. 2018b).

Other substructure-forming mechanisms could be dust sintering, the redistribution of ice molecules on the surfaces of solids due to vapor transport and other effects (Okuzumi et al. 2012a) or self-induced dust traps, due to the backreaction from the dust to the gas (Gonzalez et al. 2017).

Finally, (magneto-) hydrodynamical instabilities, encompass several different instabilities[2] which can generate perturbations in the gas pressure that will, in turn, influence the dust velocities and potentially lead to concentrations (e.g. Flock et al. 2019; Klahr & Bodenheimer 2003; Lorén-Aguilar & Bate 2015; Suriano et al. 2019; Suzuki et al. 2016; Takahashi & Inutsuka 2016; Ueda et al. 2021; Uribe et al. 2011; Vorobyov et al. 2016).

The aforementioned mechanisms could also operate in combination and lead to substructured discs, for example, the interactions of a forming planet with the disc might lead to hydrodynamical instabilities that then cause observational features. Another important realization is the fact that substructures appear also in quite young systems (e.g. Segura-Cox et al. 2020) and I will discuss the implications of this more in Chapters 5 and 6.

Regardless of how these substructures form, they could be preferential locations for planetesimal formation and, thus, serve as the location where the first planetary embryos form and potentially start accreting pebbles (in the pebble accretion scenario, see Sect. 2.4.1). In addition, it is important to obtain reliable statistics over the frequency of substructures in protoplanetary discs. While they seem prevalent in high resolution observations, these were also surveys of massive and large samples (see also discussion in Bae et al. 2022). However, a new framework (FRANK) has identified previously not seen substructure in the inner discs of the DSHARP survey (Jennings et al. 2022), which implies that the compact and small discs (e.g. in the Taurus region, Long et al. 2019) appear smooth because they are not sufficiently resolved.

[2]As they are further away from the scope of this thesis I will not elaborate on those here but a review can be found in Bae et al. (2022)

2.1.4 Vertical and radial structure

The vertical structure of a protoplanetary disc can be defined as the steady-state solutions of the hydrodynamic equation. We start with the Poisson equation for the gravitational potential (vertical component g_z), assuming that the mass of the disc $M_{disc} \ll M_\star$, where $M_\star$ is the mass of the young star and that the scale height $H \ll R_{disc}$, with R_{disc} the radius of the disc

$$\frac{1}{\rho_g}\frac{dP}{dz} = -g_z \ . \tag{2.2}$$

The solution is then

$$\rho_g(r,z) = \frac{\Sigma_g(r)}{\sqrt{2\pi}H(r)} \exp\left(-\frac{z^2}{2H(r)^2}\right), \tag{2.3}$$

however normally there will be also a time evolution.

The vertical pressure scale height H is defined as

$$H = \frac{c_s}{\Omega} \ , \tag{2.4}$$

where

$$c_s = \sqrt{P/\rho} = \sqrt{\frac{k_B T}{\mu m_p}} \ , \tag{2.5}$$

is the sound speed, with k_B the Boltzmann constant, m_p the proton mass and μ the mean molecular weight in units of the proton mass. The Keplerian angular velocity is given by

$$\Omega = \sqrt{\frac{GM_\star}{r^3}} \ , \tag{2.6}$$

where G is the gravitational constant, $M_\star$ is the stellar mass and r is the orbital distance. Combining Equations 2.5 and 2.4 we find that under hydrostatic equilibrium,

$$T = \left(\frac{H}{r}\right)^2 \frac{GM_\star}{r}\frac{\mu m_p}{k_B} \ , \tag{2.7}$$

where H/r is the aspect ratio of the disc.

The evolution equation for the surface density of the disc has been derived by Pringle (1981) as

$$\frac{\partial \Sigma}{\partial t} = \frac{3}{r}\frac{\partial}{\partial r}\left[\sqrt{r}\frac{\partial}{\partial r}\left(\nu\Sigma\sqrt{r}\right)\right] \ . \tag{2.8}$$

The above can be analytically solved if we assume that viscosity has a power-law dependency in radius ($\nu \propto r^\gamma$, Lynden-Bell & Pringle 1974).

In the above formulation it was assumed that the disc is vertically isothermal which is not a realistic assumption and not one that is being used in the models presented in this thesis. However, the relations which were introduced above are useful to have at hand for the basic understanding of the protoplanetary disc structure and evolution. For some of the models in this thesis, we follow the hydrodynamical approach, where the continuity and Navier-Stokes equations are numerically integrated

in order to solve for the disc mass transport and energy time evolution (see Sect. 3.2.1). The rest of our models follow a simpler approach, where the analytical solution of Lynden-Bell & Pringle (1974), expressed as in Lodato et al. (2017), is used as an initialization and then the surface density equation is numerically solved (see Schneider & Bitsch 2021, for more information and for the temperature solution).

2.2 From dust to pebbles, planetesimals and planetary embryos

The processes which are discussed in the following sections (Sects. 2.2.1-2.4.4) are illustrated in Fig. 2.4. This figure also serves as a visualized summary of the projects which are part of this thesis and of the motivation discussed in Chapter 1. Roughly, each panel corresponds to one (or more) specific project(s) included in this thesis. However, it should be noted that in the models of Chapter 3, we include silicates and water-ice only, in Chapters 3 and 4, drift is not included and in Chapters 5 and 6, a simplified model for the grain size distribution is used, along with a small subset of the opacities used in Chapters 3 and 4.

2.2.1 Dust dynamics

Grain growth

The dust contained in the prestellar infalling core is assumed to have the sizes of the interstellar medium, around 0.005 to 1 μm, depending on the composition of the dust grain (Mathis et al. 1977). In the classical model of star formation, it was assumed that grain growth started happening in protoplanetary discs, in later stages (Class II phase), however there is increasing observational evidence that grains even in Class 0 envelopes are larger than 1 μm, in the infrared (e.g. Pagani et al. 2010), in millimeter (e.g. Galametz et al. 2019; Kwon et al. 2009; Miotello et al. 2014) or molecular gas emission (e.g. Harsono et al. 2018). On a theoretical point of view, though, it is uncertain how dust grows under the conditions within cores and envelopes (e.g. Guillet et al. 2020; Ormel et al. 2009; Ossenkopf 1993; Silsbee et al. 2022; Xu & Armitage 2023).

Regardless of when dust grain growth starts, planet formation requires that this primordial dust reservoir grows over twelve orders of magnitude to make terrestrial planets or the cores of giant planets. The first step in this direction happens via direct collisions between dust grains which lead to coagulation (i.e. sticking) and therefore larger aggregates form. The full dust coagulation equation has been formulated (in discrete form) by Smoluchowski (1916a) but it challenging to solve and it is computationally very expensive (see for example Dullemond & Dominik 2005), therefore it is often solved in an azimuthally and vertically averaged setup (e.g. Birnstiel et al. 2010a, 2012a; Brauer et al. 2008a). It should be noted that full coagulation simulations coupled with hydrodynamical models of a gap-opening planet embedded in a protoplanetary disc have shown that simplified ways to treat the

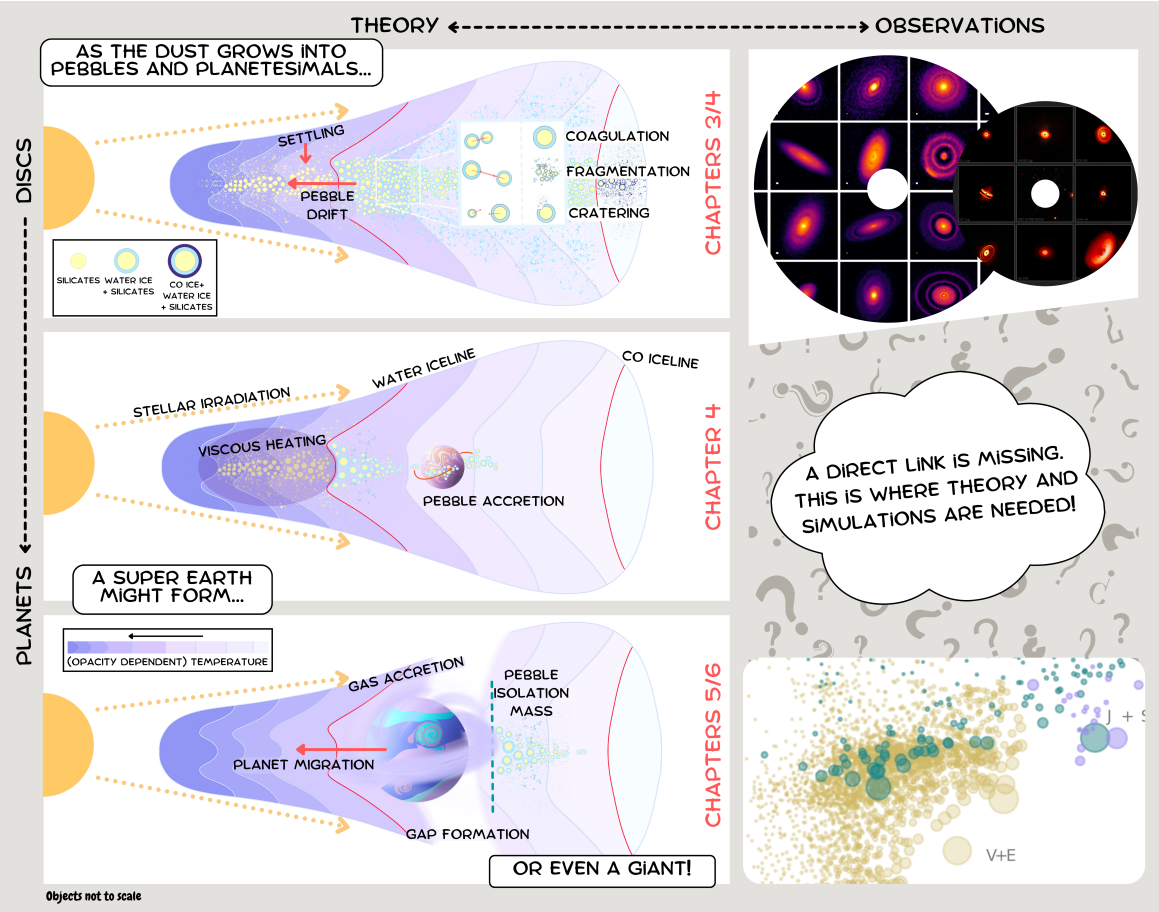

Figure 2.4. Illustration of the various processes within a protoplanetary disc related to dust growth and evolution and planet formation. From top to bottom, we go from discs to planets and from left to right, we go from theory to observations. Each panel corresponds to one (or more) projects included in this thesis (as noted in red letters next to the panels).

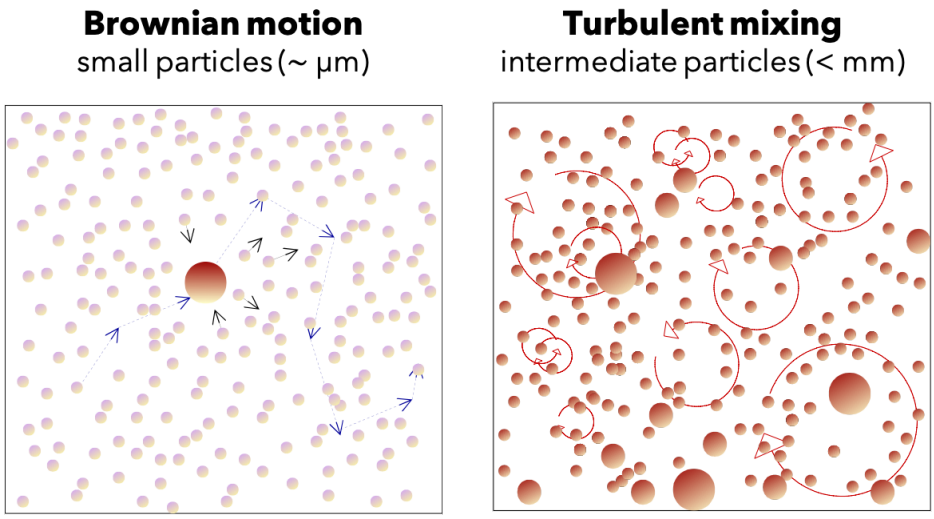

Figure 2.5. Motions which induce relative velocities for dust grains (orange spheres) on a small scale. Left: Very small particles are stochastically scattered by the gas molecules (light purple spheres). Right: Larger particles are affected by the turbulent eddies of the gas (red arrows).

dust coagulation do not recover the results (e.g. depth and shape of the planetary gap) perfectly (Drążkowska et al. 2019).

Relative velocities

The driver of these collisions is the relative velocities between the grains due to the various motions governed by their sizes. For example, very small particles are governed by Brownian motion and as a result, relative velocities can exist even between grains of the same sizes. As the particles grow, they start following the turbulent motions (eddies, L.F. 1922) of the gas, to a degree that depends on their aerodynamic properties and the strength of the turbulence, until they become large enough to get completely decoupled from it (Birnstiel et al. 2010b; Brauer et al. 2008a). The small scale motions of dust within gas are illustrated in Fig.2.5, while in the top and middle panel of Fig. 2.4, I show the dust motions on a larger scale (drift & settling, see Sect. 2.2.2), as well as a summary of the possible outcomes after a collision (top panel).

Stokes number

The evolution of the dust grains is therefore regulated by their aerodynamical properties, and so it is convenient to describe them not by their sizes, but by their Stokes number which characterizes the behavior of dust particles suspended within the gas (operating as a fluid). It is defined as the product of the particle stopping or friction time and the Keplerian angular velocity,

$$St = \tau_f \Omega_K \tag{2.9}$$

The stopping or friction time is the time it takes a dust particle to decelerate

due to gas drag and in the Epstein regime[3] it is defined as

$$\tau_f = \frac{m\Delta u}{|F_D|} = \frac{\rho_s s}{\rho_g u_{th}} \ , \tag{2.10}$$

for particles of size s, volume density ρ_s and mass $m = (4/3)\pi s^3 \rho_s$, with $|F_D|$ the drag force (Weidenschilling 1977a; Whipple 1972).

The mean thermal speed is connected to the sound speed (Eq. 2.5) since

$$u_{th} = \sqrt{\frac{8k_B T}{\pi \mu m_p}} \ , \tag{2.11}$$

where m_p is the proton mass and $\mu = 2.3$ is the mean molecular weight in proton masses. The Stokes number is then

$$St = \sqrt{\frac{\pi}{8}} \frac{\rho_s s}{c_s \rho_g} \Omega_K = \sqrt{\frac{\pi}{8}} \frac{\rho_s s}{\rho_g H_g} \ , \tag{2.12}$$

using Eq.(2.4) and at midplane

$$St_{mid} = \frac{\pi}{2} \frac{\rho_s s}{\Sigma_g} \ . \tag{2.13}$$

Vertical distribution

Theoretical studies have shown that as dust grains grow and decouple from the gas, they tend to settle towards the midplane (e.g. Dullemond & Dominik 2004). This has also been confirmed by observations which report that millimeter dust grains are confined within scale heights of a few AU (e.g. Gräfe et al. 2013; Pinte et al. 2016; Villenave et al. 2020), while the typical scale heights of the gaseous disc are assumed to be higher than 10 AU (Law et al. 2021; Rich et al. 2021).

The grains of a given size can be assumed to be vertically distributed (similarly to the gas density, Eq. 2.3) according to the following

$$\rho_d = \rho_{d,0} \exp\left(-\frac{z^2}{2H_d^2}\right) \ , \tag{2.14}$$

with

$$\rho_{d,0} = \frac{\Sigma_d}{\sqrt{2\pi} H_d} \tag{2.15}$$

the dust density at midplane and the dust scale height derived by Dubrulle et al. (1995)

$$H_d = H \sqrt{\frac{\alpha}{\alpha + St}} \ , \tag{2.16}$$

where H_d and H is the dust and gas scale height respectively, St is Stokes number of the particles in the Epstein regime and at midplane, given by Eq. 2.13. Vertical settling towards the midplane is counteracted by the turbulent motions of the gas, therefore, the Stokes number of a particles determines (how well coupled it is to the gas and thus) how much it is affected by settling.

[3] which describes the movement of the dust particle within the gas when the radius of the dust sphere is smaller compared to the mean free path of the gas molecules

2.2.2 Barriers

Fragmentation

When two dust grains collide there are other potential outcomes instead of coagulation. These are the barriers that keep the sizes of the grains the same or even smaller than their initial before the impact. These barriers can be fragmentation, cratering/erosion or bouncing (see Blum & Wurm 2008, for a review). The fragmentation barrier is defined by the fragmentation or threshold velocity u_f. When the collision speed is above this threshold velocity, then the two dust grains break up into many smaller grains. Usually, a constant value is used in studies (as we do here), however it should actually depend on the properties of the dust, such as the composition or porosity (Güttler et al. 2010a; Wurm et al. 2005).

The Stokes number of the largest possible particle size can be found by equating the relative velocity induced by turbulent motion $\Delta u = \sqrt{3\alpha St} c_s$ (Ormel & Cuzzi 2007) and the aforementioned fragmentation velocity u_f as in Birnstiel et al. (2009)

$$St_{fragm} \simeq \frac{1}{3}\frac{u_f^2}{\alpha c_s^2} \ . \tag{2.17}$$

and in terms of grain size (at midplane)

$$s_{max} = \frac{2\Sigma_g}{3\pi\alpha\rho_s}\frac{u_f^2}{c_s^2} \ , \tag{2.18}$$

with $\rho_s = 1.6$ g/cm^3 the assumed density of each particle.

Bouncing

Roughly said, when the collision speed is equal to the coagulation speed, the particles are said to be bouncing (Zsom et al. 2010a). This is an elastic collision, therefore the masses of the colliding dust grains remain unchanged. The bouncing barrier is also, highly dependent on the dust properties, for example highly compact silicate particles might be more susceptible to it (Wada et al. 2009).

Cratering

When the mass of the target body is significantly larger than that of the impactor then that smaller particles only excavates parts of the mass of the much larger body (Sirono 2004). In other words, in this case the collision speed is higher that the threshold velocity and the result is not complete fragmentation but the maximum grain size (or Stokes number) is still limited.

Radial drift

The final barrier, at least discussed here, is the drift barrier. The gaseous disc gets hotter and denser the closer to the star, therefore it has a radial pressure gradient support that leads to a sub-Keplerian velocity

$$u_\phi = u_K(1-\eta) \ , \tag{2.19}$$

where $u_K = \sqrt{GM_\star/r}$ is the Keplerian orbital velocity. The dust particles do not "feel" this pressure gradient force so they would follow Keplerian orbits if left unperturbed. Being suspended within the gas, forces them to experience a gas drag force from it, which leads to a radial drift velocity towards the star (Weidenschilling 1977a)

$$u_r = -\frac{2\eta u_K}{St + St^{-1}} \ . \tag{2.20}$$

The maximum drift velocity corresponds, thus, to particles with $St \sim 1$, the pebbles. Small dust grains with $St \ll 1$ are well coupled to the gas and follow its motion, while large objects with $St \gg 1$ are decoupled from the gas and are minimally affected by radial drift.

2.2.3 Forming the first embryos

The barriers which were discussed above, introduced, as a logical consequence, the meter-barrier problem. Following a simple dust growth approach, growth above meter-sized objects either needs "lucky particles" which overcome the barriers (Garaud et al. 2013; Windmark et al. 2012) or considering that porous aggregates will be more "sticky" (Kataoka et al. 2013; Okuzumi et al. 2012a). However, both of these pathways have been found to be very inefficient (Booth et al. 2018; Estrada et al. 2016; Homma & Nakamoto 2018; Krijt et al. 2015; Schräpler et al. 2018)

The most prevalent pathway for planetesimal formation is the streaming instability (SI), which is the concentration of pebbles into dense filaments which eventually collapse due to their self-gravity (Johansen & Youdin 2007; Youdin & Johansen 2007; Youdin & Goodman 2005). The SI is a complex mechanism, based on the interplay between the dust and gas. A clump of dust drifts inwards, but also causes a back-reaction to the gas that decreases the velocity difference between the dust and gas, therefore the gas drag, and decreases the radial drift of the dust. The super-Keplerian velocities are then bringing the dust back to enhance the initial overdensity (see Lesur et al. 2022, for a review). The SI relies on critical Stokes numbers (~ 0.1) and a critical metallicity (or in other words the dust-to-gas ratio of the column densities) which is typically found to be greater than the solar metallicity that we assume is the initial condition in the disc (Yang et al. 2017).

The size of the planetesimals created this way is still under active research with most studies refering to a range from several hundred meters to several hundred kilometers (e.g. Klahr & Schreiber 2020; Schäfer et al. 2017). When an object reaches a size of over a few kilometers, it is no longer affected by gas drag, so its orbit is maintained and it exerts a significant gravity on other bodies which leads to fast growth (either via planetesimal or via pebble accretion). Additional growth might be needed to reach embryo masses, which is assumed to happen via mutual collisions (e.g. Clement et al. 2020; Kokubo & Ida 1998) or a much larger planetesimal can form directly via the SI (e.g. Johansen et al. 2011, 2012). In this thesis (as is usually done in pebble accretion studies), we start our planet formation models with already formed planetary embryos, either with a fixed initial mass (Chapter 4) or with the

transition mass (Chapters 5/6),

$$M_t = \sqrt{\frac{1}{3}\frac{\Delta v^3}{G\Omega}} \ , \tag{2.21}$$

which is relevant to protoplanets accreting pebbles in the Hill (shear) regime (Johansen & Lambrechts 2017a; Lambrechts & Johansen 2012a). Therefore, the starting embryo mass depends on the local conditions, Δv, the sub-Keplerian speed of the particles, and Ω, the Keplerian angular frequency.

2.3 Radiative transfer

2.3.1 The formal radiative transfer equation

In Astrophysics, our way to extract information directly from our subjects is through the radiation they are emitting. However, this task requires an analysis of how this radiation is produced and how it interacts with any medium on its way (see Steinacker et al. 2013, for a review[4]). Any radiation field can be described by its intensity $I(\mathbf{x}, \mathbf{n}, \lambda)$, with $\mathbf{x}$ the location, $\mathbf{n}$ the unit vector indicating the direction and λ the wavelength of the emitted radiation. The medium can absorb all or part of the incident light. Then energy is transferred from the ray to the material and the intensity of the light is reduced (extinction).

The formal radiative transfer equation can be written as

$$\mathbf{n} \cdot \nabla I_\lambda(\mathbf{x}, \mathbf{n}) = j_\lambda(\mathbf{x}) - \kappa_\lambda(\mathbf{x})\rho(\mathbf{x})I_\lambda(\mathbf{x}, \mathbf{n}) \ , \tag{2.22}$$

where κ is the opacity (see Sect. 2.3.3), ρ the density of the medium through which a ray of light is passing, therefore the second term of the right-hand side characterizes the absorption of the radiation from the medium. The first term, the emissivity $j_\lambda(\mathbf{x})$, characterizes the stellar emission itself.

In general, the extinction of light within a protoplanetary disc is caused by the absorption and scattering from the dust particles (Bohren & Huffman 1983; van de Hulst 1957). Scattering is caused by inhomogeneities in the medium through which light travels, which in this case is a mixture of gas and dust. Any material has inhomogeneities because the molecules it consists of act as scattering centres, but their arrangement defines the efficiency of scattering. Dust grains are considered to be sufficiently distant so that scattering due to one particle does not affect the other ones. In the above formulation, multiple scattering has be neglected.

The formal radiative transfer can be numerically solved, usually with a code such as RADMC3D, using a ray tracing approach. However, in the hydrodynamical models of this thesis (Chapters 3 and 4) we use the flux-limited diffusion (FLD) approximation for the radiation flux $\mathbf{F}$ as described in Levermore & Pomraning (1981)

$$\mathbf{F} = -\frac{\lambda c}{\rho\kappa_R}\nabla E_R \ . \tag{2.23}$$

[4] or here for a nice overview

In the flux-limited diffusion equation, c is the speed of light, α_R is the radiation constant, κ_R is the Rosseland mean opacity and λ the flux-limiter of Kley (1989).

2.3.2 Solutions of the radiative transfer equation

A body that has the ability to absorb all light that hits it is called a blackbody. To a rough approximation, the stellar radiation can be described by the blackbody spectrum. The intensity of the blackbody radiation can be calculated via the Planck function which describes the amount of energy that the body emits per unit area of the body, per unit solid angle that the radiation is measured over, at a given wavelength λ and temperature T:

$$B_\lambda(\lambda, T) = \frac{2hc^2}{\lambda^5} \frac{1}{e^{\frac{hc}{\lambda k_B T}} - 1} \ , \tag{2.24}$$

with h the Planck constant, k_B the Boltzmann constant and c the speed of light.

The flux can be defined as

$$F_\lambda = \frac{\cos i}{d^2} \int B_\lambda(T_\lambda)(1 - e^{-\tau_\lambda \sec i}) 2\pi r dr \ , \tag{2.25}$$

where i is the inclination angle, however usually it is assumed that the sources are face-on, therefore $i = 0$. The flux relates to the intensity as $F = \int I_\lambda cosi \ d\Omega$, with Ω the solid angle.

The intensity of the continuum emission from dust grains (neglecting scattering) can be calculated as:

$$I_\lambda = B_\lambda(T_{dust})(1 - e^{-\tau_\lambda}) \tag{2.26}$$

There are two limiting cases:

⋆ If the dust emission is optically thick ($\tau_\lambda >> 1$), then

$$I_\lambda = B_\lambda(T_{dust}) \tag{2.27}$$

⋆ If the dust emission is optically thin ($\tau_\lambda << 1$), then

$$I_\lambda = B_v(T_{dust})\tau_\lambda \tag{2.28}$$

2.3.3 Opacity

The opacity of a medium is a measurement of its impenetrability to radiation, it, thus describes the absorption or scattering of radiation from that medium, and therefore depends on its material properties and the wavelength of the incident light (Bohren & Huffman 1983; van de Hulst 1957). The opacity within protoplanetary discs is mainly determined by dust, which has continuum opacities, covering a wide part of the electromagnetic spectrum. Based on the amount, size, structure and the composition of the dust particles, the disc (or a part of it) can be optically thin or thick. An optically thin disc lets light pass through it without absorption and it emits radiation proportionally to the emitting area of the particles, whereas in an optically

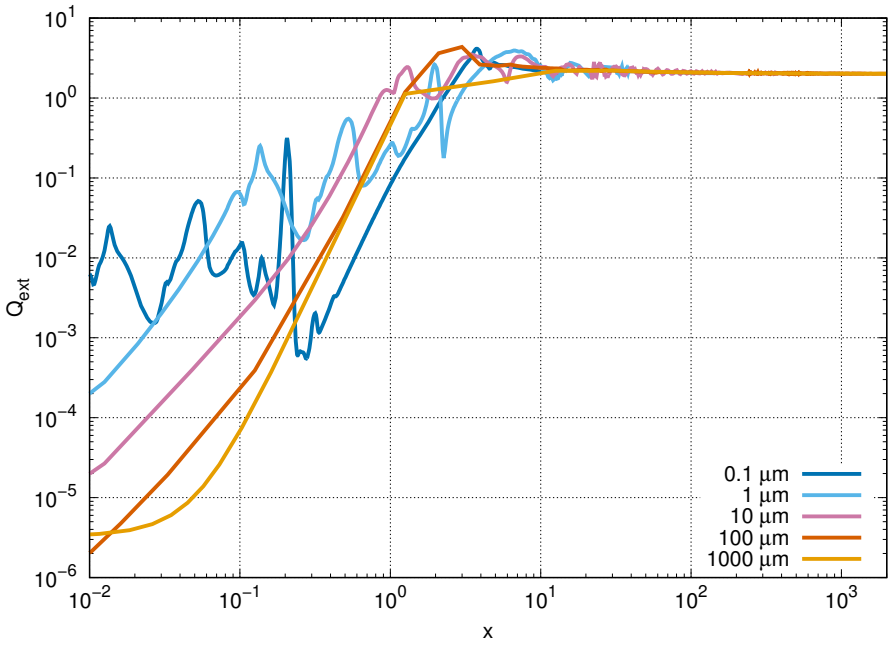

Figure 2.6. Extinction coefficient as a function of the size parameter for different grain sizes, produced using the opacity module of RADMC3D. From S.Savvidou, 2018.

thick disc that absorbs all or part of the incident light, the emission is proportional to the surface area of disc. The opacity is a very important factor of a protoplanetary disc since it defines its observational characteristics, either on the thermal continuum emission or by affecting the density structure and the temperature which produces different excitation conditions for the gas lines.

The wavelength dependent opacities κ_λ for dust particles can be calculated through Mie theory, which describes the extinction of an electromagnetic plane wave by a homogeneous, isotropic sphere. More specifically, the wavelength dependent opacity can be written as (Movshovitz & Podolak 2008)

$$\kappa_\lambda = \frac{\sigma_\lambda n_{gr}}{\rho_g} = \frac{Q_e(x)\pi s^2 n_{gr}}{\rho_g} \tag{2.29}$$

where $\sigma_\lambda = Q_e \pi s^2$ is the effective cross-section of a spherical dust grain, Q_e is the extinction efficiency and $x = 2\pi s/\lambda$ the size parameter. The number density of grains is given by $n_{gr} = f_{DG}\rho_g/m_{gr}$, where m_{gr} is the grain mass, f_{DG} is the dust-to-gas ratio, ρ_g is the gas density and s is the grain size. The extinction coefficient is a sum of the absorption and scattering coefficient so it can be expressed as (van de Hulst 1957)

$$Q_e = Q_a + Q_s \ , \tag{2.30}$$

therefore when scattering is neglected $Q_e = Q_a$.

The behavior of the extinction coefficient Q_e and therefore κ_λ is not only a function of the size parameter x, but also of the refractive index $m = n_r + in_i$, which is also dependent on wavelength and on the grain composition (see Fig. 2.6), however to understand it better, the extinction efficiency $Q_e(x)$ can be empirically

fitted as follows (Mordasini 2014)

$$Q_e(x) \approx \begin{cases} 0.3x, & \text{if } x < 0.375 \\ 0.8x^2 & \text{if } 0.375 \leq x < 2.188 \\ 2 + \frac{4}{x} & \text{if } 2.188 \leq x < 1000 \\ 2 & \text{if } x \geq 1000 \end{cases} . \tag{2.31}$$

Therefore, when the size of the particle is a lot smaller than the wavelength of the incident radiation, absorption dominates over scattering and the extinction coefficient is proportional to the grain size. When the size of the particle is a lot larger than the wavelength of the incident radiation then the extinction coefficient is approximately constant and equal to 2. This leads to the paradox that a large particle removes twice the incident energy (Bohren & Huffman 1983). The paradox is solved by considering that at this limit, while all of the incident energy is absorbed by the particle, the edges also scatter an equal amount of energy due to diffraction.

Instead of a monochromatic (single-wavelength) opacity, its often more useful and computationally easier to have "mean" opacities which are averaged over all wavelengths. These averaged opacities show the tendency of the species to absorb or scatter radiation of all wavelengths (for a given density and temperature). The difference between different mean opacities comes from the weighting with a different function. We need to choose the appropriate mean opacity depending on the physical quantity we want the opacity for. So in simple words, one thinks what they want to use the opacities for and chooses the most appropriate weighting function to better approach the correct values for this physical quantity. A more detailed discussion on the averaged opacities, and especially in regards to our models, can be found in Sect. 3.2.2.

2.4 Planet formation within the core accretion scenario

In the classical core accretion model (Pollack et al. 1996), a planetary embryo will grow further by the accretion of planetesimals. The embryo has a collisional cross section which is much larger than its physical geometric cross section, therefore for collisional velocities lower than the escape velocity, the smaller planetesimals get accreted in a runaway regime (Kokubo & Ida 1996; Safronov 1969). However, planetesimals are minimally affeted by gas drag and tend to remain in their orbits which means that planetesimal accretion is heavily regulated by the available surface density (of the planetesimals) around the planetary embryo and the growth timescales can be very long (Fortier et al. 2013; Johansen & Bitsch 2019; Lambrechts & Johansen 2012a; Levison et al. 2010; Rafikov 2004). This mechanism was not used for the models of this thesis, therefore I will instead elaborate on the mechanism that we use.

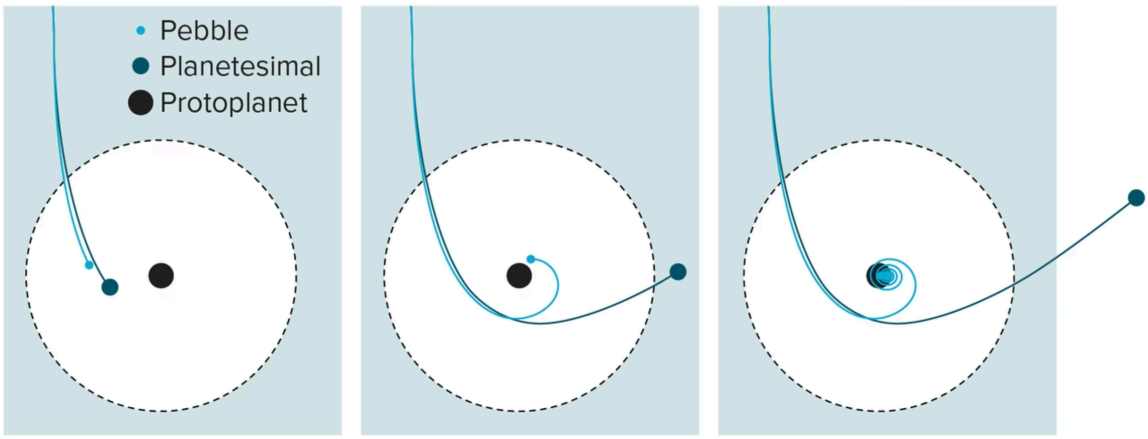

Figure 2.7. Difference between the trajectory of a pebble moving towards a protoplanet and a planetesimal. The dotted circle shows the gravitational influence of the planet. Source: M. Lambrechts and A. Johansen/L. Modica/Knowable

2.4.1 Pebble accretion

In the recent years, the emerging paradigm as a planet formation mechanism has been pebble accretion (see Johansen & Lambrechts 2017a; Liu & Ji 2020; Ormel 2017, for a review), with the first work showing the increased efficient presented by Johansen & Lacerda (2010). As discussed in Sect. 2.2.1, pebbles are a natural outcome of dust coagulation, therefore they are expected (and observed) to contain a significant part of the solids mass in a protoplanetary disc. At the same time, they are the most affected by gas drag which means that pebble accretion is not limited mainly to the vicinity of the planet but it can take advantage of the total pebble flux towards the planet exterior to its orbit (Ormel & Klahr 2010a). This significantly reduces the planetary growth timescales (Lambrechts & Johansen 2012a) which can be critical especially for giant planets (see also Chapter 5).

In our models we use the pebble accretion rates from Johansen & Lambrechts (2017a). To define the pebble accretion rate we need to distinguish between the 2D and the 3D regime, depending on how the pebble scale height H_d compares to the effective accretion radius of the planet $(St/0.1)^{1/3} r_{Hill}$, where the Hill radius is

$$r_{Hill} = r \left(\frac{M_p}{3M_\odot} \right)^{1/3} . \tag{2.32}$$

The 2D pebble accretion rate is

$$\dot{M}_{\rm 2D} = 2 \left(\frac{St_{mid}}{0.1} \right)^{2/3} r_{Hill} v_{Hill} \Sigma_d \ , \tag{2.33}$$

with $v_{Hill} = \Omega r_{Hill}$ and the 3D accretion rate is

$$\dot{M}_{\rm 3D} = \dot{M}_{\rm 2D} \left[\frac{\pi \left(\frac{St_{mid}}{0.1} \right)^{1/3} r_{Hill}}{2\sqrt{2\pi} H_d} \right] . \tag{2.34}$$

The transition from the 2D to the 3D regime happens when

$$\frac{\pi \left(\frac{St_{mid}}{0.1}\right)^{1/3} r_{Hill}}{2\sqrt{2\pi} H_d} < 1 \ , \tag{2.35}$$

following Morbidelli et al. (2015a).

Pebble isolation mass

Pebble accretion operates until the mass of the forming planet reaches the pebble isolation mass (Ataiee et al. 2018; Bitsch et al. 2018; Lambrechts et al. 2014; Morbidelli & Nesvorny 2012), which depends on the disc properties. The growing planet interacts gravitationally with the disc, pushes material away from its orbit, and eventually opens a gap in the gaseous disc (e.g. Crida & Morbidelli 2007; Crida et al. 2006; Goldreich & Tremaine 1980; Lin & Papaloizou 1986). Gas accretion (see Sect. 2.4.2) itself can even help in deepening this gap (Bergez-Casalou et al. 2020; Crida & Bitsch 2017; Ndugu et al. 2021). When the planet is massive enough and the gap is deep enough, then a pressure trap is generated which blocks the dust from drifting interior to the planet's orbit (Paardekooper & Mellema 2006). The pebble isolation mass has been approximated via hydrodynamical simulations by Bitsch et al. (2018) as

$$M_{iso} = 25 f_{\rm fit} M_\oplus \ , \tag{2.36}$$

with

$$f_{\rm fit} = \left[\frac{H/r}{0.05}\right]^3 \left[0.34 \left(\frac{\log(0.001)}{\log(\alpha)}\right)^4 + 0.66\right] \left[1 - \frac{\frac{\partial \ln P}{\partial \ln r} + 2.5}{6}\right] \ , \tag{2.37}$$

where $\frac{\partial \ln P}{\partial \ln r}$ is the radial pressure gradient.

2.4.2 Gas accretion

In a simplified picture, the planetary core first has to become massive enough before it starts accreting gas, so that it can gravitationally bind it. In principle, the planet is kept hot while it still accretes solids, therefore it needs to reach the pebble isolation mass before gas accretion begins. The formation of gaseous planets is limited by the lifetime of the gaseous disc, therefore it needs to happen on relatively short timescales, of a few million years (Haisch et al. 2001; Mamajek 2009).

Gas accretion is a very complex mechanism that it still under active research, in 2D (e.g. Crida & Bitsch 2017; Kley 1999) or 3D (e.g. Ayliffe & Bate 2009; D'Angelo et al. 2003; Lambrechts et al. 2019; Machida et al. 2010; Schulik et al. 2019; Tanigawa & Tanaka 2016), therefore various gas accretion rates exist in the literature. The simplified procedure that was described above is not necessarily realistic. For example, the JUNO mission measurements imply that Jupiter's core is not solid but rather diluted (Debras & Chabrier 2019; Vazan et al. 2018; Wahl et al. 2017). Pebbles can sublimate before they reach the core, heating up the envelope at the sublimation location (so that the next pebbles will sublimate exterior to this radius)

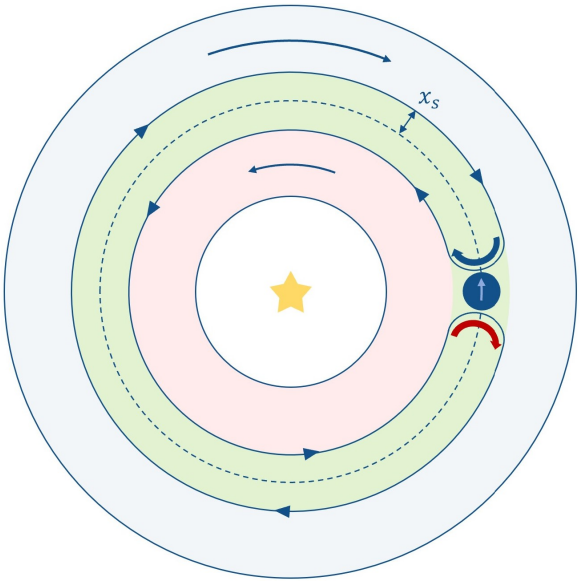

Figure 2.8. Illustration of the horseshow region (green area) of a planet (blue circle) moving in a circular orbit (dashed line) within a protoplanetary disc. The thick red (resp. blue) arrow shows the motion of the gas from the inner (resp. outer) to the outer (reps. inner) disc due to the angular momentum exchange. Figure from C. Bergez-Casalou.

and creating thus a gradual compositional gradient in the planetary interior (Ormel et al. 2021).

The core and envelope buildup are not necessariliy distinct phases and pebbles can evaporate within the envelopes increasing the heavy elements content (Lambrechts et al. 2014; Venturini et al. 2016). In our models in Chapters 5 and 6, we assume initially that 90% of the total accreted mass contributes to the core buildup and 10% already contributes to the envelope (Schneider & Bitsch 2021). When the planet reaches the pebble isolation mass, then all of the material accretes into the envelope. More details can be found in Chapter 5.

2.4.3 Gap formation

As mentioned above, the gravitational interactions between the planet (Crida et al. 2006) and the disc and gas accretion itself to some degree (depending on the disc and planet properties) (Bergez-Casalou et al. 2020) push the gas away from the planetary horseshoe orbit and this eventually results in a gap opening in the disc (Crida & Morbidelli 2007). In other words, the torque exerted by the planet, pushing the material away, is fighting the torque exerted by the viscosity of the disc working to fill the gap with gas. This way a horseshoe region is created which (in the planet's reference frame) corresponds to the ring where the gas does a "U-turn" at the planet location, orbiting in an horseshoe shape (see Fig. 2.8).

Crida et al. (2006) define that a planetary gap has opened when only 10% of the initial, unperturbed gas surface density remains and they give the gap-opening criterion as

$$P = \frac{3}{3}\frac{H_{gas}}{r_H} + \frac{50}{q\mathcal{R}} \leq 1 \ , \tag{2.38}$$

where r_H is the Hill radius, q is the planet to stellar mass ratio, $\mathcal{R}$ the Reynolds number. The depth of the gap (in our code) follows (Ndugu et al. 2021)

$$f_{gap} = f(\mathcal{P}) f_A \ , \tag{2.39}$$

with

$$f(\mathcal{P}) \approx \begin{cases} \frac{\mathcal{P}-0.541}{4}, & \text{if } \mathcal{P} < 2.4646 \\ 1.0 - exp\left(-\frac{\mathcal{P}^{3/4}}{3}\right) & \text{otherwise} \end{cases} \tag{2.40}$$

the depth of the gap caused by gravity after Crida & Morbidelli (2007) and f_A the contribution from accretion. See Schneider & Bitsch (2021) for more details.

2.4.4 Planet migration

The angular momentum exchange between the planet and the disc leads also to orbital migration. The net effect of the tidal force of the planet causes a density wake around it which exerts gravitational torque on the planet. The internal density wake causes a positive torque which accelerates the planet, while the external density wake causes a negative torque which decelerates the planet. The total torque of the two aforementioned is called Lindblad torque and usually the external torque dominates, resulting in inward migration (Goldreich & Tremaine 1979; Lin & Papaloizou 1979).

At the horseshoe region of the planet (Fig. 2.8), the gas coming from the inner disc (red region) is hotter and denser whereas the gas coming from the outer disc (blue region) is colder and less dense, therefore at the "U-turn" close to the planet, the exchange of angular momentum between these results in the corotation torque. There are actually two components in the corotation torque: the barotropic torque caused by the change of density and the entropy related componenent due to the change of temperature at the horseshoe region. In the code used for the models in Chapter 5 and 6, we use the torque formulat of (Paardekooper et al. 2011a) for the Lindblad and the corotation torques. Additionally, we include the thermal torque (Lega et al. 2014a; **?**) which is caused by the thermal heat exchange between the disc and the planet due to density perturbations and the dynamical torque (Paardekooper 2014; Pierens 2015) which is due to feedback processes of the migration rate of the planer. The resulting torque exerted on the planet from the processes discussed above leads to an orbital migration that is called **Type I migration**.

After the planet opens a gap in the disc, the gap needs to refill behind it and its migration slows down. This is called **Type II migration** (Lin et al. 1996; Papaloizou & Lin 1984) and it is regulated by the viscosity of the disc that is responsible for spreading the disc material into the gap. In addition to those, an intermediate migration regime can also emerge, the **Type III migration**, when the gap region is only partially depleted (Masset & Papaloizou 2003). As all concepts included in this thesis, planetary migration is complicated and it is still very actively researched. For example, Kimmig et al. (2020), show that in a wind-driven (rather than viscous-driven) accretion disc, planetary migration might be significantly different compared to the models discussed above.

3

Thermal structures of protoplanetary discs

From "Influence of grain growth on the thermal structure of protoplanetary discs", Savvidou et al. 2020.

In a nutshell...

The thermal structure of a protoplanetary disc is regulated by the opacity that dust grains provide. However, previous works have often considered simplified prescriptions for the dust opacity in hydrodynamical disc simulations, for example, by considering only a single particle size. In the present work, we perform 2D hydrodynamical simulations of protoplanetary discs where the opacity is self-consistently calculated for the dust population, taking into account the particle size, composition, and abundance. We first compared simulations utilizing single grain sizes to two different multi-grain size distributions at different levels of turbulence strengths, parameterized through the α-viscosity, and different gas surface densities. Assuming a single dust size leads to inaccurate calculations of the thermal structure of discs, because the grain size dominating the opacity increases with orbital radius. Overall the two grain size distributions, one limited by fragmentation only and the other determined from a more complete fragmentation-coagulation equilibrium, give comparable results for the thermal structure. We find that both grain size distributions give less steep opacity gradients that result in less steep aspect ratio gradients, in comparison to discs with only micrometer-sized dust. Moreover, in the discs with a grain size distribution, the innermost (< 5 AU) outward migration region is removed and planets embedded is such discs experience lower migration rates. We also investigated the dependency of the water ice-line position on the alpha-viscosity (α), the initial gas surface density ($\Sigma_{g,0}$) at 1 AU and the dust-to-gas ratio (f_{DG}) and find $r_{ice} \propto \alpha^{0.61}\Sigma_{g,0}^{0.8} f_{DG}^{0.37}$ independently of the distribution used in the disc. The inclusion of the feedback loop between grain growth, opacities, and disc thermodynamics allows for more self-consistent simulations of accretion discs and planet formation.

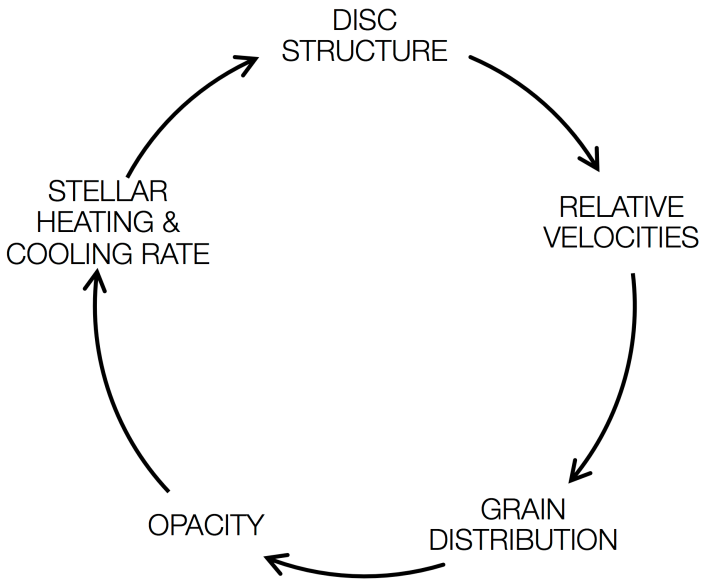

Figure 3.1. Graphical illustration of the feedback loop. The structure of a protoplanetary disc is determined by this loop: temperature affects the relative velocities for grains of different sizes. Through the relative velocities, we find the outcomes of collisions between grains, therefore a grain size distribution is created. The various particle sizes influence the opacity of the disc, which then affects its cooling rate. This way the temperature of the disc changes and subsequently its whole structure.

3.1 Context

Protoplanetary discs surround young stars for the first few million years after their formation and they are the birthplaces of planetary systems. The position of the iceline within the discs influences the formation and growth of planets. Planetesimal formation has been found to be enhanced or even initiated there because of water vapor that is diffused outwards from the hot, inner disc and recondenses after the iceline (Ros & Johansen 2013). This recondensation increases the abundances of icy pebbles, which have better sticking properties compared to dry aggregates (Gundlach & Blum 2015a; Supulver et al. 1997; Wada et al. 2009), causing a pile-up near the iceline and triggering the streaming instability (Drążkowska & Alibert 2017a; Guillot et al. 2014; Schoonenberg & Ormel 2017a).

An increase in the dust surface density after the iceline can also aid in the growth of gas giant planet cores (Stevenson & Lunine 1988). The location and the evolution of the iceline location can be defining for the innermost boundary of gas giant formation and along with other parameters, such as the disc's mass, it can also determine what kind of planets will be created (Kennedy & Kenyon 2008) and their masses (Morbidelli et al. 2016, 2015b). In addition to that, the location of the iceline transition affects the composition of exoplanetary atmospheres (Cridland et al. 2016; Madhusudhan et al. 2017a, 2014) .

The location of the iceline is determined by the local temperature in the disc (Hayashi 1981b; Podolak & Zucker 2004; Sasselov & Lecar 2000). The thermal structure of the discs is thus decisive for planetesimal and planet formation. It is,

though, greatly affected by the dust content of the protoplanetary disc and the opacity that the dust grains provide. This complex interplay is caused by the influence between gas and dust. The relative velocity for each pair of grains is determined by the aerodynamic properties of the grains, namely the Stokes number, and the local properties of the gas, such as the temperature or the volume density (Ormel & Cuzzi 2007). The variety in the relative velocities results in different collisional outcomes between grain sizes, such as coagulation or fragmentation (Birnstiel et al. 2012b, 2011a; Brauer et al. 2008b; Zsom et al. 2011a). As a result, the dust content of the protoplanetary disc is described by a distribution of grain sizes, with number densities that are not necessarily equally distributed between all existing sizes.

Each grain size population has a different opacity, therefore having a distribution instead of a single grain size means that the disc's total opacity will be affected and as a consequence it will affect the resulting structure of the disc. As stated in Birnstiel et al. (2016), the opacity, defines the observational characteristics of a protoplanetary disc by influencing the dust thermal continuum emission and the excitation conditions for the gas lines. Additionally, since opacity regulates the amount of light that can be absorbed by the disc, it determines its thermal structure. These reasons make opacity a very important factor of the structure and evolution of a protoplanetary disc.

The interplay between opacity and the thermal structure creates a feedback loop that we include in hydrodynamical simulations of equilibrium discs (Fig. 3.1). Even though the goal of theoretical models is to simulate protoplanetary discs as realistically as possible, typically they only include specific parts of the feedback loop, contrary to this work. In the following paragraphs we introduce what work has been done in parts of the feedback loop.

3.1.1 Relative velocities and grain size distribution

Early on, Safronov (1969) worked on dust growth within the context of planet formation and on the time evolution equation for grain size distributions (often called Smoluchowski equation, Smoluchowski 1916b). A lot of work was also done on dust dynamics and how they would affect collisional outcomes and, as a consequence, coagulation and fragmentation of dust particles (Brauer et al. 2008b; Nakagawa et al. 1981; Weidenschilling 1980a, 1984a). A grain size distribution has been widely assumed to follow a power-law derived from the equilibrium between coagulation and fragmentation, inspired by the work of Dohnanyi (1969) on the number density distribution of objects in the asteroid belt. The number density, thus, can be approximated as $n(s) \propto s^{\xi}$, where s is the grain size and ξ a constant. Several attempts were made in order to define this constant, mainly through analytical calculations combined with observational data for the interstellar medium grains (e.g., Mathis et al. 1977, MRN power-law), but also through experimental studies (e.g., Davis & Ryan 1990). It was shown by Tanaka et al. (1996) that the ξ constant is independent of the specific parameters of the collisional outcome model, as long as it is self-similar, which in this case means that the outcome of impacts between dust grains depends on the masses of two colliding particles only through their ratio.

However, such a description of a grain size distribution with only one power law

is a simplification, since it only takes into account the coagulation/fragmentation equilibrium. More recently, the work on grain size distributions has been aided by laboratory experiments of dust collisions (review by Blum & Wurm 2008; Güttler et al. 2010b). Such experiments determine what the collisional outcomes are between particles of equal or different size, for different relative velocities. They also help in creating models to simulate such collisions accurately and they can be used in the effort of understanding which processes are relevant within the context of planetesimal formation in protoplanetary discs (e.g., Zsom et al. 2010b). If additional effects are also taken into account, such as cratering or different regimes due to size-dependent relative velocities, then the size distribution is described by broken power laws (Birnstiel et al. 2011a). The studies discussed above focused on the local distribution of grains in a protoplanetary disc patch due to fragmentation and growth by coagulation, and typically assume that the gas disc does not evolve in time and the dust has no effect on the gas.

3.1.2 Opacity

As a first step, some work has been done on opacity alone within the context of protoplanetary discs (Cuzzi et al. 2014; Draine 2006; Miyake & Nakagawa 1993). The goal of those works is to create a simple opacity model that can describe as realistically as possible the dust opacity and can be then used in disc simulations (Bitsch et al. 2013) or help in the interpretation of disc observations (Birnstiel et al. 2018). Alongside the theoretical models, several observations of the dust emission have been performed in order to connect opacity with the particle sizes present in the protoplanetary discs (Andrews & Williams 2005b, 2007; Lommen et al. 2009; Natta et al. 2007; Ricci et al. 2010, 2011; Rodmann et al. 2006; Ubach et al. 2012).

3.1.3 Disc structure and grain size distribution.

Several works in the recent years aimed to couple the dust and gas components of protoplanetary discs in simulations and in most of the cases such models include a grain size distribution. However, the models that we discuss here simulate the gas component of a protoplanetary disc and how the dust component is affected by the gas, but the solids do not influence the gas. Even without the back-reactions of dust on gas, modeling grain size distributions can be computationally challenging, given the long list of effects and parameters to be taken into account, especially using N-body like techniques to treat dust particles. As a consequence, some of the first attempts on this kind of models were made using the Monte-Carlo method (Ormel & Spaans 2008; Ormel et al. 2007) and the goal was to examine how the internal structure of dust affects the collisional evolution of the particles and the disc structure. The Monte-Carlo method has been also used in Zsom et al. (2011a, 2010b), while in their work the experimental collisional outcomes from Güttler et al. (2010b) were implemented and the effect of the porosity and settling of the dust grains on the collisional outcomes was tested. Brauer et al. (2008b) and Birnstiel et al. (2010b) numerically solve the Smoluchowski equation for the coag-

ulation/fragmentation equilibrium in vertically isothermal steady-state gas discs, while Okuzumi et al. (2012b)studied the effects of the dust grain porosity on the dust evolution in a similar disc setup. In the works discussed above the feedback of the dust on the gas disc structure and especially its thermal part, is not taken into account.

3.1.4 Disc structure, opacity, and cooling rate

The category of models that was described above neglected the effects of opacity, even though the dust opacity regulates the cooling rate of the disc, which affects the disc structure. In recent years, some studies tried to fill this gap by including the effect of dust opacity in disc simulations. Oka et al. (2011) performed 1+1D [1] simulation focusing on the effect that water-ice opacity has on the location of the iceline. In the aforementioned study the wavelength-dependent opacities of water-ice and silicates are directly used when calculating the radiative transfer. In Bitsch et al. (2013, 2015a, 2014) the Bell & Lin (1994a) opacity profile is followed (in Bitsch et al. (2013) constant opacity discs were also modeled) and 2D simulations (radial and vertical direction, assuming axisymmetry) are performed using the NIRVANA and the FARGOCA code adding radial heat diffusion and stellar irradiation. The effect of the water-ice to silicates ratio on the resulting thermal disc structures has also been studied recently (Bitsch & Johansen 2016) using the FARGOCA code and the opacity module from the RADMC-3D code to calculate the mean opacities (as in the present work), but the opacity differences for the water-to-silicate fractions considered are then translated into differences in the Bell & Lin (1994a) opacity model. The Bell & Lin (1994a) opacity model gives approximate values for the frequency averaged opacities within specific temperature regimes (e.g., ice grains, evaporation of ice grains, metal grains, etc.) assuming micrometer-sized particles. The fixed opacity profile then gives the cooling rate and the stellar heating, therefore it defines the disc structure.

Even though including the opacity feedback in disc simulations is an important improvement, the aforementioned studies did not include the effect of grain growth and fragmentation, and ,thus, only employed opacities derived for single grain sizes. In addition to this, all of these studies assumed a uniform dust-to-gas ratio in the vertical direction of the disc which is in contrast to our approach in this work (see Sect. 3.2.4).

3.1.5 Disc structure, grain size distribution, and opacity

Schmitt et al. 1997 coupled the dust and gas evolution in 1D simulations, while they also took into consideration the grain opacity. For the mean opacity calculations they followed the approach of Henning & Stognienko (1996), which is similar to the Bell & Lin (1994a) opacity model approach. Moreover, the size distribution follows the Mathis et al. (1977) power-law. It was found that since grains determine the

[1] In the 1+1D approach, the vertical structure of each annulus is solved independently and then all of the annuli are used to construct the radial and vertical structure of the disc.

opacity, their evolution will subsequently change the opacity and therefore affect the structure and evolution of a protoplanetary disc. Prior to this study, Mizuno et al. (1988) and Mizuno (1989) included the dust component evolution in accretion discs and used the results to perform grain opacity calculations. In Suttner & Yorke (2001) the coagulation/fragmentation equilibrium is included in order to investigate how the dust emission is affected by the grain size distribution and its corresponding opacity. In this work the size distribution follows the Mathis et al. (1977) power-law and opacity was calculated using Mie theory. However, in the studies discussed above the back-reaction of the opacity onto the disc structure was not taken into account.

3.1.6 Motivation

In the previous paragraphs some examples were given of the work that has been done in the context of grain growth within protoplanetary discs. Nevertheless, previous models were based on several simplifications, most important of which was that they neglected parts of the feedback loop (Fig. 3.1) that defines protoplanetary disc structures (e.g., Birnstiel et al. 2011a) or used simplified assumptions for the opacity (e.g., Bitsch et al. 2013). The few attempts that have been made to include the dust feedback on the gas of the disc, were 1D simulations or assumed an isothermal vertical structure for the gas, in contrast to the 2D hydrodynamical models that are presented here. Secondly, the opacity is either not included in the actual simulations or the opacities were included only for single fixed grain sizes.

The motivation for this project is to approach a more realistic model for disc structures and their evolution and more specifically to simulate the whole feedback loop including a detailed opacity module. We consider how grain dynamics and more specifically how grain size distributions affect the opacity and as a consequence the thermal structure of the disc in order to simulate the whole feedback loop. As far as the grain size distribution is concerned, two models were used for the simulations of this project. A simple power-law model following Mathis et al. (1977), hereafter MRN distribution and also a more complex model following Birnstiel et al. (2011a), hereafter BOD distribution. Moreover, an opacity module was included in the 2D hydrodynamical disc simulations in order to more accurately calculate the opacity of the dust grain distribution and account for the back-reactions of dust to gas. In this opacity module, the Rosseland and Planck mean opacities as a function of temperature are used and they are calculated via Mie theory. The simulations were run until the disc reached thermal equilibrium. Such simulations offer us the opportunity to discuss the implications of the resulting disc structures to planet formation and could also serve as the basis to compare with observations (e.g., ALMA images) in future work.

3.2 Methods

3.2.1 Hydrodynamical simulations

Calculations with mean opacities derived from single grain sizes were first introduced into the FARGOCA code by Lega et al. (2014b) and Bitsch et al. (2014), who performed 2D and 3D radiation hydrodynamical simulations of discs and planet-disc interactions. The FARGOCA code solves the continuity and the Navier-Stokes equations, and uses the flux-limited diffusion approach to radiative transfer. More specifically, the time evolution of the energy profile of the protoplanetary disc is determined by

$$\frac{\partial E_R}{\partial t} + \nabla \cdot \mathbf{F} = \rho \kappa_P [B(T) - cE_R] \tag{3.1}$$

$$\frac{\partial \epsilon}{\partial t} + \nabla \cdot (\mathbf{u} \cdot \nabla)\epsilon = -P \nabla \cdot \mathbf{u} - \rho \kappa_P [B(T) - cE_R] + Q^+ + S \ . \tag{3.2}$$

The radiative energy density E_R is thus independent from the thermal energy density ϵ. In the expressions above, the blackbody radiation energy is $B(T) = 4\sigma T^4$, where σ is the Stefan-Boltzmann constant, ρ is the gas density, κ_P the Planck mean opacity (further specified in Sect. 3.2.2), u the velocity, P is the thermal pressure, Q^+ is the viscous dissipation or heating function and S is the stellar heating component (Commerçon et al. 2011; Dobbs-Dixon et al. 2010; Levermore & Pomraning 1981).

In our simulations we use the flux-limited diffusion for the radiation flux $\mathbf{F}$ (Eq. 2.23). More details on the energy equations can be found in Bitsch et al. (2013). The opacities that were introduced in the above equations are discussed in the following section. The stellar heating density received by a grid cell of width Δr is defined as (Dobbs-Dixon et al. 2010):

$$S = F_\star e^{-\tau} \frac{1 - e^{-\rho \kappa_\star \Delta r}}{\Delta r} \ , \tag{3.3}$$

with $F_\star = R_\star^2 \sigma T_\star^4 / r^2$ being the stellar flux, $R_\star$ the stellar radius, $T_\star$ the stellar surface temperature, τ the radially integrated optical depth (up to each grid cell) and $\kappa_\star$ the stellar opacity (further specified in Sect. 3.2.2).

3.2.2 Opacity-Temperature module

In the energy equations (Eqs. 3.1 and 3.2) of the hydrodynamical simulation, we use the mean opacities that are averaged over all wavelengths (see Sect 2.3.3). If we use the Planck black body radiation energy density distribution $B_\lambda(\lambda, T)$ as a weighting function we can define the Planck mean opacity as

$$\kappa_P = \frac{\int_0^\infty \kappa_{\lambda,ns}(T, \rho) B_\lambda(\lambda, T) d\lambda}{\int_0^\infty B_\lambda(\lambda, T) d\lambda} \ . \tag{3.4}$$

Since the mean free path of thermal radiation in the disc is small compared to the disc's scale height, the radiation field can be considered isotropic, blackbody emission.

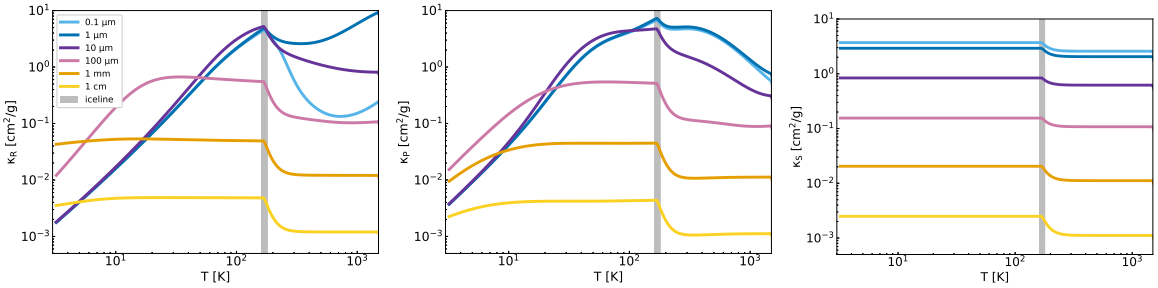

Figure 3.2. Rosseland, Planck, and stellar mean opacities (from left to right) as a function of temperature for grains of sizes 0.1, 1, 10, 100 μm, 1 mm, and 1 cm. They are independent of the gas density because they are dominated by the dust component. These values were calculated using RADMC-3D for a mixture of 50% silicates, 50% ice, and disc dust-to-gas ratio of 1%. The gray vertical line shows the location of the water iceline transition (170 K $\pm$ 10 K), causing a transition in opacity due to the evaporation/condensation of dust grains.

The Rosseland mean opacity uses the temperature derivative of the Planck distribution as a weighting function and is defined as

$$\kappa_R^{-1} = \frac{\int_0^\infty \kappa_{\lambda,s}^{-1}(T,\rho)(\partial B_\lambda(\lambda,T)/\partial T)d\lambda}{\int_0^\infty (\partial B_\lambda(\lambda,T)/\partial T)d\lambda} \ . \tag{3.5}$$

It should be noted that scattering processes are neglected (subscript ns) when calculating the wavelength dependent opacities κ_λ for the Planck mean, but are included in the Rosseland mean opacity (subscript s).

We also consider the stellar radiation and define the stellar or optical opacity as

$$\kappa_\star = \frac{\int_0^\infty \kappa_{\lambda,ns}(T,\rho)B_\lambda(\lambda,T_\star)d\lambda}{\int_0^\infty B_\lambda(\lambda,T_\star)d\lambda} \ . \tag{3.6}$$

The stellar opacity is then the Planck mean opacity taking into consideration the stellar radiation temperature instead of the local disc temperature.

We calculate the mean Rosseland, Planck, and stellar opacities as a function of temperature using the RADMC-3D [2] code. We note that dust opacities are independent of the gas density, as opposed to gas opacities. The latter are not considered in this work as opacities in the disc are dominated by the dust component and the high temperature needed for dust evaporation is not reached within our simulations. The code utilizes Mie-scattering theory and the optical constants for water-ice (Warren & Brandt 2008a) and silicates (Dorschner et al. 1995; Jaeger et al. 1994) in order to calculate the wavelength-dependent opacities, which are then averaged over all wavelengths. The main input parameters are the size of the grains and the dust-to-gas ratio of the disc. We can also choose the dust grain species, silicates, water ice, and carbon or the fraction between those in the dust mixture. In this work, we include a mixture of 50% water-ice and 50% silicates and the dust-to-gas ratio for the calculation of the opacities is 1%. Finally, the Rosseland, Planck and stellar mean opacities (see Bitsch et al. 2013) are calculated.

[2] http://www.ita.uni-heidelberg.de/~dullemond/software/radmc-3d/

In Fig. 3.2 we illustrate how each mean opacity scales with temperature for six different grain sizes, from 0.1 μm to 1 cm. The wavelength-dependent opacities and subsequently the mean opacities depend on the size parameter $x = \frac{2\pi s}{\lambda}$, but also on the refractive index of the given grain species, which is also itself dependent on wavelength (Movshovitz & Podolak 2008). By Wien's law, the wavelength is inversely proportional to the temperature. Using the size parameter we find that the regime changes at approximately x = 1 and more specifically at x $\ll$ 1 we have the Rayleigh scattering, whereas at x $\gg$ 1 we have the geometric optics regime (Bohren & Huffman 1998). Consequently, if the size of the particle is a lot smaller than the wavelength of the incident radiation, absorption dominates over scattering and the wavelength dependent opacities become independent of grain size. In the case of the larger grain sizes, or when x $\gg$ 1, the opacities become independent of wavelength (and consequently temperature) but depend on the grain size. Most of the regions though lie somewhere in between, which means that calculating the opacity depends on both the grain size with its individual refractive index and the given wavelength or temperature.

The Rosseland mean opacities (Fig. 3.2) for the largest particles of the set (100 μm, 1 mm and 1 cm) are almost flat, except for the transition around the iceline at 170 K $\pm$ 10 K. At this temperature, ice sublimates, and the opacity is then only determined by silicates. For those large particle sizes, the size parameter is greater than 1, therefore we are in the geometric optics regime and the Rosseland mean opacity is independent of temperature. However, we note that for a grain size of 100μm and temperature below 20K the opacity depends on the temperature. In this region, the regime has changed and the opacity is determined by Rayleigh scattering. Equally, the size parameter is well below 1. The same trend can be seen for the smaller particles, namely 0.1,1 and 10 μm before the iceline. The opacity of the 10 μm grain sizes goes into the geometric optics regime after the iceline and tends to become independent of temperature. In the region after the iceline for the smallest particles (0.1 and 1 μm) the size parameter is closer to 1, so the opacities are also influenced by the refractive indices.

The Planck opacities have a weaker dependency on temperature compared to the Rosseland mean opacities. The stellar opacities depend only on the stellar temperature and grain sizes, but not on the disc temperature, except for the transition at the water iceline, when water-rich particles evaporate. Both the Planck and stellar opacities are calculated using only the absorption coefficient, which does not have a strong dependency on wavelength and consequently temperature, as opposed to the extinction coefficient. The Planck mean opacities are calculated taking into account the temperature of the disc, while the stellar opacities, use the temperature of the star, which is constant.

Using the opacity module from RADMC-3D, several files are created with the mean opacity values as a function of temperature. These files are then used in the hydrodynamical code (FARGOCA). The opacity calculations from these files are interpolated and in this way, we get in the code the appropriate opacity values given the temperature of the grid cell. The reason why the interpolation is done instead of directly calculating opacity using Mie theory is that the computational time would be very long. We include the direct opacity-temperature calculations

for at least ten grain sizes, from 0.1 μm to 1 mm or 2 cm. We then create size bins and as a simplification, each grain size within a bin shares the same opacity-temperature calculations (corresponding to the logarithmic mean size of that bin). We note here that these bins are different and for computational reasons wider than the bins used for the calculations of the vertically integrated dust surface densities (see Sect. 3.2.3).

As a comparison, we also use the frequency-averaged Bell & Lin (1994a) opacity law. The opacity, in this case, depends on the local temperature and density. There are several transitions in this opacity regime caused by the processes which dominate each temperature region, such as the evaporation of ices interior to the iceline, which is also present in the prescription we are using for the discs with the grain size distributions. However, the greatest difference between the two opacity regimes is that the Bell & Lin (1994a) opacity law is based on micrometer-sized dust and does not take the opacity provided by all of the dust sizes present in the disc into account. The Bell & Lin (1994a) law also considers the gas opacities, but these are relevant for high temperatures that are not reached in the simulations presented here.

3.2.3 Grain size distributions

The collision between two dust grains can result in various outcomes., such as coagulation, fragmentation, cratering, and bouncing (review by Blum & Wurm 2008). The outcome of a collision is determined by the relative velocities of the colliding bodies and their mass ratio (Brauer et al. 2008b; Weidenschilling 1977a).

The relative velocities between grains are determined by the mass of the particles, but they are also greatly affected by the local temperature and the gas scale height. Dust dynamics involve not only collisions between grains, but also with the molecules of the protoplanetary disc's gas. These collisions with the gas cause a lag to the dust particles that leads to relative velocities between themselves.

We compare in this work two different grain size distribution models. These models provide the vertically integrated surface density of dust as a function of the grain size. The first and simple model (hereafter MRN) is inspired by the groundwork on dust distributions (Dohnanyi 1969; Mathis et al. 1977; Tanaka et al. 1996). At a given distance to the star, the equilibrium between fragmentation and coagulation results in a steady-state size distribution, where the number density of the particles can be written as

$$n(m)dm \propto m^{-\xi}dm \tag{3.7}$$

or

$$n(s)ds \propto s^{2-3\xi}ds \ , \tag{3.8}$$

with m the particle mass, s the particle size, and ξ a constant.

The mass of a specific size, within a size bin $[s_i - ds', s_i + ds'']$ is

$$M_{s_i} = \int_{s_i-ds'}^{s_i+ds''} m \cdot n(s)ds \propto \left[\frac{s^{6-3\xi}}{6-3\xi}\right]_{s_i-ds'}^{s_i+ds''} \ , \tag{3.9}$$

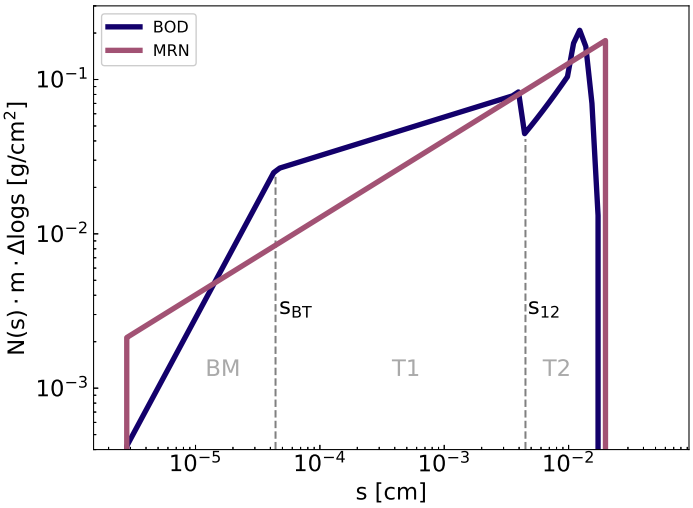

Figure 3.3. Vertically integrated dust surface density distribution per logarithmic bin of grain size as a function of grain size for the two distributions used here, after Birnstiel et al. (2011a) (BOD) and Mathis et al. (1977) (MRN), at 10 AU, for the simulation with $\alpha = 5 \times 10^{-3}$ (see Fig. A.1 for the distributions over all orbital distances). The dust to gas ratio is 1% and the gas surface density is 1000 g/cm^2 at 1 AU in both cases. For both of the distributions we additionally used $u_f = 1\ m/s$ and $\rho_s = 1.6\ g/cm^3$. The maximum value is determined by the fragmentation limit (Eq. 3.14).

assuming 5-3$\xi \neq$ -1. The grain sizes for this project are distributed over a logarithmic grid, so $s_i - ds'$ is $\sqrt{s_i \cdot s_{i-1}}$ and $s_i + ds''$ is $\sqrt{s_i \cdot s_{i+1}}$. The vertically integrated surface density of each grain size bin is then

$$\Sigma_{d,s_i} \propto f_{DG}\Sigma_g \left[\left(\sqrt{s_i \cdot s_{i+1}}\right)^{6-3\xi} - \left(\sqrt{s_i \cdot s_{i-1}}\right)^{6-3\xi} \right] , \tag{3.10}$$

where f_{DG} is the dust-to-gas ratio and Σ_g is the gas surface density.

We use a grain size grid, such as $s_{i+1} = c \cdot s_i$ and the assumption that ξ=11/6 (Dohnanyi 1969; Williams & Wetherill 1994), so then the expression for the unnormalized vertically integrated surface density for each grain size bin can be simplified to

$$\Sigma_{d,s_i} \propto s_i^{1/2} f_{DG}\Sigma_g \ . \tag{3.11}$$

The contributions from each grain size are then summed up. In order to get the normalized surface density values we divide each contribution by the aforementioned sum

$$\tilde{\Sigma}_{d,s_i} = \frac{s_i^{1/2} f_{DG}\Sigma_g}{\sum_i s_i^{1/2}}. \tag{3.12}$$

The second and more complex model (Birnstiel et al. 2011a, hereafter named BOD) takes into account fragmentation, coagulation, and also cratering, where only part of the mass of the target body is excavated after the collision with a small impactor. The input parameters for this model are the dust and gas surface densities

($\Sigma_{d,0}$ and $\Sigma_{g,0}$), the local disc temperature (T), the alpha turbulence parameter (α), the volume density of the particles (ρ_s) and finally the fragmentation velocity (u_f), which is the critical velocity above which all collisions lead to either fragmentation or cratering. The logarithmic grid for the sizes of both distributions is defined as $s_{i+1} = 1.12 s_i$, while the smallest grain size is 0.025 μm. As mentioned in Sect. 3.2.2 this grain size grid is finer than the size grid we use to determine the opacities.

Considering that different particle sizes lead to different collision outcomes, this recipe takes into account the relative velocities that particles of different sizes will develop in order to create different regimes for each size. These regimes are created according to size boundaries, within which different power-laws apply for the fit to the size distribution. It should be mentioned that these size boundaries are defined by the corresponding relative velocities of the dust grains. The smallest particles of the distribution follow Brownian motion (region noted as BM in Fig. 3.3), which means their motion is affected by collisions with the gas molecules, there is no preferred direction and they do not have angular momentum. The next regime regards larger particles that start to get affected by turbulent mixing (noted as T1 in Fig. 3.3). It was also found (Ormel & Cuzzi 2007) that when particles have stopping times approximately equal or larger compared to the turn-over time of the smallest eddy of the gas, they start to decouple from the gas, so they follow a different regime (T2 in Fig. 3.3). Finally, the distribution has an upper end or a fragmentation barrier above which particles can no longer grow and only fragmentation occurs.

Between two size boundaries, the distribution is described by a power-law $n(m) \cdot m \cdot s = s_i^{\delta_i}$ of different powers δ_i, depending on the regime (Brownian motion or turbulent mixing). In Fig. 3.3, the barrier s_{BT} is the grain size limit for Brownian motion, while the barrier s_{12} separates the two turbulent regimes. The bump near the end of the distribution is caused by cratering, since large particles only lose part of their mass this way, while small particles can only coagulate and form larger grains. This causes the distribution to be top-heavy. Within each one of the regimes, the power-law indices are different if the grains are affected by settling, given their sizes and the disc parameters (see Sect. 3.2.4 for a discussion on the vertical distribution of grains). The powers for each regime are found in Table 3.1 and using these we can create a first fit $f(s_i)$. It is necessary then to include the bump caused by cratering and the cut-off effects of the distribution that cause an increase in the fit for large enough particles. This boundary effect is caused by the fact that large particles near the upper boundary of the grain sizes grid do not have larger particles to collide with, but the mass transfer from one size bin to the other needs to be constant to keep a steady-state grain size distribution. Therefore the number density is increased. Similarly, erosion by small impactors slows down the growth of large particles, and an increase in the number density is needed to keep the flux constant. More details for this recipe can be found in Birnstiel et al. (2011a).

Finally, the fit is normalized according to the total dust surface density at the given location (Fig. 3.3, also see Sect. 5.2 in Birnstiel et al. (2011a)) as in the first model. This fit represents the vertically integrated dust surface densities per logarithmic bin of grain size, N(s)·m·Δ logs, where

$$N(s) = \int_0^{z_{max}} n(s)\, dz \tag{3.13}$$

is the vertically integrated number density.

Regime	δ_i	
	$s_i \leq s_{sett}$	$s_i \geq s_{sett}$
Brownian motion regime	$\frac{3}{2}$	$\frac{5}{4}$
Turbulent regime I	$\frac{1}{4}$	0
Turbulent regime II	$\frac{1}{2}$	$\frac{1}{4}$

Table 3.1. Power-law exponents for each regime in the grain size distribution (Birnstiel et al. 2011a). The distribution in each regime is $n(m) \cdot m \cdot s \propto s_i^{\delta_i}$.

The maximum grain size or in other words the fragmentation barrier is defined in the simulations with both of the grain size distributions as

$$s_{max} \simeq \frac{2\Sigma_g}{\pi \alpha \rho_s} \frac{u_f^2}{c_s^2} \ , \tag{3.14}$$

with $\rho_s = 1.6\ g/cm^3$* the density of each particle, $u_f = 1\ m/s$ the fragmentation threshold velocity,c_s the sound speed (Eq. 2.5), k_B the Boltzmann constant, m_p the proton mass and $\mu = 2.3$ the mean molecular weight in proton masses. The threshold velocity $u_f \sim 1\ m/s$ corresponds to the threshold after which collisions between silicates always lead to fragmentation (Poppe et al. 2000a). However, it has also been experimentally found that water-ice shows a higher threshold velocity, $u_f \sim 10\ m/s$ (Gundlach & Blum 2015a). We choose to use only the lower fragmentation threshold in the here presented work, but the composition dependency will be studied in future work. Because of Eq. 3.14, which applies to both distributions, and the different regime boundaries in BOD, which depend on the local disc parameters (see Fig. 3.3 and Table 3.1), there is not a global size distribution, but rather a self-consistent spatial distribution of grain sizes both radially and vertically (see also Sect. 3.2.4).

It is noteworthy that even though we consider the coagulation/fragmentation equilibrium and the effects of cratering and settling, we neglect in the following work the drift of grains and the effect of bouncing. However, in the simulations presented here we find that the fragmentation barrier is always smaller than the drift barrier. This means that the particles have already fragmented and replenished the smaller pieces before they would have the chance to experience drift. The small particles are less affected by radial drift (Weidenschilling 1977a) and since they coagulate, an equilibrium forms that drives the grain size distribution. The fragmentation barrier decreases with increasing α-viscosity parameter, which is expected since an increased α leads to increased turbulent relative velocities. The maximum possible grain size also decreases when the fragmentation threshold velocity decreases. Drift is an important effect acting on dust grains in protoplanetary discs, but it is a reasonable simplification to neglect it for the chosen parameters of our simulations. In future

work where, for example, the fragmentation threshold velocities are increased or the composition dependency is included, drift is an effect that needs to be taken into consideration.

3.2.4 Vertical distribution of grains

The grains of a given size are vertically distributed according to Eq. 2.14. The vertically integrated dust surface densities Σ_d as a function of orbital distance are determined by the grain growth and fragmentation equilibrium prescriptions that were introduced in Sect. 3.2.3. The BOD grain size distribution has already taken into account the effect of settling (to calculate the distribution itself), depending on the grain sizes and the disc parameters (see Sect. 3.2.3 and Table 3.1). We then distribute in our model the grains vertically according to their sizes and how much they are expected to be affected, in a fashion consistent with the assumptions made in BOD (Eqs. **??**-2.16). However, it has been shown that small particles can get trapped in lower altitudes by the concentration of larger grains due to settling (Krijt & Ciesla 2016). This effect is not taken into account here as it is beyond the scope of this work but could be an improvement in future work.

We use the volume density of dust within a grid cell to find the opacity through

$$\bar{\kappa} = \sum_i \left(\frac{\rho_{d,i}}{\rho_g} 100 \right) \kappa_i \ , \tag{3.15}$$

where κ_i is the opacity of each grain size i, as shown in Fig. 3.2, and $\rho_{d,i}/\rho_g$ the dust-to-gas volume density ratio for a given grain size i. In the case of single grain sizes summing is not needed. The dust-to-gas term for the volume densities includes the settling effect (Eq. 2.14). In this expression, we multiply the volume density dust-to-gas ratios by 100 to account for the fact that in the calculations of κ_i (with the module from RADMC-3D) a dust-to-gas ratio of 1% was assumed. This way we multiply this κ_i with the appropriate factor depending on the volume density dust-to-gas ratio.

As an example of the effect of settling, we show in Fig. 3.4 the dust density as a function of height at 3AU for 5 different grain sizes. In this simulation, the α value is 10^{-4}, the initial gas surface density at 1 AU is $\Sigma_0 = 1000\ g/cm^2$ and the grain size distribution used is the BOD. As a reference, we also plot the gas density to indicate the different volume density dust-to-gas ratios depending on the grain size and the volume density dust-to-gas ratio.

Considering the α prescription for viscosity of Shakura & Sunyaev (1973) the turbulence must be $\alpha \leq St$ for settling to become important (Armitage 2009). We see from Eq. 2.16 that the larger the Stokes number of a particle, the more it will be affected by settling for a given α. Additionally, the lower the α value is, the more effective settling will be for even smaller dust particles. For this reason,1 we choose to show an example in Fig. 3.4 of a simulation with $\alpha = 10^{-4}$ which is the lowest α value we used in our simulations.

Not only the size but the location within the disc matters, because the Stokes number for a given grain size depends on the gas density which decreases with the

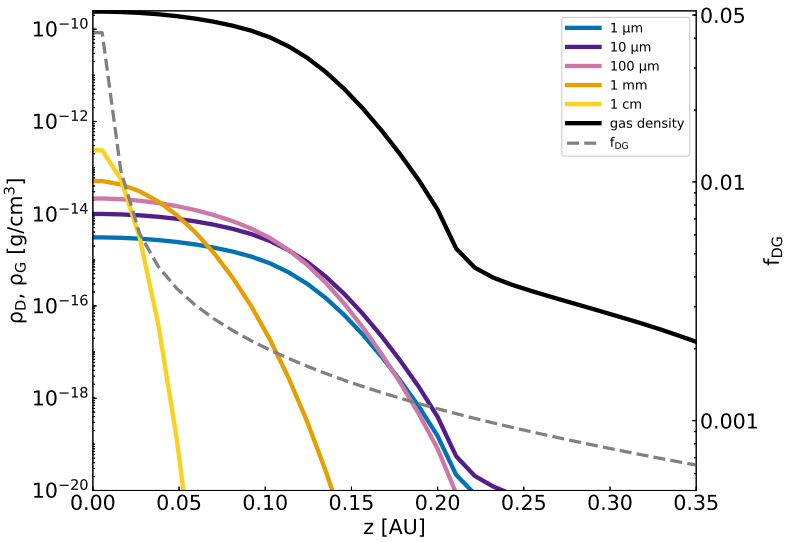

Figure 3.4. Dust density as a function of height for grains of five representative grain sizes within a disc with the BOD, $\alpha = 10^{-4}$ and $\Sigma_{g,0} = 1000\ g/cm^2$, at 3 AU. The black line shows the gas density of the disc. The dashed gray line shows the dust-to-gas ratio as a function of height for the whole grain size distribution.

increasing orbital distance. As a consequence, the same particles experience less settling the closer they are to the inner boundary of the disc.

The smallest particles which are shown in Figure 3.4, namely 1 and 10 μm are not affected by settling, despite the low turbulence strength. Their dust-to-gas ratio remains the same at all heights, so they are well coupled to the gas. Then, the larger the particle, the more effective settling is. The 100 μm sized dust particles are already affected by settling, but beyond this grain size the difference is even larger. The cm-sized dust, which is nearly the maximum grain size in this simulation, is almost constrained at the midplane. The dust-to-gas ratio (dashed gray line), ρ_d/ρ_g, is well below 1% above z=0.05 AU, but reaches 4% at midplane.

The main difference between various grain sizes is their different opacities as a function of temperature. However, as illustrated in Fig. 3.4, settling is another important effect, with a distinct efficiency depending on the grain size. Test simulations (presented in Appendix A.3) show that a significant settling changes significantly the thermal structure of the disk. Indeed, without it a constant dust-to-gas ratio leads to overestimated opacities above midplane, hence more "puffed-up" inner discs with higher temperatures, which cause a shadowing of the outermost region and prevent it from reaching an equilibrium state. Thus, settling is an important effect that needs to be taken into account in models in order to accurately study the thermal structures of protoplanetary discs.

3.2.5 Simulations setup

The stellar mass used in the simulations is $M_\star = 1M_\odot$, the temperature is 4370K, and the radius is $R_\star = 1.5R_\odot$. The total dust-to-gas ratio is $f_{DG} = 1\%$. Viscosity

in the simulations follows an α prescription (Shakura & Sunyaev 1973), where

$$\nu = \alpha \frac{c_s^2}{\Omega_K} \ . \tag{3.16}$$

Recent observations of protoplanetary discs find α values from 10^{-4} to 10^{-2} or even 10^{-1} (Andrews et al. 2009; Ansdell et al. 2018; Hueso & Guillot 2005b; Rafikov 2016), but such large α would cause discs to rapidly expand to great extent (Hartmann et al. 1998a) in contrast to observations. We use in this work five sets of simulations with $\alpha = 10^{-2}, 5 \times 10^{-3}, 10^{-3}, 5 \times 10^{-4}$, and 10^{-4} in order to test the effect of turbulence on the thermal structure of the disc. We choose these values in order to include a simulation with $\alpha = 5 \times 10^{-3}$ so that one can directly compare with the work in Bitsch et al. (2015a) and a simulation with $\alpha = 10^{-3}$ to allow comparison with the discs in Bitsch et al. (2013). In the simulations with $\alpha = 10^{-2}$ and 5×10^{-3} the grid cells are 480×70 (radial-vertical direction) and the disc extends from 2 to 50 AU, while in the simulations with $10^{-3}, 5 \times 10^{-4}$ and 10^{-4} the grid cells are 150×35 and the disc extends from 0.1 to 3.1 AU.

The gas surface density follows a profile

$$\Sigma_g = \Sigma_{g,0} \cdot (r/AU)^{-p} \ , \tag{3.17}$$

with $p = 1/2$ and we test two different initial surface densities, $\Sigma_{g,0} = 100$ and $1000\ g/cm^2$ for every α value that was mentioned above. We run more combinations of different initial gas surface densities and total dust-to-gas ratios, however these are mainly used in order to produce a fitting for the iceline position as a function of the three parameters, α, $\Sigma_{g,0}$ and f_{DG} (see Sect. 3.5.1, Appendix A.1 and A.2).

Since we simulate equilibrium discs, the surface density profile does not evolve significantly during the simulation, because the thermal equilibrium is reached faster than the viscous evolution equilibrium. At the top of the disc we manually set T=3 K, the temperature of the interstellar medium, so that the disc can be cooled by the upper boundary (as described in Bitsch et al. (2013)). The simulations run for some hundreds of orbits (typically 200-1000 orbits) until they reach thermal equilibrium. Nevertheless, some of the simulations might show signs of convection (Bitsch et al. 2013a), which means that they will remain unstable regardless of integration time.

At first, we perform simulations with single grain sizes in order to see the difference in the disc structures between them. Dust grains affect the hydrodynamical simulation through the opacity in each grid cell. Every simulation has a different grain size and the opacity values for this specific size are used (see Fig. 3.2). The simulations of single sizes offer the chance to examine the extent to which different grain sizes affect the disc's evolution and equilibrium structure and predict how much grain growth or a grain size distribution will change the outcome.

In the next step, we also consider settling and how it affects large grains. For these simulations we only use single grain sizes and the dust surface density is assumed to be $\Sigma_d = f_{DG}\Sigma_g$ or specifically $\Sigma_d = 0.01\Sigma_g$ as before. The difference between discs without and with settling is further discussed in Appendix A.3.

We, then, include the two grain size distribution models that were discussed in Sect. 3.2.3. The distributions are self-consistently calculated in the code using as

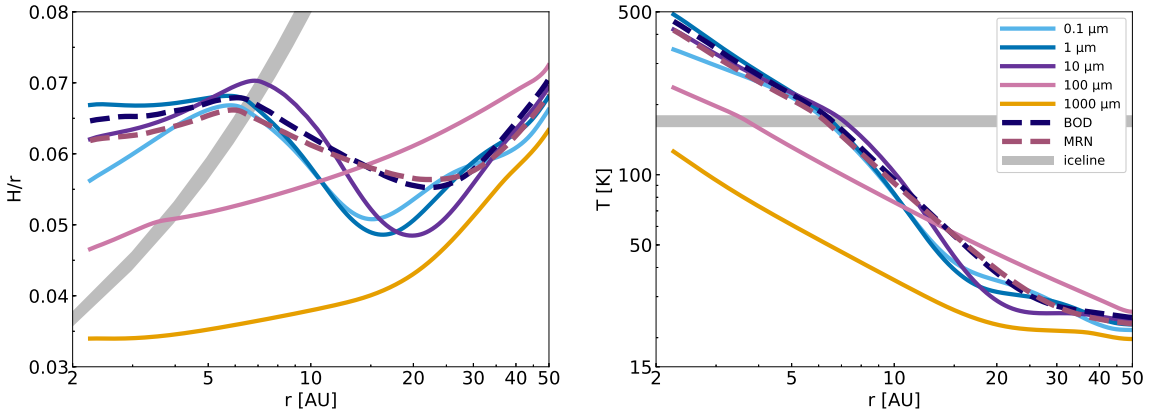

(a) (b)

Figure 3.5. Aspect ratio (left plot) and midplane temperature (right plot) as a function of orbital distance in AU, for discs with five different single grain sizes from 0.1 μm to 1 mm (see Fig. 3.2 for the opacities of those five grain sizes). All of the simulations include viscous heating and stellar irradiation, have $\alpha = 5 \times 10^{-3}$ as the turbulence parameter in viscosity, $\Sigma_{g,0} = 1000\ g/cm^2$ as the initial gas surface density, and the dust-to-gas ratio is $f_{DG} = 1\%$. In this set of simulations, we also consider settling so that we can compare with the simulations that include the grain size distributions. The gray areas in the plot indicate the water iceline transition. Overplotted with dashed lines are the discs with the MRN distribution in reddish pink and the BOD distribution in dark blue.

input parameters in each time-step and grid cell, the gas surface density (for both distributions) and the temperature (only for the BOD). The upper size boundary for the MRN power law model can be either fixed or follow the same fragmentation barrier formula as the second, more complex model (Birnstiel et al. 2011a), but in this work, we use the latter.

3.3 Grain size distributions

3.3.1 Comparison between the two grain size distributions

In this section we compare the simulations utilizing the two different grain size distributions (MRN and BOD). At first, we focus only on the case of $\alpha = 5 \times 10^{-3}$, $\Sigma_{g,0} = 1000\ g/cm^2$ and $f_{DG} = 1\%$.

In Fig. 3.5 we can see the aspect ratio as a function of orbital distance from the star for simulations of different grain sizes along with the two grain size distributions. The gray areas correspond to the iceline transition (T = 170 $\pm$ 10 K). In this area, the change in opacity is responsible for the bumps in the aspect ratios. We first focus on the simulation with 0.1 μm, which roughly corresponds to an unevolved dust population as found in the interstellar medium. The simulation with particles of 0.1 μm results in an increasing aspect ratio as a function of orbital distance up to 6 AU, where it reaches a maximum and then decreases up to approximately 15 AU. Using 1 μm-sized particles we see a similar disc structure. The aspect ratio

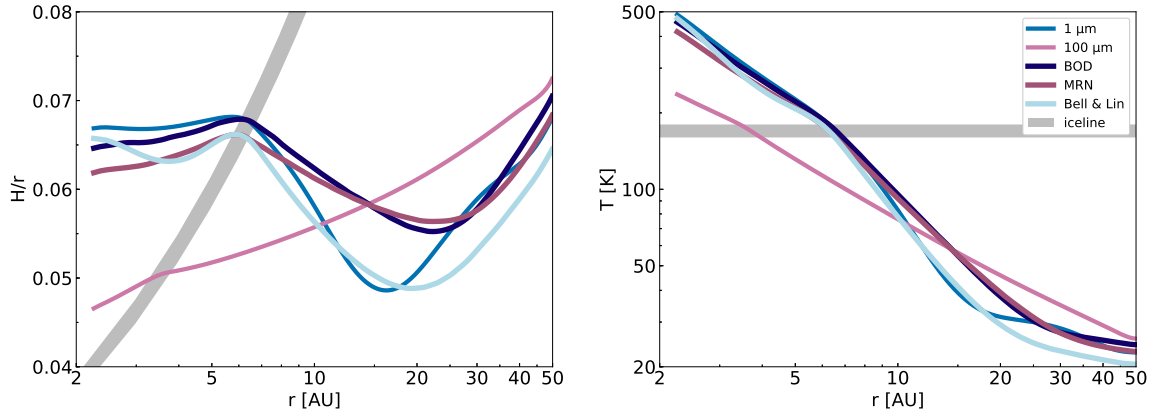

Figure 3.6. Aspect ratio (left) and midplane temperature (right) as a function of orbital distance for the discs with the BOD, the MRN distribution and a disc that utilizes the Bell & Lin (1994a) opacities. All of the simulations have $\alpha = 5 \times 10^{-3}$, $\Sigma_{g,0} = 1000\ g/cm^2$, and $f_{DG} = 1\%$. We also show the aspect ratio of the simulations with 1 and 100 μm for reference. The Bell & Lin (1994a) opacities are based on micrometer-sized particles resulting in comparable aspect ratios. The gray areas correspond to the water iceline transition.

is almost constant for the first few AU and has a small increase around 6 AU. Then it converges with the simulation of 0.1 μm up to the minimum around 15 AU. If the grain size increases to 10 μm, then the aspect ratio also increases with distance, features a bump closer to 7.5 AU and decreases with the same slope as the previous two simulations. The larger particles have distinct profiles. Specifically, the aspect ratio of the simulation with particles of 0.1 mm is a monotonically increasing function of orbital distance with a small bump at 3.5 AU. The same can be seen for the simulation with the largest particles, namely 1 mm, but in this case, a bump is not visible at any part of the aspect ratio profile since the iceline transition does not exist within the boundaries of the simulation.

The gradients in the aspect ratios for the inner region of the discs are determined by the opacity of the disc. We can compare the opacity gradients in Fig. 3.2 with the aspect ratio gradients keeping in mind that the temperature decreases as we move further away from the star. Depending on the temperature at each orbital distance of the disc, we see that the opacity gradients are responsible for the dips and bumps in the aspect ratio profiles of the discs.

The outer region of the discs is dominated by stellar irradiation, which causes the flaring of the discs. The simulation with the BOD shows influence from the smaller particles at the inner parts of the disc, but moving outwards the aspect ratio gets affected by larger particles, around 100 μm. A more detailed analysis of the grain sizes that contribute the most to the opacity of the disc is presented in Sect. 3.3.4. The simulation with the MRN distribution shows similar aspect ratio gradients. For this case, with high α, there is only a minimal difference between the dust surface densities, which leads to similar opacities in total. Both discs are affected by grains of similar sizes and for this reason, the aspect ratios are almost the same there.

In Fig. 3.5b we show the midplane temperature as a function of orbital distance for the same set of simulations. We can see that the changes in the temperature

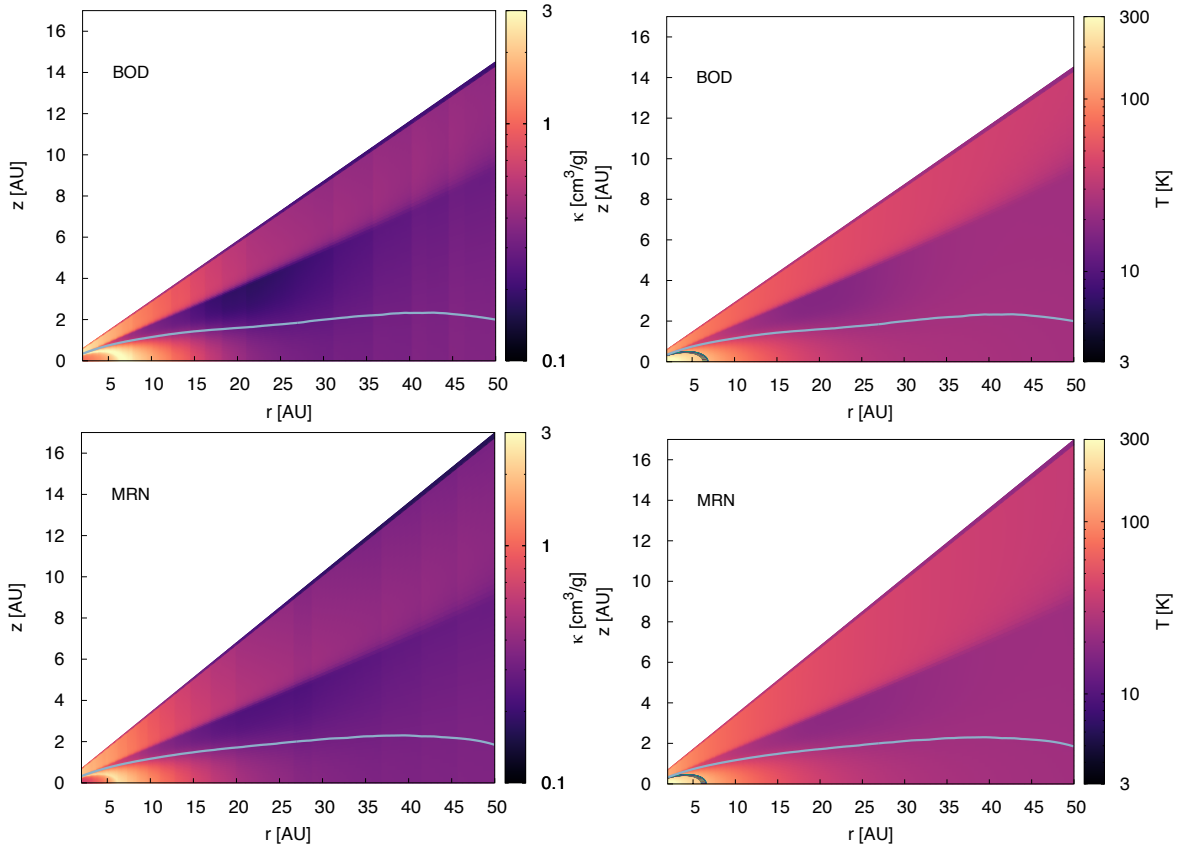

Figure 3.7. Mean Rosseland opacity values for the disc that includes the BOD distribution (top) and the MRN (bottom). These opacities correspond to the discs with the grain size distributions which were presented in Figs. 3.5 and 3.6. The highest opacity values are found at the iceline transition (gray band in the right plots). The light blue line is the location where the vertically integrated optical depth reaches unity (τ=1).

gradients correspond to the changes in the aspect ratio gradients. The gray horizontal line is again the iceline transition. The simulation with the millimeter-sized particles does not reach the iceline temperature within the extent of the simulated disc and thus does not feature the aspect ratio bump.

We can compare in Fig. 3.6 the resulting aspect ratios and midplane temperatures of the simulations with the BOD and MRN distributions with a simulation utilizing the opacities from Bell & Lin (1994a). This opacity profile is based on micrometer-sized particles, hence it is expected that it resembles the simulation with only micrometer-sized particles. It should be pointed out that the Bell & Lin (1994a) prescription includes the gas opacities as well, but these are relevant for high temperatures that are not reached within the extent of the discs here. We notice in Fig. 3.6 that the gradient after the iceline of the simulation with the Bell & Lin (1994a) prescription or only micrometer-sized particles is much steeper than the corresponding gradient in the simulations of the full distributions. This is an important difference as the gradients in the aspect ratio affect the migration speed of planets that could be embedded in such a protoplanetary disc (see Sect. 3.5.2).

In conclusion, we find that including either the BOD or the MRN distribution leads to comparable results. The differences between the two grain size distributions tested in this work for different values of the turbulence parameter α and different surface densities are discussed in Sect. 3.4. Prior to that, a more extended discussion on the dust surface densities, dominant grain sizes, opacities, and temperatures follows in the next paragraphs.

3.3.2 Opacities and temperature

The opacity and temperature within the disc for the BOD and MRN distribution are plotted in Fig. 3.7 as a function of orbital distance on the x-axis and height on the y-axis. The total opacity of the disc is determined by accounting for the contribution of each grain size according to Eq. 3.15.

The highest opacity values in the figures correspond to the iceline as it can be also seen in the temperature plot (gray band). Almost every particle size has its highest opacity at the iceline, consequently, the total opacity of the disc is the highest at the iceline, as it can be seen already in Fig. 3.2. It was already briefly mentioned in Sect. 3.3.1 (detailed discussion in Sect. 3.3.4) that the dominant grain sizes at the inner disc are small, therefore we see the same pattern in the opacity of the disc around the iceline as the opacities of the small particles, with the bump around the transition. For this reason, we are tracing the iceline at the opacity plot.

The total opacity is scaled down in the simulation with the MRN distribution compared to the one with the BOD, which is what we also find in the aspect ratio. Since the opacities have the same pattern and since the bumps in the aspect ratio are caused by opacity transitions it is expected to find there the same gradient.

Viscous dissipation is the dominant source of heating for the inner parts of the disc, while stellar irradiation becomes important at larger orbital distances and more importantly for the upper layers of the disc (Bitsch et al. 2013; Dullemond et al. 2001). Since the upper layers are heated up, the opacities are also higher there. If we move vertically up, the iceline moves inwards as viscous heating becomes

weaker. The specific radius and height at which stellar heating begins to affect the structure of the disc are, among other parameters, influenced by the strength of turbulence. The dependence of the disc's thermal structure on the turbulence strength is discussed in Sect. 3.4 and more opacity plots as a function of orbital distance and height can be found in Appendix A.2.

In Fig. 3.7 the $\tau = 1$ line is overplotted (light blue line). The optical depth τ is defined as

$$\tau = \int_{z_{max}}^{0} \kappa_R \rho_g dz \ , \tag{3.18}$$

therefore it increases as the height z is decreasing. The $\tau = 1$ line marks the difference between the optically thick and the optically thin medium. When $\tau \geq 1$, then the disc is optically thick, which means that the mean free path of the photons is much smaller than the length scale over which temperature changes. In optically thin parts of the disc, photons can "freely" travel out of the disc. The $\tau = 1$ line thus marks the region of the disc where cooling becomes efficient. A $\tau = 1$ line close to midplane corresponds to lower opacities, which results in a cooler disc. Even though the regions above this line are optically thin and cool down very efficiently, the uppermost layers are directly heated by stellar irradiation and we also see an increase in the opacity.

The transition from the optically thin part of the disc to the optically thick (moving from the top layers towards the midplane) is also where the boundary for observations would be if these were integrated over all wavelengths. Mid-infrared wavelength observations of the optically thick disc probe the temperature of the dust "photosphere", the effective surface layer of the disc. Observations are in general carried out at various wavelengths, thus probing different grain sizes and different information for the disc (Andrews 2015). The optical depth relevant for such observations might differ for individual grain sizes.

3.3.3 Dust surface densities

The vertically integrated dust surface densities per orbital distance and grain size are presented in Appendix A.1. The maximum grain sizes in both of the distributions depend on the local temperature and gas surface density, which change with time. Additionally, all of the boundary sizes of the BOD distribution depend on the local gas surface density.

We stress here the loop that is created; the dust surface densities play a major role in determining the opacity of the disc (Eq. 3.15), which then influences the cooling rate and the stellar heating and thus changes the temperature. The shift in the temperature leads to a new fragmentation barrier (and regime boundaries for the BOD), hence the dust surface densities change and so forth. Given the fact that this loop exists between the dust and the gas, it is important to consider the self-consistent calculations of the dust surface densities in the simulations.

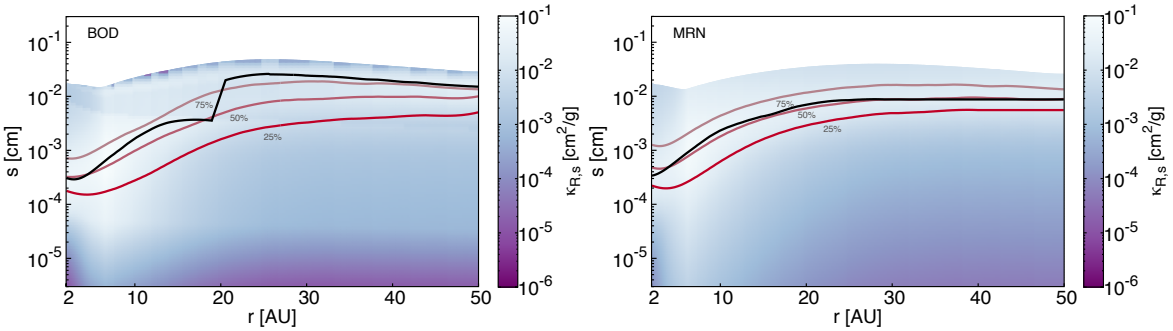

Figure 3.8. Contribution to the midplane mean Rosseland opacity per grain size for the simulation with the BOD on the top and the MRN distribution on the bottom, for the nominal disc parameters $\alpha = 5 \times 10^{-3}$, $\Sigma_{g,0} = 1000\ g/cm^2$ and $f_{DG} = 1\%$. The black line indicates the grain sizes that contribute the most to the opacity of the disc as a function of orbital distance. The total opacity at each radius is the sum of the contribution from each grain size, or in other words, it is the sum of the corresponding column. The red lines show the percentage of the contribution from the grains below the corresponding line.

3.3.4 Dominant grain sizes

Depending on the local gas disc parameters, the grain size which plays the role of the dominant opacity source will change. We find the individual contribution of each grain size to the total opacity of the disc through Eq. 3.15. For each set of particles of the same size we calculate its contribution, $\frac{\rho_{d,i}}{\rho_g} 100\kappa_i$ and we present it as a function of orbital distance in Fig. 3.8 for the nominal case of $\alpha = 5 \times 10^{-3}$, $\Sigma_{g,0} = 1000\ g/cm^2$. In order for a grain size to dominate the opacity, it needs a combination of high dust-to-gas volume density ratio (for this specific particle size) and high opacity at the given part of the disc.

We can see in the same figure, plotted as a black solid line, that the inner disc with either the BOD or the MRN distribution is influenced by very small particles, around 3 μm. Specifically, those small particles have the maximum contribution to the total opacity; their opacity dominates the opacity of the disc. The dominant grain sizes in the disc with the BOD grain size distribution feature a jump at around 20 AU. This jump is caused by the dip in the distribution in the transition between the first turbulence regime and the second (see Fig. 3.3), after which particles are large enough to get completely decoupled from the gas. After this jump, the dominant grain size is near 200 μm. The dominant grain size in the disc with the MRN distribution smoothly increases in the inner regions and then remains constant at around 90 μm exterior to 20 AU.

At the inner, hot parts of the disc, the grains around the micrometer size have surface densities that are around an order of magnitude lower than the larger grains (see Appendix A.1). However, they have the highest opacity by several orders of magnitude (see Fig. 3.2) at these high temperatures. This results in them being the dominant particles in that region. Farther out, the temperature of the disc decreases and as a consequence, larger particles carry the highest opacity. The decreased temperature means that the opacities of the larger particles get comparable with

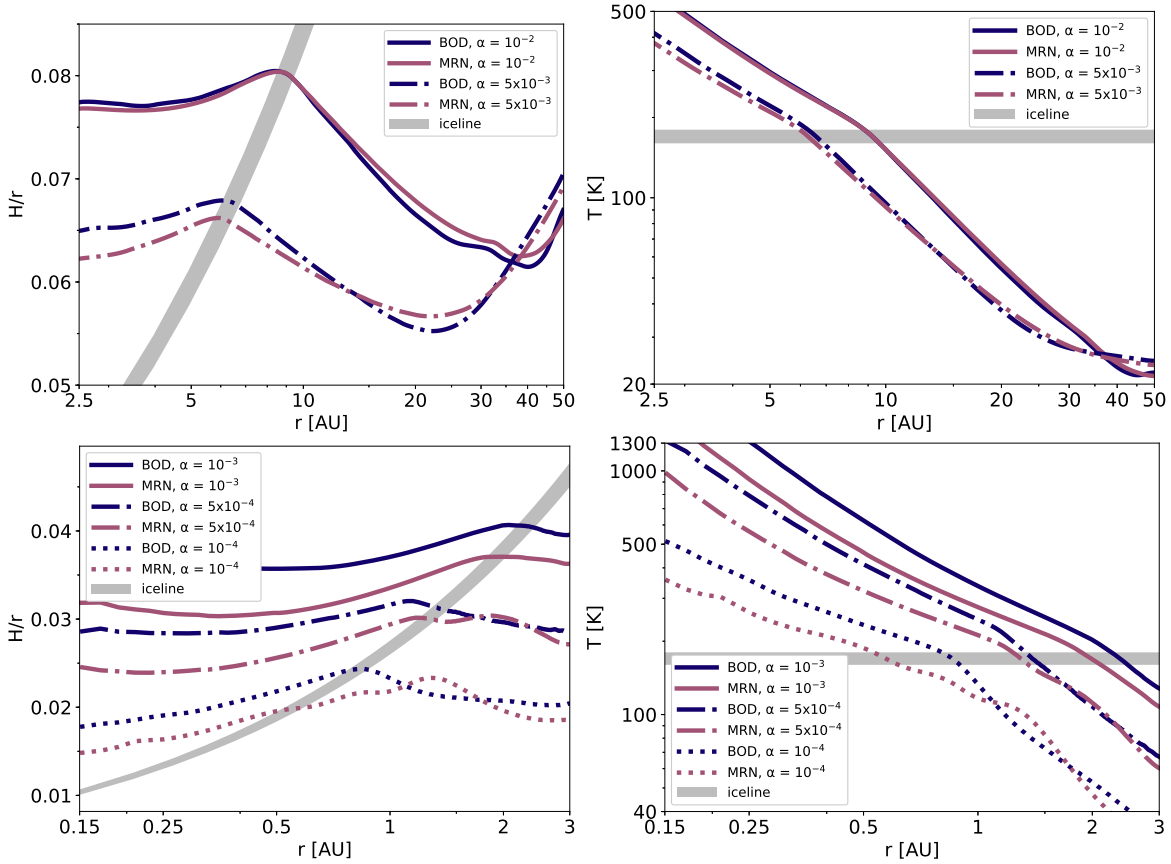

Figure 3.9. Aspect ratio as a function of orbital distance for the discs with high α-viscosity values (top left), namely $\alpha = 10^{-2}$, 5×10^{-3} and low α-viscosity values (bottom left), namely $\alpha = 10^{-3}$, 5×10^{-4} and 5×10^{-4}, for the two grain size distributions (BOD in dark blue, MRN in reddish pink). The right plots show the temperature as a function of orbital distance for the discs with high α-viscosity values (top), namely $\alpha = 10^{-2}$, 5×10^{-3} and for low α-viscosity values (bottom), namely $\alpha = 10^{-3}$, 5×10^{-4} and 10^{-4}.

those of the smaller particles. At the same time, the difference between the very small and the largest grain sizes slightly increases, aiding the dominance of the largest grains.

In Fig. 3.8 the grain sizes below the dark red line give 25% of the contribution to the total opacity, thus the grain sizes above this line give 75% contribution. The line above this divides the grain sizes into two groups, each contributing 50% to the opacity of the disc. In the same way, the uppermost line has grain sizes with 75% of the contribution beneath it and sizes with 25% contribution above it. These lines show the general trend of the contribution to the opacity, which mainly comes from the small grains in the inner disc and by the large grains in the outer disc.

For a given grain size, the contribution to the opacity shows similar patterns as the dust surface densities. The maximum opacities per grain size are seen at approximately 6.5 AU. This location corresponds to the iceline and it is expected to have the highest opacity contribution by almost all of the grain sizes (Fig. 3.2). In conclusion, what defines the grain size with the maximum contribution to the total opacity is the combination of the dust surface densities and the opacity of each grain size at a specific orbital distance (which is determined by the local temperature). Once more it is evident that the self-consistent calculations within the feedback loop (Fig. 3.1) are crucial to the disc structure evolution.

3.4 Dependence on viscosity, gas surface density and dust-to-gas ratio

Decreasing the α-viscosity values is expected to affect the discs in two ways. First of all, the viscous heating decreases, therefore the discs will cool down and their aspect ratio will be lower (see Fig. 3.9). Secondly, the lower turbulence means that particles will face less destructive collisions and thus they will be able to grow to larger sizes. The larger grains have in general lower opacities, which means that the discs experience an additional cooling because of the change in the opacities. The general trend that we show in Fig. 3.9 is that the aspect ratio indeed decreases as the turbulence parameter decreases. The location of the iceline also moves further in.

The aspect ratios and corresponding midplane temperatures in the low α models (bottom plots in Fig. 3.9) show some wiggles due to convection. Convection is caused by the vertical temperature gradient which depends on the opacity gradient in the vertical direction and is present in the optically thick regions of the disc (Bitsch et al. 2013a). This also implies that as the grains are more vertically diffused in the higher α case and the vertical temperature gradients are less steep, the effect should be less strong. Indeed, convection is also present in the high α simulations, but only at the inner, hotter regions of the disc. All regions that are affected by convection experience some sort of instability, so that reaching a steady state is very hard, if not impossible.

The vertically integrated dust surface densities as a function of orbital distance and grain size for the simulations with the two grain size distributions and the rest

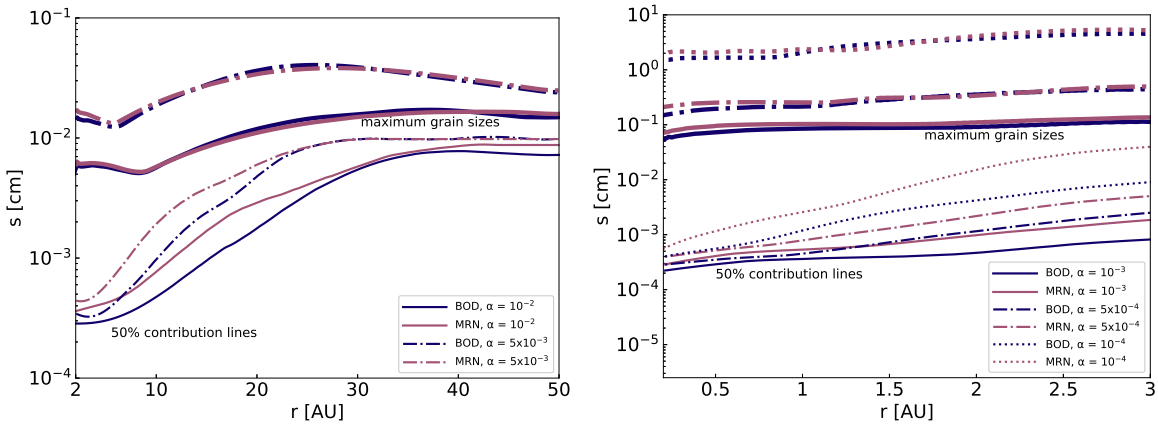

Figure 3.10. 50% contribution lines as a function of orbital distance for the discs with the high α values at the top and the low α values at the bottom. The group of thicker lines at the top corresponds to the maximum grain sizes of each disc so that the 50% contribution lines below divide the grain sizes into two groups, which contribute equally to the total opacity of the disc (see the red lines in Fig. 3.8).

of the α values $(10^{-2}, 10^{-3}, 5\times10^{-4}, 10^{-4})$ are presented in Fig. A.1 in the appendix. In Sect. 3.3 we presented the vertically integrated dust surface densities for the nominal value of $\alpha = 5 \times 10^{-3}$.

We also plotted the 50% contribution line for the same α value in Fig. 3.8. This line divides the grain sizes into two groups that contribute equally to the total opacity at the given orbital distance. In Fig. 3.10 we present the comparison of the 50% contribution lines as a function of orbital distance and α-viscosity. We plot also, in thicker lines of the same color, the maximum grain size in each disc so that the two groups of grain sizes with equal contribution to the opacity of the disc can be seen. The lower boundary of this plot corresponds to the minimum grain size (constant in all of the simulations).

We find that the position of this 50% contribution line is similar almost independently of the grain size distribution utilized in the model. Similarly the position of the 50% contribution line within the grain size range (vertical axis in Figs. 3.8 & 3.10) does not change significantly as α decreases (see Fig. 3.10), but at the same time the maximum grain size increases. The very large particles ($\geq$ 100 μm) have significantly lower opacities and thus each order of magnitude added in grain size only adds a small contribution to the total opacity of the disc.

If we decrease the gas surface density then the total dust surface density also scales down. The reduced surface density results in a colder disc because of two effects. On one hand, the viscous heating decreases and on the other hand the radiative cooling increases, as it is inversely proportional to the disc's density. This is what we find in the simulations with the lowest initial gas surface density we used, namely $\Sigma_{g,0} = 100 g/cm^2$ (Fig. 3.11). The discs with lower surface density are much colder, therefore have a significantly lower aspect ratio. In this case, the difference in the aspect ratio of the discs with the two distributions almost vanishes completely, therefore the position of the iceline is also practically the same for the two discs. This is explained by the fact that the dust surface densities of the two

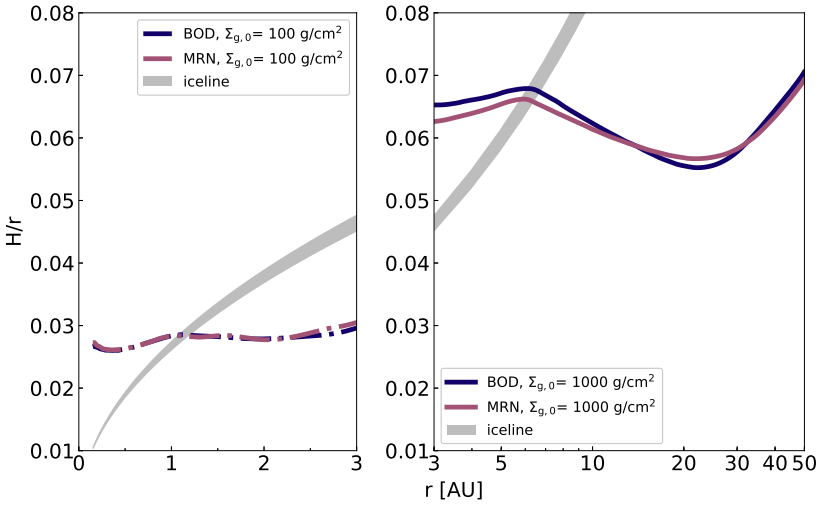

Figure 3.11. Aspect ratio as a function of orbital distance for two different surface densities ($\Sigma_{g,0} = 100\ g/cm^2$ and $\Sigma_{g,0} = 1000\ g/cm^2$).

distributions are comparable, leading to contributions to the opacity from similar grain sizes (see Fig.A.1).

On the contrary, if we increase the dust-to-gas ratio the total dust surface density is by definition enhanced. This means that the viscous heating is higher and the cooling rate decreased, resulting in hotter discs with higher aspect ratios. In addition to that, the opacity increases because of the enhanced total dust surface densities and as a consequence the optically thick region of the discs extends to higher heights compared to the discs with lower dust-to-gas ratio (see an example of a disc with $f_{DG} = 3\%$ in Appendix A.1).

The opacities as a function of orbital distance and height for the discs with the two distributions and the rest of the α values ($10^{-2}, 10^{-3}, 5 \times 10^{-4}, 10^{-4}$) can be found in Fig. A.2 in the appendix. The turbulence strength affects the viscous heating and the orbital distance and height at which stellar heating takes over. This direct influence on the thermal structure of the disc leads to different opacities at each position in the disc, depending on the α-viscosity value. A decrease in the gas surface density, as mentioned, decreases the viscous heating and increases the cooling rate, but the lower temperature decreases the opacity of the disc, and cooling is enhanced. A comparison between the opacities in discs with all of the α values can be found in Fig. A.2 in the appendix. We also show in Appendix A.1 the opacity of the disc with the lowest initial gas surface density $\Sigma_{g,0} = 100\ g/cm^2$ (with $\alpha = 10^{-2}$, $f_{DG} = 1\%$) and the opacity of the disc with the highest dust-to-gas ratio, $f_{DG} = 3\%$ (with $\alpha = 10^{-2}$ again and $\Sigma_{g,0} = 1000\ g/cm^2$).

3.5 Implications

3.5.1 Iceline

The location of the iceline can be theoretically calculated by considering the viscous and stellar radiation heating and the partial pressure of water vapor (e.g., Ciesla

& Cuzzi 2006; Davis 2005; Podolak & Zucker 2004). But it is also well predicted by setting a single sublimation temperature (e.g Hayashi 1981b; Min et al. 2011) as we do here as well. Nevertheless, the location where this sublimation temperature is reached depends on several parameters, as described by the feedback loop (Fig. 3.1).

Planet formation studies indicate that the iceline in protoplanetary disc models should be outside of 1 AU, the Earth's orbit. Otherwise, mechanisms like blocking the inward flow of pebbles from the outer disc by growing planets need to be invoked to keep the planets in the inner system dry (Morbidelli et al. 2016). If we take into consideration the observations of the composition of the bodies in the asteroid belt, the iceline at the time of formation of the asteroids would be at ∼2.7 AU. But if icy planetesimals were formed at such small orbital distances and contributed to the formation of the terrestrial planets, we would observe larger amounts of water on Earth than what we observe today. The composition of asteroids from the inner region of the asteroid belt suggests that at their time of formation they should have been interior to the iceline.

Evolving disc models indicate that at the time of the formation of terrestrial planets the iceline has already moved towards 1 AU (Bitsch et al. 2015a). In Oka et al. (2011) it is suggested that in order to reach a better conclusion about the location of the iceline a grain size distribution is required, rather than uniform dust grain sizes. In Garaud & Lin (2007) the decoupling of dust particles from gas is discussed as a potential influence on the thermal structure of the disc. Lecar et al. (2006) argue that in order to move the iceline outside 3 AU one possible solution would be to increase the opacity used in their model. Here we do not include the opacity of a single grain size, but use an evolving grain size distribution that regulates the opacity of the disc more realistically because we take into account their individual contributions.

All of these suggested effects have been therefore taken into account in the here presented work where we study the influence of α-viscosity, initial gas surface density, and total dust-to-gas ratio on the position of the iceline. In Appendix A.2 we present the simulations which were used and the procedure that was followed to do the fitting of the iceline position as a function of those three disc parameters. We find that the location of the iceline is independent of the grain size distribution which was utilized in the disc and it follows

$$r_{ice} = 9.2 \cdot \left(\frac{\alpha}{0.01}\right)^{0.61} \cdot \left(\frac{\Sigma_{g,0}}{1000\ g/cm^2}\right)^{0.8} \cdot \left(\frac{f_{DG}}{0.01}\right)^{0.37} \text{AU}. \tag{3.19}$$

In order to investigate the theoretical background of the above power law fit we can start, as in Bitsch et al. (2013), by considering the heating and cooling balance, $Q^+ = Q^-$, which means

$$2\sigma T_{eff}^4 = \frac{9}{4}\Sigma_g \nu \Omega_K^2 \ . \tag{3.20}$$

Given that the midplane temperature can be expressed as $T_{mid} = \left(\frac{3\tau_d}{4}\right)^{1/4} T_{eff}$, the above equation becomes

$$\frac{8\sigma}{3\tau_d} T_{mid}^4 = \frac{9}{4}\Sigma_g \nu \Omega_K^2 \ . \tag{3.21}$$

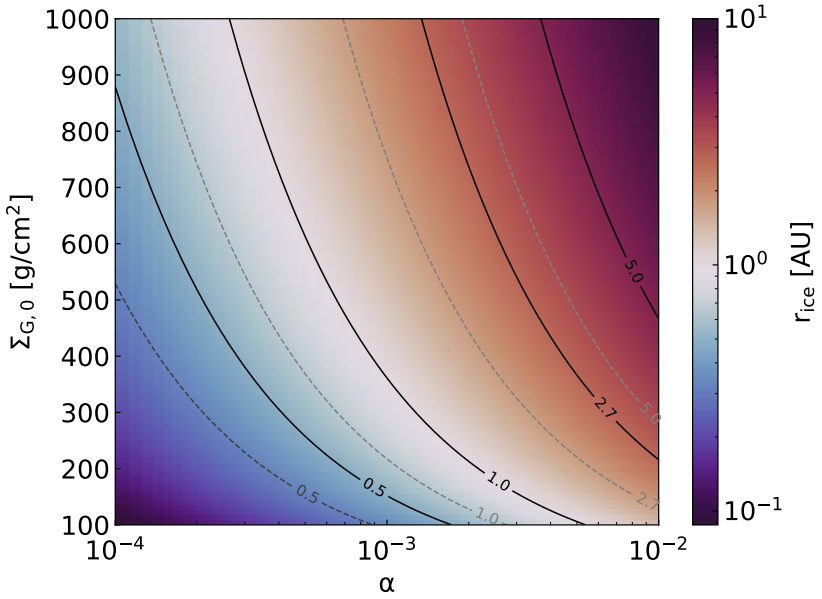

Figure 3.12. Iceline position as a function of α turbulence and initial gas surface density at 1AU with a constant $f_{DG} = 1\%$ (Eq. 3.19). The iceline transition is defined as $T = 170 \pm 10\ K$. The black lines mark $r_{ice} = 0.5, 1, 2.7$ and $5\ AU$. Higher viscosity or gas surface density leads to hotter discs, with the iceline located at greater distances from the star. The same applies to higher total dust-to-gas ratio. The gray dashed lines mark $r_{ice} = 0.5, 1, 2.7$ and $5\ AU$ for a disc with $f_{DG} = 3\%$.

We also substitute viscosity with the α prescription (Eq. 3.16 and Eq. **??** for the sound speed) and express the vertical optical depth as $\tau_d = \frac{1}{2}\Sigma_g f_{DG} \kappa$, so we get

$$T_{mid}^3 = \left(\frac{27}{64}\frac{k_B}{\sigma \mu m_H}\right) \Sigma_g^2\ f_{DG}\ \kappa\ \alpha\ \Omega_K\ . \tag{3.22}$$

The surface density profile follows $\Sigma_g = \Sigma_{g,0}\left(\frac{r}{AU}\right)^{-1/2}$ and $\Omega_K = \sqrt{\frac{GM_*}{r^3}}$, so we obtain

$$T_{mid}^3 \propto \Sigma_{g,0}^2\ f_{DG}\ \kappa\ \alpha\ r^{-5/2}\ . \tag{3.23}$$

We can then solve for the position of the iceline $r = r_{ice}$ where $T_{mid} = T_{ice}$,

$$r_{ice} \propto \Sigma_{g,0}^{4/5}\ f_{DG}^{2/5}\ \kappa^{2/5}\ \alpha^{2/5}\ . \tag{3.24}$$

We thus find that the power-law indices for the dependencies on $\Sigma_{g,0}$ and f_{DG} are very similar to what we find in our fitting (Eq. 3.19). Comparing Eqs. 3.19 and 3.24 suggests that at the iceline $\kappa \propto \alpha^{1/2}$, but is almost independent of $\Sigma_{g,0}$ and f_{DG}. The reason for this dependency has no easy analytical explanation, but it appears to be the outcome of the feedback between the disc structure and the dust evolution. This further illustrates, as we also discuss in Sect. 3.3.4, that we cannot rely on single grain size opacities to accurately describe the disc structure.

The position of the iceline as a function of the α-turbulence parameter and the initial gas surface density $\Sigma_{g,0}$ from our fitting formula is presented in Fig. 3.12, for discs with constant $f_{DG} = 1\%$. The iceline transition is defined as the location where $T = (170 \pm 10)\ K$. Increasing values of either one of the three parameters, α,

$\Sigma_{g,0}$, f_{DG}, leads to hotter discs so that the iceline moves closer to the star (see Sect. 3.4). In the models with any of the grain size distributions, the iceline is located outside 1 AU for $\alpha \geq 2.6 \times 10^{-4}$ and exterior to 2.7 AU only when $\alpha \geq 1.4 \times 10^{-3}$ for a disc with $\Sigma_{g,0} = 1000\ g/cm^2$ and $f_{DG} = 1\%$. However, this also depends on the disc's surface density and total dust-to-gas ratio. If the surface density reduces in time, the disc becomes cooler and the iceline moves inwards, even for the high viscosity cases. For example, for $\Sigma_{g,0} = 100\ g/cm^2$ the iceline is located outside 1 AU for $\alpha \geq 5.4 \times 10^{-3}$ and exterior to 2.7 AU only when $\alpha \geq 2.8 \times 10^{-2}$ (again with a constant $f_{DG} = 1\%$). In contrast, if the total dust-to-gas ratio is increased to 3%, then we find the iceline outside 1 AU even for $\alpha \geq 1.4 \times 10^{-4}$ and outside 2.7 AU for $\alpha \geq 6.9 \times 10^{-4}$.

We can conclude that utilizing Mie theory for the opacities of the grains and taking into account a distribution of grain sizes helps in keeping the iceline sufficiently far out from the star, especially for high α and $\Sigma_{g,0}$ values. In general, the location of the iceline might also depend on the composition of the grains, which will be examined in future work. In contrast to Oka et al. (2011), who suggest that grain size distributions might help to keep the iceline at larger distances compared to single grain size discs, we actually find the opposite. Including a distribution in a disc simulation results in a similar position of the iceline to the discs with the smallest grain sizes (0.1 and 1 μm). At low viscosities, the opacity is dominated by larger grains and thus the disc becomes colder. Unrealistic single grain opacities (typically of micrometer size particles) result in discs that are too hot. This implies that potentially other heating sources are needed to keep the iceline at large orbital distances, especially if viscous heating is low (Mori et al. 2019).

3.5.2 Planet migration

The protoplanetary disc's structure also affects planet migration. Very roughly said, if the aspect ratio increases with orbital distance then planets migrate inwards (Type-I migration, Paardekooper et al. (2011b)). On the contrary, if the aspect ratio is a decreasing function of orbital distance, planets will migrate outwards (Bitsch et al. 2013, 2015a, 2014), if the viscosity is large enough (Baruteau & Masset 2008).

We focus here on the results with $\alpha = 5 \times 10^{-3}$, a viscosity large enough to trigger outward migration by the entropy driven corotation torque. For the discs with the grain size distributions, we see an aspect ratio which is a decreasing function of orbital distance beyond the iceline, therefore in those disc regions planets could migrate outwards. Interior to the iceline the aspect ratio is an increasing function of orbital distance which means that planets embedded in this region of the disc would only migrate inwards. The minima in the aspect ratio are locations where planets could get trapped and if (as it is more likely) more than one planet existed, they could get into resonance and remain at those fixed orbital distances until the local parameters of the discs changed sufficiently to force them to migrate again (Cossou et al. 2014a, 2013; Horn et al. 2012; Izidoro et al. 2019a, 2017a).

Simulations with single particle sizes larger than 100 μm show a monotonically increasing aspect ratio with orbital distance (Fig. 3.5), implying that planets in these colder discs would migrate inwards. The speed of the migration scales with

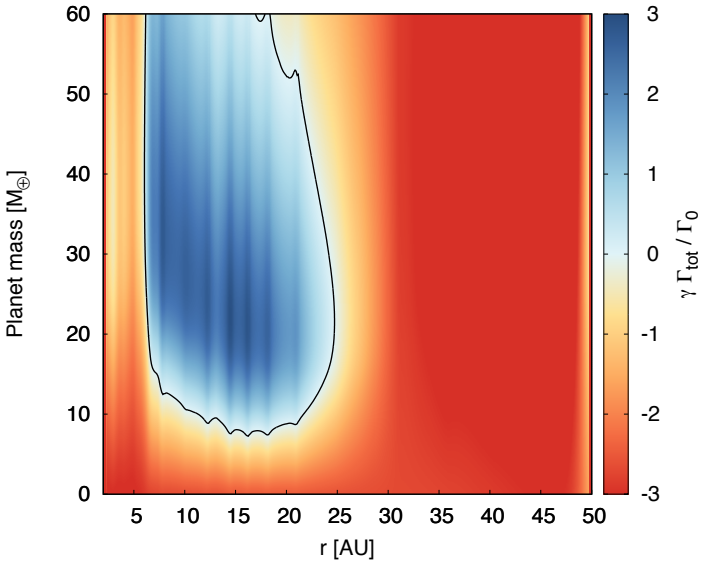

Figure 3.13. Torque acting on planets with different masses for the disc utilizing the BOD distribution for the nominal viscosity of $\alpha = 5 \times 10^{-3}$. The black line encircles the regions of outward migration and corresponds to the region of the disc where the aspect ratio decreases as a function of the orbital distance. The temperature in the same region shows the steepest gradient.

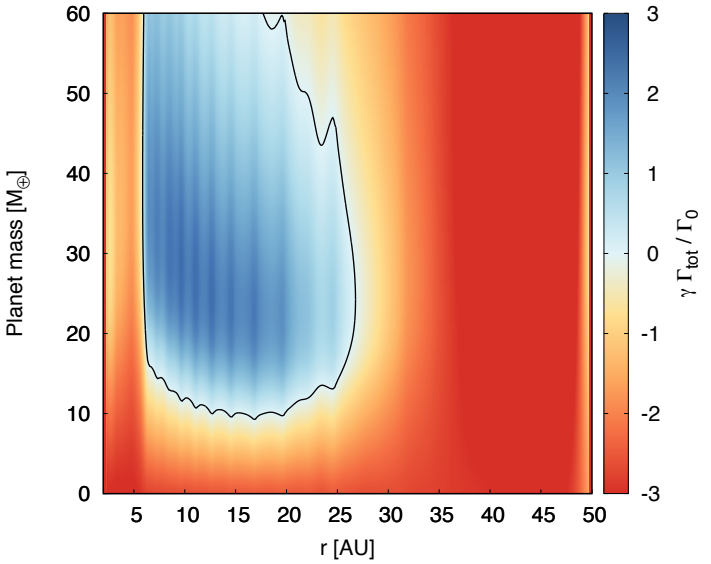

Figure 3.14. Same as Fig. 3.13 for the disc with the MRN distribution. The difference to the BOD distribution is small regarding the size of the region of outward migration, however, the torque is weaker for the MRN distribution. This could lead to different migration and growth behavior of planets forming in the outer disc.

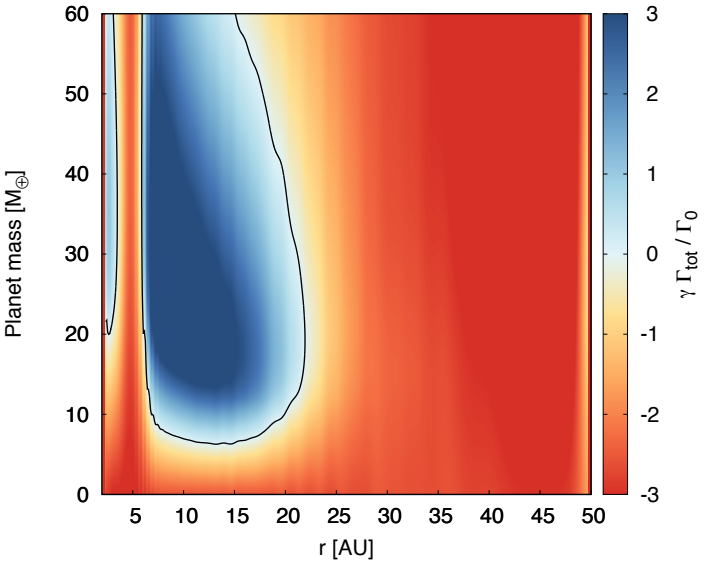

Figure 3.15. Same as Fig. 3.13 for the disc with the Bell & Lin (1994a) opacity profile. In contrast to the discs with the BOD or the MRN grain size distribution, the disc simulated with the Bell & Lin (1994a) opacity law shows an inner region of outward migration, which is caused by another bump in the H/r profile in the inner disc (Fig.5).

the inverse of the square of the aspect ratio. If the aspect ratio decreases, then the migration is faster (for a review see Baruteau et al. 2014). Therefore, generally speaking, migration would be faster in the single grain size models with large particles and the exact migration speed of planets depends on their exact position in the protoplanetary disc.

To predict more precisely the migration of planets in the discs presented here, we include the migration maps for two discs with the distributions (Figs. 3.13 and 3.14). Migration rates are derived from the torque formula of Paardekooper et al. (2011b). For comparison, we also show the migration map of the disc with the Bell & Lin (1994a) opacities (Fig. 3.15), as these were the opacities used in Bitsch et al. (2015a) in Fig.18. The black solid line in Figs. 3.13, 3.14, 3.15 encircles the regions of outward migration. Planets with masses less than approximately 10 $M_{\oplus}$ always migrate inwards in the simulations with the distributions, whereas for the simulation using the Bell & Lin (1994a), pure micrometer opacities, inward migration is the only possibility for planets less than 6 $M_{\oplus}$.

The innermost region of outward migration in Fig.3.15 corresponds to the area where the aspect ratio decreases as the orbital distance increases (Fig. 3.6). We can also see that this area has a steeper temperature gradient (Fig. 3.6) both interior and exterior to the water iceline transition. The increased torques and consequently migration speeds at the outer region of outward migration between 5 and 20 AU in the Bell & Lin (1994a) disc simulations are caused by the steep increase of opacity for temperatures larger than 170 K, which is not the case for the BOD and MRN distribution, as these distributions are not dominated by micrometer grains, in contrast to the Bell & Lin (1994a) opacity model. This illustrates that the grain sizes which dominate or contribute the most to the opacity of the disc have significant implications, not only for the disc structure itself but also indirectly for the planets embedded in that disc. In addition, this has important effects on the formation of planetary systems, because the migration rates determine how close planets can migrate towards each other, which sets the stability of the planetary system (Chambers 2006; Matsumoto et al. 2012).

3.5.3 Implications for planet formation and protoplanetary disc simulations

Our simulations presented here are the first step towards more self-consistent protoplanetary disc structure and evolution simulations as well as planet formation simulations. Planet formation in the pebble assisted core accretion scenario relies crucially on the pebble sizes and distributions (e.g., Johansen & Lambrechts 2017b; Lambrechts & Johansen 2012b; Ormel & Klahr 2010b, for review), as well as on the disc structure to calculate the planet migration rates as the planets grow (Bitsch et al. 2015c). The here presented model opens the avenue to simulations with self-consistent disc structures and pebble sizes, which can then be accreted onto planets. This can increase the accuracy of future planet formation simulations by pebble accretion.

The here used FARGOCA code also allows for 3D hydrodynamical simulations

with embedded planets. A combination with the presented model of thermal structures calculated from full grain size distributions allows a very detailed comparison with observations, which are more advanced that the most frequently used 2D isothermal simulations followed by 3D radiative transfer (e.g., Zhang et al. 2018a). This could potentially change our interpretation of observed protoplanetary discs featuring substructures potentially caused by planets.

3.6 Summary

We perform 2D hydrodynamical simulations including the whole feedback loop shown in Fig. 3.1. Specifically, we include and test two full grain size distributions and mean opacities (calculated via Mie theory) and study their influence on the disc structure. The particles have a minimal size of 0.025 μm and the upper boundary is regulated by the fragmentation barrier (Eq. 3.14). We test five different α-viscosity values ($10^{-2}, 5 \times 10^{-3}, 10^{-3}, 5 \times 10^{-4}, 10^{-4}$), five values of initial gas surface density $\Sigma_{g,0}$ (100, 250, 500, 750 and 1000 g/cm^2) and five values of dust-to-gas ratio f_{DG} (1%, 1.5%, 2%, 2.5%, 3%). We also perform simulations with only single grain sizes and with the Bell & Lin (1994a) opacity law for comparison and in order to understand to greater extent the influence of grains of different sizes on the thermal structures of protoplanetary discs.

The dust component in protoplanetary discs is believed to follow a size distribution, regulated by a coagulation-fragmentation equilibrium (Birnstiel et al. 2011a; Brauer et al. 2008b). We utilize and compare two different grain size distributions. The first and simple model (MRN) (Dohnanyi 1969; Mathis et al. 1977; Tanaka et al. 1996) results from the equilibrium between fragmentation and coagulation, whereas the second and more complex model (Birnstiel et al. 2011a, BOD) takes into account fragmentation, coagulation and also cratering and adjusts the dust surface densities according to the grain sizes and how they compare to the size of the gas molecules and the gas turbulent eddies.

The dust surface densities are calculated as dictated by the aforementioned grain size distributions and the dust grains are also vertically distributed according to their sizes taking into account the effect of settling. We also have a spatial distribution radially, since the size distribution depends on the local disc parameters and changes self-consistently. In conclusion, a whole loop of growth, fragmentation, and settling of the resulting grains for each vertical slice of the disk is modeled in our simulations and updated at every timestep according to the local disc parameters.

We show disc structures calculated with the full grain size distributions and single grain sizes in Figs. 3.5 and 3.5b. Additionally, we show that the grain sizes which dominate or contribute the most to the opacity of the disc are not the same at all orbital distances of the disc (Figs. 3.8 and 3.10). As

a consequence, the opacity prescriptions which assume a single dust size lead to inaccurate calculations of the thermal structures of the discs.

It is also important to stress that the dust surface densities, or in other words the distribution of mass among the grain sizes, play a major role in determining the disc opacity (Eq. 3.15), which in turn influences the cooling rate and the stellar heating and changes the temperature and surface density of the gas. This shift in the local disc parameters leads to a new fragmentation barrier (and regime boundaries for the BOD), therefore the dust surface densities change and so on. For this reason, it is important to include the self-consistent calculations of the dust surface densities in the simulations.

The two grain size distributions show minimal differences in the dust surface densities (Fig. A.1). The reason for this is that both of the grain size distributions we have used in the discs feature the same fragmentation barrier. Therefore the grain size range in the discs with either one of the distributions is similar. Any difference between the discs with the BOD distribution and the discs with the MRN distribution comes mainly from the difference in the surface densities as a function of grain size (see Figs. 3.3 and A.1), which is usually smaller than an order of magnitude. The dominant grain sizes (Sect. 3.3.4) might not be the same, because of the small differences in the dust surface densities per grain size, but the total opacity of the disc is similar independently of the grain size distribution.

With this accurate prescription, we investigate the dependency of the iceline position on the α-viscosity, the initial gas surface density and the dust-to-gas ratio, where we see the effect of the feedback loop and find $r_{ice} \propto \alpha^{0.61}\Sigma_{g,0}^{0.8} f_{DG}^{0.37}$ (Eq. 3.19, Fig. 3.12) independently of the grain size distribution utilized in the disc model. Specifically, for high gas surface density ($\Sigma_{g,0} = 1000\ g/cm^2$) the position of the iceline is exterior to 1 AU for $\alpha \geq 2.64 \times 10^{-4}$ and exterior to 2.7 AU only when $\alpha \geq 1.35 \times 10^{-3}$. For higher values than the nominal $f_{DG} = 1\%$ we find that the iceline moves closer to the star as it is expected by the enhanced dust surface densities and the consequent hotter discs. However, for the nominal $f_{DG} = 1\%$, lowering the gas surface density results in colder discs and the iceline is below 2.7 AU, even for the high viscosity models.

The changes in the aspect ratio gradient as a function of orbital distance affect the regions where outward migration is possible for planets that could be embedded in the disc (Figs. 3.13, 3.14, 3.15). Utilizing an α-viscosity of 5×10^{-3}, $\Sigma_{g,0} = 1000\ g/cm^2$ and $f_{DG} = 1\%$ we find that the regions where outward migration could be possible in the discs with the two distributions are similar to the one present in a disc with the Bell & Lin (1994a) opacities, that feature only micrometer-sized grains, at around 5-15 AU for planets with masses greater than 10 $M_\oplus$. However, the region is more extended for the disc with the BOD distribution (up to 20 AU) and the disc with the Bell & Lin (1994a) opacities has one more outward migration regions, near the inner boundary (2-3 AU), which is not present in the discs with the grain size distributions.

We can hence conclude that given the complexity and computational expense of the BOD distribution and the fact that it does not take into account radial drift or bouncing of the dust particles it is not necessary to prefer it over a simple MRN-like power-law distribution.

As the iceline can be the starting point for planetesimal formation (Drążkowska & Alibert 2017a; Guillot et al. 2014; Schoonenberg & Ormel 2017a) it is important to have as realistic models as possible, therefore include the feedback loop of grain growth and thermodynamics in hydrodynamical models (Fig. 3.1). Given also the fact that dust in protoplanetary discs follows a size distribution regulated by a coagulation-fragmentation equilibrium, the opacity prescription of a single grain size is not able to accurately calculate the thermal structures of discs.

The here presented model has some limitations that we wish to further investigate in future work. Both of the distributions tested here neglect radial drift (Birnstiel et al. 2012b; Brauer et al. 2008b) and bouncing (Lorek et al. 2018; Zsom et al. 2010b) which can be detrimental for grain growth and in general affect the dust dynamics and subsequently the disc's thermal structure. Also the onset of convection in some regions and for a subset of α and $\Sigma_{g,0}$ values might change the vertical distribution of the grains beyond settling and turbulent stirring by viscosity, as taken into account here. A very important future step is to model accretion discs instead of equilibrium discs and in this way, we will be able to also study different evolutionary steps of the protoplanetary disc. The particle composition and abundances are also determinants for dust dynamics and opacities, so it is important to consider a population that is as realistic as possible and use more accurate fragmentation velocities depending on our dust composition. Similarly, we are assuming a dust population consisting of 50% silicates and 50% water-ice, but we can relax this assumption and test different fractions (as done for example, in Bitsch & Johansen (2016)).

It is, therefore, evident that the prescription that we used and present for this work opens up new avenues for protoplanetary disc simulations and planet formation. The inclusion of the feedback loop of grain growth and disc thermodynamics leads to more self consistent simulations of protoplanetary accretion discs and planet formation simulations in the pebble accretion scenario. Eventually, such models target a more precise comparison of protoplanetary disc observations to simulations that allow us to move away from simple 2D isothermal models with post-processing of radiation transfer.

4

The growth of super-Earths.

From "The Growth of Super-Earths: The Importance of a Self-Consistent Treatment of disc Structures and Pebble Accretion", Savvidou & Bitsch 2021

In a nutshell...

The conditions in the protoplanetary disc are determinant for the various planet formation mechanisms. We present a framework that combines self-consistent disc structures with the calculations of the growth rates of planetary embryos via pebble accretion, in order to study the formation of super-Earths. We first perform 2D hydrodynamical simulations of the inner discs, considering a grain size distribution with multiple chemical species and their corresponding size and composition dependent opacities. The resulting aspect ratios are almost constant with orbital distance, resulting in radially constant pebble isolation masses, the mass where pebble accretion stops. This supports the "peas-in-a-pod" constraint from the Kepler observations. The derived pebble sizes are used to calculate the growth rates of planetary embryos via pebble accretion. Discs with low levels of turbulence (expressed through the α-viscosity) and/or high dust fragmentation velocities allow larger particles, hence lead to lower pebble isolation masses, and the contrary. At the same time, small pebble sizes lead to low accretion rates. We find that there is a trade-off between the pebble isolation mass and the growth timescale; the best set of parameters is an α-viscosity of 10^{-3} and a dust fragmentation velocity of 10 m/s, mainly for an initial gas surface density (at 1 AU) greater than 1000 g/cm^2. A self-consistent treatment between the disc structures and the pebble sizes is thus of crucial importance for planet formation simulations.

4.1 Context

Observational data have so far shown that planets of a few Earth masses are one of the most abundant groups of planets in the exoplanetary systems (e.g., Batalha et al. 2013; Borucki et al. 2010; Fressin et al. 2013; Mulders et al. 2018; Petigura et al. 2013). Additionally, the super-Earth planets have recently been shown to be

of similar sizes within the same planetary system (Weiss et al. 2018), even though this was put into question by another analysis (Zhu et al. 2018). It is therefore of utmost interest to understand the mechanisms leading to their formation, especially given the fact that super-Earths are absent from the Solar System (Martin & Livio 2015).

The formation of planets is initiated by the coagulation (Birnstiel et al. 2012a; Brauer et al. 2008a; Testi et al. 2014; Weidenschilling 1980b, 1984b; Zsom et al. 2011b) and condensation (Ros & Johansen 2013) of small dust particles, or nucleation on icy particles (Ros et al. 2019). There are several conditions that limit dust growth, such as the fragmentation barrier, the bouncing barrier, and the radial drift barrier (Birnstiel et al. 2010a; Brauer et al. 2007; Zsom et al. 2010a). However, these barriers help in the rapid formation of millimeter- to centimeter-sized particles or pebbles, which is an essential contributor to planet formation.

Planet formation can continue with the creation of larger bodies, for example via the streaming instability where the dust particles concentrate into filaments with sufficient densities to gravitationally collapse into planetesimals (Chiang & Youdin 2010; Johansen & Youdin 2007; Youdin & Johansen 2007; Youdin & Goodman 2005). In the classical core accretion scenario, a sufficiently large planetesimal serves as a planetary embryo, which accretes other planetesimals, and forms the planetary core (Helled et al. 2014; Pollack et al. 1996, for a review). However, this procedure has some drawbacks, among others the growth timescale, which can be even longer than the lifetime of the protoplanetary disc (Fortier et al. 2013; Johansen & Bitsch 2019; Lambrechts & Johansen 2012a; Levison et al. 2010; Pollack et al. 1996; Rafikov 2004), unless the dust density is significantly enhanced (Kobayashi et al. 2011).

One of the proposed mechanisms to form super-Earths is the accretion of pebbles (millimeter- to centimeter-sized particles) onto a preexisting planetesimal or protoplanet (Johansen & Lacerda 2010; Johansen & Lambrechts 2017a; Lambrechts & Johansen 2012a; Ormel & Klahr 2010a; Ormel et al. 2017). The accretion of solids is not limited by the available material closely around the planetary seed, but is aided by the drift of small solids or pebbles (Weidenschilling 1977b). Pebble accretion thus acts on much shorter timescales compared to planetesimal accretion, especially in the outer disc regions (Bitsch et al. 2015b; Izidoro et al. 2019b; Johansen & Bitsch 2019; Lambrechts & Johansen 2014; Lambrechts et al. 2019).

In this work we focus on the accretion of the small particles by an already formed planetary seed. The planet grows until it reaches the pebble isolation mass (Ataiee et al. 2018; Bitsch et al. 2018; Lambrechts et al. 2014; Morbidelli & Nesvorny 2012; Surville et al. 2020); it then carves a gap in the protoplanetary disc, thus trapping the pebbles in a pressure trap exterior to the planet. This critical mass depends on the disc parameters, mainly the aspect ratio, and not on the available amount of solids. Wu (2019) showed that protoplanetary cores could grow to the thermal mass in discs, which corresponds to the typical masses of planets in the mass-constrained subsample of the Kepler systems. Bitsch (2019) expanded on this, showing that the pebble isolation mass could be the main driver for this observation, with a crucial dependence on the underlying protoplanetary disc structure.

The protoplanetary disc structure thus holds most of the key parameters and conditions that define the planet formation mechanisms. On the other hand, the

grain size distribution and the subsequent opacity play a very important role in the determination of the disc structure and the disc evolution (Savvidou et al. 2020). A change in opacity directly affects the cooling rate of the disc, and the new thermal structure leads to an updated grain size distribution. The opacity of the disc is then altered because the mass fractions of the grain sizes are different. This feedback loop operates until the disc reaches thermal equilibrium, which means that the resulting disc structure is heavily influenced by the grain size distribution and the opacity provided by the dust grains (Savvidou et al. 2020), and will then determine the evolution of planet formation.

In this work we obtain disc models from hydrodynamical simulations, including self-consistent grain distribution and opacities according to the grain sizes and compositions, following our previous work (Savvidou et al. 2020). We thus have a framework that allows a self-consistent disc structure with the corresponding pebble sizes to calculate the growth rates of planetary embryos via pebble accretion. We focus on the innermost parts of a disc to study how the grain size distribution and the chemical compositions of the grains affect the formation of super-Earths.

4.2 Methods

4.2.1 Opacities

We calculate the mean Rosseland, Planck, and stellar opacities as a function of temperature using the RADMC-3D[1] code. These mean opacities are used in the energy equations of the protoplanetary disc model. In particular, the energy time evolution utilizes the Planck mean opacity, which uses as a weighting function the Planck black-body radiation energy density distribution ($B_\lambda(\lambda, T)$). The radiation flux is inversely proportional to the Rosseland mean opacity, which is calculated using the temperature derivative of the Planck distribution ($\partial B_\lambda(\lambda, T)/\partial T$). Therefore, in contrast to the Planck mean opacity, the Rosseland mean opacity describes the optically thick regions well. For both of the above-mentioned opacities the temperature taken into account is the local disc temperature. However, when we want to describe the absorption of stellar photons, we use the stellar mean opacities, which are calculated in a similar manner to the Planck mean opacities, taking into account the temperature of the stellar radiation ($B_\lambda(T_\star)$), assuming isotropic radiation), which in our models is $T_\star = 4370$ K.

In contrast to our previous work (Savvidou et al. 2020), where only water ice and silicates were used, we include here all of the major rock- and ice-forming species. We present them in Table 4.1, along with their volume mixing ratios and mass fractions, following Bitsch & Battistini (2020). We discuss in detail how we obtained these opacities in Appendix B. In Fig. 3.2 we show the opacity as a function of temperature for six representative grain sizes. The gray vertical dashed lines correspond to the evaporation fronts for the species we include in our model. After each evaporation front, the corresponding species sublimates and no longer contributes to the overall

[1] http://www.ita.uni-heidelberg.de/~dullemond/software/radmc-3d/

Table 4.1. Condensation temperatures and volume mixing ratios for the chemical species used in this work. Also shown are the densities and mass fractions considered to calculate the mean opacities as a function of temperature, along with the references of the refractive indices.

Species	T_{cond} [K]	ρ_s [g/cm^3]	Volume mixing ratios	Mass fraction	Reference for refractive indices
CO	20	1.0288	0.45 × C/H	21.68%	1,◇
CH_4	30	0.47	0.25 × C/H	6.882%	1,◇
CO_2	70	1.5	0.1 × C/H	7.574%	1,◇
H_2O	170	1.0	O/H - (3 × $MgSiO_3$/H + 4 × Mg_2SiO_4/H + CO/H + 2 × CO_2/H + 3 × Fe_2O_3/H + 4 × Fe_3O_4/H)	21.28%	2,●
Fe_3O_4	371	5.0	(1/6) × (Fe/H - S/H)	4.231%	3,⋆
C	626	2.1	0.2 × C/H	4.129%	4
FeS	704	4.84	S/H	6.908%	5,⋆
Mg_2SiO_4	1354	3.275	Mg/H - Si/H	13.45%	6,⋆
Fe_2O_3	1357	5.24	0.25 × (Fe/H -S/H)	4.377%	3,⋆
$MgSiO_3$	1500	3.2	Mg/H - 2 × (Mg/H - Si/H)	9.489%	6,⋆

References: [1] Hudgins et al. (1993), [2] Warren & Brandt (2008b), [3] Amaury H.M.J. Triaud; unpublished, [4] Preibisch et al. (1993), [5] Henning & Mutschke (1997), [6] Jäger et al. (2003)
Data can be found in: [◇] http://vizier.u-strasbg.fr, [●] https://atmos.uw.edu/ice_optical_constants/, [⋆] https://www.astro.uni-jena.de/Laboratory/OCDB/

α	$\Sigma_{g,0}$ [g/cm^2]	u_f [m/s]
10^{-3}	100	1
5×10^{-4}	500	
10^{-4}	1000	10
	2000	
$M_\star$	1 $M_\odot$	
$T_\star$	4370 K	
$R_\star$	1.5 $M_\odot$	
total f_{DG}	1.5%	

Table 4.2. Parameters used in the simulations

opacity, so the mass fractions are adjusted accordingly.

4.2.2 Hydrodynamical simulations

The viscosity in the simulations follows an α-prescription (Shakura & Sunyaev 1973). We run simulations with three α-viscosity values, namely $\alpha = 10^{-3}$, 5×10^{-4}, and 10^{-4}, and list all parameters of the model in Table 4.2.

The gas surface density follows a profile

$$\Sigma_g = \Sigma_{g,0} \cdot (r/AU)^{-p} \ , \tag{4.1}$$

with $p = 1/2$. For each α-viscosity we run a set of four initial gas surface densities, $\Sigma_{g,0}$ = 100, 500, 1000, and 2000 g/cm^2.

In all of the simulations the stellar mass is $M_\star = 1\ M_\odot$, the stellar temperature is $T_\star = 4370$ K, and the stellar radius is $R_\star = 1.5\ R_\odot$. The total dust-to-gas ratio is $f_{DG} = 1.5\%$. The discs extend from 0.1 to 4 AU, except for the simulations with $\Sigma_{g,0}$ = 2000 g/cm^2, where the inner boundary is at 0.2 or 0.3 AU. We do not include gas opacities in our model, hence this was a necessary choice to prevent the overheating of the innermost edge and a strong shadowing that would cool down the rest of the disc. The simulations run until they reach thermal equilibrium. The disc structures from the hydrodynamical simulations are used afterward to determine the pebble isolation masses and the pebble accretion rates, which we discuss in the following sections.

In this work we use the Mathis, Rumpl, & Nordsieck (1977, MRN) distribution[2], where the normalized vertically integrated dust surface densities are calculated at each orbital distance as

$$\tilde{\Sigma}_{d,s_i} = \frac{s_i^{1/2} f_{DG,r} \Sigma_g}{\sum_i s_i^{1/2}}, \tag{4.2}$$

[2]We find that the disc structure itself is only slightly influenced if a more complex grain size distribution (Birnstiel et al. 2011b) is used (Savvidou et al. 2020). For simplicity we use the MRN distribution.

with s_i the grain size and Σ_g the gas density. In order to calculate these dust surface densities, we consider the evaporation of the chemical species as we move farther-in in the disc and use $f_{DG,r}$, which is the appropriate fraction of the total dust-to-gas ratio of the disc depending on how many species have evaporated at the given location (Fig. 4.1). It is important to note that we do not use a constant upper boundary for the grain sizes. Instead, we use the local disc parameters to calculate the fragmentation barrier (Eq.3.14).

The threshold velocity u_f corresponds to the threshold after which collisions between particles always lead to fragmentation (Poppe et al. 2000b). For this work we test two different fragmentation velocities, $u_f = 1$ m/s and $u_f = 10$ m/s, corresponding to the limits of laboratory experiments (Gundlach & Blum 2015b; Musiolik & Wurm 2019).

4.2.3 Pebble accretion

We start the planetary seeds at 0.01 $M_\oplus$, assuming they have already formed. For simplicity, we only take the Hill regime into account, which should start around this planetary mass (Johansen & Lambrechts 2017a), and we follow the Lambrechts & Johansen (2014) accretion recipes. This implies that the accretion radius and the accretion rates of the planet are determined by the Stokes numbers of the pebbles (Equation 2.13). For consistency, for the planet growth we only use the Stokes numbers at midplane because this is the approximation we follow in our hydrodynamical models (see a more detailed discussion on the vertical distribution of the grains in Savvidou et al. 2020). The range of grain sizes at each location of the disc is determined by the local disc properties (see maximum grain size, Eq. **??**).

We calculate the accretion rates in the 2D and 3D regime for each grain size of the distribution (Eq. 4.2), and then add up all of the contribution to get the total accretion rate.

Within this approach we assume that the pebbles that are accreted by the planet are replenished at the planet's location by radial drift, so that the dust surface density does not change at the planets location during pebble accretion. Future work has to consider the grain drift and its influence on the disc's structure with accreting planets more accurately.

4.2.4 Pebble isolation mass

Planetary growth halts when the planet reaches the pebble isolation mass (Eq. **??**). At this mass the planet has accreted enough material so that it carves a gap in the gas of the protoplanetary disc and creates a pressure bump around it (Paardekooper & Mellema 2006). This bump prevents the dust from drifting onto the planet core, and growth via pebble accretion stops (Ataiee et al. 2018; Bitsch et al. 2018; Lambrechts et al. 2014; Morbidelli & Nesvorny 2012; Surville et al. 2020).

Here we let the planets grow via pebble accretion until they reach the pebble isolation mass and track the time it takes them to monitor whether the planet can reach this mass during the disc's lifetime. However, we stop the growth at 100 Myr

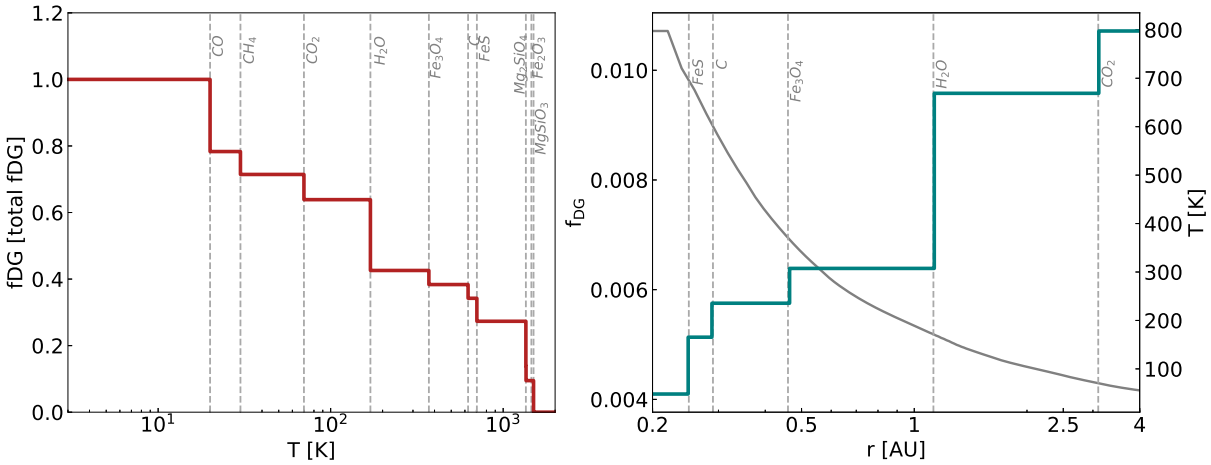

Figure 4.1. Influence of the evaporation of the different chemical species on the dust-to-gas ratio in the protoplanetary disc. *Left plot*: Dust-to-gas ratio in terms of the total dust-to-gas ratio in the disc as a function of temperature. After each species evaporates the total mass fraction decreases by the corresponding mass fraction (see Table 4.1) until all species evaporate beyond 1500 K. *Right plot*: Example of the dust-to-gas ratio as a function of orbital distance for the disc with $\alpha = 10^{-3}$, $\Sigma_{g,0} = 2000$ g/cm^2, and $u_f = 10$ m/s, and a global dust-to-gas ratio of 1.5%. Overplotted is the temperature of the disc where the evaporation fronts are easy to locate.

as this time exceeds the lifetime of protoplanetary discs quite clearly (e.g., Mamajek 2009).

4.2.5 Advantages and limitations of our model

Compared to 1D models, our 2D model has the advantage that the vertical structure is solved self-consistently. Furthermore, shadowing effects inside the disc caused by bumps in the disc structure that block stellar irradiation are self-consistently resolved, leading to an accurate thermal disc structure, which is not possible in 1D models. The 2D models (radial-azimuthal) of Drążkowska et al. (2019) take into account the full coagulation and drift of particles, but are limited to the isothermal approach, thus ignoring the feedback of the grain size distribution on the thermal disc structure.

One-dimensional models, on the other hand, have the possibility to be evolved over several million years (Myr), which is not possible with our 2D models. These 1D models (Birnstiel et al. 2012a) can then accurately resolve the time evolution of the grain size distribution, and also investigate pileups of material in the inner disc in time, but they cannot accurately model shadowing effects. Furthermore, 1D models that self-consistently take into account grain growth, grain drift, the corresponding grain opacities, and the resulting thermal structure of the disc do not exist yet. We thus show simulations with increased dust-to-gas ratios in Sect. 4.4 corresponding to a pileup of grains in the inner regions caused by radial drift (Birnstiel et al. 2012a; Brauer et al. 2008a).

Our 2D approach allows us to explore the influence of the self-consistent disc

models on pebble accretion (admittedly in a simplified way), and to emphasize that the grain size distributions, their corresponding sizes, and composition dependent opacities affect the disc structure, and in turn the planet formation. This effect thus needs to be included in future planet formation simulations, which to date have mostly operated with disc structures independently of the pebble size distribution (e.g., Bitsch et al. 2015; Bitsch et al. 2019b; Johansen & Lambrechts 2017a; Venturini et al. 2020b).

4.3 disc structure

4.3.1 Dependence on viscosity, gas surface density, and fragmentation velocity

We investigate the influence of different α-viscosities, initial gas surface densities, and fragmentation velocities on the grain sizes and disc structures. The specific values used are shown in Table 4.2. The influence of the different α-viscosities and surface densities $\Sigma_{g,0}$ on the resulting disc structure is discussed in detail in Savvidou et al. (2020). In a nutshell, as the α-viscosity decreases, the disc gets colder. There are two reasons for this. Since the viscous heating decreases, the disc cools down more efficiently. At the same time the dust particles face less destructive collisions, and grow to larger sizes that have lower opacities. This further aids the cooling of the disc.

We present the results of our simulations with different α-parameters and for different initial gas surface densities, utilizing a fragmentation velocity of 1 m/s in Fig. 4.2. Clear trends with viscosity and gas surface density are visible.

Decreasing the gas surface density scales down the total dust surface density. As a consequence, the disc is colder because the viscous heating is less efficient and radiative cooling is enhanced, given that the cooling is inversely proportional to the disc's density. However, for very low α-viscosity values the difference between discs with different surface density diminishes (Savvidou et al. 2020). We also find that for $\alpha = 10^{-4}$ (third column in Fig. 4.2), the aspect ratio of the discs is very low, and is almost independent of the gas surface density. In this case the disc is mainly optically thin and the dominant heating mechanism is stellar irradiation, resulting in very similar disc structures.

The same applies to the simulations using higher fragmentation velocities. In this case larger grains are available and dominate the opacity of the disc, and hence the cooling of the disc is very efficient (Fig. 4.3 for $\alpha = 5 \times 10^{-4}$ and 10^{-4}). Even for the highest value, $\alpha = 10^{-3}$ (first column in Fig. 4.3), the difference in the aspect ratios of discs with varying surface densities is not as pronounced as in the corresponding discs with lower fragmentation velocity (Fig. 4.2). This shows that the larger grain sizes provide such low opacities that even an α-viscosity of 10^{-3} cannot heat the disc sufficiently. As a result, the water ice line is already close to 1 AU, even for the highest gas surface density.

In Figs. 4.2 and 4.3 we see some radial variations in some of the disc profiles,

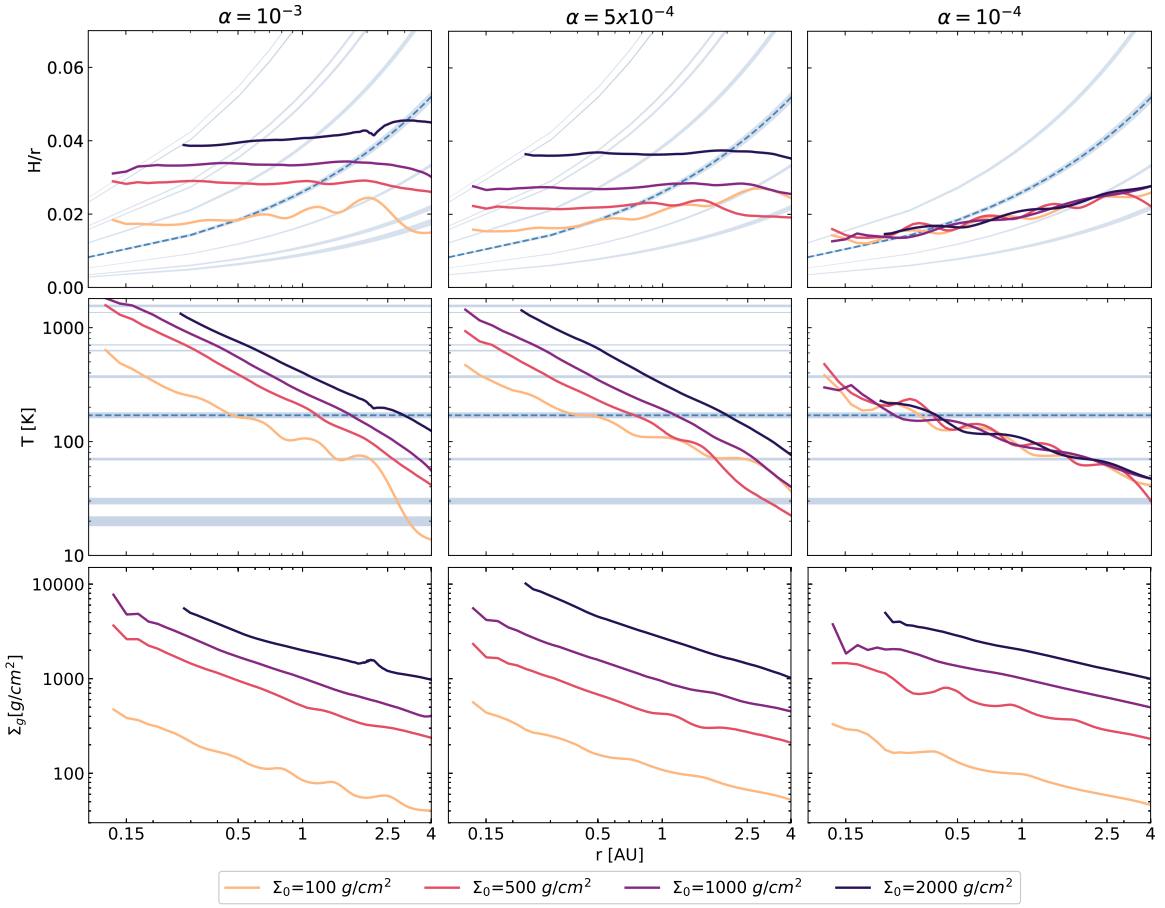

Figure 4.2. Aspect ratio (upper plot), temperature (middle plot), and gas surface density (bottom plot) as a function of orbital distance for four different initial gas surface densities, from 100 g/cm^2 to 2000 g/cm^2. The turbulence parameter in viscosity is $\alpha = 10^{-3}$ in the left panel, $\alpha = 5 \times 10^{-4}$ in the middle panel, and $\alpha = 10^{-4}$ in the right panel. The fragmentation velocity is $u_f = 1$ m/s. The light blue areas in the aspect ratio and temperature plots indicate the evaporation fronts ($\pm$ 2 K around the evaporation temperatures of CH_4, CO_2; $\pm$ 10 K for the other species). Starting from the outer boundary, for $\alpha = 10^{-3}$ the species that evaporate are CO, CH_4, CO_2, H_2O, Fe_3O_4, C, FeS, Mg_2SiO_4, and $MgSiO_3$. For $\alpha = 5 \times 10^{-4}$ the evaporation fronts are of CO_2, H_2O, Fe_3O_4, C, FeS, Mg_2SiO_4, and $MgSiO_3$ and for $\alpha = 10^{-4}$ they are CO_2, H_2O, and Fe_3O_4. The water ice line is shown as a dashed line.

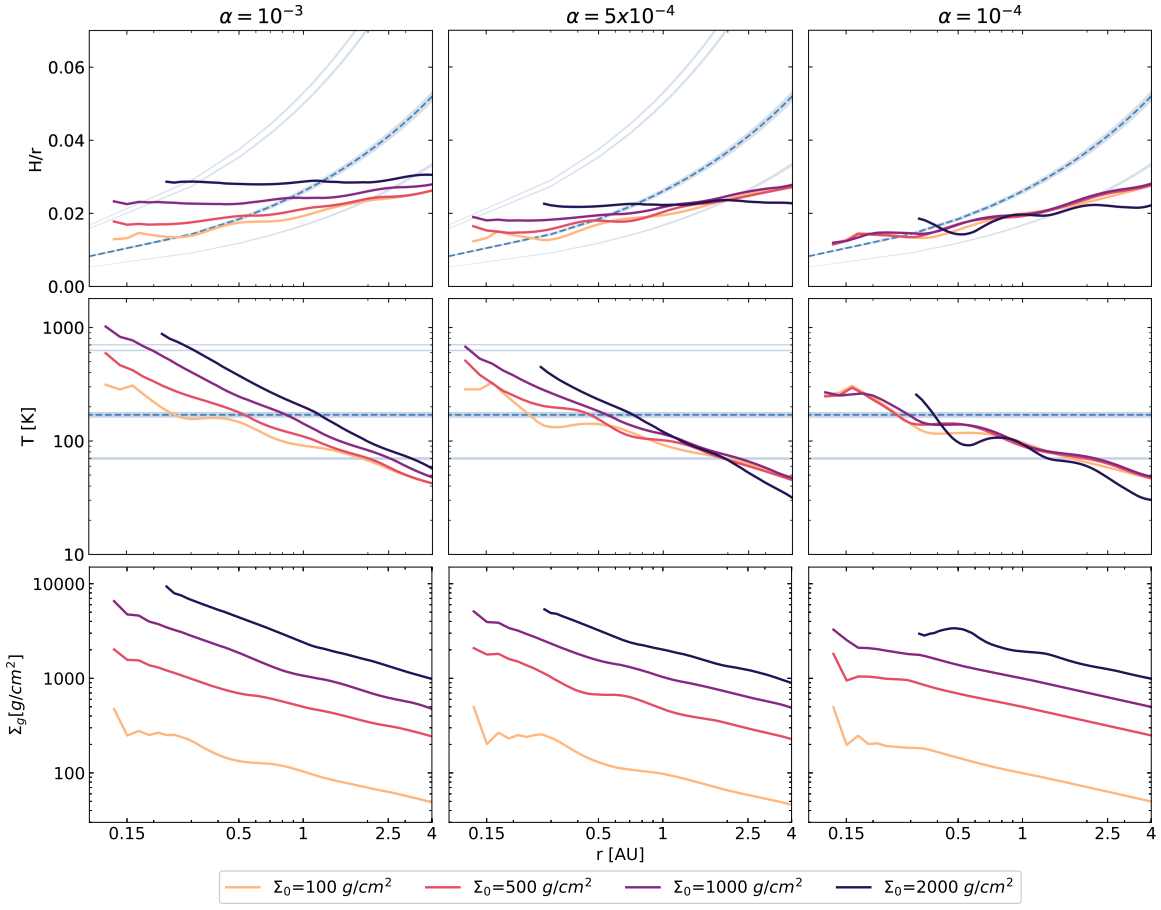

Figure 4.3. Same as Fig. 4.2, but using a fragmentation velocity of $u_f = 10$ m/s. Starting from the outer boundary, for $\alpha = 10^{-3}$ the species that evaporate are CO_2, H_2O, Fe_3O_4, C, and FeS. For $\alpha = 5 \times 10^{-4}$ the ice lines are of CO_2, H_2O, Fe_3O_4, C, and FeS and for $\alpha = 10^{-4}$ they are CO_2 and H_2O. The water ice line is shown as a dashed line.

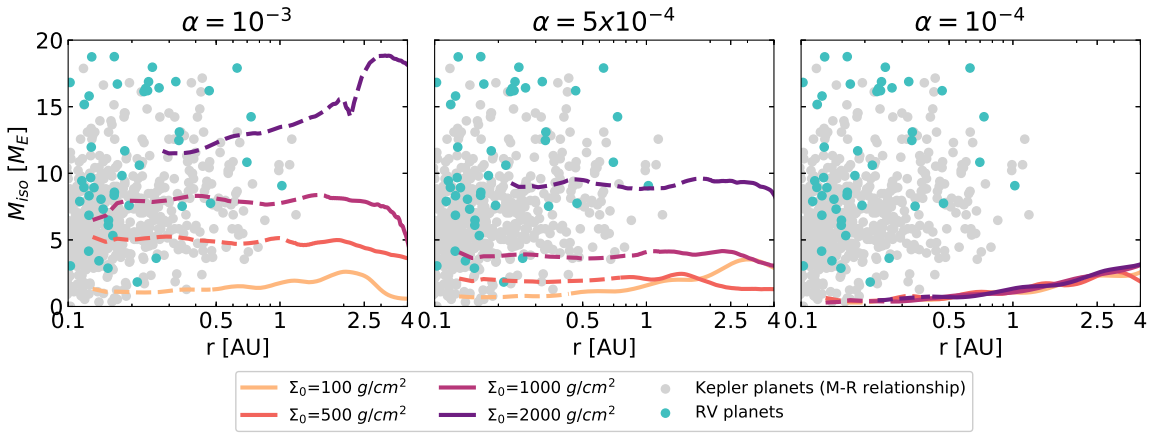

Figure 4.4. Pebble isolation mass as a function of orbital distance for discs with four different initial gas surface densities, from 100 g/cm^2 to 2000 g/cm^2. The turbulence parameter in viscosity is $\alpha = 10^{-3}$ in the left panel, $\alpha = 5 \times 10^{-4}$ in the middle panel, and $\alpha = 10^{-4}$ in the right panel. The fragmentation velocity is $u_f = 1$ m/s. We also include the planetary masses of Kepler systems, with radii up to 4 $R_\oplus$, derived through the `Forecaster` package (Chen & Kipping 2017) (gray circles) and super-Earths detected by RV (blue circles). The dashed lines correspond to the disc regions interior to the ice line, whereas the solid lines are the regions exterior to the ice line, where the forming planets are water rich.

especially for very low surface densities. This is caused mainly by convection, created by the vertical temperature gradient which depends on the opacity gradient in the vertical direction and is present in the optically thick regions of the disc (Bitsch et al. 2013b). However, in this work we have included multiple chemical species in our opacity prescription, and this creates dips in the opacity as a function of temperature at the evaporation fronts of the various species[3] (see Fig. 3.2). Even if these dips are minimal, they can create small bumps in the aspect ratio profiles, which are amplified by the convection and lead to an enhancement of these perturbations.

The protoplanetary discs in our models, or the regions within them, that are not strongly affected by convection do not show a significant influence from the multiple evaporation fronts of the chemical species we have included because the changes in the opacity are small. The strongest effect remains with the evaporation of water ice, which causes a strong dip in the opacity and hence a more enhanced bump in the aspect ratio (Figs. 4.2 and 4.3). Nevertheless, the overall opacity is slightly different to a prescription where only water ice and silicates are used (Savvidou et al. 2020). In addition, including multiple chemical species is important because they could be used in future work to predict the possible compositions of the planets growing within the discs of our models.

In our previous work (Savvidou et al. 2020), we discuss the dependence of the water ice line position on the α-viscosity, the gas surface density, and the dust-to-gas ratio. We also find here that it moves farther in if the gas surface density or the α-viscosity decreases. Here, we also use $u_f = 10$ m/s, and find that the higher

[3]In contrast, our previous simulations (Savvidou et al. 2020) only included two species, resulting in fewer variations in the disc profile.

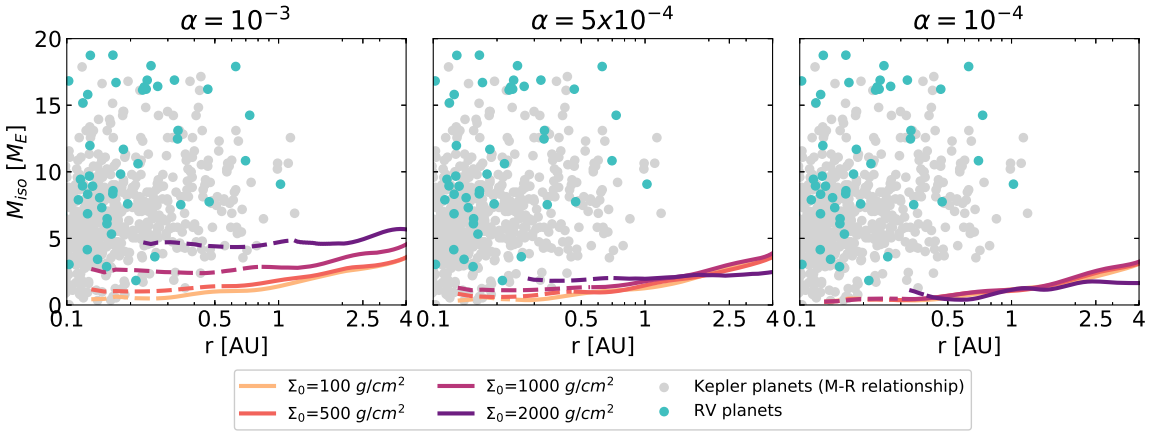

Figure 4.5. Same as Fig. 4.4, but for a fragmentation velocity of $u_f = 10$ m/s.

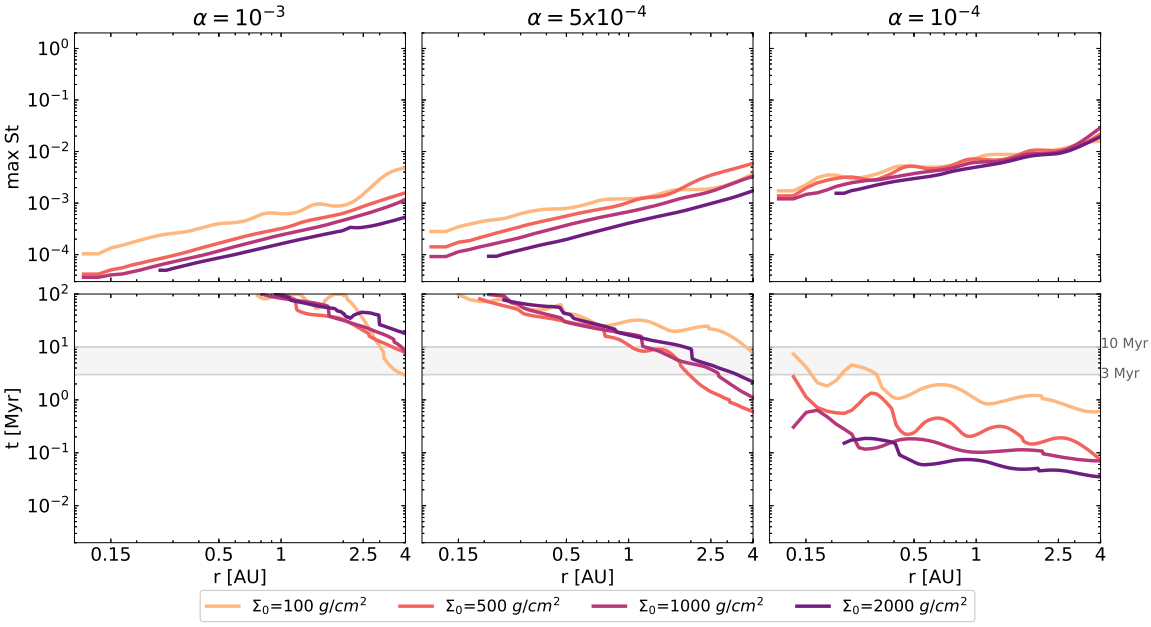

Figure 4.6. Maximum Stokes number (top plot) and planetary growth timescale until the pebble isolation mass is reached (bottom plot) as a function of orbital distance, for the discs with the four different initial gas surface densities: $\alpha = 10^{-3}$ (left plot), $\alpha = 5 \times 10^{-4}$ (middle plot), $\alpha = 10^{-4}$ (right plot), and $u_f = 1$ m/s. The gray lines show the typical lifetime range of a protoplanetary disc of 3 to 10 Myr.

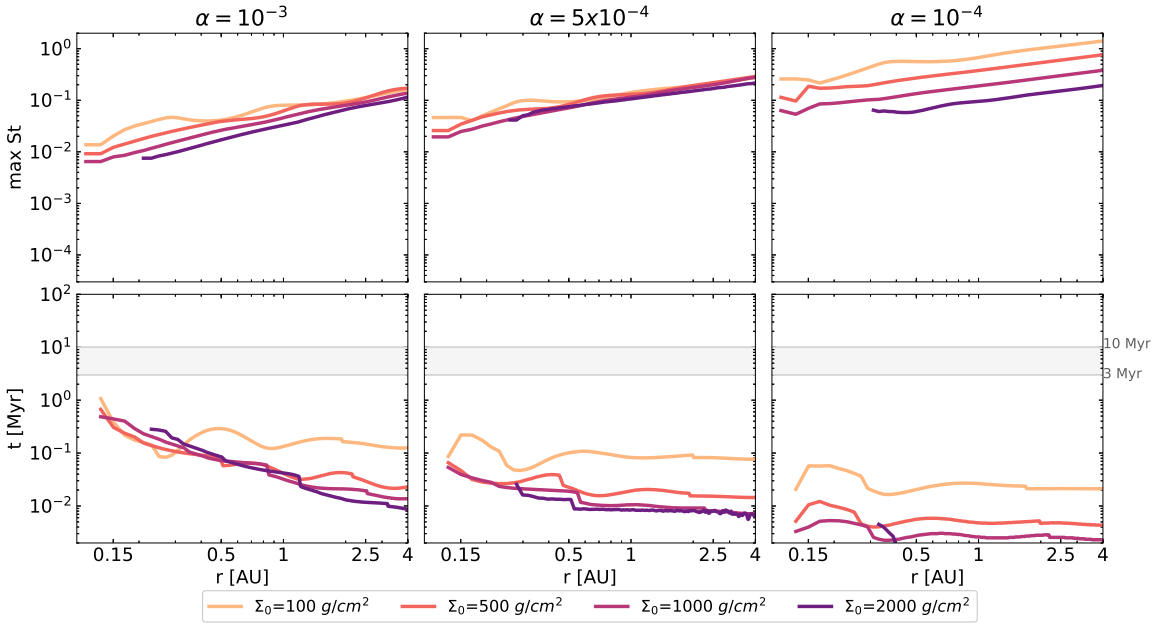

Figure 4.7. Same as Fig. 4.6, but for $u_f = 10$ m/s.

fragmentation velocity moves the ice line inward compared to $u_f = 1$ m/s. This has consequences, not only for the planet formation mechanisms, but also for the potential compositions of the created planets (Bitsch et al. 2019b; Schoonenberg et al. 2019; Venturini et al. 2020b). A more detailed discussion about planet growth within the discs of our models follows in Sect. 4.4.

4.3.2 Disc evolution

Our 2D hydrodynamical models cannot be integrated over several Myr, due to computational limitations. Instead, the disc evolution can be mimicked by reducing the overall gas surface density, where lower disc surface densities correspond to lower stellar accretion rates, and thus to older discs (Hartmann et al. 1998b). As a consequence the viscous heating is reduced and the discs become colder as they age. However, assigning an absolute age to the disc structures presented here is difficult because the exact time evolution of a disc depends on more than just the viscosity and the gas surface density, and because disc winds can drive the evolution of the disc (Bai et al. 2016; Suzuki et al. 2016).

In our model the evaporation fronts of different solids depend on the temperature (table 4.1) and consequently are also closer to the central star in discs with lower gas surface density. At the evaporation fronts, solids evaporate and the solid surface density is thus reduced (Fig. 4.1), leading to lower opacities and more efficient cooling, which can cause bumps in the disc structure if the solid abundances change by a large factor, for example at the water ice line. However, the maximum pebble size by fragmentation does not change because the maximum pebble size does not depend on dust surface density (Eq. 3.14). As a consequence, the pebble sizes are smooth across the evaporation fronts, implying that even if disc evolution over several Myr was taken into account, it would happen smoothly and no bumps or

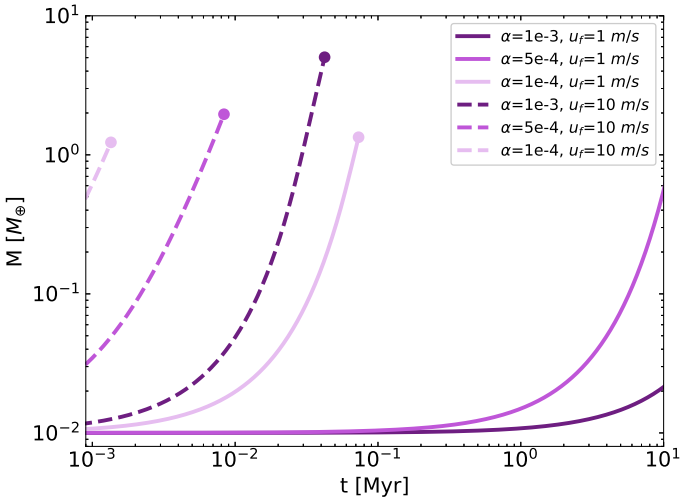

Figure 4.8. Planetary mass as a function of time for the simulations with $\Sigma_{g,0} = 2000$ g/cm^2, all α-viscosities, and both of the fragmentation velocities at 1 AU. The dots give the final planetary mass determined by the pebble isolation mass (Figs. 4.4 and 4.5). The growth timescale is longer than 10 Myr in discs with $\alpha > 5 \times 10^{-4}$ when particle collisions are limited by a fragmentation velocity of 1 m/s.

dips will be generated at the evaporation fronts. As the disc becomes older and its surface density reduces in time, the maximum pebble size increases. We discuss the consequences of this on planet formation via pebble accretion in the next section.

4.4 Planet formation

An important implication that can be derived from the disc structures of the presented models is that the aspect ratio profiles, independently of the parameters used, are almost constant with orbital distance. This is expected in these inner regions where viscous heating dominates over stellar irradiation, which would flare up the disc (Bitsch et al. 2015b; Chiang & Goldreich 1997; Dullemond & Dominik 2004; Ida et al. 2016; Savvidou et al. 2020).

The implication of this observation is that the planetary systems that could potentially form in these discs would have very similar masses since the pebble isolation mass depends on the aspect ratio (see Eq. 2.36). It has been recently observed among the *Kepler* systems that planets within the same system have similar sizes (Weiss et al. 2018). Millholland et al. (2017) suggested that the "peas-in-a-pod" trend is also true for the planetary masses within the same system.

We now compare the pebble isolation masses derived from our disc simulations with the super-Earth population, and then discuss planetary growth within these disc environments. We note here again that discs with high gas surface densities could correspond to young discs, while the discs with low gas surface densities could correspond to older discs. As the exact time evolution of discs is complicated (e.g., Bai et al. 2016; Suzuki et al. 2016) and not self-consistently included in our model, we do not link our disc structures to a time evolution, but just discuss the implications of the fixed-disc structures on planetary growth via pebble accretion under the simple assumption that the disc structure does not evolve over time.

4.4.1 Pebble isolation mass

We use the equilibrium disc structures from the 2D hydrodynamical simulations to study the growth of super-Earths via pebble accretion. It is assumed that planets grow to the pebble isolation mass because then they carve a gap in the protoplanetary disc and create a pressure bump exterior to their orbits which traps pebbles and prevents them from being accreted. We thus calculate the pebble isolation mass for each of our disc models to find the maximum mass that our planets could reach. The pebble isolation mass (Eq. 2.36) depends on the disc structure and, specifically, its aspect ratio, α-viscosity, and the radial pressure gradient. We present the pebble isolation mass derived from our hydrodynamical simulations in Fig. 4.4 and Fig. 4.5, where we also overplot the masses of close-in super-Earths inferred, using a mass–radius relationship (Chen & Kipping 2017) from the *Kepler* observations and for planets with RV mass determinations.

The aspect ratio profiles for the disc range in our models are almost constant with orbital distance, so we expect and find a low dependence of the pebble isolation mass on the orbital distance. For $\alpha = 10^{-3}$ and $u_f = 1$ m/s the pebble isolation mass reaches almost 19 $M_\oplus$ for the highest initial gas surface density, $\Sigma_{g,0} = 2000$ g/cm^2. With the same fragmentation velocity and $\alpha = 5 \times 10^{-4}$ we still get high enough isolation masses that match the majority of the observed super-Earths and mini-Neptunes, mainly for the highest surface density, $\Sigma_{g,0} = 2000$ g/cm^2. However, for lower α-values or higher fragmentation velocities the pebble isolation mass hardly exceeds 3-4 $M_\oplus$. This also means that with these sets of parameters it is hard to explain the bulk of the masses of close-in super-Earths and mini-Neptunes by pure pebble accretion.

Increasing the fragmentation velocity to $u_f = 10$ m/s, we find that the pebble isolation masses are significantly reduced. This happens because of the larger particles (Eq. 3.14), which lead to a smaller aspect ratio (see Sect. 4.3 and Eq. 2.36). The highest mass we find is around 5 $M_\oplus$ for $\alpha = 10^{-3}$ and again the highest initial gas surface density, $\Sigma_{g,0} = 2000$ g/cm^2. For the rest of the simulations, the pebble isolation mass is so low that the masses of the inner super-Earths might not be reached without a significant number of collisions between the bodies.

Considering only the pebble isolation masses of the discs discussed here, we can conclude that in order to explain the inferred masses from *Kepler* detections, we would need a relatively high viscosity of $\alpha = 10^{-3}$. However, it is also important to consider whether pebble accretion can operate efficiently enough so that the planets reach these masses in a timely manner. We discuss this in the following section.

4.4.2 Planet growth until pebble isolation mass

To study planet growth we calculate the pebble accretion rate using Eqs. 2.33 and 2.34. The Stokes numbers are determined by the MRN distribution. For simplicity we ignore planetary migration. We show the maximum Stokes numbers as a function of orbital distance in the upper plots of Figs. 4.6 and 4.7 for all of the parameters used. The Stokes numbers are inversely proportional to the gas density of the disc (Eq. 2.13). The maximum Stokes numbers are hence an increasing function of the

orbital distance. They also show some radial variations for the same reason.

We show the growth timescales for our different simulations in the bottom plots of Figs. 4.6 and 4.7. These timescales represent the time it takes for the planets to reach the pebble isolation mass at the given orbital distance (Figs. 4.4 and 4.5) accreting pebbles with a size distribution corresponding to the planets' locations. The growth timescales are not entirely smooth. This is related, firstly, to the variations in the Stokes number (upper plots of Figs. 4.6 and 4.7 for the maximum values). Secondly, there are also some variations in the dust surface density because of the evaporation fronts (see the steps for the dust-to-gas ratio in Fig. 4.1).

When considering the time it takes to reach the isolation masses, it is important to compare it with the time of the gas dispersal (gray band in the bottom plots of Fig. 4.6 and Fig. 4.7). After this event, planets can continue to grow via mutual collisions; however, the formation pathway is different, and if the planets have not reached sufficient masses already, they will end up being terrestrial rather that super-Earths (Lambrechts et al. 2019).

For fragmentation velocities of 1 m/s and $\alpha = 10^{-3}$ pebble accretion is inefficient in the inner disc regions (with a slight dependence on the gas surface density, Fig. 4.6), and thus longer than the typical lifetimes of protoplanetary discs. These timescales get significantly shorter for a decrease in the α-viscosity or an increase in the fragmentation velocity to 10 m/s (Fig. 4.7), which allow larger grains to be accreted (Eq. 3.14), enhancing pebble accretion (Eqs. 2.33 and 2.34). Our simulations thus indicate that either a low α-viscosity or larger grain fragmentation velocities are needed to allow fast enough growth via pebble accretion.

In Fig. 4.8 we show the planetary growth of embryos located at 1 AU as a function of time for planets growing in discs with $\Sigma_{g,0} = 2000$ g/cm^2 for all α-viscosities and fragmentation velocities. The planet grows fastest in environments with low viscosities and large fragmentation velocities. However, the pebble isolation mass is small in these cases. Only for cases of high α and low fragmentation velocity is the pebble isolation mass high enough to match the observed exoplanet population.

The larger grains carry lower opacities, which enhances the cooling of the disc. The low temperature also translates to a low aspect ratio (Fig. 4.3), hence the isolation masses are very low (Fig. 4.5), and even though the timescales to reach them are very short, the planets that could potentially form cannot explain the majority of the masses of super-Earths and mini-Neptunes. The best options for sufficiently high isolation masses and short growth timescales are $\alpha = 10^{-3}$ and $u_f = 10$ m/s, which leads to masses from 0.4 to 5.7 $M_\oplus$, depending on the gas surface density and the orbital distance.

In the following section we explore whether planet formation at earlier stages (high gas surface densities) and higher dust-to-gas ratios could increase the pebble isolation mass and keep the planetary growth timescales short at the same time.

4.4.3 Testing higher dust-to-gas ratio, gas surface density, and initial planetary seed mass

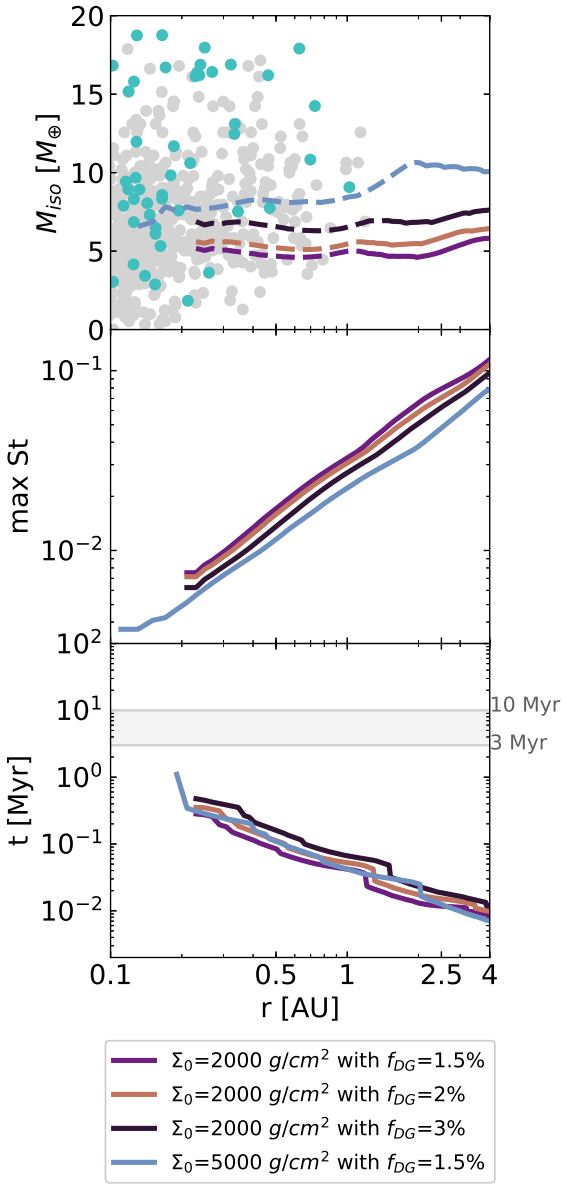

Figure 4.9. Pebble isolation mass (top plot), maximum Stokes number (middle plot), and planetary growth timescale until the pebble isolation mass is reached (bottom plot) as a function of orbital distance, for discs with $\alpha = 10^{-3}$ and $u_f = 10$ m/s. Shown are discs with higher dust-to-gas ratios, $f_{DG} = 2\%$ and $f_{DG} = 3\%$ and higher initial surface density $\Sigma_{g,0} = 5000$ g/cm^2. For reference the nominal run with $\Sigma_{g,0} = 2000$ g/cm^2 and $f_{DG} = 1.5\%$ is included.

We have concluded that the best parameters for super-Earth formation via pebble accretion are $\alpha = 10^{-3}$ and $u_f = 10$ m/s. In this case the pebble isolation mass is reached before the dispersal of the gaseous disc regardless of the surface density and the location within the disc. The isolation mass itself depends on the surface density and with the highest surface density ($\Sigma_{g,0} = 2000$ g/cm^2) planets of around 5 M$_\oplus$ could form by pure pebble accretion.

We investigate here how higher gas surface densities and higher dust-to-gas ratios influence the pebble isolation masses and the accretion times by pebble accretion. We show in Fig. 4.9 (top and middle panels) the pebble isolation masses and the maximum Stokes numbers from the additional simulations. We used two different total dust-to-gas ratios ($f_{DG} = 2\%$ and $f_{DG} = 3\%$) with $\Sigma_{g,0} = 2000$ g/cm^2, and a higher gas surface density of $\Sigma_{g,0} = 5000$ g/cm^2 for the nominal total dust-to-gas ratio ($f_{DG} = 1.5\%$).

The difference between the nominal dust-to-gas ratio and the 2% value is very small, so the pebble isolation masses are very similar. We find slightly higher pebble isolation masses with a dust-to-gas ratio of 3%, but the strongest improvement comes from the simulation with $\Sigma_{g,0} = 5000$ g/cm^2. In this case the maximum pebble isolation masses can be around 11 M$_\oplus$ near the outer boundary of the disc.

The growth timescales (bottom panel in Fig. 4.9) are also very similar between the simulation with the nominal total dust-to-gas ratio and the one with $f_{DG} = 2\%$. If we double the amount of solids ($f_{DG} = 3\%$), then the growth timescale is longer because of the higher isolation mass and the similar maximum Stokes numbers. If we increase the gas surface density to $\Sigma_{g,0} = 5000$ g/cm^2, there is enough material to accrete pebbles fast enough and reduce the growth timescale

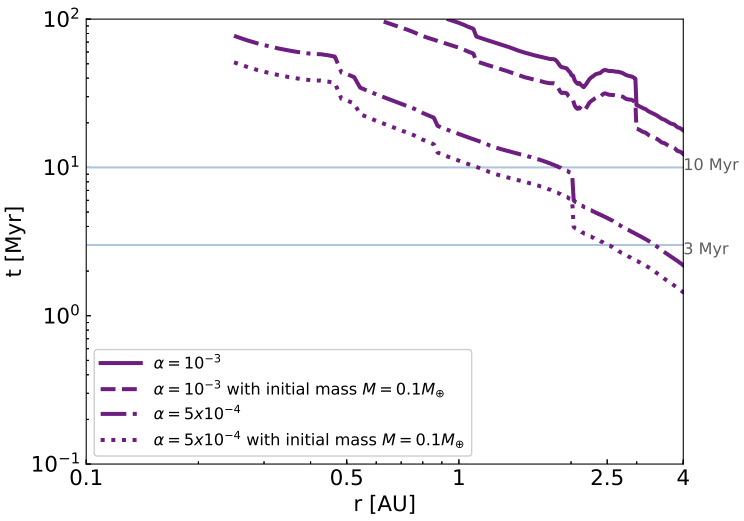

Figure 4.10. Planetary growth timescale until the pebble isolation mass is reached as a function of orbital distance with initial planetary seed masses M_{init} = 0.1 $M_\oplus$. We tested two α-viscosities, 10^{-3} and 5×10^{-4} with a fragmentation velocity, u_f = 1 m/s. Overplotted are the nominal disc models with initial planetary seed masses M_{init} = 0.01 $M_\oplus$.

compared to the high dust-to-gas ratio simulations; however, it is very similar to the nominal simulation.

In Fig. 4.10 we show how the growth timescales change depending on the assumed initial mass of the planetary seed. We compare our nominal simulations with $\alpha = 10^{-3}$ and $\alpha = 5 \times 10^{-4}$ for u_f = 1 m/s and an initial planetary mass of M_{init} = 0.01 $M_\oplus$ with an increased initial mass of M_{init} = 0.1 $M_\oplus$. We only used $\Sigma_{g,0}$ = 2000 g/cm^2 because this surface density leads to the highest pebble isolation masses. The higher initial mass reduces the growth timescale, but the difference is small and for most of the regions of the inner discs the pebble isolation mass is not reached within the lifetime of the disc.

4.5 Discussion

4.5.1 Planet growth

The aspect ratios and the temperatures in our discs are relatively low, as expected for the low viscosity we used (Savvidou et al. 2020). The same is true for the discs with higher fragmentation velocities (u_f= 10 m/s in contrast to u_f = 1 m/s) because the collisions are less destructive and the larger particles, which are allowed, carry lower opacities. In the context of pebble accretion, this means that the pebble isolation masses we calculate do not correlate sufficiently with the bulk of the planetary masses that are observations unless $\alpha = 10^{-3}$ and u_f = 1 m/s. In this specific case, we have small enough particles, so that the opacity is sufficient to prevent significant cooling and hence high enough aspect ratios.

However, in order to have fast growth of the planets, we need either $\alpha \leq 10^{-4}$ and u_f = 1 m/s or any $\alpha \leq 10^{-3}$ and u_f = 10 m/s (Figs. 4.6 and 4.7) since the maximum Stokes numbers are up to two orders of magnitude larger (Figs. 4.4 and 4.5). Therefore, there seems to be a trade-off between the possible pebble isolation mass and the timescale to reach it. The most efficient parameters that provide both high enough isolation masses and short enough timescales are $\alpha = 10^{-3}$ and u_f =

10 m/s.

Venturini et al. (2020b) find that $\alpha < 10^{-4}$ is needed to reach the pebble isolation mass in time. The maximum masses they find are around 7 $M_\oplus$ for an $\alpha = 10^{-5}$. They use slightly different parameters for their nominal runs (e.g., initial dust-to-gas ratio of 1% which can increase through radial drift in the inner disc with only a small difference if the initial dust-to-gas ratio is higher) and a different disc model where dust opacities do not contribute self-consistently to the disc model. Specifically, the dust opacities follow the Bell & Lin (1994b) opacity law, which has been shown to produce misleading disc structures, especially when multiple grain sizes are included because they are based on micrometer-sized dust (Savvidou et al. 2020). Our model suggests that a higher viscosity is needed to prevent a too low pebble isolation mass. However, their conclusions remain consistent with our work: A high enough Stokes number of the particles is needed to allow fast and efficient enough growth, and that more massive ice-rich planets can emerge from the exterior to the snow line.

We do not include gas accretion into our model, because gas accretion might not be efficient for low-mass planets in the inner regions of the protoplanetary disc (Cimerman et al. 2017; Ikoma et al. 2000; Lambrechts & Lega 2017a; Lee et al. 2014). Furthermore, observational constraints indicate that planets up to four Earth radii in size mostly have only a few per cent of their mass in hydrogen and helium envelopes (Zeng et al. 2019). This implies that the majority of the planetary mass for these close-in super-Earths and mini-Neptunes has to originate from solid accretion, justifying our first approach of ignoring gas accretion.

4.5.2 Comparison to the Kepler data

We find almost flat aspect ratios independently of the disc parameters used. This is an important observation as it could lead to planetary systems with similar masses. In Millholland et al. (2017) it is suggested that similar masses in a system would also lead to similar radii, hence the constant with orbital distance aspect ratios we note in our discs support the "peas-in-a-pod" scheme (Weiss et al. 2018). In order to reach more specific conclusions on this matter it would be important to consider multiple growing embryos at the same time.

Judging by the almost flat, slightly flaring aspect ratios, planets allowed to migrate would be expected to migrate inward (Bitsch et al. 2015b; Savvidou et al. 2020). The pebble isolation masses have a low dependence on the orbital distance, hence the maximum mass that planets can reach would remain unchanged within our simulations, even if we were to include planet migration. Nevertheless, we expect discs to be flared (e.g., Chiang & Goldreich 1997), thus increasing the pebble isolation mass at larger distances to the star. The growth rate, though, is slower near the innermost regions of the discs, caused by the evaporation of solids, making growth to super-Earth masses even harder.

It is important to include migration in future work, not only to reach more robust conclusions on the "peas-in-a-pod" configuration, but also for the role it can play in determining the composition of the planets (Bitsch et al. 2019b; Izidoro et al. 2019b; Raymond et al. 2018). Even though we include several chemical species here, we do not discuss the influence they could have on the planetary compositions.

Even if we only consider the pebble isolation masses that we find here (Fig. 4.4 and Fig. 4.5), and not whether there will be time to reach them, we find that most of the observed planetary masses are above the pebble isolation masses in our simulations. This can be explained by our self-consistent disc model with the grain size distribution leading to much lower aspect ratios than used in previous models, due to the size and composition dependent opacities. The growth of the planets, though, can be aided by collisions, either before or after the dissipation of the gas disc (Cossou et al. 2014b; Izidoro et al. 2019b, 2017b; Kominami & Ida 2004; Ogihara & Ida 2009; Ogihara et al. 2018).

The low masses that we find could also be explained if these planets are not super-Earths, but terrestrial planets. If the pebble flux is low, then we expect to have low planetary masses before the gas dissipation. Even with collisions after the gas dissipation, the masses cannot exceed a few $M_\oplus$ (Lambrechts et al. 2019), which is consistent with the mass we find in this work for $\alpha = 10^{-3}$ and $u_f = 10$ m/s. However, we would need to discuss the composition of the planets to define whether they are terrestrial or super-Earths. This would be important because planets formed during the gas phase could accrete small gaseous envelopes in contrast to planets that formed similarly to the terrestrial planets via collisions after the gas phase.

4.5.3 Disc parameters

We have explored a few pathways to either increase the pebble isolation masses or shorten the growth timescales. As a reminder, the fastest growth timescales with high enough isolation masses come from the models with $\alpha = 10^{-3}$ and $u_f = 10$ m/s. The nominal dust-to-gas ratio is 1.5%. As a consequence, we tested models with the above-mentioned α-viscosity and fragmentation velocity and the highest surface density with $\Sigma_{g,0} = 2000$ g/cm^2 because this density provides the highest isolation masses. We also tested the nominal dust-to-gas ratio with higher surface density, $\Sigma_{g,0} = 5000$ g/cm^2.

We find that the higher dust-to-gas ratio does indeed improve the isolation masses, mainly for the case with 3%, which is twice our nominal value. However, the masses remain just above 5 $M_\oplus$. The most significant improvement comes with the higher initial gas surface density. Especially near the outer boundary, the pebble isolation mass with $\Sigma_{g,0} = 5000$ g/cm^2 reaches approximately 10 $M_\oplus$. This implies that in order to explain the constraints of the *Kepler* observations (Weiss et al. 2018) we would need very high disc masses or a significant enhancement of the dust-to-gas ratio. Local enhancements could occur in the inner regions from radial drift (e.g., Birnstiel et al. 2012a) or via pebble traps. These could be planet-induced pressure bumps or "traffic jams" at the evaporation fronts (Drążkowska & Alibert 2017b; Ida & Guillot 2016; Ros & Johansen 2013; Ros et al. 2019; Schoonenberg & Ormel 2017b).

In addition, it is worth noting the Venturini et al. (2020a) claim that the more massive inner super-Earths (the planets that would populate the second peak at larger radii in the radius distribution; e.g., Fulton et al. 2017) are actually water-rich planets originating from beyond the ice line where the pebble isolation mass is higher, which is in agreement with our model. Migration should be included in

future works in order to determine the final positions and masses of the planets.

The ice line position is located around 3 AU for $\alpha = 10^{-3}$, $\Sigma_{g,0} = 2000$ g/cm^2, and $u_f = 1$ m/s. Lower α-viscosities, gas surface densities, or fragmentation velocities move the ice line inward (see Sect. 4.3 and Savvidou et al. 2020). The higher dust-to-gas ratios or gas surface densities thus also help in keeping the ice line farther out from the star. However, the position and evolution of the ice line location, along with the possibility of migration for planets defines their compositions (Bitsch et al. 2019b).

4.6 Summary

In this work we used the self-consistent protoplanetary disc model presented in Savvidou et al. (2020), with additional chemical species and the corresponding opacities (see Table 4.1 and Fig. 3.2), focusing on the inner parts of the disc. We used the MRN grain size distribution (Mathis et al. 1977), with a disc-dependent upper boundary for the grain sizes (Eq. 3.14). We then combined the equilibrium disc structures from the hydrodynamical simulations with a framework to study planet growth via pebble accretion. The disc parameters we used are summarized in Table 4.2. In this work, we did not take into account planetary migration and did not discuss the planetary compositions for simplicity. Furthermore, because the growing planets are in the low-mass regime we did not model gas accretion. Additionally, we used only fixed-disc structures in time, because our 2D model cannot be evolved for several Myr.

We present the equilibrium disc structures in Figs. 4.2 and 4.3. The aspect ratio profiles are almost constant with orbital distance. This is expected because at these innermost parts of the protoplanetary discs, viscous heating dominates over stellar irradiation and the disc does not flare up (Bitsch et al. 2015b; Chiang & Goldreich 1997; Dullemond & Dominik 2004; Ida et al. 2016; Savvidou et al. 2020). This implies that the planets forming in the inner disc would have similar masses in the pebble accretion scenario because the pebble isolation mass is a strong function of the aspect ratio, supporting the "peas-in-a-pod" scheme (Millholland et al. 2017; Weiss et al. 2018).

We calculated the pebble isolation masses following the approximation by Bitsch et al. (2018) (Figs. 4.4 and 4.5) and then estimated the time it takes to reach them depending on the disc parameters (Figs. 4.6 and 4.7). Including opacities which are grain size and composition dependent means that when the disc parameters allow large particles to form, the aspect ratios will be lower. This leads to low pebble isolation masses because they directly depend on the aspect ratio of the disc (Eq. 2.36). We find the highest pebble isolation masses for $\alpha = 10^{-3}$ and 5×10^{-4} when the fragmentation velocity is $u_f = 1$ m/s and for $\alpha = 10^{-3}$ when $u_f = 10$ m/s, mainly for high gas surface densities, with $\Sigma_{g,0} \geq 1000$ g/cm^2.

However, high pebble isolation masses also mean longer growth timescales

because of the smaller pebbles inside the disc. Compared with the typical lifetimes of protoplanetary discs (3 to 10 Myr), we find that for low fragmentation velocities ($u_f = 1$ m/s) the timescales for planetary growth are too long (with a small dependence on the gas surface density and the orbital distance). Hence, there is a trade-off between the pebble isolation masses and the growth timescales, and we conclude that the best set of parameters is $\alpha = 10^{-3}$ and $u_f = 10$ m/s within our model. With a gas surface density of $\Sigma_{g,0} = 2000$ g/cm^2 the pebble isolation masses reach almost 6 $M_\oplus$, which the planets can reach in less than 1 Myr.

The maximum mass that a planet can reach by pure pebble accretion is relatively low, and thus the masses of the majority of the observed planets can probably not be explained via pebble accretion only. We also tested higher dust-to-gas ratios and a higher surface density (Fig. 4.9). Even though they do help in increasing the pebble isolation masses, they also bring longer or comparable timescales for planetary growth compared to the nominal simulations.

We also tested whether a higher planetary seed mass can shorten the growth timescales, by starting with $M_{init} = 0.1$ $M_\oplus$ instead of $M_{init} = 0.01$ $M_\oplus$. We find and show in Fig. 4.10 that even though the increased initial planetary mass shortens the growth timescale, the difference is very small and growing planets still fail to reach the isolation mass within the lifetime of the disc for $\alpha = 10^{-3}$. For discs with lower alpha values, even smaller initial embryos (0.01 Earth masses) can grow fast enough to reach pebble isolation mass before the end of the disc's lifetime.

The growth of planets via pebble accretion, can be aided by collisions either before or after the dissipation of the gas (Cossou et al. 2014b; Izidoro et al. 2019b, 2017b; Kominami & Ida 2004). It is also possible that the low pebble isolation masses we find mean that this formation mechanism leads to planet formation after gas disc dispersal rather than to planet formation during the gas disc phase. However, even with some collisions, the expected masses are not very high (Lambrechts et al. 2019), if the initial planetary masses are small. However, in order to reach a definite conclusion on this, future simulations including N-body interactions are needed.

We have shown in this work that a self-consistent treatment between the pebble sizes and disc structures is of crucial importance for planet formation simulations. In particular, we find that discs that support a large pebble isolation mass also harbor low pebble accretion rates due to the small particle sizes, hence the growth timescales can be very long.

5

The growth of giant planets.

From "How to make giant planets via pebble accretion", Savvidou & Bitsch, submitted to A&A"

In a nutshell...

Planet formation is directly linked to the birthing environment that protoplanetary discs provide. The disc properties determine if a giant planet forms and how it evolves. The number of exoplanet and disc observations is ever-increasing, however, it is still not possible to directly link these two populations, therefore a deep theoretical understanding of how planets form is crucial. Giant planets are not the most common exoplanets, but their presence in a disc can have significant consequences for the evolution of the disc itself, the forming planetary system, and it also offers more chances of observational features in the disc structure. We perform numerical simulations of planet formation via pebble and gas accretion, including migration, in a viscously evolving protoplanetary disc, with dust growing, drifting, and evaporating at the icelines, investigating the most favorable conditions for giant planet formation. We find that the most favorable conditions for giant planet formation are high disc masses, early formation, and a large enough disc for a long-lasting pebble flux so that efficient core growth can happen before the pebble flux decays in time. Specifically, core growth needs to start before 0.9 Myr in order to form a giant, the initial disc mass has to be 0.04 $M_{\odot}$ or higher, and the disc radius needs to be larger than 50 AU. However, small discs with the same mass allow more efficient gas accretion onto already-formed planetary cores leading to more massive gas giants. Given the right conditions, high viscosity ($\alpha = 10^{-3}$) leads to more massive cores (compared to $\alpha = 10^{-4}$) and it also enhances gas accretion. At the same time, it causes faster type II migration rates, so the giants have a decreasing final position for increasing viscosity. Intermediate dust fragmentation velocities, between 4 and 7 m/s, provide the necessary pebble sizes and radial drift velocities for maximized pebble accretion with optimal pebble flux. The starting location of a planetary embryo defines whether a giant planet will form, with the highest fraction of giants originating between 5 and 25 AU. Finally, a dust-to-gas ratio of 0.03

can compensate for lower disc masses with $f_{DG} \leq 0.015$, but early formation is still important in order to form giant planets. We conclude that there is no specific initial parameter that leads to giant planet formation, but it is the outcome of a combination of beneficial factors. This also implies that the diversity of the exoplanet systems is the product of the intrinsic diversity of the protoplanetary discs and it is crucial to take advantage of the increasing number and quality of observations to constrain the disc population properties and ultimately planet formation theories.

5.1 Context

Protoplanetary discs provide the materials and environmental conditions for forming planets. This has been recently reinforced by direct images of planets forming inside protoplanetary discs (Haffert et al. 2019; Keppler et al. 2018; Müller et al. 2018b). Their properties could determine whether a planetary system contains a giant planet or not. Giant planets could then influence the evolution of the planetary system and that of the disc itself, for example by influencing the dust mass evolution (van der Marel & Mulders 2021). At the same time, the presence of a giant planet offers more chances for observable features in protoplanetary discs (e.g. Dipierro et al. 2015; Dong et al. 2015a,b; Eriksson et al. 2020; Fedele et al. 2017; Jin et al. 2016; Liu et al. 2019; Muley et al. 2019; Pinilla et al. 2012b; Pinte et al. 2020, 2018; Teague et al. 2018; van der Marel et al. 2021; Zhang et al. 2018b), which sometimes do not even coincide with the location of the planet(s) (Bae et al. 2018; Bergez-Casalou et al. 2022; Zhang et al. 2018b).

The current exoplanet detection methods favor large planets at small distances from their host star, however, the ever-increasing number of detections allows for a statistical analysis of the exoplanet population, as long as each survey is combined with proper detection efficiency and completeness estimates (see Winn & Fabrycky 2015; Zhu & Dong 2021, for a review). Through the observations we can thus estimate the occurrence fractions of planets, meaning the number of planets per star for a specific type of planet (e.g. divided by the planet's mass, radius or orbital period) (Mulders et al. 2018; Petigura et al. 2013; Suzuki et al. 2016; Wright et al. 2012). This can then be converted to the fraction of stars hosting the specific type of planet. A combination of the detection surveys results in occurrence fractions of 10-20% for all giant planets, 16% for warm and cold giants with orbits beyond 10 days (Cumming et al. 2008; Fernandes et al. 2019; Fulton et al. 2021; Mayor et al. 2011; Rosenthal et al. 2022).

Extracting information about the natal protoplanetary discs from exoplanet observations is almost unfeasible, even though the atmospheric abundances and the elemental ratios (such as C/O) could shed light on the formation pathways (e.g. Ali-Dib et al. 2014; Bitsch et al. 2022; Cridland et al. 2019; Helling et al. 2014; Madhusudhan et al. 2017b; Marboeuf et al. 2014; Mollière et al. 2015; Mordasini et al. 2016; Schneider & Bitsch 2021; Thiabaud et al. 2014; Öberg et al. 2011). However, definitively linking observed atmospheric abundances to planet formation remains

challenging (Mollière et al. 2022). It is, thus, of utmost importance to understand well the theoretical connection between the initial (disc) conditions and the possible planetary formation pathways.

We focus here on core formation via pebble accretion (Johansen & Lacerda 2010; Johansen & Lambrechts 2017a; Lambrechts & Johansen 2012a; Ormel & Klahr 2010a; Ormel et al. 2017), starting with an already formed planetary embryo, and operating until its mass reaches the pebble isolation mass (Ataiee et al. 2018; Bitsch et al. 2018; Lambrechts et al. 2014; Morbidelli & Nesvorny 2012), which depends on the disc properties. In the classical core accretion scenario (Pollack et al. 1996), when the core has acquired enough mass, gas accretion starts dominating the growth of the planet. The growing planet interacts gravitationally with the disc, pushing material away from its orbit, and in doing so, it opens a gap in the gas (e.g. Crida & Morbidelli 2007; Crida et al. 2006; Goldreich & Tremaine 1980; Lin & Papaloizou 1986). Gas accretion itself can even help in deepening this gap (Bergez-Casalou et al. 2020; Crida & Bitsch 2017; Ndugu et al. 2021). If this gap is deep enough, then a pressure trap is generated and blocks the dust from drifting inside the planet's orbit (Paardekooper & Mellema 2006). However, even planets with 10% the mass of Jupiter can create spiral shocks that decouple the larger dust particles from the gas and subsequently create a gap in the dust without forming a corresponding gap in the gas beforehand (Paardekooper & Mellema 2004, 2006).

Planet formation via pebble accretion has been widely studied in the recent years (e.g. Bitsch 2019; Bitsch et al. 2015; Bitsch et al. 2021; Brügger et al. 2018; Chambers 2016; Lambrechts et al. 2014; Levison et al. 2015; Morbidelli et al. 2015a; Ndugu et al. 2018; Savvidou & Bitsch 2021) but in regards to giant planets, it often focused on core growth, neglecting gas accretion (Andama et al. 2022; Lambrechts & Johansen 2014), concentrated on specific examples (Johansen & Lambrechts 2017a), or investigated the influence of pebble flux calculations (Bitsch et al. 2019a), instead of including dust evolution self-consistently. In the aforementioned studies, some initial parameters were varied, such as the disc mass, dust-to-gas ratio, or viscosity but the main goal was often to recreate the Solar System or the observed exoplanet populations.

In this work we use a model that includes pebble and gas accretion, gap opening, and type-I/type-II migration as previous models (Bitsch et al. 2015; Bitsch et al. 2018; Voelkel et al. 2022), but also includes self-consistent grain growth, drift and pebble evaporation at ice lines (Schneider & Bitsch 2021). Using this framework, we strive to generalize the results from previous studies through a parameter study and directly link the initial (disc) conditions to the formation of giant planets.

5.2 Methods

5.2.1 Model description

We use the code `chemcomp` (Schneider & Bitsch 2021) which simulates planet formation via pebble and gas accretion and migration in a semi-analytical 1D model of a viscously evolving protoplanetary disc, while taking into consideration dust growth,

Parameter	Values	
M_0 $[M_\odot]$	0.01, 0.04, 0.07, **0.1**	initial disc mass
R_0 $[R_\odot]$	50, 100, 150, **200**	initial disc radius
α	**0.0001**, 0.0005, 0.001	α-viscosity parameter
t_0 [Myr]	**0.1**, 0.5, 0.9, 1.3	starting time of embryo
$\alpha_{p,0}$ [AU]	1-50 every 1	initial position of embryo
u_{frag} [m/s]	1, 4, 7, **10**	fragmentation velocity
f_{DG}	0.01, **0.015**, 0.03	dust-to-gas ratio

Table 5.1. Parameters used in the simulations. We mark in bold the standard set, which is used as a reference in Fig. 5.1-5.4.

drift, and evaporation/condensation at the evaporation fronts, for multiple chemical species. The following prescriptions are listed in more detail in Schneider & Bitsch 2021. In this code, planet formation begins by inserting planetary embryos in the disc with the transition mass (Eq. 2.21) that depends on the local conditions, Δv, the sub-Keplerian speed of the particles, and Ω, the Keplerian angular frequency.

The viscosity in the model follows an α-prescription (Shakura & Sunyaev 1973) and we choose to keep the vertical stirring/settling parameter always constant to $a_z = 10^{-4}$ motivated by Pinilla et al. 2021 who suggest that a low vertical mixing and different from turbulent velocities, radial diffusion, and gas viscous evolution leads to better agreement with observations. The midplane temperature is set by considering the viscous heating and the irradiation from the star. The midplane temperature sets the aspect ratio of the disc, which in turn determines the pebble isolation mass. However, we keep here the temperature fixed in time for simplicity, unlike our previous work (Savvidou et al. 2020) where we linked the disc thermodynamics self-consistently with the dust sizes.

Dust growth is modeled using the two populations approach described in Birnstiel et al. 2012a, which means that we take growth, fragmentation, and drift, along with drift-induced fragmentation into account. This also means that the dust surface density, which is used in the pebble accretion prescription, is a product of the disc evolution itself, similar to our previous work (Savvidou & Bitsch 2021) and others (e.g. Drążkowska et al. 2021; Venturini et al. 2020c), in contrast to more simplified approaches (e.g Bitsch et al. 2015; Lambrechts & Johansen 2014; Ndugu et al. 2018). The pebble accretion rates are according to Johansen & Lambrechts 2017a.

The planetary embryos are inserted at a given time and the core starts growing with a 90% contribution of the pebble accretion rate. The remaining 10% contributes to the primary envelope to account for pebble evaporation during the core buildup,

in a simplified way. For the pebble isolation mass, we use

$$M_{iso} = 25 f_{\rm fit} M_{\oplus} \ , \tag{5.1}$$

with

$$f_{\rm fit} = \left[\frac{H/r}{0.05}\right]^3 \left[0.34 \left(\frac{\log(0.001)}{\log(\alpha)}\right)^4 + 0.66\right] \ , \tag{5.2}$$

adapted from Bitsch et al. 2018 (Eq 2.36) without the dependence on the radial pressure gradient that is not very strong and not well studied around icelines. When this limiting mass is reached, pebble accretion ends and the core has reached its final mass (Ataiee et al. 2018; Bitsch et al. 2018; Lambrechts et al. 2014; Morbidelli & Nesvorny 2012). The envelope then quickly contracts and starts accreting gas. The approach followed in this model is the same as in Ndugu et al. 2021, where the gas accretion rate is given by the minimum between the accretion rates given by Ikoma et al. 2000, Machida et al. 2010 and by the gas that the disk can viscously provide into the horseshoe region after the planet has emptied it (Ndugu et al. 2021).

The forming planet migrates using the Paardekooper et al. 2011a type-I migration rates related to the Lindblad, the barotropic, and the entropy-related corotation torques. The code also includes the effects of the thermal (Masset 2017) and the dynamical torques (Paardekooper 2014). If gas accretion becomes efficient, the planet can then open a gap, first via the gravitational interaction of the disc and the planet and then due to the gas accretion as in Ndugu et al. 2021. If the planet carves a deep enough gap, it starts migrating in the type-II regime with a viscosity-dependent rate. The chemical model and a more detailed description of the code can be found in Schneider & Bitsch (2021).

5.2.2 Initial conditions

We perform a parameter study varying the disc mass (M_{disc}), disc radius (R_{disc}), α-viscosity, the dust fragmentation velocity (u_{frag}), and finally the time (t_0) and location (a_p) of the inserted planetary embryo. The values chosen for each of those parameters are summarized in Table **??**. The nominal dust-to-gas ratio is chosen as $f_{DG} = 1.5\%$, but we also compare with $f_{DG} = 1\%$ and $f_{DG} = 3\%$. The maximum disc mass is chosen based on the maximum disc masses from the current disc mass estimations (Manara et al. 2022) and the minimum based on a reasonable value for solar-type stars, keeping in mind that our goal is to form giant planets. We also choose the disc radii range to cover the most commonly observed ranges (e.g. Ansdell et al. 2020, 2017, 2016; Long et al. 2019; Maury et al. 2019; Pascucci et al. 2016; Sanchis et al. 2021; Sheehan et al. 2020; Tobin et al. 2020).

We already expect that early formation will be helpful for giant planet formation, so we choose all planetary embryos to be inserted before 1.3 Myr and we position them from 1 to 50 AU every 1 AU. It should be noted that we always simulate the growth of one planet at a time for each disc, therefore the interactions between multiple planets are neglected. However, planet formation by pebble accretion is more efficient in the inner disc regions, meaning that if giant planets form in the outer disc, they would also form in the inner disc. At the same time, if the pebble

flux allows for the formation of one giant, multiple giants can form, because planets growing by pebble accretion only reduce the pebble flux by a few percent (Bitsch et al. 2019a; Lambrechts et al. 2014; Matsumura et al. 2021).

The star in the simulations is of solar mass. The integration stops at around 3 Myr, assuming that at this point, photoevaporation significantly depletes the disc from the gas. Specifically, at 3 Myr, we introduce an exponential decay of the surface density of the disc, reducing it to 0 within 100 kyr. If a planet migrates to the inner edge of the disc, we stop the accretion onto the planet. This is, in part, motivated by recycling flows that can prevent the accretion of atmospheres at close distances (e.g. Cimerman et al. 2017; Lambrechts & Lega 2017b; Moldenhauer et al. 2021). However, we let the simulation run until the end of the disc's lifetime to trace the dust evolution that follows, which we will discuss in future work. In addition, approaching this inner edge does not necessarily mean that the planet will be lost to the star because there could be a migration trap near the inner rim (Ataiee & Kley 2021; Chrenko et al. 2022; Flock et al. 2019; Masset et al. 2006; Romanova et al. 2019). This migration trap would probably be mainly efficient for low-mass planets, however, we choose to keep the planets in the disc, so that we track how the disc would evolve with the presence of a planet. Given the uncertainty of their fate, we also choose to keep them in our sample.

The fragmentation velocity is the relative threshold velocity at which dust growth is halted and particles fragment instead. Within the two populations model, (Birnstiel et al. 2012a) the maximum dust size before fragmentation (Eq. 3.14) is defined as

$$s_{max} = f_f \frac{2\Sigma_g}{3\pi\alpha\rho_s} \frac{u_{frag}^2}{c_s^2} \ , \tag{5.3}$$

where f_f=0.37 is a best-fit parameter to the full grain growth model, ρ_s is the dust grain density and c_s the local sound speed. We choose to test a range from 1 to 10 m/s to cover different measurements from laboratory experiments (e.g. Gundlach & Blum 2015b; Güttler et al. 2010a). We keep the value constant in our model throughout the disc, motivated by laboratory experiments that show no difference in the sticking properties of water-ice and silicate aggregates (Musiolik & Wurm 2019; Steinpilz et al. 2019). Our goal is to constrain giant planet formation via pebble accretion, by examining which of the aforementioned initial conditions are the most favorable to form gas giants.

5.3 Growth tracks

In this section, we discuss how the initial disc conditions influence the formation of giant planets through the growth tracks of specific example cases. We firstly show in Fig. 5.1, the evolution of the planetary mass as a function of position for a specific set of parameters. The disc in this nominal case has the initial parameter values which are individually expected to be the most favorable for giant planet formation; high disc mass (0.1 $M_\odot$), large disc radius (200 AU), low viscosity (10^{-4}), early formation time (0.1 Myr) and high dust fragmentation velocity (10 m/s). These standard parameters are highlighted in bold in Table **??**. The embryos of the

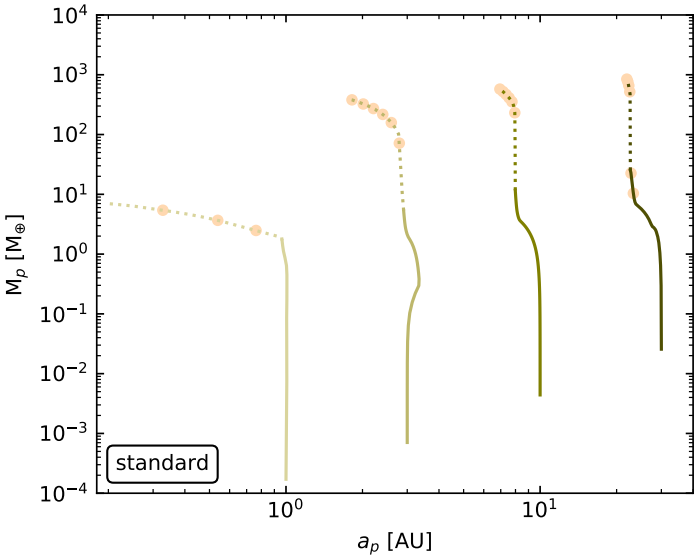

Figure 5.1. Evolution of planetary mass as a function of position using the standard set of parameters (highlighted in bold in Table **??**). The dots mark timesteps of 0.5 Myr after the embryos start growing unless the planet has reached the inner edge, in which case they are omitted. The solid lines represent pebble accretion, while the dashed lines represent gas accretion.

examples shown here were placed at 1, 3, 10 and 30 AU. If the cores reach pebble isolation mass and the core mass has grown to several Earth masses, the envelope starts to slowly contract, followed by runaway gas accretion. The solid lines in Fig. 5.1 correspond to the core building phase, while the dashed lines correspond to the gas accretion phase. The dots mark timesteps of 0.5 Myr, counting from the time the embryo is inserted, but we omit them if the planet reaches the inner edge of the disc.

Pebble accretion dominates over migration during the core buildup and the planets do not migrate inwards significantly. The planet starting at 3 AU also migrates slightly outwards within the first 0.5 Myr, as expected for low-mass planets around a few AU because of a positive heating torque (Baumann & Bitsch 2020; Benítez-Llambay et al. 2015). The low viscosity leads also to a very slow type II migration during the gas accretion phase. However, the planet that starts at 1 AU has already reached the pebble isolation mass by 0.5 Myr, and 1.5 Myr later, it reaches the inner edge of the disc. Having only a slow gas contraction phase, which is proportional to the core mass, it ends up being a 7 $M_\oplus$ sub-Neptune. For planets starting further out and this set of parameters, gas giants' formation is very efficient. There is enough material due to the initial high disc mass, the pebble flux can be sustained for a long time because of the large initial disc radius, and the low viscosity and large fragmentation velocity allow large pebbles to form, enhancing the accretion rates.

The pebble isolation mass increases as a function of orbital distance because of the increasing aspect ratio of the disc, owing to stellar irradiation (Eq. 5.1), but most of the planets reach it before 0.5 Myr because of the abundant solid content of the disc. Nevertheless, it takes 1 Myr for the outermost planet (a_p=30 AU) to reach the pebble isolation mass because it is closer to the outer edge of the disc, where the surface density is decreased. In this case, in which the planets reach the pebble isolation mass, the higher core masses with increasing orbital distance lead to more efficient and timely gas accretion, therefore, the further out the embryo starts growing, the higher the final mass of the planet. Overall, the planets injected at 3, 10 and 30 AU grow to become cold gas giants with final masses of a few hundred

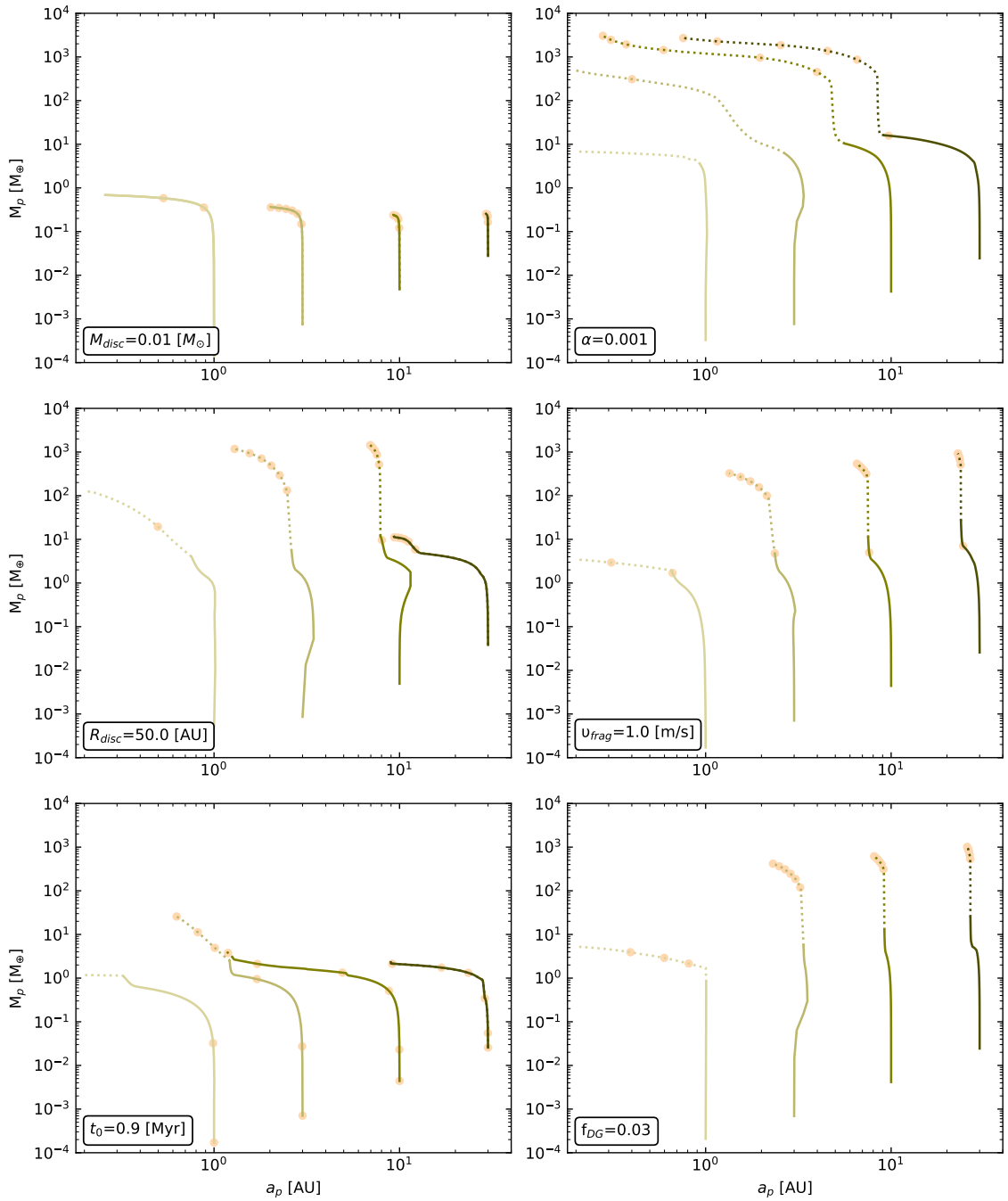

Figure 5.2. Same as in Fig. 5.1, with one parameter changed (marked in each panel) compared to the standard model.

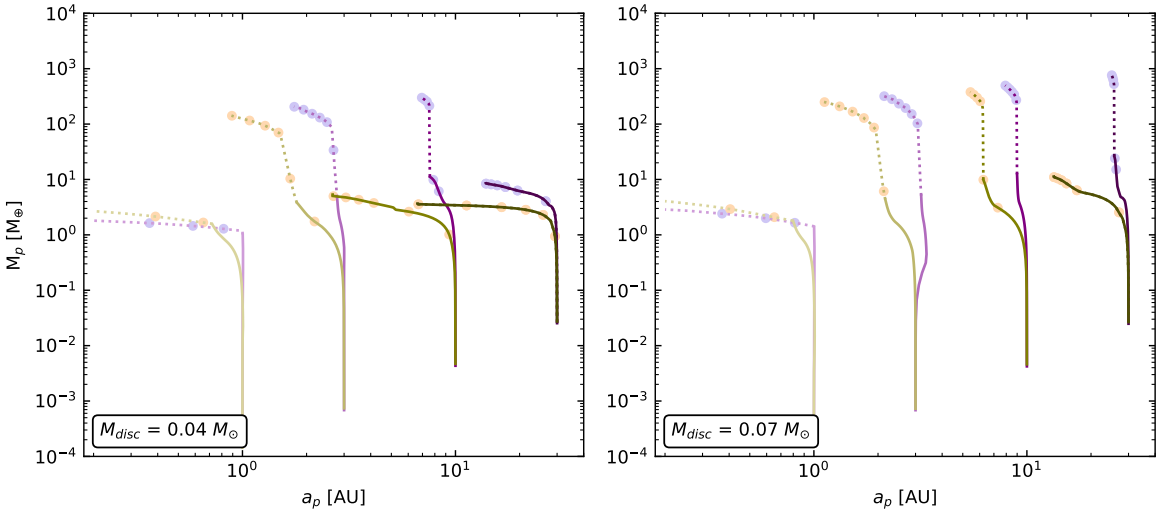

Figure 5.3. Evolution of planetary mass as a function of position for two sets of simulations with f_{DG}=0.01 (green colors) and f_{DG}=0.03 (purple colors) and two different initial disc masses. The rest of the parameters are the same as in the standard case (bold in Table **??**).

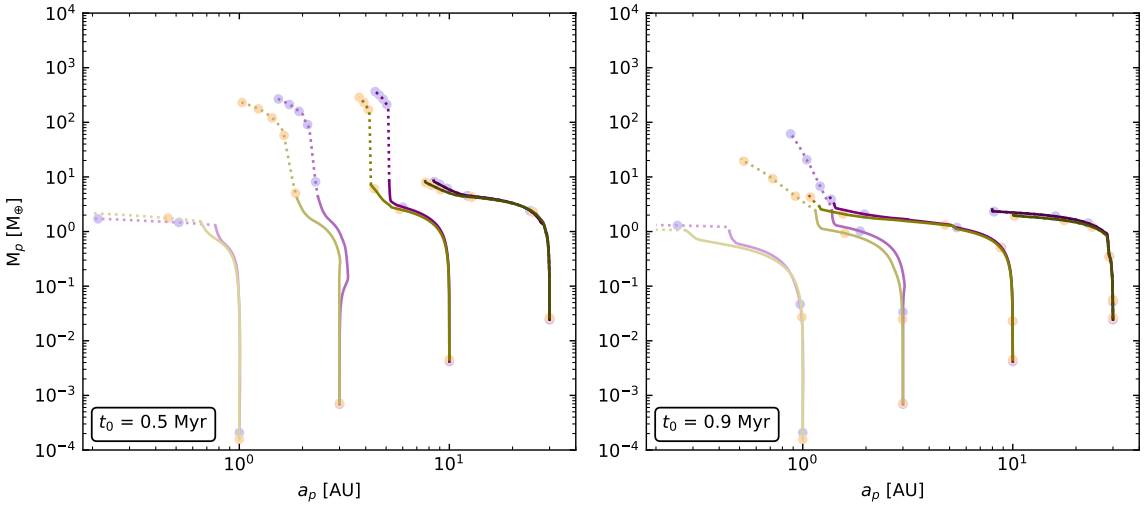

Figure 5.4. Same as Fig. 5.3, for two different initial embryo injection times.

$M_\oplus$.

In Fig. 5.2, only one initial disc parameter is changed in each plot. As expected, the initial disc mass is a very crucial parameter for giant planet formation. In the top, left plot the disc mass is reduced to 1% of a solar mass and we see that at the end of the disc's lifetime the planets are still in their core-building phase. The solid material is not enough for efficient core growth and the planets do not reach the pebble isolation mass before the disc disperses. All of their final masses are below 1 $M_\oplus$ and the innermost planet reaches the inner edge of the disc again, only this time after 1 Myr.

If the initial disc radius is decreased (middle, left plot of Fig. 5.2), then even the planet that started at 1 AU becomes a gas giant of around 100 $M_\oplus$ but it still migrates to the inner edge before 1 Myr. There is outward migration for both planets that start at 3 and 10 AU because of the heating torque. In this case, the disc radius is smaller but the total amount of material is the same in the disc, thus locally the dust and gas surface density are higher, which results in higher accretion rates. The heating torque is directly proportional to the solid accretion rate and since the latter is increased in this case, outward migration is more extended compared to the standard case in Fig. 5.1. However, the closer the planets are to the outer edge, the more limited the available pebbles are. Especially for the planet starting at 30 AU in this 50 AU disc, the pebble flux is significantly decreased and this leads to low accretion rates so the planet does not reach the pebble isolation mass and thus does not accrete gas, so it ends up as an ice giant of 11.5 $M_\oplus$.

The time that the embryo has to grow is also a very crucial parameter. In the bottom, left plot of Fig. 5.2, we show the growth tracks for a starting time of 0.9 Myr instead of the nominal 0.1 Myr. We see that in this case only the planet starting from 3 AU accretes a gaseous envelope and its final mass is only a few Earth masses above Neptune's mass. If the injection time is delayed, then the dust has more time to radially drift inwards, so for the planets starting their growth at 10 And 30 AU, the pebble surface density has already decreased significantly, hence leading to slow pebble accretion rates. The embryo starting at 1 AU, reaches the pebble isolation mass, as the ones starting at 3 and 10 AU, and it starts accreting gas but the low accretion rates mean that it migrates more and reaches the inner edge of the disc within 1 Myr. The embryo originating at 10 AU takes almost 3 Myr to reach the pebble isolation mass and for this reason, it only accretes around 1 $M_\oplus$ of gas.

In the top, right plot the α-viscosity parameter is instead 10^{-3}. The higher viscous heating leads to higher pebble isolation masses (Eq. 5.1) and it causes increased collisions, which keep the pebbles smaller (Eq. 3.14), leading to lower pebble accretion rates. Therefore, during the core-building phase, the planet accretes less material, in comparison to the model with $\alpha = 10^{-4}$, and migrates inwards more. For this reason, the pebble isolation mass that the planet reaches is lower with $\alpha = 10^{-3}$ and it is, thus, reached sooner, giving way to earlier gas accretion. At the same time, the gas accretion rate of the disc is larger due to the higher disc viscosity, resulting in more material delivered to the planetary horseshoe region, consequently increasing the planetary mass. The higher viscosity directly affects the type-II migration rates, so the planet migrates faster also during its gas accretion phase. The two planets that start growing closer to the star migrate to the inner

edge of the disc before the end of the disc's lifetime. The planets that started at 10 and 30 AU end up as gas giants at 0.3 and 0.8 AU respectively. The final masses are higher compared to the standard case, with the ones of the outermost gas giants being from a few hundred to around 3000 $M_\oplus$, compared to a few hundred in the standard case.

The fragmentation velocity (middle, right plot of Fig. 5.2) affects the final planetary masses only minimally in these examples. With this lower value, the pebble sizes remain small (Eq. 3.14), leading to slower pebble accretion but the radial drift velocities are also lower and the total pebble content remains enough for efficient and timely core growth. The final masses of the planets are slightly lower than the corresponding ones in the standard case of Fig. 5.1 because of the additional time it took for the planets to reach their pebble isolation masses and start accreting gas. The difference in the final positions is also minimal because migration is not directly affected by the different fragmentation velocity, it is only influenced by the competition with accretion.

The final plot of Fig. 5.2 (bottom, right) shows the growth tracks of the four example planets with double the dust-to-gas ratio of the standard case shown in Fig. 5.1. We find reduced migration because of the increased growth rates with the larger amounts of material available that cause a faster transition into the slower type-II migration, but the final masses remain almost the same. For the innermost planet, the pebble isolation mass is lower with the higher dust-to-gas ratio, even though at the beginning the higher dust-to-gas ratio leads to higher viscous heating because of the increased optical depth and the decrease in the gas surface density (check Eq. B.3 in Schneider & Bitsch 2021) that both increase overall the temperature of the disc. The aspect ratio is then

$$H = \frac{c_s}{\Omega_K} \ , \tag{5.4}$$

where Ω_K is the Keplerian angular velocity and the sound speed is

$$c_s = \sqrt{\frac{k_B T_{mid}}{\mu m_p}} \tag{5.5}$$

with k_B the Boltzmann constant, T_{mid} the midplane temperature, μ the mean molecular weight and m_p the proton mass. Therefore, the higher temperature leads to a higher aspect ratio and this directly influences the pebble isolation mass (Eq. 5.1). However, the aspect ratio is actually evolving because of the evaporation of inward drifting pebbles that increases the vapor content of the gas, locally and in time (Eq. E.13 in Schneider & Bitsch 2021). For this reason, in the disc with the higher dust-to-gas ratio, the gas gets more enriched and the mean molecular weight increases more over time, leading to a lower aspect ratio and subsequently a lower pebble isolation mass, mainly interior to the water iceline where the enrichment is significant. The innermost planet in the disc with $f_{DG} = 0.03$ is, thus, less massive compared to the corresponding one in the disc with $f_{DG} = 0.01$. Being so close to the inner edge of the disc, the planet originating at 1 AU reaches it before the disc dispersal, as all of the innermost planets for the different example simulations that we discussed above.

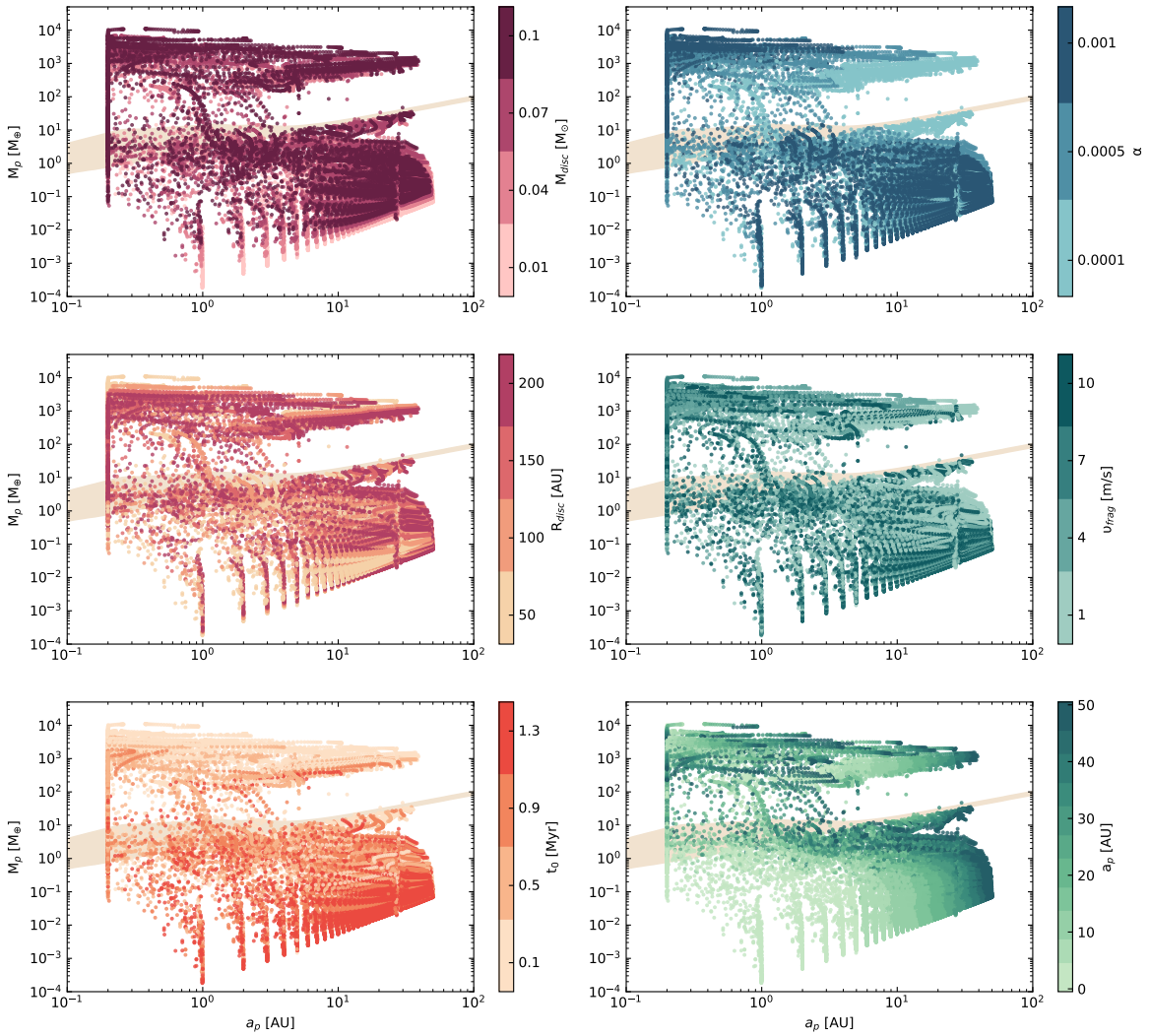

Figure 5.5. Final planetary masses and final positions for all simulations with f_{DG}=0.015. The color-coding in each plot represents the different initial conditions tested for the corresponding parameter. The beige area shows the range of the initial pebble isolation masses, as calculated by the disc properties.

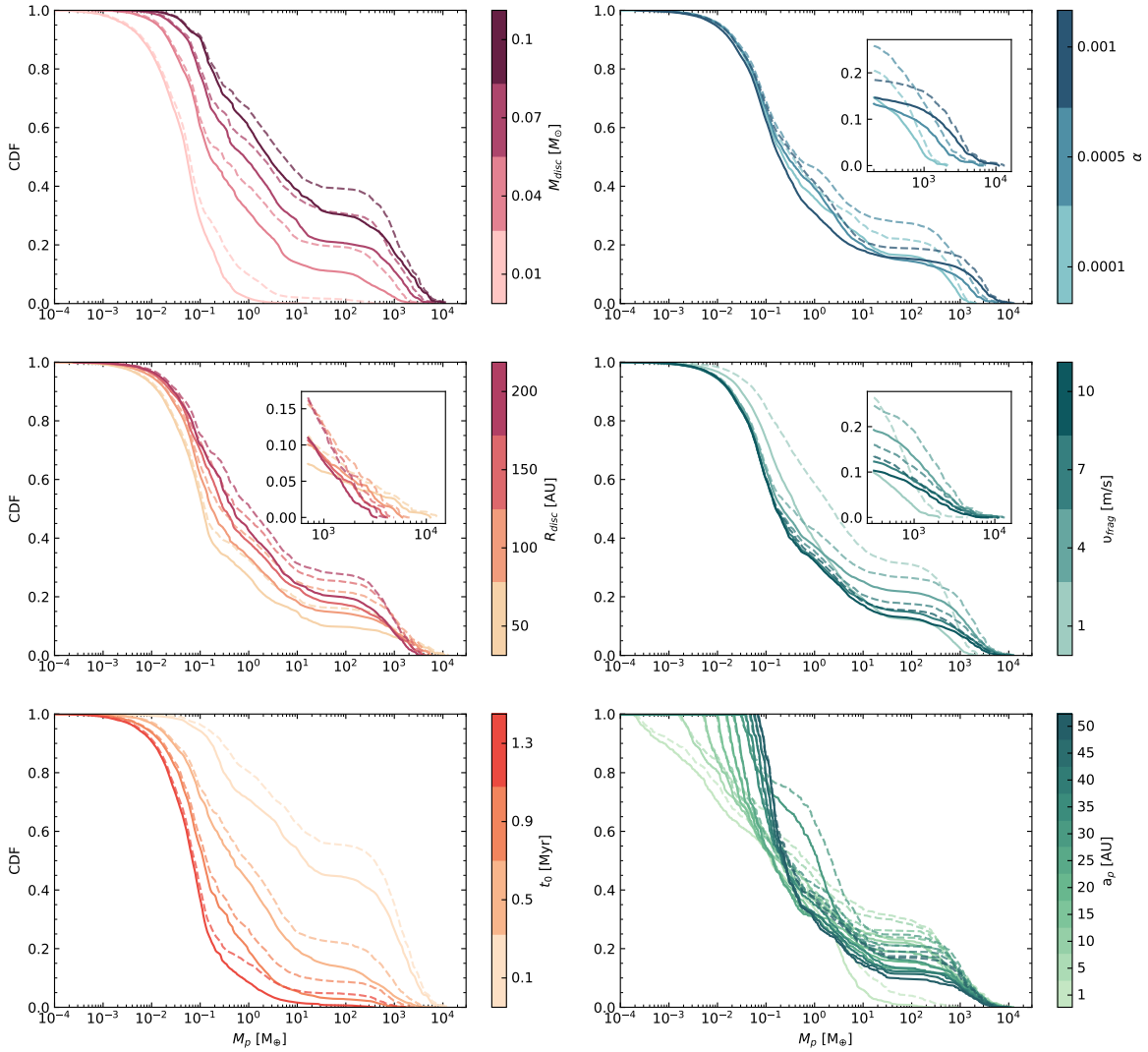

Figure 5.6. Cumulative distribution functions (inversed) of final planetary masses, for different initial conditions. Each plot shows the effect of one parameter and the color-coding shows the different values for each parameter. The solid lines show simulations with f_{DG}=0.015, while the dashed lines show the ones with f_{DG}=0.03.

We have shown above that with a very low disc mass, the planets in these examples cannot grow efficiently. One wonders, whether increasing the dust-to-gas ratio can compensate for a lower disc mass. Indeed, as shown in Fig. 5.3, increasing the dust-to-gas ratio of the disc provides the necessary solid content for efficient core growth. We note that in this plot we compare two sets of simulations with f_{DG}=0.01 and f_{DG}=0.03 (in contrast to the standard case of Figs. 5.1 and 5.2 with f_{DG}=0.015). For an initial disc mass of 0.04 $M_{\odot}$ and the enhanced dust-to-gas ratio of f_{DG}=0.03 (purple colors), the planet starting at 10 AU reaches the pebble isolation mass within 1 Myr, therefore it has enough time left to accrete gas efficiently. It becomes a Jupiter-mass gas giant, in contrast to the planet at the same starting position in the disc of the same mass with f_{DG}=0.01 (green colors). The same is true for a disc mass of 0.07 $M_{\odot}$ and the planet starting at 30 AU. While it failed to reach the pebble isolation mass with the lower dust-to-gas ratio, it reaches almost 3 M_J with f_{DG}=0.03. In Fig. 5.4, we also test later embryo injection times with a higher dust-to-gas ratio and find a minimal difference in the final planetary masses. Even with the enhanced solid content, there is not enough time for the cores to grow efficiently if they did not do so with f_{DG}=0.01, given that most of the pebbles have already drifted inwards before the embryo is injected.

5.4 Favorable conditions for giant planet formation

We can now zoom out to the results of our whole sample of the parameter study. The parameters that we varied are presented in Table **??** and all possible combinations have been tested, for two dust-to-gas ratio values (f_{DG}=0.015 and f_{DG}=0.03), yielding a total number of 76800 runs. In Fig. 5.5, we present the final planetary masses as a function of final orbital distance, color-coding for the different initial parameters, only for the nominal f_{DG}=0.015. The beige region encloses the initial pebble isolation masses for all simulations, as calculated by each corresponding disc.

The inner edge of the disc in our model is at 0.2 AU and this causes the pile-up of the planets in a vertical ”line” at this position of the plots. The other vertical ”lines” further out and near the bottom of the plots are caused by our choice of initial positions for the embryos. The gap, roughly above the maximum pebble isolation mass, is caused by the nature of gas accretion. If the conditions are such that a core can reach the pebble isolation mass, then envelope contraction most likely happens fast and runaway gas accretion begins. The pebble isolation mass generally increases with increasing orbital distance (Eq. 5.1) and the gas accretion rates scale with the core mass, therefore the planets that reach the pebble isolation mass will have an increasing core mass as a function of orbital distance. This leads to this gap by gas accretion in Fig. 5.5 to become larger at larger distances.

We also notice a more distinct diagonal ”line” of points in Fig.5.5 around 1 AU which corresponds to embryos with an intermediate disc radius of 100 AU with otherwise beneficial initial parameters for core growth; high disc mass, low viscosity and initial position of the embryo at 5 to 25 AU. In these cases, the fragmentation velocity is 10 m/s and this leads to larger dust grain sizes that drift, though, at larger speeds. However, the embryos in these cases are injected at 0.5 Myr so there

are still enough pebbles left in the disc. The low accretion rates mean that migration outperforms growth and the type I inward migration of the planets stops when they reach the pebble isolation mass around 1 AU because of the enhanced surface density exterior to the water iceline. Then the disc is dispersed before they can accrete more gas and they remain with sub-Neptune to Jupiter masses.

Even though we vary a lot of the initial parameters in the simulations, we do not randomize the choices as in population synthesis simulations (e.g. Emsenhuber et al. 2021; Ida & Lin 2004; Mordasini et al. 2009; Mulders et al. 2019; Ndugu et al. 2018; Voelkel et al. 2022), noting that determining distributions of the initial condition parameters still harbors several uncertainties. For example, it is still unknown what the initial mass distribution of protoplanetary discs is. The scope of this work is to investigate which initial conditions favor, from a theoretical point of view, the formation of giant planets, without comparing to the observed exoplanet populations and occurrence rates. For this reason, we have chosen our initial parameters within reasonable ranges constrained by observations, laboratory experiments, and theory, focusing more on the conditions which would be beneficial to giant planet formation.

We show in Fig. 5.6 the (inverse) cumulative distribution functions (CDF) as a function of the final planetary masses, which describe the probability of finding a simulated planet of our sample above a certain final mass. In these plots, we also color-code for the values tested of a specific parameter, e.g. disc mass in the first one, including all of the possible combinations of the other parameters. The solid lines represent the simulations with f_{DG}=0.015 and the dashed lines show the simulations with f_{DG}=0.03.

In the following discussion, we will focus on the most favorable conditions to make a gas-giant planet. As such, we will refer to any planet with a mass above 100 $M_{\oplus}$, and given that our discs extend only down to 0.2 AU we will thus discuss the analogs of warm and cold Jupiters. As mentioned above, we do not use randomized initial parameters and do not intend to directly compare with the occurrence rates of giant planets, so the presented fractions represent a measure of how "easy" it was to form a giant planet given the initial conditions compared to all of the planets formed in our simulations. However, we can conclude that if a specific parameter produces a much higher fraction than 10-20% (e.g. Cumming et al. 2008; Fernandes et al. 2019; Mayor et al. 2011; Wittenmyer et al. 2016) then this means that the initial condition that produced it cannot be the main condition that is true for the exoplanet population. And inversely, if a condition does not reproduce the occurrence rates, then it is probably also not the main condition leading to exoplanet formation.

5.4.1 Dependence on the initial conditions

Disc mass

The total disc mass determines the total content of the building blocks that form planets. Giant planet formation is not necessarily a two-step process, of pebble and then gas accretion, but regardless of when gas contraction happens and how the efficiency evolves, giant planets require a massive core to be formed. We expect that a large solid content of the disc will be beneficial given that the pebble accretion rates

will increase. Once a sufficiently massive core has formed, a larger gas component can also help with efficient gas accretion that increases the total planetary mass.

We see in the left, top plot of Fig. 5.6 that a clear trend emerges with the increasing disc mass. An initial mass of 0.01 $M_{\odot}$ does not provide enough solid material for cores to grow and this makes it impossible for the planets to accrete gas and grow to Jupiter masses. Then we find that gas giants with masses above 100 $M_{\oplus}$ are 10% of our sample with a disc mass of 0.04 $M_{\odot}$, 20% with $M_{disk} = 0.07M_{\odot}$ and 30% with $M_{disk} = 0.1M_{\odot}$. In the simulations with f_{DG}=0.03 we find that 10% of our sample with a disc mass of 0.01 $M_{\odot}$ form a planet with a mass higher than 1 $M_{\oplus}$ but only around 1% of the sample is giants.

With the increased dust-to-gas ratio, the initial dust mass increases, therefore the available content for core growth increases and if the cores are more massive, then as discussed above, the gas accretion rates will also increase. For example, the CDF with a disc mass of $0.04M_{\odot}$ and f_{DG}=0.03 (dashed lines) is very similar to the one with $M_{disk} = 0.07M_{\odot}$ and the nominal f_{DG}=0.015. Accordingly, the CDF with $M_{disk} = 0.07M_{\odot}$ and f_{DG}=0.03 is almost the same as the one with $M_{disk} = 0.1M_{\odot}$ and f_{DG}=0.015.

Disc radius

A large disc radius ensures a long-lasting pebble flux which benefits core growth via pebble accretion. We show, in the left, middle plot of Fig. 5.6, that the different initial disc radii lead to similar fractions of giant planets, decreasing from 20% for a 200 AU disc to 10% for a 50 AU disc. Interestingly, the trend is flipped for high planetary masses, as shown in the zoomed inset. The planetary mass for which this "flip" happens is strongly influenced by our choice of initial parameters for the whole set of simulations. Therefore, the critical mass cannot be quantified from this work but we can conclude that if the conditions are favorable for a timely core growth to several Earth masses and subsequent gas accretion, then a smaller disc leads to more massive giants. The smaller disc radius means that more solid and gas material is in the vicinity of the planets and their masses increase rapidly. Essentially, the smaller disc has a higher accretion rate due to the increased surface density.

The fractions of giants are significantly enhanced if we increase the dust-to-gas ratio, specifically we find more than 20% giants formed with a disc size of 100 AU, which is higher than the largest disc size (200 AU) with half the dust-to-gas ratio and 35% for the largest disc size (200 AU). There is again a flip for the highest planetary masses; the larger the disc, the lower the fraction of very massive giants. Additionally, above 1000 $M_{\oplus}$ the difference between the models with f_{DG}=0.03 and the ones with f_{DG}=0.015 gradually diminishes.

Starting time of the embryo

We find, as expected, that the injection time of the embryo plays a decisive role in the growth of a giant planet. When the planetary embryo starts growing 0.1 Myr after the disc in our model starts evolving, then the fraction of giants produced is almost 45% (left, bottom plot in Fig. 5.6) and 50% with f_{DG}=0.03. In contrast, injecting

the embryo as late as 1.3 Myr leaves us with almost no giants. There is simply not enough material to build the core fast because the pebbles have mostly drifted inwards. Even if the core reaches pebble isolation mass before the disc dispersion, it will do so very late, leaving not enough time to accrete large amounts of gas. This is marginally improved by increasing the dust-to-gas ratio. In this case, we find <5% of giants in our sample for a starting time of 1.3 Myr.

The few giants that are formed with this late injection time had otherwise very beneficial initial parameters, as we see in the few dots above 100 $M_\oplus$ in Fig. 5.5. Specifically, high disc mass, large disc radius, low viscosity, and fragmentation velocity (Sect. 5.4.1) and starting locations at 2 to 19 AU. Reducing the injection time to 0.9 Myr is still not very helpful, producing only around 2.5% giants and the fraction is below 15% even for an injection time of 0.5 Myr. Nevertheless, the corresponding fractions with $f_{DG} = 0.03$ are 10% and approximately 23%.

We should also mention that the implications of the starting time for the embryo are heavily influenced by the dust fragmentation velocity. A low fragmentation velocity results in small pebbles and they are thus kept in the disc longer, while a disc with a larger fragmentation velocity will get depleted of its pebbles too fast. This can be seen for example in Fig. 5.5 (left, bottom and right, middle plots), where the few giants that are formed when the embryo is injected at 1.3 Myr correspond to a disc with $u_{frag} = 1$ m/s, that kept the pebbles long enough for the planets to reach the pebble isolation before the gas dissipation so that they still had time to accrete gas.

Disc viscosity

A higher α-viscosity parameter means that the viscous heating is higher, the temperature of the disc and its aspect ratio increase, and this leads to higher pebble isolation masses, in the inner disc. The increased viscosity also means increased destructive collisions between dust grains and this decreases the available pebble-sized material, which in turn leads to decreased pebble accretion rates. In total, this results in a less efficient formation of planets of a few Earth masses.

On the other hand, gas accretion benefits from the cores that could be formed from the higher pebble isolation mass. Hence, viscosity plays a different role for low-mass and high-mass planets, similarly to the disc radius (right, top plot in Fig. 5.6). We find that very high-mass giants can be formed with high viscosity and for this population, the higher the viscosity, the more massive the giants become. The key, however, for this, is early formation (see also Fig. 5.5), so that the core can take advantage of as much solid material as possible before it is lost due to radial drift, and the fact that at high viscosity the gas accretion rate is higher. Even when the horseshoe region has been emptied, a higher viscosity will provide more material to the planet and it will thus become more massive.

Higher viscosity also leads, in general, to faster migration rates because it delays gap opening to higher planetary masses so that the planets remain in type-I migration longer and migrate inwards further before the slow type-II migration sets in. At the same time, at high viscosity, the entropy-driven corotation torque can operate, which would actually slow down type-I migration. But type II migration is directly

dependent on the viscosity of the disc, so a lower α will slow down migration for the planets that have opened a gap in the disc and prevents them from migrating to the inner edge of the disc. For this reason, we find (Fig. 5.5) that high-mass gas giants have a decreasing final position for increasing α-viscosity values.

The overall difference in the CDFs between various α-viscosity values is small, with all of them leading to similar fractions of gas giants in our sample around 15-18%. In contrast, the increased dust-to-gas ratio models lead to more distinct CDFs that are also flipped and the highest α-viscosity leads to the lowest fractions of planets up to a few hundred $M_\oplus$. This was also the case with f_{DG}=0.015 but up to lower planetary masses because of the less efficient core growth and the lower pebble isolation masses. The fraction of giants with $\alpha = 10^{-3}$ and $f_{DG} = 0.03$ is higher than for all α-viscosities with the nominal dust-to-gas ratio, then around 25% for $\alpha = 10^{-4}$ and the highest fraction, 35%, comes from the discs with the intermediate $\alpha = 5 \times 10^{-4}$, that maintains a balance between the pebble and gas accretion rates.

Dust fragmentation velocity

The fragmentation velocity defines the threshold relative velocity at which collisions between dust grains lead to destruction into smaller aggregates. The higher this threshold is, the larger the dust grains can become and this is not only directly beneficial to pebble accretion but it also increases the radial drift velocities, which can also increase the pebble flux towards the growing core. Nevertheless, this can actually hinder core growth if the planetary embryo is injected later into the disc and a significant fraction of the dust has already drifted inward to the embryo location.

The most beneficial fragmentation velocity out of the ones tested is 4 m/s with a fraction of gas giants slightly more than 20% of the whole sample, while the 7m/s threshold results in a 15% giant planet fraction (right, middle plot in Fig. 5.6). These intermediate values offer the necessary pebble sizes for maximized accretion and at the same time their radial drift velocities provide an optimal pebble flux, that can also last a long time. In contrast, the highest value of 10 m/s and the lowest of 1 m/s both yield a fraction of approximately 10%.

When the fragmentation velocity is low, the dust particles are kept small, hence mostly well-coupled to the gas and so, pebble accretion is delayed. It takes longer to reach the pebble isolation mass and this consequently leaves less time for the accretion of a massive envelope. At the same time, the smaller pebbles mean lower radial drift velocities, so the pebble flux can be maintained longer. When the fragmentation velocity is high, then large particles can form, that allow better accretion to the embryo. However, the large Stokes numbers also lead to high radial drift velocities that require an early formation of the core so that they are not lost before accretion onto the embryo can start.

Interestingly, with $f_{DG} = 0.03$, the most favorable fragmentation velocity is 1 m/s, with the fraction of giants exceeding 30% of our sample. This can be linked to the decreased drift velocities, in combination with the higher solid content, that compensates efficiently for the smaller pebble sizes, given that the pebble accretion rates have a stronger dependence on the surface density than the (Stokes numbers of the) pebble sizes. The fractions drop significantly beyond 1000 $M_\oplus$ and become

again the lowest compared to higher fragmentation velocities.

Starting location of the embryo

In the right, bottom plot of Fig. 5.6, we only show some of the starting positions for better readability. At 1 AU, almost no embryos grow to become gas giants because they migrate to the inner edge of the disc, where we stop the accretion onto the planet. The highest fraction of giants can be found with embryos that start at 5 AU and then it decreases up to 25 AU. The embryos that originate at 30 AU, then, have higher fractions of giants compared to those interior to this orbital distance, but injecting the embryo further out results in a decrease to the fraction of giants again because the further out the embryo is located, the closer it is to the outer edge of the disc (especially for the very small 50 AU discs), where the solids' surface density is significantly lower and pebble accretion needs to surmount radial drift.

The fractions of very massive giants ($M_p \geq 1000\ M_\oplus$), are very similar for all starting locations, except for the ones starting their growth at 1 AU. Reaching such high mass is a product of a combination of beneficial conditions and an absence of adverse ones, such as high disc mass (0.1 $M_\odot$) and early injection of the embryo (0.1 Myr), viscosity dictated by $\alpha \geq 5 \times 10^{-4}$ and fragmentation velocities higher than 1 m/s, but it dependents weakly on where the embryo originates.

With the increased dust-to-gas ratio, we find ∼5% of giants form even when the embryo originates at 1 AU because the enhanced solid content aids the core growth before the planet migrates to the inner edge and stops accreting. In general, the enhanced core growth with f_{DG}=0.03 leads to less inward migration. The highest fraction of giants corresponds again to starting their growth at 5 AU because of the high solids surface density that is additionally enhanced at the water iceline and the fact that the pebble flux exterior to them can be sustained longer, compared to starting locations further out. The location of the water iceline is close to 1 AU, but it depends on the disc properties that define viscous heating, specifically, the disc mass that sets the gas surface density, the viscosity, and the dust-to-gas ratio, therefore embryos originating at 1 AU could also benefit from the higher solids surface density at the water iceline in some of the cases. However, they most likely migrate to the inner edge of the disc, where we stop their growth, unlike the planets that start growing at 5 AU. Additionally, the planets originating at 5 AU can migrate outwards (depending on the disc parameters) due to the heating torque and this also prevents them from migrating to the inner edge (very soon).

Dust-to-gas ratio

A higher dust-to-gas ratio means that the solid component of the disc is increased and that the initial pebble isolation mass is higher because of an increase in the viscous heating component of the temperature (Eq. B.3 in Schneider & Bitsch 2021). It should be noted, however, that the pebble isolation mass is also influenced by the mean molecular weight that is evolving in time and space as the inward drifting dust evaporates at the icelines and the gas vapor content gets enhanced (Eq. E.13 in Schneider & Bitsch 2021) and this can lead to a lower pebble isolation

mass in the inner disc.

We compare here f_{DG}=0.03 to the nominal value of f_{DG}=0.015. We see in the dashed lines of Fig. 5.6 (for all different parameters) that the small planets, around 1 $M_\oplus$ and below are not significantly influenced by an increase in the dust-to-gas ratio because, in most of the cases, the conditions remain limiting for planet growth, independently of the dust content, and the fact that the pebble isolation mass can be higher, makes it harder to reach this mass. Overall though, as expected, the higher solid content leads to higher planetary masses and thus higher fractions of giants.

However, if the conditions are not favorable for giant planet formation, then the higher dust-to-gas ratio increases the fractions but cannot compensate efficiently enough. For example, when the embryo is injected late in the disc (bottom, left plot of Fig. 5.6), we find in this case less than 5% of giants compared to almost zero with the nominal dust-to-gas ratio. In this case, a significant amount of pebbles is still lost due to radial drift before the core starts to accrete material. Similarly, even though we find that almost no giants form when the embryo originates at 1 AU, the fraction is also around 5% with double the dust-to-gas ratio because the enhanced pebble accretion helps in reaching the pebble isolation mass sooner and slows down their migration. On the contrary, we find that the lowest disc mass we tested (M_{disc}=0.01 $M_\odot$) is very limiting and even for the increased amount of solids, the pebble flux is too low for planet formation in general and prohibits the formation of giants.

5.5 Discussion

Global models have been increasingly emerging in an effort to self-consistently link the dust and gas evolution with planet formation. Bitsch et al. 2019a investigate the conditions that allow the formation of gas giants, located outside 1 AU, through N-body simulations, varying the pebble flux and the viscosity in relation to migration and accretion, whereas, the viscosity of the disc is fixed to 0.0054. In the accompanying work, Lambrechts et al. 2019 used the pebble flux as a free parameter. Their findings are in line with our findings in the present work but our goal is to generalize the conclusions about the favorable conditions for giant planet formation and to link it directly to the conditions dictated by the interplay with the protoplanetary disc.

Lambrechts et al. 2019 find that if the total dust mass is less than around 110 $M_\oplus$, then the masses of the formed planets are below 0.1 $M_\oplus$, even with the inclusion of growth through embryo collisions after the gas dissipation. Here, our 0.01 $M_\odot$ discs correspond to a total $M_{dust} \approx 50$ $M_\oplus$ for the nominal f_{DG}=1.5% and these produce almost no planets with masses above 1 $M_\oplus$ (Fig. 5.6). Growth is highly dependent on the Stokes number, which can be slightly different between our models, given some different initial conditions. In total, though, it is not surprising that even with f_{DG}=3% we find only $\leq$ 2.5% of the final planetary masses of our sample are above 10 $M_\oplus$.

Even though we focus here on gas giant formation (like Jupiter and Saturn), we have shown that ice giants (like Neptune and Uranus) can also be formed with our

model. According to the model proposed in Lambrechts et al. 2014, ice giants are planets in wide orbits that do not grow enough to reach their pebble isolation masses before the gas is lost, so the heating from the continued pebble accretion prevents them from contracting a massive gaseous envelope. In our example cases, we show in the left, middle plot of Fig.5.2 an embryo that originates at 30 AU, accretes pebbles slowly because of the limited supply this close to the outer edge of the disc, and by the end of the disc's lifetime, it is just above 10 $M_{\oplus}$ but has not reached the pebble isolation mass yet, which means that the planet is still hot and might not go into envelope contraction. Similarly, in Fig. 5.3 and 5.4 some of the outermost embryos have final masses around 10 $M_{\oplus}$ and in Fig. 5.5, we show several planets in wide orbits (>10 AU) with masses 10-50 $M_{\oplus}$ and just around their pebble isolation mass, which means that they have not undergone runaway gas accretion. Interestingly, all of these potential ice giants are formed in discs with $\alpha = 0.0001$ (left, top plot of Fig. 5.5).

In this work, our model does not yet include planetesimal accretion, however, forming giant planet cores via pure planetesimal accretion (e.g. Emsenhuber et al. 2021; Ida & Lin 2004; Mordasini et al. 2009, 2012) faces many difficulties, especially with giant planet formation (Drążkowska et al. 2022), mainly due to the long growth timescales that either compete with the disc lifetimes (Fortier et al. 2013; Guilera et al. 2014; Pollack et al. 1996), or are overpowered by migration (Voelkel et al. 2020). Brügger et al. 2020 present a comparison between pebble and planetesimal accretion in population synthesis models, concluding that pebble accretion is less efficient in giant planet formation. Their study is limited to a disc with M_{disc}=0.017 $M_{\odot}$, α=0.002, f_{DG}=0.01 and R_{disc}=30 AU. As we have shown in the present work, this combination of initial conditions is unfavorable for giant planet formation, given that all of them prevent efficient pebble accretion.

Voelkel et al. 2022 conclude that even though efficient growth can happen via pebble accretion, it might actually be a destructive mechanism for inner disc embryos that form early on because of fast and extended migration. However, they also stress that the choice of initial disc parameters is limited, specifically, they use M_{disc}=0.1 $M_{\odot}$, α=0.0003, f_{DG}=0.0134, R_{disc}=20 AU and u_{frag}=2 m/s. In the present work, we find that these specific parameters are not necessarily inefficient for planet growth, in line with their conclusions, even though this combination is probably not one of the most favorable. Several planets reach indeed the inner edge of the disc but, as we show here, this happens mainly to the embryos that originated at 1 AU, it is, thus, expected because of the small disc radius they are testing and it is not a common phenomenon in planet formation models. In general, we show here that the pebble accretion framework can be very efficient at forming giant planets (and broadly planets), especially when at least one of the initial conditions is beneficial.

In the present work, as well as in several pebble accretion models, the initial planetary embryos are assumed to be already formed and their injection locations are handpicked (what we do here) or chosen from a distribution in a randomized way. This does leave space for questions on how these embryos form and whether some disc locations are favorable or forbidden. Voelkel et al. 2020 link the dust and gas distribution to the formation of planetesimals and subsequently to the spatial distribution of planetary embryos and show that the location is crucial, with the

innermost regions of the disc being more favorable due to the higher concentration of solid content.

At the same time, other studies have discussed that certain locations in the disc can be the birthing locations of planetary embryos, such as the water iceline (Drążkowska & Alibert 2017b; Müller et al. 2021; Schoonenberg & Ormel 2017b) or the silicate sublimation line (Izidoro et al. 2021; Morbidelli et al. 2022). Our choice of a wide range of initial locations serves the scope of this paper to connect the starting position of an embryo with the final position and mass of a formed planet, regardless of whether some of these locations are more probable than others. Additionally, we conclude that forming giant planets is not severely limited by the initial location of the embryo but there are locations that are more favorable (Fig 5.6), for example around 5 AU and around 25-30 AU (depending also on the rest of the disc parameters).

Coleman 2021 uses a global model that includes both pebble and planetesimal accretion, along with planetesimal formation, to study the embryo formation and determine their mass, size, and spatial distribution in the disc. In the combined (pebble & planetesimal) accretion scenario, they find that planetesimal accretion is mainly effective around the iceline and a few AU exterior to it. They find that including planetesimals can actually aid pebble accretion, despite the fact that planetesimal formation will use some of the available mass in solids (Voelkel et al. 2021). Specifically, planetesimal accretion can help the planetary embryos become more massive and reach the transition mass sooner, thus enhancing the efficiency of pebble accretion.

The dust-to-gas ratio can be used as a proxy for the metallicity of the disc through

$$[Fe/H] = log_{10}\left(\frac{f_{DG}}{f_{DG,\odot}}\right) \ . \tag{5.6}$$

Setting our nominal simulations to [Fe/H]=0 leads to [Fe/H]=$\log_{10}(3/1.5) \approx 0.3$ dex for the simulations with $f_{DG} = 0.03$. Previous studies have established a positive correlation between metallicity and giant planet occurrence rate (Fischer & Valenti 2005; Fulton et al. 2021; Johnson et al. 2010; Santos et al. 2004). In the pebble accretion framework, the core mass is heavily influenced by the initial dust-to-gas ratio (Lambrechts et al. 2014), and the heavier cores will contract faster and move on to rapid gas accretion sooner (Ikoma et al. 2000).

We find here, unsurprisingly, that a higher dust-to-gas ratio leads in general to more massive planets (Fig. 5.6), however, another factor could be preventing giant planet formation. As an example, we show in Fig. 5.3 that the higher dust-to-gas ratio could provide enough material so that migration slows down and the pebble isolation mass can be reached sooner to give way to efficient gas accretion. However, in Fig. 5.3, we do not include the lowest disc masses we tested (0.01 $M_{\odot}$) because in this case, the higher dust-to-gas ratio cannot compensate efficiently for the low solid content, and again almost no giants form. We see, additionally, in Fig. 5.4 that the early formation is more important than the high dust-to-gas ratio because of the radial drift that depletes the disc from the solids even before the planet starts growing. In the general picture (left, bottom plot in Fig. 5.6), there is only a minimal increase in the fraction of giants produced with f_{DG}=0.03 and late injection times.

Interestingly, though, we see in Fig. 5.6 that the CDF with a disc mass of 0.04 $M_{\odot}$ and f_{DG}=0.03 is very similar to the one with a disc mass of 0.07 $M_{\odot}$ and f_{DG}=0.015 and the CDF of the discs with M_{disk} = 0.07 $M_{\odot}$, f_{DG}=0.03 are almost the same as the one of the discs with M_{disk} = 0.1 $M_{\odot}$, f_{DG}=0.015. It is thus very clear that further constraints (from observations and theory) on the initial disc mass fraction are needed as input for planet formation simulations.

One could argue that our choice of initial disc masses is on the higher side (looking for example Fig. 6 in Manara et al. 2022), thus expected to form more giant planets but maybe not in line with the observed disc masses. Nevertheless, we note that on one hand, the mass estimates come from observations around mm wavelength and on the other hand, the disc mass is evolving in time and as the dust drifts radially, a significant percentage of it becomes accreted, either by forming planets or by the host star. We will expand on this dust mass evolution in future work, but we can already conclude that this process will naturally decrease the dust mass over time, hence the disc mass of our models closer to the dissipation of the gaseous disc would also populate the lowest disc masses presented in Manara et al. 2022.

We have tried in this work to use the existing observational constraints in order to decide the ranges of our tested parameters and have discussed above some of our assumptions. Even with improved assumptions or new physics added to our models, we would not expect the general trends that we find to be altered but rather the specific fractions for giant planets (or other types of planets in general). We want to note that significant constraints can be made from our findings even for initial parameters that overproduce giants (e.g. M_{disc}=0.1 $M_{\odot}$ or t_0=0.1 Myr) or struggle to produce any planets at all (e.g. M_{disc}=0.01 $M_{\odot}$). The latter, for instance, places a constraint on the masses of the discs that we would expect to host a planet unless other mechanisms can increase the planetary masses. Such a mechanism could be growth by collisions (Cossou et al. 2014b; Izidoro et al. 2019b, 2017b; Kominami & Ida 2004; Ogihara & Ida 2009; Ogihara et al. 2018), however, we would not expect the final masses to be enhanced more than a few $M_{\oplus}$ (Lambrechts et al. 2019). We have also shown that even with a higher dust-to-gas ratio, a very small fraction of planets with masses above 1 $M_{\oplus}$ form, therefore we would expect that a limiting disc mass exists, especially for higher-mass planets.

One cannot point to a specific parameter being the determinant initial condition for gas giant planet formation but it is rather a combination of beneficial factors that are in play. If we wanted to reproduce, for instance, a specific system or star-forming region, we could use an appropriate ”mixture” of the initial conditions that would reproduce the observed conditions accordingly. For these reasons, we would expect that the diversity of the exoplanetary systems comes from an intrinsic diversity in their natal protoplanetary discs and our most important conclusion is that we need to understand and constraint the underlying disc population better in order to understand and constrain planet formation.

5.6 Summary

In this paper, we connect the initial conditions in a protoplanetary disc to the formation efficiency of giant planets. In order to do so, we perform 1D semi-analytical numerical simulations of planet formation via pebble (Johansen & Lambrechts 2017a) and gas accretion (Ndugu et al. 2021) in a viscously evolving protoplanetary disc using `chemcomp` (Schneider & Bitsch 2021). Our model includes a two-populations approach for the dust growth and drift (Birnstiel et al. 2012a), evaporation at the icelines[a], type-I (Paardekooper et al. 2011a) and type-II migration, the effects of the thermal (Masset 2017) and dynamical torques (Paardekooper 2014) and gap opening as described in Ndugu et al. 2021. We assume that planetary embryos have already formed in the disc, with masses equal to the transition mass (Eq. 2.21, Johansen & Lambrechts 2017a), therefore dependent on the local conditions and at which the embryos accrete pebbles in the (relevant to larger protoplanets) Hill (shear) regime.

We perform a parameter study, testing different values for the disc mass, the disc radius, the time when the embryo is injected, the α-viscosity parameter, the dust fragmentation velocity, the location where the embryo is injected and the dust-to-gas ratio of the disc (Table **??**). We summarize here our findings for each parameter:

- ⋆ A high disc mass is very important in order to make a gas giant because they need a massive core that has reached the pebble isolation mass and can start accreting gas efficiently. Of course, the high total disc mass can also provide more gas to the planet during gas accretion. We find that with a disc mass of 0.01 M_{disc}, no giant planets can form, even with a higher dust-to-gas ratio.

- ⋆ A large disc radius ensures a long-lasting pebble flux that aids core formation. We find, however, that if the conditions are favorable for a giant planet to form in the first place, then the smaller the disc, the more massive the planet can get. Given that the total mass is the same, the increased surface density leads to enhanced pebble and gas accretion rates.

- ⋆ The time when we inject the embryo plays a decisive role because there is competition with the radial drift of the pebbles. When the embryo is injected, enough mass in pebbles needs to remain in the disc and this is also determined by the fragmentation velocity that sets the pebble sizes and consequently the radial drift velocities. We find that when the embryo starts growing at 1.3 Myr, it is very improbable that it can grow beyond 10 $M_{\oplus}$, thus very few planets reach the pebble isolation mass and accrete any gas at all. A higher dust-to-gas ratio can make this late

starting time less restricting, however, the fraction of giants that formed is still low, giving further indication that planet formation might start early in discs (e.g. Segura-Cox et al. 2020).

⋆ Viscosity, and thus viscous heating, directly influence the temperature of the disc, which changes its aspect ratio and consequently the pebble isolation mass. An increase in the viscosity also increases the dust collisions, so it leads to smaller pebbles that are better coupled to the gas and less easily accreted by a growing planet. However, a high viscosity means higher pebble isolation masses and if the conditions are otherwise favorable for the core to reach the pebble isolation mass, then gas accretion is enhanced by the more massive core. At the same time, the high viscosity replenishes faster the horseshoe region with new gas, further enhancing gas accretion and increasing the envelope mass. The fact that there is a trade-off between core growth and gas accretion for different viscosities leads to small differences between the gas giant fractions from different α parameters.

⋆ The fragmentation velocity sets the maximum grain size, thus determining the pebble accretion rates and the radial drift velocities. We find that the most beneficial value for giant planet formation is an intermediate one, compared to results from laboratory experiments, namely 4 m/s, however with double the dust-to-gas ratio we find that the most favorable threshold velocity is 1 m/s because of the increased pebble surface density. In general, the pebble accretion rates are maximized with a combination of optimal pebble sizes and surface density, so the most favorable fragmentation velocity is strongly influenced by the available amount of solids.

⋆ We find that the fractions of giants peak close to 5 AU and 30 AU but in general, giant planet formation is not strongly dependent on the starting location of the embryo. Injecting the embryos very close to the star increases the chances that it migrates to the inner edge well before the gas dissipation, while injecting them very close to the outer edge, where the pebble flux is reduced, significantly increases the growth timescales.

⋆ The fractions of giants generally increase with increasing dust-to-gas ratio because the solid content that is used for core growth is higher, so the pebble accretion rates are higher and the pebble isolation mass can be reached sooner, giving way to efficient gas accretion and increasing the chances that the planet can accrete a massive envelope before the end of the lifetime of the gas disc. However, the improvement is marginal if the rest of the initial conditions are unfavorable for giant planet formation, as it is, for example, if the disc mass is very low (0.01 $M_{\odot}$).

Even if one of the more adverse conditions exists in the protoplanetary disc, when the rest of the conditions are favorable or at least not adverse, then it is still possible for a giant planet to form. In general, giant planet formation is dictated by a combination of beneficial conditions and we cannot simplify it by pointing to one defining parameter. While we do not choose our initial conditions in a randomized way and, thus, can not directly compare with the occurrence rates of the exoplanet systems, we suggest that if one of the initial conditions that we tested in this work overproduces or underproduces giants (or planets in general) compared to the estimated occurrence rates of exoplanets, then the fraction of protoplanetary discs with this conditions should be small. Most importantly, we conclude that the diversity of the exoplanetary systems is directly linked to the diversity of their natal protoplanetary disc, therefore we need to understand and constrain the disc population better through observations and obtain realistic initial distributions for the initial conditions in order to understand and constrain planet formation.

[a]Multiple chemical species are considered in the disc, however, we do not discuss the composition of the planets here and they only affect our work by the spikes of the surface density around the icelines.

6

How planet formation affects the dust mass evolution of protoplanetary discs

From "A giant solution to the disc mass budget problem of planet formation", in prep.

In a nutshell...

The inferred dust masses from Class II protoplanetary disc observations are lower or equal to the observed exoplanet systems which poses the question of how do planets form if their natal environments do not contain enough mass; this is the mass budget problem hypothesis. We utilize numerical simulations of planet formation via pebble and gas accretion, including migration, in a viscously evolving protoplanetary disc which simultaneously trace the dust mass time evolution. As expected, we find that the presence of a giant planet in the disc can greatly influence the evolution of the disc itself and prevent rapid dust mass loss by trapping the dust outside its orbit. Early formation is crucial for giant planet formation, therefore our findings strengthen the hypothesis that planet formation has already happened or is ongoing in Class II discs. Most importantly, we find that the optically thin dust mass significantly underestimates the total dust mass in the presence of a giant planet and could be the answer to the hypothetical mass budget problem.

6.1 Context

In the last decade, dust masses of discs have been estimated for several star-forming regions, for example Taurus (Andrews et al. 2013), Lupus (Ansdell et al. 2016), Upper Scorpius (Barenfeld et al. 2016), Chameleon I (Pascucci et al. 2016), σ Orionis (Ansdell et al. 2017), Ophiuchus (Cieza et al. 2019), Corona Australis (Cazzoletti et al. 2019), Perseus (Tychoniec et al. 2020, 2018), Chameleon II (Villenave et al. 2021), Orion (Tobin et al. 2020; van Terwisga et al. 2022) as well as some open clusters, e.g. the Orion Nebula Cluster (Eisner et al. 2018) and IC 348 (Ruíz-Rodríguez et al. 2018). However an open question remains: how accurately do we

measure the dust and gas mass budget of disks? If the answer is that we do have accurate measurements and we assume that Class II discs are the natal environments of forming planets, then a mass budget problem arises because the estimated disc masses are much lower than the estimated planetary system masses of the observed exoplanets (Greaves & Rice 2010; Mulders et al. 2015, 2018; Najita & Kenyon 2014), potentially implying that there is not enough material to form planets.

The dust mass estimations in studies, such as the ones mentioned above, follow a flux-to-mass conversion initially proposed by Hildebrand (1983), which is, therefore, based on modeling and several assumptions. Among others, universal and constant (average) opacity and temperature, optically thin emission, unknown chemical abundances or grain structure, and uncertain stellar ages are used, which would generally lead to underestimated masses. In addition, it is assumed that most of the solid mass is still in mm-sized grains. Alternative ways to measure the dust mass have been explored, for example through the dust lines (Franceschi et al. 2022; Powell et al. 2019, 2017) but these still have some limitations and lead to overestimated masses. For a more thorough analysis of the dust observations and the limitations see the relevant Protostars and Planets VII chapters (Manara et al. 2022; Miotello et al. 2022). Regardless of the caveats, we can relatively safely assume that we observe a mass loss analogous to the disc evolutionary stage.

After the dust mass has been obtained, the conversion to total disc mass (gas+dust) is usually done considering an interstellar medium-like or solar-like dust-to-gas ratio of 1% to 1.5%. However, it has not been widely explored whether this is always the case for protoplanetary discs. A better constraint on disc masses could come from directly obtaining gas masses, given that the main component of a protoplanetary disc is gas, with molecular hydrogen (H_2) being the most abundant species. The emission of H_2, though, is faint at cold temperatures (Field et al. 1966) and can only be traced (if at all) at the innermost hot disc regions which do not represent the bulk disc mass (e.g. Pascucci et al. 2013). Other gas mass tracers could be the isotopologue of H_2, hydrogen deuteride (HD), or carbon monoxide (CO) and its isotopologues (e.g. Schwarz et al. 2016; Zhang et al. 2017). However, these species are not always a good tracer of the disc gas bulk mass and/or are not easy to measure for various reasons Miotello et al. (see 2022, for more details). Yoshida et al. (2022) presented a novel method for measuring the midplane gas surface density using ALMA archival data of TW Hya. They detected broad line wings in the shape of the CO lines and attributed them to pressure broadening, thus deriving the gas surface density profile in the inner region of the disk. Such alternative methods might be explored more in future studies and shed more light to the disc masses.

Most of the disc mass estimations to date, come mainly from the flux-to-mass conversion from dust observations or secondarily from the molecular lines of gas tracers we discussed above. Recently, there has been increasing work contemplating whether the limitations of the dust mass estimates could lead to significantly underestimated masses (Ballering & Eisner 2019; Bergez-Casalou et al. 2022; Galván-Madrid et al. 2018; Zhu et al. 2019). Manara et al. (2018) suggest that another possible way out of this problem could be early planet formation so that it is already ongoing in observations of early protoplanetary disc evolutionary stages (before 3 Myr).

There is increasing evidence that this is the case, for instance, Harsono et al. (2018) reported dust growth to millimeters for a very young disc (around 0.1 Myr) around a solar-type prototar, while Segura-Cox et al. (2020); Sheehan & Eisner (2018), and Cieza et al. (2021) find disc substructures already in very young discs and the latter suggest that this is not necessarily expected by the formation of the disc. Such observed substructures in discs (e.g. gaps or rings) can be theoretically expected outcomes of the formation processes for planets with high enough masses. There are, also, meteoritic analyses confirming that some of the solar system building blocks have formed within 1 Myr (Kruijer et al. 2017; Wadhwa et al. 2020). These observations all point to dust growth being very efficient even while the disc itself still forms and would, thus, allow for early planet formation. This possibility is also supported, from a theoretical point of view, by the pebble accretion scenario, as it can provide high pebble accretion rates at the earliest stages of evolution (Johansen et al. 2019; Tanaka & Tsukamoto 2019).

In our previous work (Savvidou & Bitsch 2022, Chapter 5), we performed numerical simulations of planet formation via pebble and gas accretion, including migration, in a viscously evolving protoplanetary disc, investigating how the disc conditions influence the resulting planetary masses. We focused on which conditions are the most favorable for giant planet formation and in this work, we utilize the same set of simulations and discuss how the dust evolves after a planet has formed, focusing again on the implications of a giant planet.

6.2 Methods

6.2.1 Model and parameters used

The model was described in detail in Sect. 5.2 of the previous chapter. Briefly, the numerical simulations of planet formation in a protoplanetary disc include pebble growth and drift (Birnstiel et al. 2012a), pebble evaporation and condensation at ice lines (Schneider & Bitsch 2021), planet growth via pebble (Johansen & Lambrechts 2017a) and gas accretion (Ndugu et al. 2021) as well as planet migration (Paardekooper et al. 2011a). The initial planetary mass for the embryos is set by the pebble transition mass, at which the planet starts efficient accretion from the Hill regime (Lambrechts & Johansen 2012a).

The standard set of parameters that we use to discuss example cases, in this work, is presented in Table 6.1. As a reminder, each simulation contains one growing planet. We also present here the dust mass evolution of our whole sample. For these, we have done a parameter study where the α-viscosity parameter ranges from 0.0001 to 0.001, the initial disc mass ranges from 0.01 to 0.1 $M_\odot$, the initial disc radius ranges from 50 to 200 AU, the dust fragmentation velocity ranges from 1 to 10 m/s and the planetary embryos are placed in the disc from 1 to 50 AU, with starting times from 0.1 to 1.3 Myr. The parameters and the study results were discussed in detail in Sect. 5.2.

standard set of parameters		
M_0	0.1 $M_\odot$	initial disc mass
R_0	200 $R_\odot$	initial disc radius
α	0.0001	α-viscosity parameter
t_0	0.1 Myr	starting time of embryo
$\alpha_{p,0}$	1, 3, 10, 30 AU	initial position of embryo
u_{frag}	10 m/s	fragmentation velocity

Table 6.1. Standard set of parameters used in the simulations.

6.2.2 Optically thin dust mass estimates

The continuum flux of the dust emission obtained from observations is converted to a dust mass via the Hildebrand (1983) approximation

$$F_\nu = \frac{B_\nu(\overline{T_d})\overline{\kappa_d}}{d^2} M_d \ . \tag{6.1}$$

In the above, it is assumed that the emission is optically thin and described well by an average temperature $\overline{T_d}$ and an average opacity $\overline{\kappa_d}$ (Andrews & Williams 2005). In the Rayleigh-Jeans approximation, which is relevant for low frequencies, the Planck spectrum (Eq. 2.24) is written

$$B_\nu(T) = \frac{2\nu^2 k_B T}{c^2} \ , \tag{6.2}$$

therefore Eq. 2.28 writes as

$$I_\lambda = \frac{2ck_B\overline{T_d}}{\lambda^4}\tau_\lambda = \frac{2ck_B\overline{T_d}}{\lambda^4}\overline{\kappa_d}\Sigma_{d,\tau_\lambda<1} \ . \tag{6.3}$$

The surface density $\Sigma_{d,\tau_\nu<1}$ corresponds to the disc regions, in our models, where $\tau<1$.

Then the corresponding flux, assuming that the discs are face-on, is

$$F_\nu = \frac{1}{d^2}\int_{r_0}^{R_{disc}} 2\pi r I_\nu(r) dr \tag{6.4}$$

(see also Sect.2.3). We use the flux-to-mass approximation of Eq. 6.1 to calculate the disc dust masses from our models with the same assumptions as in the observed sources and we adopt some standard assumptions κ_d=2.3 cm^2/g, T_d=20 K and d=140 pc.

6.3 Dust mass evolution after the gas giant formation

In Fig. 6.1, I show the time evolution of the dust mass for the same simulations as in Fig. 5.1, along with the one for a simulation without a planet. The embryos

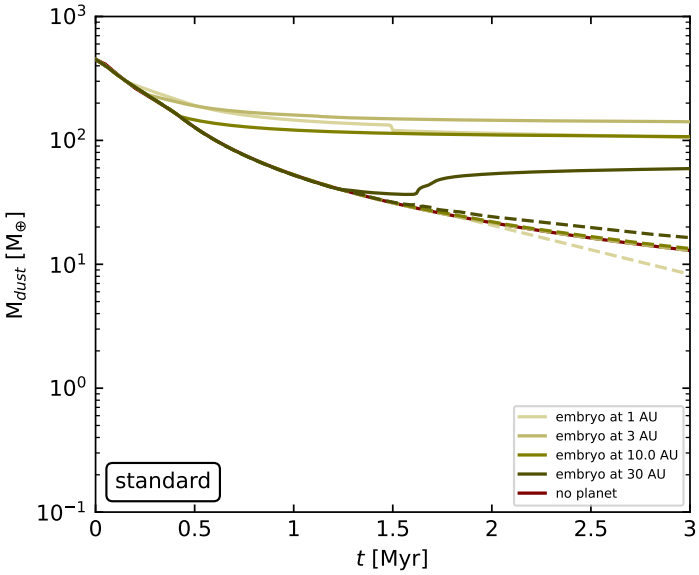

Figure 6.1. Dust mass as a function of time for the same planets as in Fig. 5.1, using the standard set of parameters (Table 6.1). The dashed lines show the time evolution of the optically thin dust mass and the red line is the dust mass time evolution for a simulation without a planet.

originate from 1, 3, 10 and 30 AU (solid lines, green colors). We also estimate the dust mass according to Eq. 6.1, using the surface density in the optically thin regions only in Eq. 6.3.

Without any planet growing (red, solid line), the dust is decreasing as it drifts inwards and gets evaporated at the icelines or lost by stellar accretion. The total dust mass evolution in our models where planets are growing is heavily dependent on the growth evolution of the planet. As I show in Fig. 5.1, the embryos originating at 1, 3 and 10 AU quickly (within 0.5 Myr) reach the pebble isolation mass and start effectively blocking the drifting dust exterior to their orbit. Therefore, the dust content in these discs almost plateaus beyond 0.5 Myr. The amount of dust blocked depends on several things, such as the location of the embryo and how long it took until the planet reached the pebble isolation mass and trapped the dust. For example, the planet originating at 10 AU reaches the pebble isolation mass earlier and there is more dust mass exterior to each orbit compared to the one originating at 30 AU, therefore it keeps more dust trapped.

We notice that in the disc with the planet originating at 30 AU, the dust mass is increasing shortly after 1.5 Myr. Initially the pebbles drift inwards and evaporate, thus the dust mass goes down. Then the planet starts growing and opens a gap, however, the position of the gap is such that the pressure bump generated by the gap is close to an evaporation front and material is pushed outwards with a large amount of volatiles. These diffuse over the evaporation front again, they recondense and thus increase the dust mass.

The optically thin dust mass for all of the models (dashed lines, green colors) evolves similarly to the dust mass in a disc without a planet, regardless of the initial location of the embryo, its orbital evolution and its final mass. This means that the difference between the total dust mass and the optically thin dust mass is almost one order of magnitude.

In Fig. 6.2, we only change one parameter at a time similarly to Fig. 5.2. In Chapter 5, we show that no giant planet forms when the initial disc mass is lower (left, top plot), due to the lack of enough solid material to build a massive core or

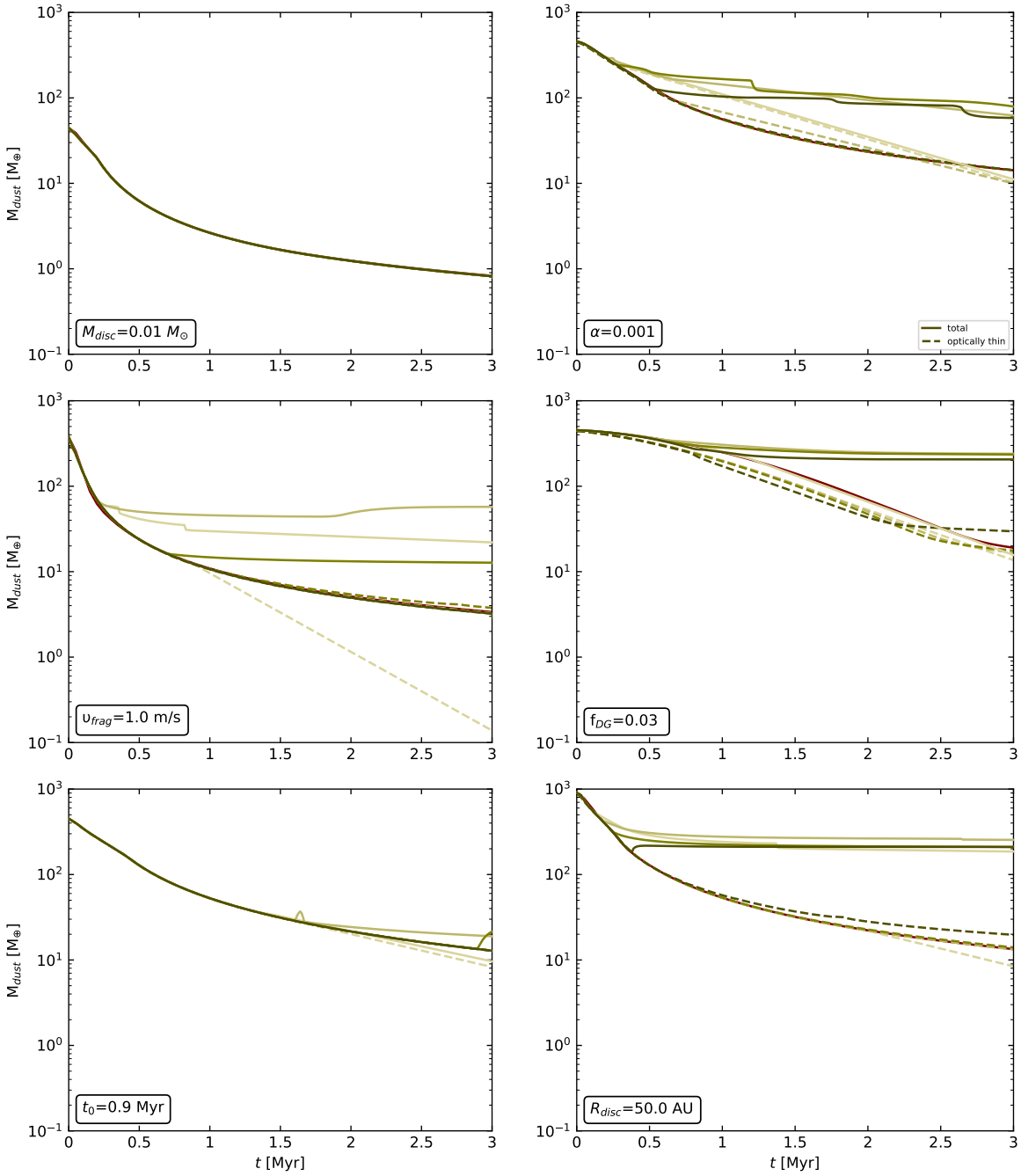

Figure 6.2. Same as Fig. 6.1 with the same planets as in Fig. 5.2.

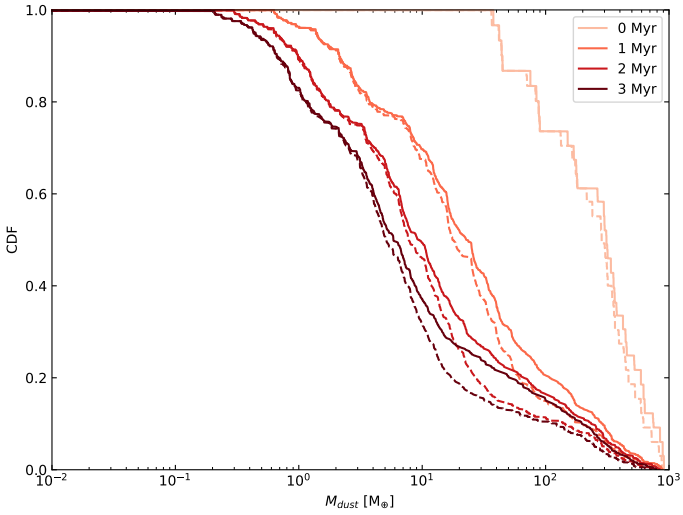

Figure 6.3. Cumulative distribution functions for the disc dust mass of our models at different times (0-3 Myr). The dashed lines correspond to the dust mass excluding the optically thick regions of each disc.

when the embryo is injected too late (left, bottom plot). Without a giant planet to block the dust, it quickly drifts and decreases, even within the first 0.5 Myr. The evolution is, hence, the same under the optically thin assumption and for the model without a planet. The same is true for the planet originating at 30 AU in the disc with R_{disc} = 50 AU that did not reach the pebble isolation mass in time.

In general, as the planet moves, it carries the pressure bump with it (and thus the pebbles). Once it crosses an evaporation front, pebbles evaporate and there is a "jump" (decrease) in the total dust mass, as we see in Fig. 6.1, for the disc with a planet originating at 1 AU. These "jumps" are proportional to the amount of material that evaporates, so larger "jumps" are expected if the planet crosses evaporation fronts corresponding to more abundant species. For example, the "jumps" are larger for α=0.001, because the planets migrate faster in that case and cross multiple evaporation fronts[1].

We generalize, now, our results to our whole sample of 76800 runs (all possible combinations of the first six parameters in Table 5.1 and two different values of the dust-to-gas ratio) and present the CDFs of the dust mass at different times, from the beginning of the simulations, until 3 Myr (near the end of the lifetime of the disc), every 1 Myr. We find that the difference between the total dust mass (solid lines) and the optically thin dust mass (dashed lines) increases in time. If there is nothing to prevent radial drift, the dust decreases in time and this is reflected in the optically thin dust mass estimates. As we show in Figs. 6.1 and 6.2, the time evolution of the optically thin dust mass closely resembles that of the models without any planet.

The time evolution from our models, resembles the time evolution that we find from observations. A direct comparison with the observed dust mass estimates is not trivial (see for example Fig. 2 in Drążkowska et al. 2022), however we note that CDF at the end of our simulations resembles closely the ones for Class II discs. In other words, the most similar CDF to the observed Class II discs is the one in our models, where planet formation has already happened, especially accounting for

[1]The straight lines are caused by a lack in available timestamps when the planet reaches the inner edge. We, then, only get the output fromt the final timestamp.

the optically thin dust mass estimates of our models. Additionally, we also show a mass loss in time, similarly to the CDFs of observed discs in ascending evolutionary stages.

Regardless of the comparison to the observations, we want to point out that the optically thin dust emission assumption for ALMA observations could be leading to an underestimation of the dust mass estimates. The trapped dust due to a giant planet induced pressure bump could be unresolved and thus not accounted for accurately. This also highly depends on the location of the giant planet, given that the inner regions are, generally, harder to resolve.

6.4 The mass budget problem

The burst of millimeter disc surveys, in several star-forming regions, the last decade, has led to extensive total mass estimations which appear to be not high enough to explain planet formation, especially without 100% efficiency in the formation mechanisms (Greaves & Rice 2010; Manara et al. 2018; Najita & Kenyon 2014). Several solutions to this hypothetical problem have been discussed but two categories seem to be the most plausible. One one hand, there could be an underestimation of the masses caused by the assumptions in the flux-to-mass conversion or contributions from optically thick regions. On the other hand, Class II discs could contain mainly the leftovers from planet formation if it starts much earlier than previously assumed.

I will begin the discussion with the first point, regarding the underestimation of the disc masses. First and foremost, the flux-to-mass conversion (Eq. 6.1) relies by default on a mostly optically thin emission for the dust at (sub-)millimeter wavelengths (also when assuming that the Rayleigh-Jeans aproximation is valid). Zhu et al. (2019) suggested that the observed discs could be optically thick if dust scattering is considered but this mainly applies to ALMA observations interior to 40-50 AU. Similarly, optically thick emission, perhaps concentrated in smaller regions, such as the observed rings, has been evoked to explain the disc size-luminosity relation Andrews et al. (2018); Tripathi et al. (2017). Alternatively, Andrews et al. (2018) suggest that the optical depths profile shapes could be independent of the disc properties. The rings in the discs of the DSHARP survey have been found to all have optical depths around 0.2-0.5 but they could be higher if scattering is included or if they contain unresolved optically thick clumps (Dullemond et al. 2018).

Tychoniec et al. (2020) estimate the disc masses in the Perseus star-forming region using ALMA (1.1-1.3 mm) and VLA (9 mm) and compare it with the dust masses in other regions. They mention that the ALMA observations could be probing optically thick emission, especially at the inner parts of the discs. At the same time, their estimated disc dust mass medians with the VLA for Class 0 and I discs are higher compared to the estimates from the ALMA observations. However, this is not the case for the Class II discs of their sample. This could be pointing towards an early formation of planets but I will discuss this possibility more in the next paragraphs. In a very recent study, Xin et al. (2023), perform SED modeling to constrain the disc dust masses in Lupus and find $\sim$1.5-6 times higher mass estimates compared to the ones estimated via Hildebrand (1983). Additionally, their

work suggests that the observed discs could be optically thick up to $\sim$ 3mm.

Even if the millimeter emission can be reliably assumed to be optically thin, the terms that go into Eq. 6.1 all have great uncertainties. For example, the standard temperature assumption is that T=20 K but this was estimated by fitting the SEDs of extended discs (100 AU in radius) (Andrews & Williams 2005a) and may not be appropriate for more compact sources. In LkHα 330, Pinilla et al. (2022) find that if the outer disc is as cold as the interstellar medium, then the estimated optical depth of observed discs could be well above unity.

Opacity itself is a rather complicated subject which is oversimplified when assuming one constant value is appropriate regardless of the disc or even population (related to the specific star forming region) properties or the evolutionary stage of the disc. To account for this, studies sometimes use the a frequency dependent opacity coefficient Andrews et al. (2013); Beckwith et al. (1990), however in most cases a constant value is used, even regardless of the evolutionary stage (Class) of the disc.

Even if we leave the flux-to-mass conversion aside, we still need to make an educated guess about the dust-to-gas ratio to convert the dust masses into total disc masses. As expected and as we show in the present work and the previous (Chapter 5), the initial dust-to-gas ratio is directly linked to the amount of dust that will remain in the disc after it evolves (with or without planet formation). Several studies find a dust-to-gas ratio, higher than 1% (e.g. Kama et al. 2020, where the gas mass is also constrained). Appelgren et al. (2020) also find this in simulations, after 1 Myr for dust with sizes or 100 μm and after 0.35 Myr for sizes of 1 mm. Especially in regions with significant dust trapping, it is unreasonable to assume that any initial dust-to-gas ratio will remain relevant. In Pinilla et al. (2022), they compare the mass estimate of LkHα 330 using a dust-to-gas ratio of 0.01 to the value they obtain from a hydrodynamical simulation (around 0.2 at the peak of the concentrated mass) and they find a difference of one order of magnitude.

Besides all the above, other factors could also play a role. For example, there might be influence by discs in stellar clusters, they could be affected by fly-bys, mergers, etc., which will strip away mass from discs, therefore fewer giants may form in comparison to discs in "quieter" star-forming regions and change the structure and evolution of the dust. In addition to that, Liu et al. (2022) perform radiative transfer models to study how much the estimated dust mass could be underestimated under the assumptions discussed above (in relation to the use of (Hildebrand 1983)) and suggest that uncertainties in the disc radius can lead to a significant underestimation of the dust masses.

The other possible explanation of the discrepancy between the masses of the observed exoplanets and the observed protoplanetary discs could be that planet formation starts in Class 0/I discs, in which the estimated mass seems to be sufficient (e.g. Tychoniec et al. 2018). The observed decrease in the masses of the Class II discs in different star forming regions suggests that the initial solid content is lost due to radial drift (e.g. evaporates at the icelines, gets accreted by the star or is contained into some inner optically thick region), transformed into larger bodies or gets trapped in pressure bumps that could lead to optically thick substructures that are not necessarily accounted for in the dust mass estimations (see discussions in

Manara et al. 2022; Miotello et al. 2022).

The observed substructures even in young disks (Class I) could be another indication of the early planet formation, however it is still debatable how common substructures are in an unbiased sample, given that they are mainly observed in massive discs and could thus be related to the disc mass (see Bae et al. 2022; Drążkowska et al. 2022, for related discussions). However, they are also found in almost all observed sources at high resolution, therefore their lack in smaller discs might imply that they are not sufficiently resolved. For example, a new framework (`FRANK`) has been developed that identifies previously not found substructure in the inner discs of the DSHARP survey (Jennings et al. 2022). More analysis is, thus, needed to resolve this debate.

Even if substructures are indeed more commonly found in massive discs, we find in our previous work (Chapter 5) that a higher disc mass leads to more giant planets and these could in turn be responsible for at least some of substructures observed in discs and consequently trap a part of the dust that is then not accounted for in the disc dust mass estimates. Or as shown in Jennings et al. (2022), the information might be lost if another deconvolution technique is used (`CLEAN`) (Clark 1980; Cornwell 2008; Högbom 1974).

Analyzing a sample study of protoplanetary disc observations, van der Marel & Mulders (2021) suggest that structure is an evolutionary signature, pointing to early giant planet formation that creates dust traps and/or observable features. As structured they consider transition, ringed or extended discs, arguing that dust at large radii could only remain for long if there are pressure bumps to reduce radial drift. The structures are found in massive discs but, importantly, they remain massive even at older ages. By comparing the frequency of these discs and the occurrence rates of giant planets, they conclude that giants could be the creators of pressure bumps that give structure to the discs.

This is consistent with our findings from the present study. Giant planets cut off the pebble flow when they reach pebble isolation mass (Johansen & Lambrechts 2017a) by creating a pressure bump that traps dust exterior to their orbits and keeps the dust mass higher, even at later times (Figs. 6.1 & 6.2). At the same time, we also find that planets with masses lower than Neptune are formed later and no substructure is expected in their natal discs (see the first panel in the third row of Fig. 5.5 and Fig. 6.2, along with Fig. 5.2). Outer disc rings shown in e.g. ALMA data (e.g. 50AU) could be giants blocking the rest of the material and in general, highly structured discs could indicate giant planet formation in contrast to relatively uniform and compact discs.

In a recent study, Bergez-Casalou et al. (2022) coupled hydrodynamic disc simulations with dust evolution and produced synthetic observations at $\lambda = 1.3mm$. They found that the total mass is underestimated by even more than two orders of magnitude using the synthetic observations or the optically thin region, similarly to our approach here.

We should aim at multiwavelength observations (longer wavelengths with VLA or SKA) whenever possible, given that dust emission at longer wavelengths is more probable to be optically thin, and potentially combine them to acquire more accurate dust mass estimates. At the same time, we should consider whether the current

algorithms used sufficiently resolve the sources and whether some information could still be elusive, especially at the inner regions of discs or in less massive sources. We find here that the existence of a giant planet in the disc leads to sufficient trapping of the dust exterior to its orbit that then is not accounted for under the optically thin emission assumption. It is, therefore, also important to constrain the occurence rates of giant planets well, especially at the inner disc radii, which will be harder to directly resolve within the natal protoplanetary discs.

Additionally, the CDF from our models at 3 Myr resembles the ones estimated for the observed Class II discs but planet formation has already happened in our simulations. Even if we observe low dust masses in discs with ages of several Myr, there are high chances that the planet is already there. Therefore, regardless of whether the flux-to-mass conversion offers good estimates, there is still no mass budget problem because the planets are already formed.

6.5 Summary

We utilize the sets of simulations presented in Chapter 5 and show how the dust mass evolves after a planet has formed. We compare the dust mass evolution for planets with varying migration and growth histories to the corresponding dust evolution of these systems under the commonly used optically thin emission assumptions and the average, constant values used in Hildebrand (1983) flux-to-mass conversion relation. We show that the optically thin dust time evolution resembles the one of a disc with the same initial properties but without any forming planet.

Additionally, we compute the CDFs of the dust masses of our whole sample at different evolutionary stages (0, 1, 2 and 3 Myr near the end of the lifetime of the disc) to generalize the difference between the total disc dust mass and the optically thin dust mass. We find that the CDF at end of the planet formation processes resembles closely the observed CDFs of Class II discs and earlier times of our models (when planet formation begins) resemble more the slopes and masses of the CDFs of Class 0 and Class I sources, however a direct comparison is non-trivial.

We show that, as expected, solids are either quickly lost or blocked by the forming giant planets and we also offer the idea that the absence of a giant planet in a planetary system could reinforce the rapid drift of dust. This means that more evolved disks with higher dust masses could have increased possibilities to host a giant planet and inversely. We support the idea that the observed substructures and ringed morphologies of discs could be caused by massive planets which clear the gas around them and trap the dust outside their orbits.

However, the optically thin assumptions (along with constant dust-to-gas ratios) which are used in dust mass estimates for the observed discs might significantly underestimate their total masses. At the same time, in our pre-

vious work, we showed that early planet formation is crucial for giant planet formation and in combination with the CDFs of the dust mass in our models from the present work, we also support the hypothesis that planet formation starts before the Class II phase of the protoplanetary discs. We conclude that the mass budget problem hypothesis is not an issue and it is not necessary to have 100% efficiency for planet formation.

7

Summary and outlook

The goal of this thesis is to study how the dust influences the thermal structure of protoplanetary discs and what the implications for planet formation via pebble accretion, in particular super-Earths and giant planets are.

- ⋆ As a first step, in Chapter 3, we investigate through hydrodynamical simulations, coupled with two different grain size distributions, how the dust grains and their corresponding opacities influence the thermal structure of the disc. Our simulations show that especially in discs with significant viscous heating, the often-used opacity models, based on micrometer sized dust grains only, are not a good approximation to model the structure of protoplanetary discs.

- ⋆ In Chapter 4, we focus on the inner disc and a simple grain size distribution and study how the thermal structure of the disc influences the pebble isolation mass and how long it takes for forming planets to reach it. We find that there is a trade-off between the pebble isolation mass and the planetary growth timescale and discuss the growth of super-Earths via pebble accretion and the most appropriate disc properties (viscosity, fragmentation velocity and surface density) to explain the observed super-Earths.

- ⋆ In the third study of Chapter 5, we use numerical simulations of planet formation via pebble and gas accretion, including migration, in a viscously evolving protoplanetary disc, to examine which are the most favorable conditions for the growth of giant planets. While we find that the most favorable ones are high disc mass, early formation, and a large enough disc, we conclude that their formation is mainly the outcome of a combination of beneficial factors or lack of adverse ones.

- ⋆ In the final work presented in Chapter 6, we utilize the same simulations

as Chapter 5 and explore how the disc dust mass evolves while a (giant) planet grows in the disc. We compare this dust mass evolution in time with simulations where no planet is growing and use a flux-to-mass conversion to estimate the dust mass under the assumption of an optically thin emission. Our findings strengthen the hypothesis that planet formation has already happened or is ongoing in Class II discs. However, we also show that the optically thin dust mass significantly underestimates the total dust mass in the presence of a giant planet that traps the dust exterior to its orbit.

If one wants to conclude one thing, it is that the field of planet formation is a very fruitful one, with plenty more work to be done and knowledge to be gained. Several observational results have established interesting patterns in the exoplanet demographics or features in the protoplanetary discs, sometimes even unexpected ones. There are several things, in regards to our models, which can be improved or explored in the future.

For example, we can use the observed disc population properties as the initial conditions in our models from Chapters 5 and 6, along with the CDFs in different star-forming regions to constrain the appropriate fractions of the various initial properties and study the population of exoplanets that will be produced. Even though, as I mention in Chapter 1, the observed discs and exoplanets are likely two distinct populations, it would, nonetheless, be an interesting result and comparison.

We assume in all of our projects that the star is of solar mass and the disc is a Class II disc. However, it is important to explore both of these initial conditions if one wants to produce as general models as possible or compare with the observed (disc or exoplanet) populations. The stellar mass-disc mass relation is non-trivial. Andrews et al. (2013) find that the disc mass is increasing for increasing stellar masses, however Pascucci et al. (2016) suggest a steeper than linear relation (for the discs in the Chamaeleon I star-forming region and similar for the young regions of Taurus and Lupus). Pinilla (2022) summarize this for multiple regions and adds the relation for discs with substructures around brown dwarfs and very low mass stars, showing that the relation steepens in time. Such studies, open up the road for more work on planet formation around different types of stars.

There is emerging evidence (discussed in extend in this thesis) that planet formation starts in earlier stages than previously assumed in the classical star and planet formation theory. This can have important implications for our models, given that the initial conditions related to Class II discs might not be appropriate to paint a realistic picture. Nevertheless, a lot more work needs to be done to understand how dust grain grow and evolve in protostellar systems still embedded in their envelopes.

A significant direction which was not explored in this thesis concerns the chemical composition of protoplanetary discs and the composition of planets. The recent ALMA large program MAPS (Molecules with ALMA at Planet-Forming Scales, Öberg et al. 2021) explored the molecular gas lines of five discs showing substructures with the aims, among others, to study how the dust and chemical substructures are linked and what are the C/N/O/S ratios, the metallicity (O/H, C/H) and deu-

terium fractionation at planet-forming regions. The atmospheric characterization of exoplanets has been an uprising field in the recent years and more results are expected with the JWST observations. It is, thus, of crucial importance to use the information from such studies about the chemical composition or the elemental ratios in discs and exoplanets as constraints in our theoretical models.

The diversity of the exoplanet systems is the product of the intrinsic diversity of the protoplanetary discs and it is, hence, essential to take advantage of the increasing number and quality of observations to constrain the disc population properties and improve our understanding of their thermal and chemical structure. This way we can create more realistic theoretical disc models and, consequently, improve our planet formation models. These projects were, hopefully, the first steps in this direction in general and specifically for me as a reseacher...

A

Additional material to Chapter 3

A.1 Dust surface densities for different α-viscosity values

We present here the vertically integrated dust surface densities and the opacities for the simulations using the rest of the α values and the two grain size distributions. The maximum grain sizes of the BOD and MRN discs are approximately the same because they follow the same fragmentation barrier formula (Eq. 3.14). The vertically integrated dust surface densities are around one order of magnitude **lower** in the discs with the BOD grain size distribution compared to the discs with the MRN distribution for small particles (Fig. A.1). On the other hand, they are always comparable for the largest particles in the discs. This is already evident by the shape of the two grain size distributions (Fig. 3.3).

As α decreases, the surface densities of the smallest particles in the discs with the BOD distribution are several orders of magnitude lower than these of the largest particles. The gradients are smoother in the discs with the MRN distribution as α decreases. The fragmentation barrier depends on the initial gas surface density so when the latter decreases, the maximum grain size gets smaller (Eq. 3.14).

In Fig. A.2 we show the opacities as a function of orbital distance and height for a selection of the simulated discs for this work. The τ=1 line is located at similar heights in all of the discs with high α-viscosity (around 2 AU at the outer edge). The same applies to the low α-viscosity discs where the τ=1 line is always around 0.15 AU at the outer edge. As expected the optically thick region is extended towards higher altitudes with a higher total dust-to-gas ratio and contained near the midplane for low gas surface densities. Above the τ=1 line opacity always decreases as cooling is more efficient. However, the uppermost layers show increased opacities because of the stellar irradiation that directly heats them up.

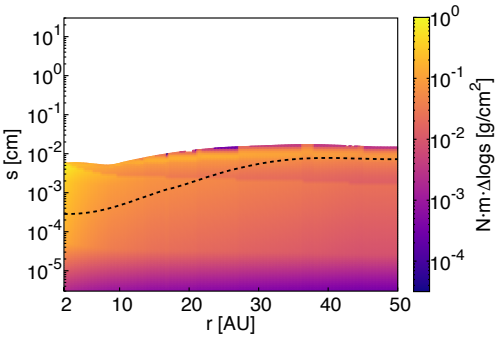

(a) BOD, $\alpha = 10^{-2}$, $\Sigma_{g,0} = 1000\ g/cm^2$, $f_{DG} = 1\%$

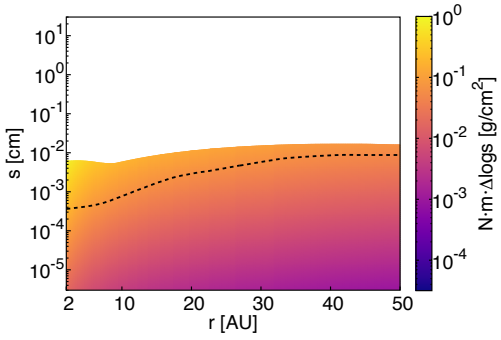

(b) MRN, $\alpha = 10^{-2}$, $\Sigma_{g,0} = 1000\ g/cm^2$, $f_{DG} = 1\%$

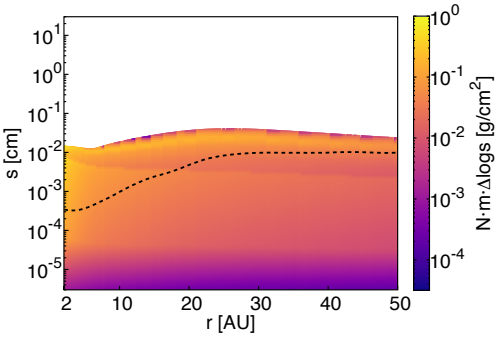

(c) BOD, $\alpha = 5 \times 10^{-3}$, $\Sigma_{g,0} = 1000\ g/cm^2$, $f_{DG} = 1\%$

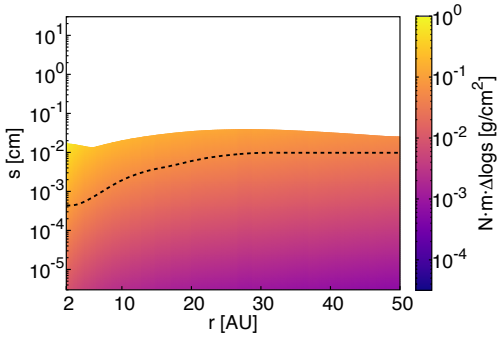

(d) MRN, $\alpha = 5 \times 10^{-3}$, $\Sigma_{g,0} = 1000 g/cm^2$, $f_{DG} = 1\%$

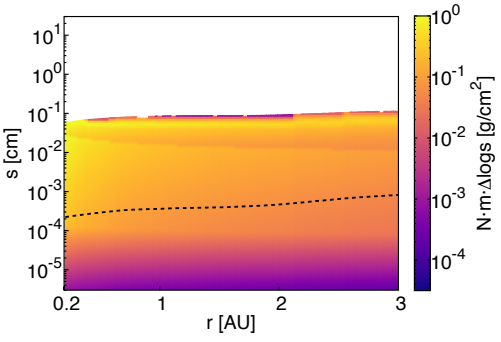

(e) BOD, $\alpha = 10^{-3}$, $\Sigma_{g,0} = 1000\ g/cm^2$, $f_{DG} = 1\%$

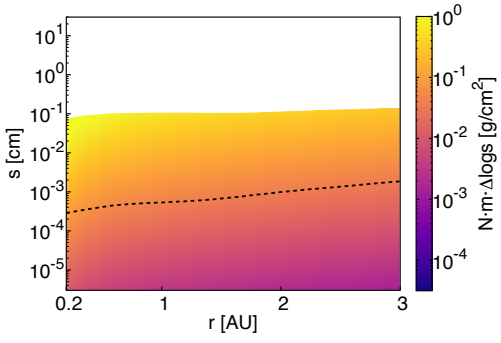

(f) MRN, $\alpha = 10^{-3}$, $\Sigma_{g,0} = 1000\ g/cm^2$, $f_{DG} = 1\%$

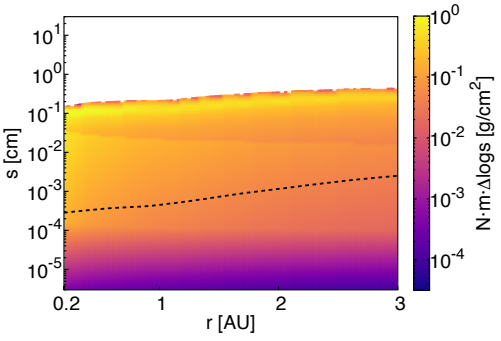

(g) BOD, $\alpha = 5 \times 10^{-4}$, $\Sigma_{g,0} = 1000\ g/cm^2$, $f_{DG} = 1\%$

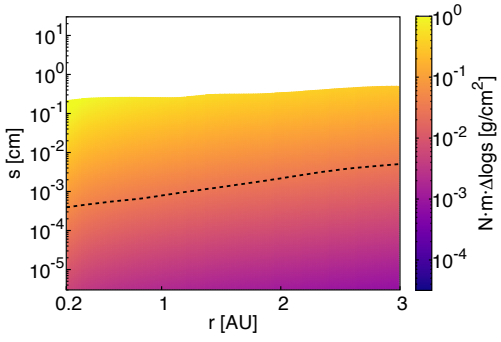

(h) MRN, $\alpha = 5 \times 10^{-4}$, $\Sigma_{g,0} = 1000\ g/cm^2$, $f_{DG} = 1\%$

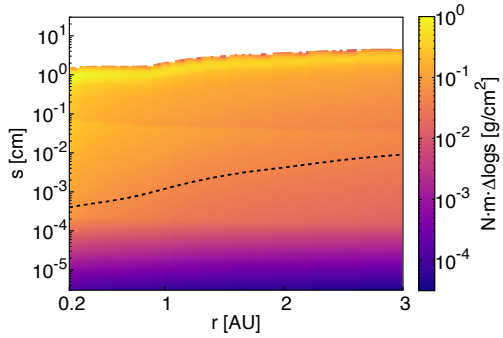

(i) BOD, $\alpha = 10^{-4}$, $\Sigma_{g,0} = 1000\ g/cm^2$, $f_{DG} = 1\%$

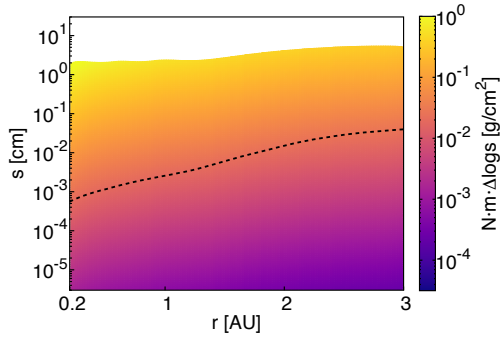

(j) MRN, $\alpha = 10^{-4}$, $\Sigma_{g,0} = 1000\ g/cm^2$, $f_{DG} = 1\%$

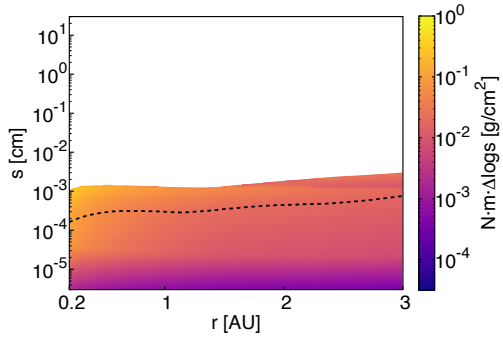

(k) BOD, $\alpha = 1 \times 10^{-2}$, $\Sigma_{g,0} = 100\ g/cm^2$, $f_{DG} = 1\%$

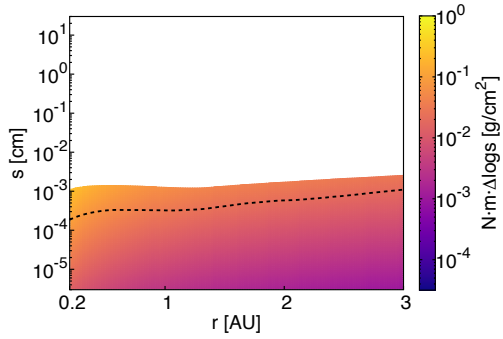

(l) MRN, $\alpha = 1 \times 10^{-2}$, $\Sigma_{g,0} = 100\ g/cm^2$, $f_{DG} = 1\%$

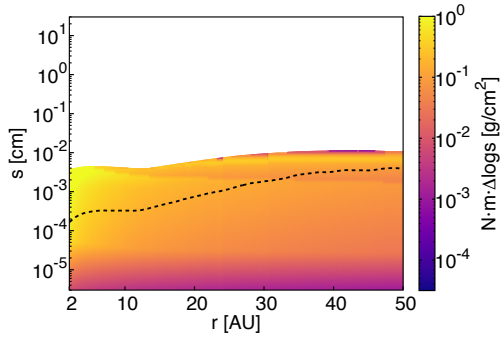

(m) BOD, $\alpha = 1 \times 10^{-2}$, $\Sigma_{g,0} = 1000\ g/cm^2$, $f_{DG} = 3\%$

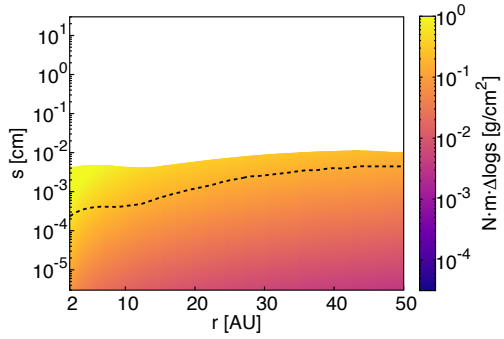

(n) MRN, $\alpha = 1 \times 10^{-2}$, $\Sigma_{g,0} = 1000\ g/cm^2$, $f_{DG} = 3\%$

Figure A.1. Dust surface densities as a function of orbital distance and grain size for the different α values used here, and for additional simulations with the lowest gas surface densities and with the highest dust-to-gas ratio that we have tried. The dashed lines divide the grain sizes into two groups which contribute equally to the total opacity of the disc (see Figs. 3.8 and 3.10).

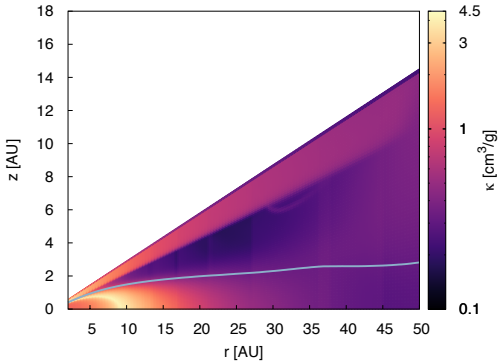

(a) BOD, $\alpha = 10^{-2}$, $\Sigma_{g,0} = 1000\ g/cm^2$, $f_{DG} = 1\%$

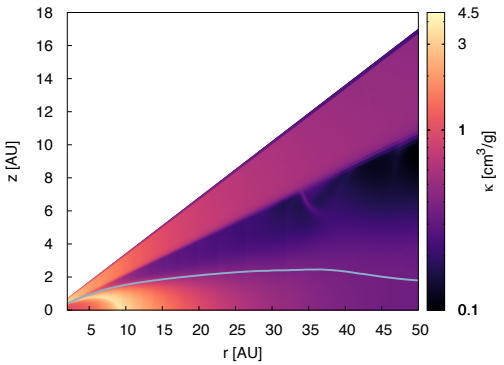

(b) MRN, $\alpha = 10^{-2}$, $\Sigma_{g,0} = 1000\ g/cm^2$, $f_{DG} = 1\%$

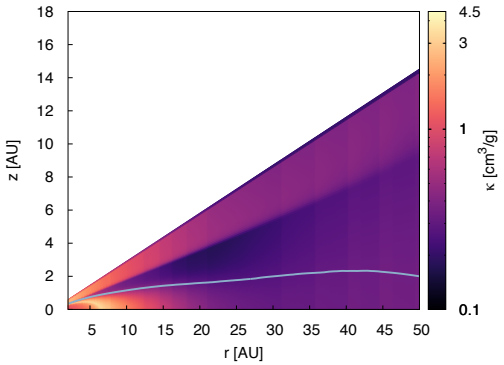

(c) BOD, $\alpha = 5 \times 10^{-3}$, $\Sigma_{g,0} = 1000\ g/cm^2$, $f_{DG} = 1\%$

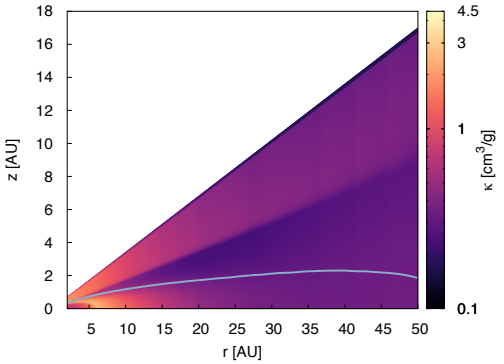

(d) MRN, $\alpha = 5 \times 10^{-3}$, $\Sigma_{g,0} = 1000\ g/cm^2$, $f_{DG} = 1\%$

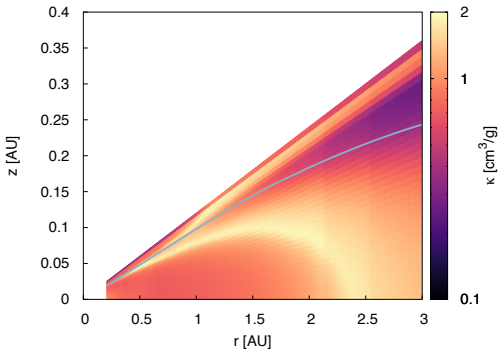

(e) BOD, $\alpha = 10^{-3}$, $\Sigma_{g,0} = 1000\ g/cm^2$, $f_{DG} = 1\%$

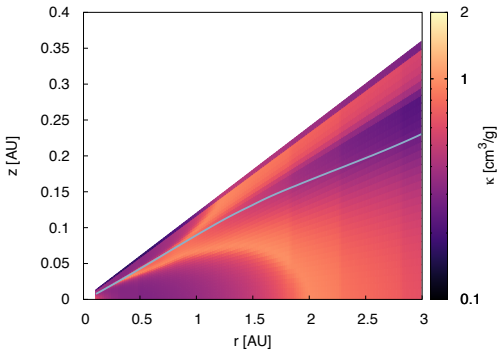

(f) MRN, $\alpha = 10^{-3}$, $\Sigma_{g,0} = 1000\ g/cm^2$, $f_{DG} = 1\%$

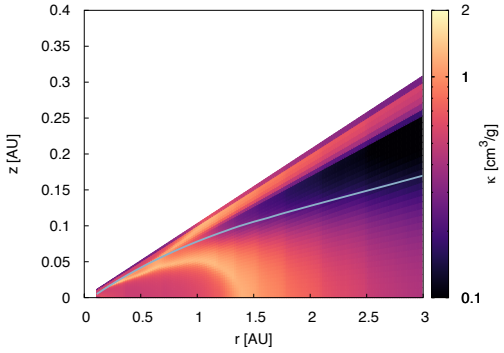

(g) BOD, $\alpha = 5 \times 10^{-4}$, $\Sigma_{g,0} = 1000\ g/cm^2$, $f_{DG} = 1\%$

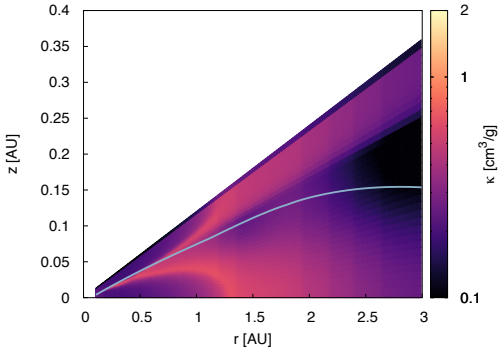

(h) MRN, $\alpha = 5 \times 10^{-4}$, $\Sigma_{g,0} = 1000\ g/cm^2$, $f_{DG} = 1\%$

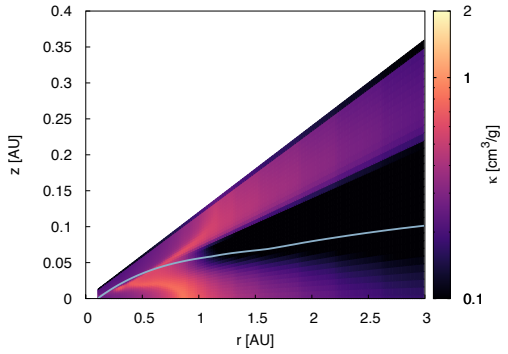

(i) BOD, $\alpha = 10^{-4}$, $\Sigma_{g,0} = 1000\ g/cm^2$, $f_{DG} = 1\%$

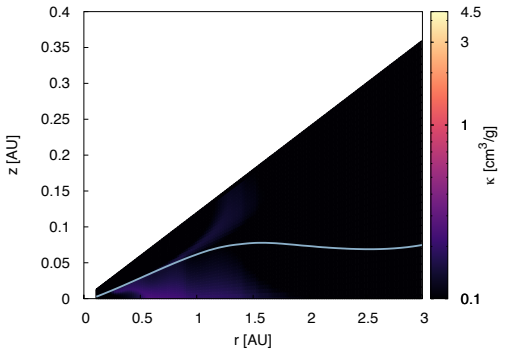

(j) MRN, $\alpha = 10^{-4}$, $\Sigma_{g,0} = 1000\ g/cm^2$, $f_{DG} = 1\%$

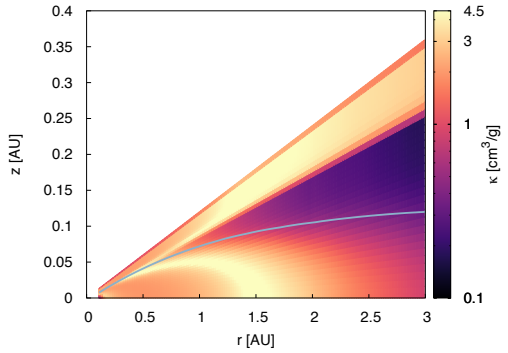

(k) BOD, $\alpha = 1 \times 10^{-2}$, $\Sigma_{g,0} = 100\ g/cm^2$, $f_{DG} = 1\%$

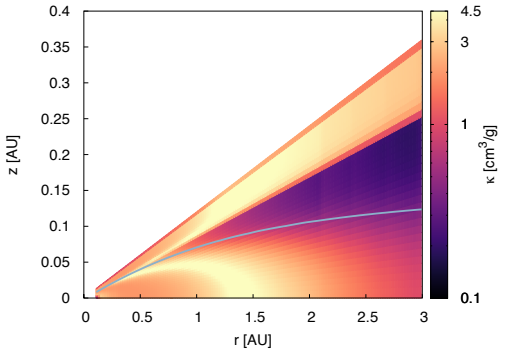

(l) MRN, $\alpha = 1 \times 10^{-2}$, $\Sigma_{g,0} = 100\ g/cm^2$, $f_{DG} = 1\%$

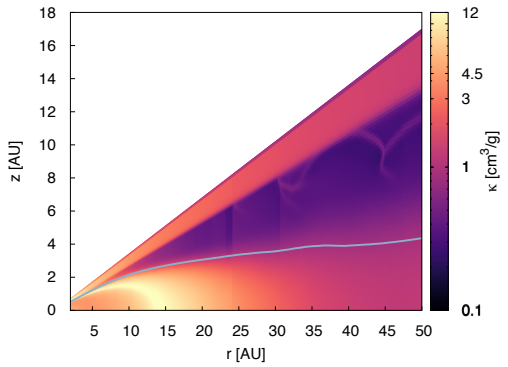

(m) BOD, $\alpha = 1 \times 10^{-2}$, $\Sigma_{g,0} = 1000\ g/cm^2$, $f_{DG} = 3\%$

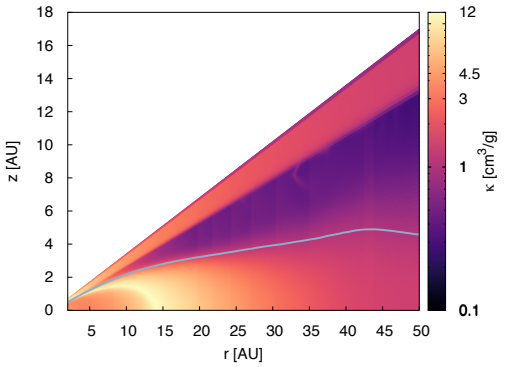

(n) MRN, $\alpha = 1 \times 10^{-2}$, $\Sigma_{g,0} = 1000\ g/cm^2$, $f_{DG} = 3\%$

Figure A.2. Mean Rosseland opacities as a function of orbital distance and height for the different α values, the lowest gas surface densities, and the highest dust-to-gas ratio. The light blue line corresponds to optical depth $\tau = 1$ integrated vertically starting from infinity towards midplane.

A.2 Iceline position as a function of α-viscosity, initial gas surface density and dust-to-gas ratio

In Sec. 3.5.1 we present the position of the iceline as a function of the α-viscosity parameter, the initial gas surface density, $\Sigma_{g,0}$, and the total dust-to-gas ratio f_{DG}. In order to do this fitting, we used five simulations for each parameter (see Table A.1). In Fig. A.3 we show the individual fitting over each one of the parameters. The fit to the three parameters writes

$$f = C \cdot \left(\frac{\alpha}{0.01}\right)^{p_1} \cdot \left(\frac{\Sigma_{g,0}}{1000\ g/cm^2}\right)^{p_2} \left(\frac{f_{DG}}{0.01}\right)^{p_3} , \tag{A.1}$$

with C=9.20±0.05 AU, $p_1 = 0.61 \pm 0.03$, $p_2 = 0.77 \pm 0.03$, $p_3 = 0.37 \pm 0.01$. The resulting fit is the same regardless of the grain size distribution used in the disc (solid line in Fig. A.3).

A.3 The effect of settling

We implement in our work the effect of settling for the grains in the disc as described in Sect. 3.2.4, in order to vertically distribute the grains according to their sizes and the local disc parameters. This implies that the disc structure can be affected both by a change in the grain size due to the different opacities that each size provides (Fig. 3.1) and by a change in the settling efficiency of the given grain size. In order to test if both of these effects are significant factors that define the disc structure, we run one simulation where the disc only contains millimeter grains and compare with a disc which also contains only millimeter grains but does not take settling into account. Thus in this latter case, the millimeter grains are vertically distributed according to a constant dust-to-gas ratio throughout the whole disc. Additionally, we run a simulation where the opacities of the grains correspond to millimeter grains, but we assume that the grains are vertically distributed as micrometer grains (so we assume $s = 1\ \mu m$ in the equations describing settling, Eq. 2.14 - **??**). We choose $\alpha = 10^{-4}$ for which the settling of millimeter grains will be very effective. However, micrometer dust grains are not expected to be affected by settling even at this low α-viscosity. The models also have an initial gas surface density of $\Sigma_{g,0} = 1000\ g/cm^2$ and total dust-to-gas ratio $f_{DG} = 1\%$.

In Figure A.4 we present the aspect ratio of these three disc models. The aspect ratio as a function of orbital distance for the disc where grains are vertically distributed as micrometer-sized dust resembles the one of a disc where the dust-to-gas ratio is constant all over the disc. This is expected because micrometer-sized dust is not significantly affected by settling even at the low α-viscosity of 10^{-4} (see Fig. 3.4). However, we find that the aspect ratio is lower in the inner regions of discs when the millimeter grains are allowed to settle with their corresponding properties. When settling is included, the millimeter grains are mainly concentrated near the midplane (see also Fig. 3.4), while at higher altitudes the opacity diminishes. Without settling or with reduced efficiency of settling the opacity is similar at all

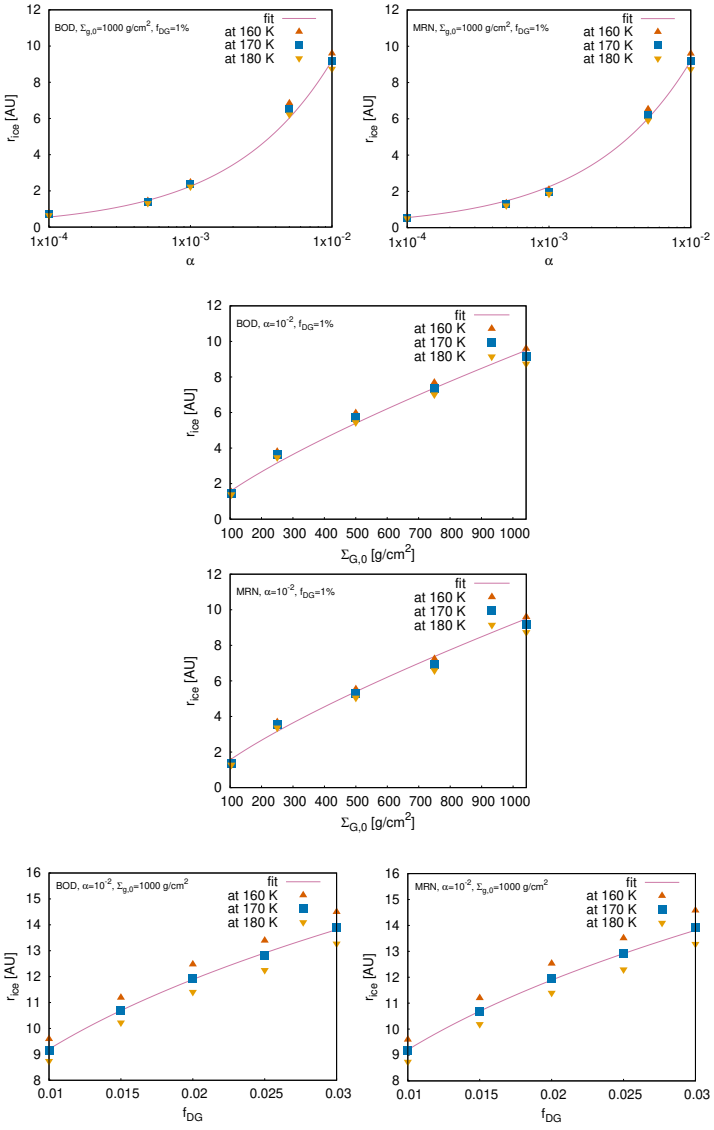

Figure A.3. Iceline position as a function of α-viscosity (top), initial gas surface density (middle), and dust-to-gas ratio (bottom) for the discs with the BOD distribution (left column) and the discs with the MRN distribution (right column). The iceline transition is defined as $T = (170 \pm 10)K$. The specific parameters used for the simulations presented in this plot are shown in Table A.1. The solid lines are the fits to each parameter and are the same for the discs with either one of the distributions.

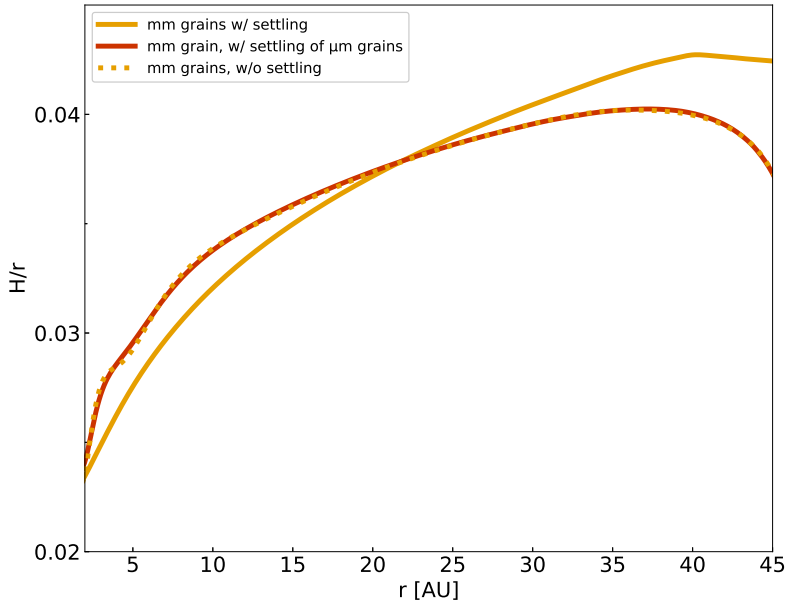

Figure A.4. Comparison of the aspect ratio as a function of orbital distance for discs with mm grains with settling, without settling and with the settling of μm grains.

altitudes, which leads to a reduced cooling rate and higher aspect ratio in the inner regions.

Without settling of the millimeter grains according to their size properties, the outer regions are not sufficiently heated. Due to the increased aspect ratio in the inner disc, stellar irradiation to the outer disc is diminished, creating a shadow that cools down the outer region. At the same time, the millimeter grains have very low opacity so they cannot absorb the stellar heating efficiently in the outer disc. The disc at the outermost radii might keep cooling down until it reaches the temperature of the surroundings (Dullemond & Dominik 2004). Hence including settling is very important to avoid such complications and inconsistencies in the disc structures.

Different grain sizes lead to different disc structures even without any settling implemented. The distinctive structures of discs with different grain sizes come mainly by their individual opacities (Fig. 3.2). However, without settling the disc opacity above midplane is overestimated so the discs are hotter in the inner regions and thus do not allow the stellar irradiation to heat the outer regions. In order to consistently take into account the influence of a grain size distribution to the resulting disc structures, it is important to include settling.

$\boldsymbol{\alpha}$ ($\Sigma_{g,0} = 1000\ g/cm^2$, $f_{DG} = 1\%$)	$\boldsymbol{\Sigma_{g,0}}$ $\boldsymbol{[g/cm^2]}$ ($\alpha = 10^{-2}$ $f_{DG} = 1\%$)	$\boldsymbol{f_{DG}}$ ($\alpha = 10^{-2}$, $\Sigma_{g,0} = 1000\ g/cm^2$)
10^{-2}	100	1%
5×10^{-3}	250	1.5%
10^{-3}	500	2%
5×10^{-4}	750	2.5%
10^{-4}	1000	3%

Table A.1. Parameters used in the simulations performed for the fitting of the iceline position to α-viscosity, initial gas surface density, and total dust-to-gas ratio for the BOD and the MRN distribution.

B

Additional material to Chapter 4

Refractive indices

In Table 4.1 we include the sources of the refractive indices used to calculate the opacities per grain size and the composition as a function of temperature. The refractive indices are not only dependent on the wavelength of the incident radiation, but also on the temperature of the surrounding medium. Hence, we find for some of the species used in this work different refractive indices for measurements at different temperatures.

From Henning & Mutschke (1997) we obtain refractive indices as a function of wavelength for FeS measured at T = 10 and 100 K. In our disk models we assume that the dust temperature is the same as the temperature of the surrounding gas, which is a good approximation for the optically thick parts of the disk (Kamp & Dullemond 2004). For this reason, we chose to combine the refractive indices obtained for different temperatures, so that the new refractive indices correspond to the values for T = 10 K for low temperatures, but gradually switch to the values corresponding to T = 100 K for high temperatures. In Fig. B.1 we show the Rosseland opacity as a function of temperature, calculated with the refractive indices measured at T = 10 and 100 K, and the combination of those used in the opacity module of this work.

In Hudgins et al. (1993), the refractive indices are given for CO_2 for T = 10, 30, 50, and 70 K. We plot the resulting Rosseland opacities for some of these different measurements in Fig. B.2a. We chose to use the refractive indices only for 50 K in our simulations because the differences are very small between the three different sets.

Similarly, for CH_4 we find refractive indices for T = 10, 20, and 30 K. The resulting mean Rosseland opacities are plotted in Fig. B.2b. They are almost the same, independently of the temperature at which the measurement was made. We chose for this work to use the refractive indices at T = 20 K.

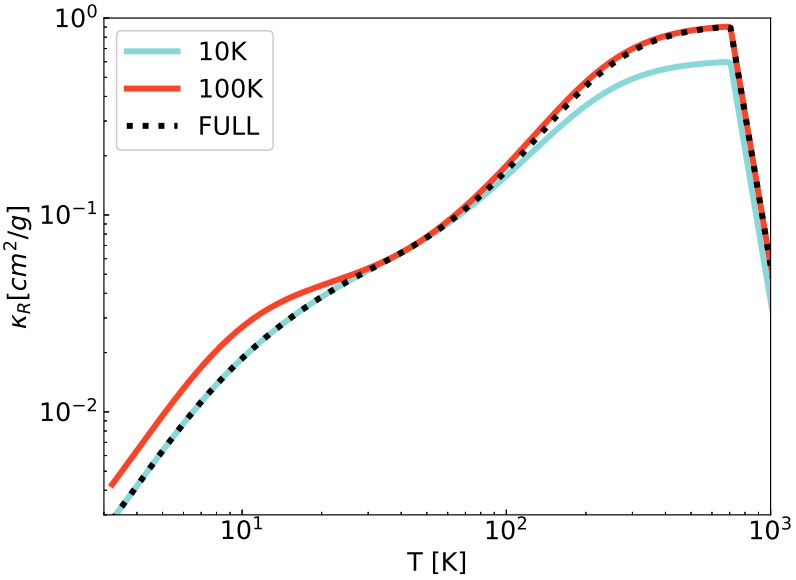

Figure B.1. Rosseland opacity as a function of temperature for FeS calculated using refractive indices measured at two different temperatures. The black dashed line shows the opacity used here which combines the opacities derived from the two temperatures.

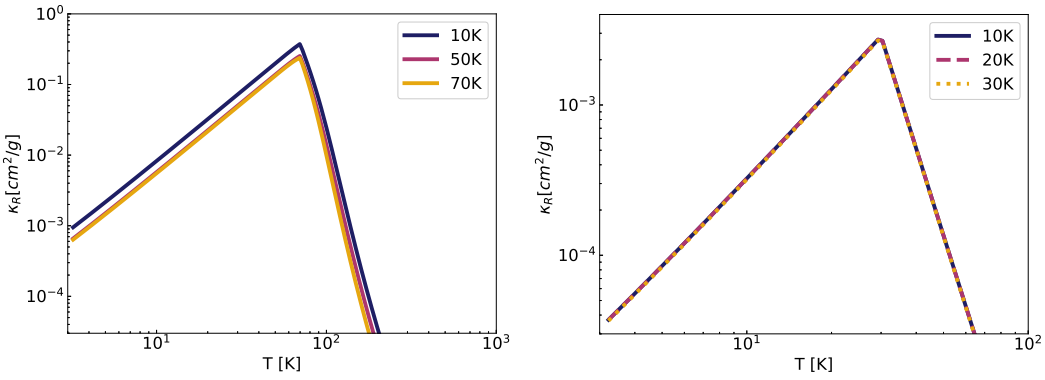

(a) CO_2 **(b)** CH_4

Figure B.2. Rosseland opacity as a function of temperature for the specified species calculated using refractive indices measured at three different temperatures.

List of Figures

1.1 Number of exoplanets per discovery year . . . 2
1.2 Observed exoplanets vs Class II discs . . . 3
1.3 Types of planets . . . 4
1.4 Field of view for current (Kepler and TESS) and future (Nancy Grace Roman Telescope) exoplanet hunting surveys. . . . 5

2.1 Evolutionary stages of star formation. . . . 12
2.2 SED shapes for YSOs . . . 13
2.3 Classification of YSOs . . . 14
2.4 Thesis summary cartoon! . . . 18
2.5 Motions which induce relative velocities for dust grains (orange spheres) on a small scale. Left: Very small particles are stochastically scattered by the gas molecules (light purple spheres). Right: Larger particles are affected by the turbulent eddies of the gas (red arrows). . . . 19
2.6 Extinction coefficient as a function of the size parameter for different grain sizes, produced using the opacity module of RADMC3D. . . . 25
2.7 PebbleAccretion . . . 27
2.8 Illustration of the horseshow region (green area) of a planet (blue circle) moving in a circular orbit (dashed line) within a protoplanetary disc. The thick red (resp. blue) arrow shows the motion of the gas from the inner (resp. outer) to the outer (reps. inner) disc due to the angular momentum exchange. Figure from C. Bergez-Casalou. . . . 29

3.1 Graphical illustration of the feedback loop. . . . 32
3.2 Rosseland, Planck, and stellar mean opacities (from left to right) as a function of temperature for grains of sizes 0.1, 1, 10, 100 μm, 1 mm, and 1 cm. They are independent of the gas density because they are dominated by the dust component. These values were calculated using RADMC-3D for a mixture of 50% silicates, 50% ice, and disc dust-to-gas ratio of 1%. The gray vertical line shows the location of the water iceline transition (170 K $\pm$ 10 K), causing a transition in opacity due to the evaporation/condensation of dust grains. . . . 38
3.3 Grain size distributions at 10 AU . . . 41
3.4 Dust density as a function of height for grains of five representative grain sizes within a disc with the BOD, $\alpha = 10^{-4}$ and $\Sigma_{g,0} = 1000\ g/cm^2$, at 3 AU. . . . 45
3.5 Aspect ratio and midplane temperature as a function of orbital distance in AU, for discs with five different single grain sizes. . . . 47

3.6 Aspect ratio and midplane temperature as a function of orbital distance for the discs with the BOD, the MRN distribution and a disc that utilizes the Bell & Lin (1994a) opacities. 48

3.7 Mean Rosseland opacity values for the disc that includes the BOD distribution (top) and the MRN (bottom). 49

3.8 Mean Rosseland opacity per grain size 52

3.9 Aspect ratio and temperature as a function of orbital distance for the two grain size distributions. 53

3.10 50% contribution lines as a function of orbital distance 55

3.11 Aspect ratio as a function of orbital distance for two different surface densities ($\Sigma_{g,0} = 100\ g/cm^2$ and $\Sigma_{g,0} = 1000\ g/cm^2$). 56

3.12 Iceline position as a function of α turbulence and initial gas surface density at 1AU with a constant $f_{DG} = 1\%$ (Eq. 3.19). The iceline transition is defined as $T = 170 \pm 10\ K$. The black lines mark $r_{ice} = 0.5, 1, 2.7$ and $5\ AU$. Higher viscosity or gas surface density leads to hotter discs, with the iceline located at greater distances from the star. The same applies to higher total dust-to-gas ratio. The gray dashed lines mark $r_{ice} = 0.5, 1, 2.7$ and $5\ AU$ for a disc with $f_{DG} = 3\%$. 58

3.13 Torque acting on planets with different masses for the disc utilizing the BOD distribution for the nominal viscosity of $\alpha = 5 \times 10^{-3}$. The black line encircles the regions of outward migration and corresponds to the region of the disc where the aspect ratio decreases as a function of the orbital distance. The temperature in the same region shows the steepest gradient. 60

3.14 Same as Fig. 3.13 for the disc with the MRN distribution. The difference to the BOD distribution is small regarding the size of the region of outward migration, however, the torque is weaker for the MRN distribution. This could lead to different migration and growth behavior of planets forming in the outer disc. 60

3.15 Same as Fig. 3.13 for the disc with the Bell & Lin (1994a) opacity profile. In contrast to the discs with the BOD or the MRN grain size distribution, the disc simulated with the Bell & Lin (1994a) opacity law shows an inner region of outward migration, which is caused by another bump in the H/r profile in the inner disc (Fig.5). 60

4.1 Influence of the evaporation of the different chemical species on the dust-to-gas ratio in the protoplanetary disc. 71

4.2 Aspect ratio, temperature, and gas surface density as a function of orbital distance 73

4.3 Same as Fig. 4.2 for a fragmentation velocity of $u_f = 10$ m/s. 74

4.4 Pebble isolation mass as a function of orbital distance for discs. . . . 75

4.5 Same as Fig. 4.4, but for a fragmentation velocity of $u_f = 10$ m/s. . 76

4.6 Maximum Stokes number (top plot) and planetary growth timescale until the pebble isolation mass is reached (bottom plot) as a function of orbital distance, for the discs with the four different initial gas surface densities: $\alpha = 10^{-3}$ (left plot), $\alpha = 5 \times 10^{-4}$ (middle plot), $\alpha = 10^{-4}$ (right plot), and $u_f = 1$ m/s. The gray lines show the typical lifetime range of a protoplanetary disc of 3 to 10 Myr. 76
4.7 Same as Fig. 4.6, but for $u_f = 10$ m/s. 77
4.9 Pebble isolation mass, maximum Stokes number, and planetary growth timescale until the pebble isolation mass is reached as a function of orbital distance 81
4.10 Planetary growth timescale until the pebble isolation mass is reached as a function of orbital distance with initial planetary seed masses $M_{init} = 0.1$ $M_\oplus$. We tested two α-viscosities, 10^{-3} and 5×10^{-4} with a fragmentation velocity, $u_f = 1$ m/s. Overplotted are the nominal disc models with initial planetary seed masses $M_{init} = 0.01$ $M_\oplus$. . . . 82

5.1 Evolution of planetary mass as a function of position using the standard set of parameters 93
5.2 Same as in Fig. 5.1, with one parameter changed (marked in each panel) compared to the standard model. 94
5.3 Evolution of planetary mass as a function of position for two sets of simulations with f_{DG}=0.01 (green colors) and f_{DG}=0.03 (purple colors) and two different initial disc masses. The rest of the parameters are the same as in the standard case (bold in Table **??**). 95
5.4 Same as Fig. 5.3, for two different initial embryo injection times. . . 95
5.5 Final planetary masses and final positions for all simulations with f_{DG}=0.015. 98
5.6 Cumulative distribution functions (inversed) of final planetary masses, for different initial conditions. 99

6.1 Dust mass as a function of time for the same planets as in Fig. 5.1, using the standard set of parameters (Table 6.1). The dashed lines show the time evolution of the optically thin dust mass and the red line is the dust mass time evolution for a simulation without a planet. 117
6.2 Same as Fig. 6.1 with the same planets as in Fig. 5.2. 118
6.3 Cumulative distribution functions for the disc dust mass of our models at different times (0-3 Myr). The dashed lines correspond to the dust mass excluding the optically thick regions of each disc. 119

A.1 Dust surface densities as a function of orbital distance and grain size for the different α values used here, and for additional simulations with the lowest gas surface densities and with the highest dust-to-gas ratio that we have tried. 131
A.2 Mean Rosseland opacities as a function of orbital distance and height for the different α values, the lowest gas surface densities, and the highest dust-to-gas ratio. 133

A.3 Iceline position as a function of α-viscosity, initial gas surface density, and dust-to-gas ratio for the discs with the BOD and the discs with the MRN distribution. 135
A.4 Comparison of the aspect ratio as a function of orbital distance for discs with mm grains with settling, without settling and with the settling of μm grains. 136

B.1 Rosseland opacity as a function of temperature for FeS calculated using refractive indices measured at two different temperatures. . . . 140
B.2 Rosseland opacity as a function of temperature for the specified species calculated using refractive indices measured at three different temperatures. 140
B.3 My little helper! 173

List of Tables

3.1 Power-law exponents for each regime in the grain size distribution (Birnstiel et al. 2011a). The distribution in each regime is $n(m) \cdot m \cdot s \propto s_i^{\delta_i}$. 43

4.1 Condensation temperatures and volume mixing ratios for the chemical species used in this work. Also shown are the densities and mass fractions considered to calculate the mean opacities as a function of temperature, along with the references of the refractive indices. . . . 68

4.2 Parameters used in the simulations 69

5.1 Parameters used in the simulations. We mark in bold the standard set, which is used as a reference in Fig. 5.1-5.4. 90

6.1 Standard set of parameters used in the simulations. 116

A.1 Parameters used in the simulations performed for the fitting of the iceline position to α-viscosity, initial gas surface density, and total dust-to-gas ratio for the BOD and the MRN distribution. 137

List of own publications

The following scientific publications have been published or submitted during the course of my PhD.

Part of this thesis

- ⋆ **Savvidou, S.**, Bitsch, B., Lambrechts, M., 2020, Astronomy & Astrophysics, 640, A63,

  "Influence of grain growth on the thermal structure of protoplanetary discs"

- ⋆ **Savvidou, S.**, Bitsch, B., 2021,Astronomy & Astrophysics, 650, A132,

  "The growth of super-Earths. The importance of a self-consistent treatment of disk structures and pebble accretion"

- ⋆ **Savvidou, S.**, Bitsch, B., *submitted to Astronomy & Astrophysics*,

  "How to make giant planets via pebble accretion"

- ⋆ **Savvidou, S.**, Bitsch, B., *in prep*,

  "A giant solution to the disc mass budget problem of planet formation"

Not part of this thesis

- ⋆ Bitsch, B., **Savvidou, S.**, 2021, Astronomy & Astrophysics, 647, A96,

  "Influence of grain size and composition on the contraction rates of planetary envelopes and on planetary migration"

- ⋆ Müller, J., **Savvidou, S.**, Bitsch, B., Astronomy & Astrophysics, 650, A185,

  "The water-ice line as a birthplace of planets: implications of a species-dependent dust fragmentation threshold"

- ⋆ Dietrich, J., ..., **Savvidou, S.**, et al. 2023, *submitted to ApJ*,

  "EDEN Survey: Small Transiting Planet Detection Limits and Constraints on the Occurrence Rates for Late M Dwarfs within 15 pc"

Bibliography

Adams, F. C., Lada, C. J., & Shu, F. H. 1987, , 312, 788

Ali-Dib, M., Mousis, O., Petit, J.-M., & Lunine, J. I. 2014, , 785, 125

Allègre, C., Manhès, G., & Lewin, É. 2001, Earth and Planetary Science Letters, 185, 49

ALMA Partnership, Brogan, C. L., Pérez, L. M., et al. 2015, , 808, L3

Amelin, Y., Krot, A. N., Hutcheon, I. D., & Ulyanov, A. A. 2002, Science, 297, 1678

Andama, G., Ndugu, N., Anguma, S. K., & Jurua, E. 2022, , 510, 1298

André, P., Di Francesco, J., Ward-Thompson, D., et al. 2014, in Protostars and Planets VI, ed. H. Beuther, R. S. Klessen, C. P. Dullemond, & T. Henning, 27–51

Andre, P. & Montmerle, T. 1994, , 420, 837

Andre, P., Ward-Thompson, D., & Barsony, M. 1993, , 406, 122

Andre, P., Ward-Thompson, D., & Barsony, M. 2000, in Protostars and Planets IV, ed. V. Mannings, A. P. Boss, & S. S. Russell, 59

Andrews, S. M. 2015, Publications of the Astronomical Society of the Pacific, 127, 961

Andrews, S. M. 2020, Annual Review of Astronomy and Astrophysics, 58, 483–528

Andrews, S. M., Huang, J., Pérez, L. M., et al. 2018, , 869, L41

Andrews, S. M., Rosenfeld, K. A., Kraus, A. L., & Wilner, D. J. 2013, , 771, 129

Andrews, S. M. & Williams, J. P. 2005a, , 631, 1134

Andrews, S. M. & Williams, J. P. 2005b, , 631, 1134

Andrews, S. M. & Williams, J. P. 2005, The Astrophysical Journal, 631, 1134–1160

Andrews, S. M. & Williams, J. P. 2007, , 671, 1800

Andrews, S. M., Wilner, D. J., Hughes, A. M., Qi, C., & Dullemond, C. P. 2009, , 700, 1502

Ansdell, M., Haworth, T. J., Williams, J. P., et al. 2020, , 160, 248

Ansdell, M., Williams, J. P., Manara, C. F., et al. 2017, , 153, 240

Ansdell, M., Williams, J. P., Trapman, L., et al. 2018, , 859, 21

Ansdell, M., Williams, J. P., van der Marel, N., et al. 2016, , 828, 46

Appelgren, J., Lambrechts, M., & Johansen, A. 2020, , 638, A156

Armitage, P. J. 2009, Astrophysics of Planet Formation

Ataiee, S., Baruteau, C., Alibert, Y., & Benz, W. 2018, , 615, A110

Ataiee, S. & Kley, W. 2021, , 648, A69

Avenhaus, H., Quanz, S. P., Garufi, A., et al. 2018, , 863, 44

Avenhaus, H., Quanz, S. P., Meyer, M. R., et al. 2014, , 790, 56

Ayliffe, B. A. & Bate, M. R. 2009, , 393, 49

Bae, J., Isella, A., Zhu, Z., et al. 2022, arXiv:2210.13314 [astro-ph]

Bae, J., Pinilla, P., & Birnstiel, T. 2018, , 864, L26

Bai, X. N., Ye, J., Goodman, J., & Yuan, F. 2016, ApJ, 818, id. 152

Baker, J., Bizzarro, M., Wittig, N., Connelly, J., & Haack, H. 2005, , 436, 1127

Ballering, N. P. & Eisner, J. A. 2019, , 157, 144

Barenfeld, S. A., Carpenter, J. M., Ricci, L., & Isella, A. 2016, , 827, 142

Baruteau, C., Crida, A., Paardekooper, S. J., et al. 2014, in Protostars and Planets VI, ed. H. Beuther, R. S. Klessen, C. P. Dullemond, & T. Henning, 667

Baruteau, C. & Masset, F. 2008, , 672, 1054

Bashi, D. & Zucker, S. 2022, , 510, 3449

Batalha, N. M., Rowe, J. F., Bryson, S. T., et al. 2013, , 204, 24

Baumann, T. & Bitsch, B. 2020, , 637, A11

Beckwith, S. V. W. & Sargent, A. I. 1991, , 381, 250

Beckwith, S. V. W., Sargent, A. I., Chini, R. S., & Guesten, R. 1990, , 99, 924

Bell, K. R. & Lin, D. N. C. 1994a, , 427, 987

Bell, K. R. & Lin, D. N. C. 1994b, , 427, 987

Benisty, M., Juhasz, A., Boccaletti, A., et al. 2015, , 578, L6

Benítez-Llambay, P., Masset, F., Koenigsberger, G., & Szulágyi, J. 2015, , 520, 63

Bergez-Casalou, C., Bitsch, B., Kurtovic, N. T., & Pinilla, P. 2022, , 659, A6

Bergez-Casalou, C., Bitsch, B., Pierens, A., Crida, A., & Raymond, S. N. 2020, , 643, A133

Birnstiel, T., Dullemond, C. P., & Brauer, F. 2009, , 503, L5

Birnstiel, T., Dullemond, C. P., & Brauer, F. 2010a, , 513, A79

Birnstiel, T., Dullemond, C. P., & Brauer, F. 2010b, , 513, A79

Birnstiel, T., Dullemond, C. P., Zhu, Z., et al. 2018, , 869, L45

Birnstiel, T., Fang, M., & Johansen, A. 2016, , 205, 41

Birnstiel, T., Klahr, H., & Ercolano, B. 2012a, , 539, A148

Birnstiel, T., Klahr, H., & Ercolano, B. 2012b, , 539, A148

Birnstiel, T., Ormel, C. W., & Dullemond, C. P. 2011a, , 525, A11

Birnstiel, T., Ormel, C. W., & Dullemond, C. P. 2011b, , 525, A11

Bitsch, B. 2019, , 630, A51

Bitsch, B. & Battistini, C. 2020, , 633, A10

Bitsch, B., Boley, A., & Kley, W. 2013a, , 550, A52

Bitsch, B., Boley, A., & Kley, W. 2013b, , 550, A52

Bitsch, B., Crida, A., Morbidelli, A., Kley, W., & Dobbs-Dixon, I. 2013, Astronomy & Astrophysics, 549, A124

Bitsch, B., Crida, A., Morbidelli, A., Kley, W., & Dobbs-Dixon, I. 2013, , 549, A124

Bitsch, B., Izidoro, A., Johansen, A., et al. 2019a, , 623, A88

Bitsch, B. & Johansen, A. 2016, , 590, A101

Bitsch, B., Johansen, A., Lambrechts, M., & Morbidelli, A. 2015a, , 575, A28

Bitsch, B., Johansen, A., Lambrechts, M., & Morbidelli, A. 2015b, , 575, A28

Bitsch, B., Lambrechts, M., & Johansen, A. 2015c, , 582, A112

Bitsch, B., Lambrechts, M., & Johansen, A. 2015, A&A, 582, id.A112

Bitsch, B., Morbidelli, A., Johansen, A., et al. 2018, , 612, A30

Bitsch, B., Morbidelli, A., Lega, E., & Crida, A. 2014, , 564, A135

Bitsch, B., Raymond, S. N., Buchhave, L. A., et al. 2021, , 649, L5

Bitsch, B., Raymond, S. N., & Izidoro, A. 2019b, , 624, A109

Bitsch, B., Schneider, A. D., & Kreidberg, L. 2022, , 665, A138

Blum, J. & Wurm, G. 2008, Annual Review of Astronomy and Astrophysics, 46, 21

Bohren, C. & Huffman, D. R. 1998, Absorption and Scattering of Light by Small Particles (Wiley Science Paperback Series)

Bohren, C. F. & Huffman, D. R. 1983, Absorption and scattering of light by small particles

Booth, R. A., Meru, F., Lee, M. H., & Clarke, C. J. 2018, , 475, 167

Borucki, W. J., Koch, D., Basri, G., et al. 2010, Science, 327, 977

Brauer, F., Dullemond, C. P., & Henning, T. 2008a, , 480, 859

Brauer, F., Dullemond, C. P., & Henning, T. 2008b, , 480, 859

Brauer, F., Dullemond, C. P., Johansen, A., et al. 2007, , 469, 1169

Braukmüller, N., Wombacher, F., Funk, C., & Münker, C. 2019, Nature Geoscience, 12, 564

Brügger, N., Alibert, Y., Ataiee, S., & Benz, W. 2018, , 619, A174

Brügger, N., Burn, R., Coleman, G. A. L., Alibert, Y., & Benz, W. 2020, , 640, A21

Campbell, B., Walker, G. A. H., & Yang, S. 1988, , 331, 902

Casassus, S., van der Plas, G. M., Perez, S., et al. 2013, , 493, 191

Cazzoletti, P., Manara, C. F., Liu, H. B., et al. 2019, , 626, A11

Cazzoletti, P., van Dishoeck, E. F., Pinilla, P., et al. 2018, , 619, A161

Chambers, J. E. 2006, , 652, L133

Chambers, J. E. 2016, , 825, 63

Chen, J. & Kipping, D. 2017, , 834, 17

Chevance, M., Krumholz, M. R., McLeod, A. F., et al. 2022, arXiv e-prints, arXiv:2203.09570

Chiang, E. & Youdin, A. N. 2010, Annual Review of Earth and Planetary Sciences, 38, 493

Chiang, E. I. & Goldreich, P. 1997, , 490, 368

Chrenko, O., Chametla, R. O., Nesvorný, D., & Flock, M. 2022, , 666, A63

Ciesla, F. J. & Cuzzi, J. N. 2006, , 181, 178

Cieza, L. A., González-Ruilova, C., Hales, A. S., et al. 2021, , 501, 2934

Cieza, L. A., Ruíz-Rodríguez, D., Hales, A., et al. 2019, , 482, 698

Cimerman, N. P., Kuiper, R., & Ormel, C. W. 2017, , 471, 4662

Clark, B. G. 1980, , 89, 377

Clement, M. S., Kaib, N. A., & Chambers, J. E. 2020, , 1, 18

Codella, C., Cabrit, S., Gueth, F., et al. 2014, , 568, L5

Coleman, G. A. L. 2021, , 506, 3596

Commerçon, B., Teyssier, R., Audit, E., Hennebelle, P., & Chabrier, G. 2011, , 529, A35

Connelly, J. N., Bizzarro, M., Krot, A. N., et al. 2012, Science, 338, 651

Cornwell, T. J. 2008, IEEE Journal of Selected Topics in Signal Processing, 2, 793

Cossou, C., Raymond, S. N., Hersant, F., & Pierens, A. 2014a, , 569, A56

Cossou, C., Raymond, S. N., Hersant, F., & Pierens, A. 2014b, , 569, A56

Cossou, C., Raymond, S. N., & Pierens, A. 2013, , 553, L2

Crapsi, A., van Dishoeck, E. F., Hogerheijde, M. R., Pontoppidan, K. M., & Dullemond, C. P. 2008, , 486, 245

Crida, A. & Bitsch, B. 2017, , 285, 145

Crida, A. & Morbidelli, A. 2007, , 377, 1324

Crida, A., Morbidelli, A., & Masset, F. 2006, , 181, 587

Cridland, A. J., Eistrup, C., & van Dishoeck, E. F. 2019, , 627, A127

Cridland, A. J., Pudritz, R. E., & Alessi, M. 2016, , 461, 3274

Cumming, A., Butler, R. P., Marcy, G. W., et al. 2008, , 120, 531

Cuzzi, J. N., Estrada, P. R., & Davis, S. S. 2014, The Astrophysical Journal Supplement Series, 210, 21

D'Angelo, G., Kley, W., & Henning, T. 2003, , 586, 540

Davis, D. R. & Ryan, E. V. 1990, , 83, 156

Davis, S. S. 2005, , 620, 994

Debras, F. & Chabrier, G. 2019, , 872, 100

DeMeo, F. E. & Carry, B. 2014, , 505, 629

Dipierro, G., Price, D., Laibe, G., et al. 2015, , 453, L73

Dobbs-Dixon, I., Cumming, A., & Lin, D. N. C. 2010, , 710, 1395

Dohnanyi, J. S. 1969, Journal of Geophysical Research, 74, 2531

Dong, R., Liu, S.-y., Eisner, J., et al. 2018, , 860, 124

Dong, R., Zhu, Z., Rafikov, R. R., & Stone, J. M. 2015a, , 809, L5

Dong, R., Zhu, Z., & Whitney, B. 2015b, , 809, 93

Dorschner, J., Begemann, B., Henning, T., Jaeger, C., & Mutschke, H. 1995, , 300, 503

Draine, B. T. 2006, , 636, 1114

Drążkowska, J. & Alibert, Y. 2017a, , 608, A92

Drążkowska, J. & Alibert, Y. 2017b, , 608, A92

Drążkowska, J., Bitsch, B., Lambrechts, M., et al. 2022, arXiv e-prints, arXiv:2203.09759

Drążkowska, J., Li, S., Birnstiel, T., Stammler, S. M., & Li, H. 2019, , 885, 91

Drążkowska, J., Stammler, S. M., & Birnstiel, T. 2021, , 647, A15

Dubrulle, B., Morfill, G., & Sterzik, M. 1995, , 114, 237

Dullemond, C. P., Birnstiel, T., Huang, J., et al. 2018, , 869, L46

Dullemond, C. P. & Dominik, C. 2004, , 417, 159

Dullemond, C. P. & Dominik, C. 2005, , 434, 971

Dullemond, C. P., Dominik, C., & Natta, A. 2001, , 560, 957

Dullemond, C. P., Hollenbach, D., Kamp, I., & D'Alessio, P. 2007, in Protostars and Planets V, ed. B. Reipurth, D. Jewitt, & K. Keil, 555

Dullemond, C. P. & Monnier, J. D. 2010, , 48, 205

Eisner, J. A., Arce, H. G., Ballering, N. P., et al. 2018, , 860, 77

El Albani, A., Bengtson, S., Canfield, D. E., et al. 2014, PLoS ONE, 9, e99438

Emsenhuber, A., Mordasini, C., Burn, R., et al. 2021, , 656, A69

Eriksson, L. E. J., Johansen, A., & Liu, B. 2020, , 635, A110

Estrada, P. R., Cuzzi, J. N., & Morgan, D. A. 2016, , 818, 200

Fedele, D., Carney, M., Hogerheijde, M. R., et al. 2017, , 600, A72

Fernandes, R. B., Mulders, G. D., Pascucci, I., Mordasini, C., & Emsenhuber, A. 2019, , 874, 81

Field, G. B., Somerville, W. B., & Dressler, K. 1966, , 4, 207

Fischer, D. A. & Valenti, J. 2005, , 622, 1102

Flock, M., Turner, N. J., Mulders, G. D., et al. 2019, , 630, A147

Follette, K. B., Grady, C. A., Swearingen, J. R., et al. 2015, , 798, 132

Fortier, A., Alibert, Y., Carron, F., Benz, W., & Dittkrist, K. M. 2013, , 549, A44

Franceschi, R., Birnstiel, T., Henning, T., et al. 2022, , 657, A74

Fressin, F., Torres, G., Charbonneau, D., et al. 2013, , 766, 81

Fulton, B. J., Petigura, E. A., Howard, A. W., et al. 2017, , 154, 109

Fulton, B. J., Rosenthal, L. J., Hirsch, L. A., et al. 2021, , 255, 14

Galametz, M., Maury, A. J., Valdivia, V., et al. 2019, , 632, A5

Galván-Madrid, R., Liu, H. B., Izquierdo, A. F., et al. 2018, , 868, 39

Garaud, P. & Lin, D. N. C. 2007, , 654, 606

Garaud, P., Meru, F., Galvagni, M., & Olczak, C. 2013, , 764, 146

Gaudel, M., Maury, A. J., Belloche, A., et al. 2020, , 637, A92

Goldreich, P. & Tremaine, S. 1979, , 233, 857

Goldreich, P. & Tremaine, S. 1980, , 241, 425

Goldreich, P. & Ward, W. R. 1973, , 183, 1051

Gonzalez, J. F., Laibe, G., & Maddison, S. T. 2017, , 467, 1984

Goodman, A. A., Benson, P. J., Fuller, G. A., & Myers, P. C. 1993, , 406, 528

Gräfe, C., Wolf, S., Guilloteau, S., et al. 2013, , 553, A69

Greaves, J. S. & Rice, W. K. M. 2010, , 407, 1981

Greene, T. P., Wilking, B. A., Andre, P., Young, E. T., & Lada, C. J. 1994, , 434, 614

Guilera, O. M., de Elía, G. C., Brunini, A., & Santamaría, P. J. 2014, , 565, A96

Guillet, V., Hennebelle, P., Pineau des Forêts, G., et al. 2020, , 643, A17

Guillot, T., Ida, S., & Ormel, C. W. 2014, , 572, A72

Gundlach, B. & Blum, J. 2015a, , 798, 34

Gundlach, B. & Blum, J. 2015b, , 798, 34

Güttler, C., Blum, J., Zsom, A., Ormel, C. W., & Dullemond, C. P. 2010a, , 513, A56

Güttler, C., Blum, J., Zsom, A., Ormel, C. W., & Dullemond, C. P. 2010b, , 513, A56

Guzmán, V. V., Huang, J., Andrews, S. M., et al. 2018, , 869, L48

Haffert, S. Y., Bohn, A. J., de Boer, J., et al. 2019, Nature Astronomy, 3, 749

Haisch, Karl E., J., Lada, E. A., & Lada, C. J. 2001, , 553, L153

Harsono, D., Bjerkeli, P., van der Wiel, M. H. D., et al. 2018, Nature Astronomy, 2, 646

Harsono, D., Jørgensen, J. K., van Dishoeck, E. F., et al. 2014, , 562, A77

Hartmann, L., Calvet, N., Gullbring, E., & D'Alessio, P. 1998a, , 495, 385

Hartmann, L., Calvet, N., Gullbring, E., & D'Alessio, P. 1998b, ApJ, 495, p.385

Hartmann, L., Herczeg, G., & Calvet, N. 2016, , 54, 135

Hatzes, A. P., Cochran, W. D., Endl, M., et al. 2003, The Astrophysical Journal, 599, 1383

Hayashi, C. 1981a, Progress of Theoretical Physics Supplement, 70, 35

Hayashi, C. 1981b, Progress of Theoretical Physics Supplement, 70, 35

Helled, R., Bodenheimer, P., Podolak, M., et al. 2014, in Protostars and Planets VI, ed. H. Beuther, R. S. Klessen, C. P. Dullemond, & T. Henning, 643

Helled, R., Stevenson, D. J., Lunine, J. I., et al. 2022, , 378, 114937

Helling, C., Woitke, P., Rimmer, P. B., et al. 2014, Life, 4, 142

Henning, T. & Mutschke, H. 1997, , 327, 743

Henning, T. & Stognienko, R. 1996, , 311, 291

Hildebrand, R. H. 1983, , 24, 267

Högbom, J. A. 1974, , 15, 417

Homma, K. & Nakamoto, T. 2018, , 868, 118

Horn, B., Lyra, W., Mac Low, M.-M., & Sándor, Z. 2012, , 750, 34

Huang, J., Andrews, S. M., Pérez, L. M., et al. 2018, , 869, L43

Hudgins, D. M., Sandford, S. A., Allamandola, L. J., & Tielens, A. G. G. M. 1993, , 86, 713

Hueso, R. & Guillot, T. 2005a, , 442, 703

Hueso, R. & Guillot, T. 2005b, , 442, 703

Hunter, C. 1977, , 218, 834

Ida, S. & Guillot, T. 2016, , 596, L3

Ida, S., Guillot, T., & Morbidelli, A. 2016, , 591, A72

Ida, S. & Lin, D. N. C. 2004, , 604, 388

Ikoma, M., Nakazawa, K., & Emori, H. 2000, , 537, 1013

Isella, A., Pérez, L. M., Carpenter, J. M., et al. 2013, , 775, 30

Izidoro, A., Bitsch, B., Raymond, S. N., et al. 2019a, arXiv e-prints, arXiv:1902.08772

Izidoro, A., Bitsch, B., Raymond, S. N., et al. 2019b, arXiv e-prints, arXiv:1902.08772

Izidoro, A., Dasgupta, R., Raymond, S. N., et al. 2021, Nature Astronomy, 6, 357

Izidoro, A., Ogihara, M., Raymond, S. N., et al. 2017a, , 470, 1750

Izidoro, A., Ogihara, M., Raymond, S. N., et al. 2017b, , 470, 1750

Jaeger, C., Mutschke, H., Begemann, B., Dorschner, J., & Henning, T. 1994, aap, 292, 641

Jäger, C., Dorschner, J., Mutschke, H., Posch, T., & Henning, T. 2003, , 408, 193

Jennings, J., Booth, R. A., Tazzari, M., Clarke, C. J., & Rosotti, G. P. 2022, , 509, 2780

Jin, S., Li, S., Isella, A., Li, H., & Ji, J. 2016, , 818, 76

Johansen, A. & Bitsch, B. 2019, , 631, A70

Johansen, A., Ida, S., & Brasser, R. 2019, , 622, A202

Johansen, A., Klahr, H., & Henning, T. 2011, , 529, A62

Johansen, A. & Lacerda, P. 2010, , 404, 475

Johansen, A. & Lambrechts, M. 2017a, Annual Review of Earth and Planetary Sciences, 45, 359

Johansen, A. & Lambrechts, M. 2017b, Annual Review of Earth and Planetary Sciences, 45, 359

Johansen, A. & Youdin, A. 2007, , 662, 627

Johansen, A., Youdin, A. N., & Lithwick, Y. 2012, , 537, A125

Johnson, J. A., Aller, K. M., Howard, A. W., & Crepp, J. R. 2010, , 122, 905

Joy, A. H. 1945, , 102, 168

Kama, M., Trapman, L., Fedele, D., et al. 2020, , 634, A88

Kamp, I. & Dullemond, C. P. 2004, , 615, 991

Kant, I. 1755, Allgemeine Naturgeschichte und Theorie des Himmels

Kataoka, A., Tanaka, H., Okuzumi, S., & Wada, K. 2013, , 557, L4

Kennedy, G. M. & Kenyon, S. J. 2008, , 673, 502

Keppler, M., Benisty, M., Müller, A., et al. 2018, , 617, A44

Kimmig, C. N., Dullemond, C. P., & Kley, W. 2020, , 633, A4

Klahr, H. & Schreiber, A. 2020, , 901, 54

Klahr, H. H. & Bodenheimer, P. 2003, , 582, 869

Kley, W. 1989, , 208, 98

Kley, W. 1999, , 303, 696

Kobayashi, H., Tanaka, H., & Krivov, A. V. 2011, , 738, 35

Kokubo, E. & Ida, S. 1996, , 123, 180

Kokubo, E. & Ida, S. 1998, , 131, 171

Kominami, J. & Ida, S. 2004, , 167, 231

Krijt, S. & Ciesla, F. J. 2016, , 822, 111

Krijt, S., Ormel, C. W., Dominik, C., & Tielens, A. G. G. M. 2015, , 574, A83

Kroupa, P. 2001, , 322, 231

Kruijer, T. S., Burkhardt, C., Budde, G., & Kleine, T. 2017, Proceedings of the National Academy of Science, 114, 6712

Kruijer, T. S., Touboul, M., Fischer-Gödde, M., et al. 2014, Science, 344, 1150

Kwon, W., Looney, L. W., Mundy, L. G., Chiang, H.-F., & Kemball, A. J. 2009, , 696, 841

Lada, C. J. 1987, in Star Forming Regions, ed. M. Peimbert & J. Jugaku, Vol. 115, 1

Lada, C. J. & Wilking, B. A. 1984, , 287, 610

Lambrechts, M. & Johansen, A. 2012a, , 544, A32

Lambrechts, M. & Johansen, A. 2012b, , 544, A32

Lambrechts, M. & Johansen, A. 2014, , 572, A107

Lambrechts, M., Johansen, A., & Morbidelli, A. 2014, , 572, A35

Lambrechts, M. & Lega, E. 2017a, , 606, A146

Lambrechts, M. & Lega, E. 2017b, , 606, A146

Lambrechts, M., Morbidelli, A., Jacobson, S. A., et al. 2019, , 627, A83

Laplace, P. 1797, Exposition du systeme du monde

Larson, R. B. 1969, , 145, 271

Latham, D. W., Mazeh, T., Stefanik, R. P., Mayor, M., & Burki, G. 1989, , 339, 38

Law, C. J., Teague, R., Loomis, R. A., et al. 2021, , 257, 4

Lay, O. P., Carlstrom, J. E., & Hills, R. E. 1997, , 489, 917

Lay, O. P., Carlstrom, J. E., Hills, R. E., & Phillips, T. G. 1994, , 434, L75

Lecar, M., Podolak, M., Sasselov, D., & Chiang, E. 2006, , 640, 1115

Lee, E. J., Chiang, E., & Ormel, C. W. 2014, , 797, 95

Lega, E., Crida, A., Bitsch, B., & Morbidelli, A. 2014a, , 440, 683

Lega, E., Crida, A., Bitsch, B., & Morbidelli, A. 2014b, , 440, 683

Lesur, G., Ercolano, B., Flock, M., et al. 2022, arXiv:2203.09821 [astro-ph], arXiv: 2203.09821

Levermore, C. D. & Pomraning, G. C. 1981, , 248, 321

Levison, H. F., Kretke, K. A., & Duncan, M. J. 2015, , 524, 322

Levison, H. F., Thommes, E., & Duncan, M. J. 2010, , 139, 1297

Leya, I., Schönbächler, M., Wiechert, U., Krähenbühl, U., & Halliday, A. N. 2008, Earth and Planetary Science Letters, 266, 233

L.F., R. 1922, Weather prediction by numerical process (Cambridge (University Press))

Li, Z. Y., Banerjee, R., Pudritz, R. E., et al. 2014, in Protostars and Planets VI, ed. H. Beuther, R. S. Klessen, C. P. Dullemond, & T. Henning, 173–194

Lin, D. N. C., Bodenheimer, P., & Richardson, D. C. 1996, , 380, 606

Lin, D. N. C. & Papaloizou, J. 1979, , 188, 191

Lin, D. N. C. & Papaloizou, J. 1986, , 307, 395

Liu, B. & Ji, J. 2020, Research in Astronomy and Astrophysics, 20, 164

Liu, Y., Dipierro, G., Ragusa, E., et al. 2019, , 622, A75

Liu, Y., Linz, H., Fang, M., et al. 2022, , 668, A175

Lodato, G., Scardoni, C. E., Manara, C. F., & Testi, L. 2017, , 472, 4700

Lommen, D., Maddison, S. T., Wright, C. M., et al. 2009, , 495, 869

Long, F., Herczeg, G. J., Harsono, D., et al. 2019, , 882, 49

Long, F., Pinilla, P., Herczeg, G. J., et al. 2018, , 869, 17

Lorek, S., Lacerda, P., & Blum, J. 2018, , 611, A18

Lorén-Aguilar, P. & Bate, M. R. 2015, , 453, L78

Luque, R. & Pallé, E. 2022, Science, 377, 1211

Lynden-Bell, D. & Pringle, J. E. 1974, , 168, 603

Machida, M. N., Kokubo, E., Inutsuka, S.-I., & Matsumoto, T. 2010, , 405, 1227

Madhusudhan, N., Bitsch, B., Johansen, A., & Eriksson, L. 2017a, , 469, 4102

Madhusudhan, N., Bitsch, B., Johansen, A., & Eriksson, L. 2017b, , 469, 4102

Madhusudhan, N., Crouzet, N., McCullough, P. R., Deming, D., & Hedges, C. 2014, , 791, L9

Mamajek, E. E. 2009, in American Institute of Physics Conference Series, Vol. 1158, Exoplanets and Disks: Their Formation and Diversity, ed. T. Usuda, M. Tamura, & M. Ishii, 3–10

Manara, C. F., Ansdell, M., Rosotti, G. P., et al. 2022, arXiv e-prints, arXiv:2203.09930

Manara, C. F., Morbidelli, A., & Guillot, T. 2018, , 618, L3

Marboeuf, U., Thiabaud, A., Alibert, Y., Cabral, N., & Benz, W. 2014, , 570, A36

Marino, S., Perez, S., & Casassus, S. 2015, , 798, L44

Martin, R. G. & Livio, M. 2015, , 810, 105

Masset, F. S. 2017, , 472, 4204

Masset, F. S., Morbidelli, A., Crida, A., & Ferreira, J. 2006, , 642, 478

Masset, F. S. & Papaloizou, J. C. B. 2003, , 588, 494

Mathis, J. S., Rumpl, W., & Nordsieck, K. H. 1977, , 217, 425

Matsumoto, Y., Nagasawa, M., & Ida, S. 2012, , 221, 624

Matsumura, S., Brasser, R., & Ida, S. 2021, , 650, A116

Maury, A. J., André, P., Testi, L., et al. 2019, , 621, A76

Mayor, M., Marmier, M., Lovis, C., et al. 2011, arXiv e-prints, arXiv:1109.2497

Mayor, M. & Queloz, D. 1995, , 378, 355

McKee, C. F. & Tan, J. C. 2003, , 585, 850

Miguel, Y. & Vazan, A. 2023, Remote Sensing, 15, 681

Millholland, S., Wang, S., & Laughlin, G. 2017, , 849, L33

Min, M., Dullemond, C. P., Kama, M., & Dominik, C. 2011, , 212, 416

Miotello, A., Kamp, I., Birnstiel, T., Cleeves, L. I., & Kataoka, A. 2022, arXiv e-prints, arXiv:2203.09818

Miotello, A., Testi, L., Lodato, G., et al. 2014, , 567, A32

Miyake, K. & Nakagawa, Y. 1993, , 106, 20

Mizuno, H. 1989, , 80, 189

Mizuno, H., Markiewicz, W. J., & Voelk, H. J. 1988, , 195, 183

Moldenhauer, T. W., Kuiper, R., Kley, W., & Ormel, C. W. 2021, , 646, L11

Mollière, P., Molyarova, T., Bitsch, B., et al. 2022, , 934, 74

Mollière, P., van Boekel, R., Dullemond, C., Henning, T., & Mordasini, C. 2015, , 813, 47

Morbidelli, A., Baillié, K., Batygin, K., et al. 2022, Nature Astronomy, 6, 72

Morbidelli, A., Bitsch, B., Crida, A., et al. 2016, , 267, 368

Morbidelli, A., Lambrechts, M., Jacobson, S., & Bitsch, B. 2015a, , 258, 418

Morbidelli, A., Lambrechts, M., Jacobson, S., & Bitsch, B. 2015b, , 258, 418

Morbidelli, A. & Nesvorny, D. 2012, , 546, A18

Mordasini, C. 2014, , 572, A118

Mordasini, C., Alibert, Y., & Benz, W. 2009, , 501, 1139

Mordasini, C., Alibert, Y., Benz, W., Klahr, H., & Henning, T. 2012, , 541, A97

Mordasini, C., van Boekel, R., Mollière, P., Henning, T., & Benneke, B. 2016, , 832, 41

Mori, S., Bai, X.-N., & Okuzumi, S. 2019, , 872, 98

Movshovitz, N. & Podolak, M. 2008, , 194, 368

Mulders, G. D., Mordasini, C., Pascucci, I., et al. 2019, , 887, 157

Mulders, G. D., Pascucci, I., & Apai, D. 2015, , 798, 112

Mulders, G. D., Pascucci, I., Apai, D., & Ciesla, F. J. 2018, , 156, 24

Mulders, G. D., Pascucci, I., Ciesla, F. J., & Fernandes, R. B. 2021, , 920, 66

Muley, D., Fung, J., & van der Marel, N. 2019, , 879, L2

Müller, A., Keppler, M., Henning, T., et al. 2018a, , 617, L2

Müller, A., Keppler, M., Henning, T., et al. 2018b, , 617, L2

Müller, J., Savvidou, S., & Bitsch, B. 2021, , 650, A185

Mundy, L. G., Looney, L. W., Erickson, W., et al. 1996, , 464, L169

Murillo, N. M., Lai, S.-P., Bruderer, S., Harsono, D., & van Dishoeck, E. F. 2013, , 560, A103

Musiolik, G. & Wurm, G. 2019, , 873, 58

Najita, J. R. & Kenyon, S. J. 2014, , 445, 3315

Nakagawa, Y., Nakazawa, K., & Hayashi, C. 1981, , 45, 517

Natta, A., Testi, L., Calvet, N., et al. 2007, in Protostars and Planets V, ed. B. Reipurth, D. Jewitt, & K. Keil, 767

Ndugu, N., Bitsch, B., & Jurua, E. 2018, , 474, 886

Ndugu, N., Bitsch, B., Morbidelli, A., Crida, A., & Jurua, E. 2021, , 501, 2017

Nimmo, F. & Kleine, T. 2007, , 191, 497

Nomura, H., Furuya, K., Cordiner, M. A., et al. 2022, arXiv e-prints, arXiv:2203.10863

Ogihara, M. & Ida, S. 2009, , 699, 824

Ogihara, M., Kokubo, E., Suzuki, T. K., & Morbidelli, A. 2018, , 615, A63

Oka, A., Nakamoto, T., & Ida, S. 2011, , 738, 141

Okuzumi, S., Tanaka, H., Kobayashi, H., & Wada, K. 2012a, , 752, 106

Okuzumi, S., Tanaka, H., Kobayashi, H., & Wada, K. 2012b, , 752, 106

Ormel, C. W. 2017, in Astrophysics and Space Science Library, Vol. 445, Formation, Evolution, and Dynamics of Young Solar Systems, ed. M. Pessah & O. Gressel, 197

Ormel, C. W. & Cuzzi, J. N. 2007, , 466, 413

Ormel, C. W. & Klahr, H. H. 2010a, , 520, A43

Ormel, C. W. & Klahr, H. H. 2010b, , 520, A43

Ormel, C. W., Liu, B., & Schoonenberg, D. 2017, , 604, A1

Ormel, C. W., Paszun, D., Dominik, C., & Tielens, A. G. G. M. 2009, , 502, 845

Ormel, C. W. & Spaans, M. 2008, , 684, 1291

Ormel, C. W., Spaans, M., & Tielens, A. G. G. M. 2007, , 461, 215

Ormel, C. W., Vazan, A., & Brouwers, M. G. 2021, , 647, A175

Ossenkopf, V. 1993, , 280, 617

Osterloh, M. & Beckwith, S. V. W. 1995, , 439, 288

Paardekooper, S. J. 2014, , 444, 2031

Paardekooper, S. J., Baruteau, C., & Kley, W. 2011a, , 410, 293

Paardekooper, S. J., Baruteau, C., & Kley, W. 2011b, , 410, 293

Paardekooper, S. J. & Mellema, G. 2004, , 425, L9

Paardekooper, S. J. & Mellema, G. 2006, , 453, 1129

Pagani, L., Steinacker, J., Bacmann, A., Stutz, A., & Henning, T. 2010, Science, 329, 1622

Palme, H., Lodders, K., & Jones, A. 2014, in Planets, Asteriods, Comets and The Solar System, ed. A. M. Davis, Vol. 2, 15–36

Papaloizou, J. & Lin, D. N. C. 1984, , 285, 818

Pascucci, I., Cabrit, S., Edwards, S., et al. 2022, arXiv:2203.10068 [astro-ph], arXiv: 2203.10068

Pascucci, I., Herczeg, G., Carr, J. S., & Bruderer, S. 2013, , 779, 178

Pascucci, I., Testi, L., Herczeg, G. J., et al. 2016, , 831, 125

Patterson, C. 1956, , 10, 230

Pearce, B. K. D., Tupper, A. S., Pudritz, R. E., & Higgs, P. G. 2018, Astrobiology, 18, 343

Penston, M. V. 1969, , 144, 425

Pérez, L. M., Carpenter, J. M., Andrews, S. M., et al. 2016, Science, 353, 1519

Petigura, E. A., Marcy, G. W., & Howard, A. W. 2013, , 770, 69

Pierens, A. 2015, , 454, 2003

Pineda, J. E., Arzoumanian, D., André, P., et al. 2022, arXiv e-prints, arXiv:2205.03935

Pinilla, P. 2022, European Physical Journal Plus, 137, 1206

Pinilla, P., Benisty, M., & Birnstiel, T. 2012a, , 545, A81

Pinilla, P., Benisty, M., & Birnstiel, T. 2012b, , 545, A81

Pinilla, P., Benisty, M., Kurtovic, N. T., et al. 2022, , 665, A128

Pinilla, P., Lenz, C. T., & Stammler, S. M. 2021, , 645, A70

Pinilla, P., Pérez, L. M., Andrews, S., et al. 2017, , 839, 99

Pinte, C., Dent, W. R. F., Ménard, F., et al. 2016, , 816, 25

Pinte, C., Price, D. J., Ménard, F., et al. 2020, , 890, L9

Pinte, C., Price, D. J., Ménard, F., et al. 2018, , 860, L13

Podolak, M. & Zucker, S. 2004, Meteoritics and Planetary Science, 39, 1859

Pollack, J. B., Hubickyj, O., Bodenheimer, P., et al. 1996, , 124, 62

Poppe, T., Blum, J., & Henning, T. 2000a, , 533, 454

Poppe, T., Blum, J., & Henning, T. 2000b, , 533, 454

Powell, D., Murray-Clay, R., Pérez, L. M., Schlichting, H. E., & Rosenthal, M. 2019, , 878, 116

Powell, D., Murray-Clay, R., & Schlichting, H. E. 2017, , 840, 93

Preibisch, T., Ossenkopf, V., Yorke, H. W., & Henning, T. 1993, , 279, 577

Pringle, J. E. 1981, , 19, 137

Racki, G. 2021, Encyclopaedia of Geology, 3. (Academic Press - Elsevier)

Rafikov, R. R. 2004, , 128, 1348

Rafikov, R. R. 2016, , 831, 122

Raymond, S. N., Boulet, T., Izidoro, A., Esteves, L., & Bitsch, B. 2018, , 479, L81

Raymond, S. N., Izidoro, A., & Morbidelli, A. 2020, in Planetary Astrobiology, ed. V. S. Meadows, G. N. Arney, B. E. Schmidt, & D. J. Des Marais, 287

Raymond, S. N. & Morbidelli, A. 2022, in Astrophysics and Space Science Library, Vol. 466, Demographics of Exoplanetary Systems, Lecture Notes of the 3rd Advanced School on Exoplanetary Science, ed. K. Biazzo, V. Bozza, L. Mancini, & A. Sozzetti, 3–82

Ricci, L., Testi, L., Natta, A., & Brooks, K. J. 2010, , 521, A66

Ricci, L., Testi, L., Williams, J. P., Mann, R. K., & Birnstiel, T. 2011, , 739, L8

Rich, E. A., Teague, R., Monnier, J. D., et al. 2021, , 913, 138

Rodmann, J., Henning, T., Chandler, C. J., Mundy, L. G., & Wilner, D. J. 2006, , 446, 211

Rojas-Ayala, B. 2023, arXiv e-prints, arXiv:2301.03442

Romanova, M. M., Lii, P. S., Koldoba, A. V., et al. 2019, , 485, 2666

Ros, K. & Johansen, A. 2013, , 552, A137

Ros, K., Johansen, A., Riipinen, I., & Schlesinger, D. 2019, , 629, A65

Rosenthal, L. J., Knutson, H. A., Chachan, Y., et al. 2022, , 262, 1

Rosotti, G. P., Juhasz, A., Booth, R. A., & Clarke, C. J. 2016, , 459, 2790

Ruíz-Rodríguez, D., Cieza, L. A., Williams, J. P., et al. 2018, , 478, 3674

Safronov, V. 1969, Evolution of the protoplanetary cloud and formation of the earth and planets (Translated from Russian in 1972)

Saito, E. & Sirono, S.-i. 2011, , 728, 20

Sanchis, E., Testi, L., Natta, A., et al. 2021, , 649, A19

Santos, N. C., Israelian, G., & Mayor, M. 2004, , 415, 1153

Sasselov, D. D. & Lecar, M. 2000, , 528, 995

Savvidou, S. & Bitsch, B. 2021, , 650, A132

Savvidou, S. & Bitsch, B. 2022, arXiv

Savvidou, S., Bitsch, B., & Lambrechts, M. 2020, , 640, A63

Schäfer, U., Yang, C.-C., & Johansen, A. 2017, , 597, A69

Schmitt, W., Henning, T., & Mucha, R. 1997, , 325, 569

Schneider, A. D. & Bitsch, B. 2021, Astronomy & Astrophysics, 654, A71

Schoonenberg, D., Liu, B., Ormel, C. W., & Dorn, C. 2019, , 627, A149

Schoonenberg, D. & Ormel, C. W. 2017a, , 602, A21

Schoonenberg, D. & Ormel, C. W. 2017b, , 602, A21

Schräpler, R., Blum, J., Krijt, S., & Raabe, J.-H. 2018, , 853, 74

Schulik, M., Johansen, A., Bitsch, B., & Lega, E. 2019, , 632, A118

Schwarz, K. R., Bergin, E. A., Cleeves, L. I., et al. 2016, , 823, 91

Segura-Cox, D. M., Schmiedeke, A., Pineda, J. E., et al. 2020, , 586, 228

Shakura, N. I. & Sunyaev, R. A. 1973, , 500, 33

Sheehan, P. D. & Eisner, J. A. 2018, , 857, 18

Sheehan, P. D., Tobin, J. J., Federman, S., Megeath, S. T., & Looney, L. W. 2020, , 902, 141

Shu, F. H. 1977, , 214, 488

Silsbee, K., Akimkin, V., Ivlev, A. V., et al. 2022, , 940, 188

Sirono, S.-i. 2004, , 167, 431

Smith, B. A. & Terrile, R. J. 1984, Science, 226, 1421

Smoluchowski, M. V. 1916a, Zeitschrift fur Physik, 17, 557

Smoluchowski, M. V. 1916b, Zeitschrift fur Physik, 17, 557

Standing, M. R., Sairam, L., Martin, D. V., et al. 2023, arXiv e-prints, arXiv:2301.10794

Steinacker, J., Baes, M., & Gordon, K. D. 2013, , 51, 63

Steinpilz, T., Teiser, J., & Wurm, G. 2019, , 874, 60

Stevenson, D. J. & Lunine, J. I. 1988, , 75, 146

Stevenson, K., L. J. e. a. 2023

Stolker, T., Sitko, M., Lazareff, B., et al. 2017, , 849, 143

Supulver, K. D., Bridges, F. G., Tiscareno, S., Lievore, J., & Lin, D. N. C. 1997, , 129, 539

Suriano, S. S., Li, Z.-Y., Krasnopolsky, R., Suzuki, T. K., & Shang, H. 2019, , 484, 107

Surville, C., Mayer, L., & Alibert, Y. 2020, arXiv e-prints, arXiv:2009.04775

Suttner, G. & Yorke, H. W. 2001, , 551, 461

Suzuki, D., Bennett, D. P., Sumi, T., et al. 2016, , 833, 145

Swedenborg, E. 1734, Principia Latin: Opera Philosophica et Mineralia (English: Philosophical and Mineralogical Works)

Takahashi, S. Z. & Inutsuka, S.-i. 2016, , 152, 184

Tanaka, H., Inaba, S., & Nakazawa, K. 1996, , 123, 450

Tanaka, Y. A. & Tsukamoto, Y. 2019, , 484, 1574

Tanigawa, T. & Tanaka, H. 2016, , 823, 48

Teague, R., Bae, J., Bergin, E. A., Birnstiel, T., & Foreman-Mackey, D. 2018, , 860, L12

Testi, L., Birnstiel, T., Ricci, L., et al. 2014, in Protostars and Planets VI, ed. H. Beuther, R. S. Klessen, C. P. Dullemond, & T. Henning, 339

Thiabaud, A., Marboeuf, U., Alibert, Y., et al. 2014, , 562, A27

Thorngren, D. P., Fortney, J. J., Murray-Clay, R. A., & Lopez, E. D. 2016, , 831, 64

Tobin, J. J., Hartmann, L., Chiang, H.-F., et al. 2012, , 492, 83

Tobin, J. J., Sheehan, P. D., Megeath, S. T., et al. 2020, , 890, 130

Tripathi, A., Andrews, S. M., Birnstiel, T., & Wilner, D. J. 2017, , 845, 44

Tsukagoshi, T., Momose, M., Kitamura, Y., et al. 2019, , 871, 5

Tychoniec, Ł., Manara, C. F., Rosotti, G. P., et al. 2020, , 640, A19

Tychoniec, Ł., Tobin, J. J., Karska, A., et al. 2018, , 238, 19

Ubach, C., Maddison, S. T., Wright, C. M., et al. 2012, , 425, 3137

Ueda, T., Flock, M., & Birnstiel, T. 2021, , 914, L38

Uribe, A. L., Klahr, H., Flock, M., & Henning, T. 2011, , 736, 85

van de Hulst, H. C. 1957, Light Scattering by Small Particles

van der Marel, N., Birnstiel, T., Garufi, A., et al. 2021, , 161, 33

van der Marel, N. & Mulders, G. D. 2021, , 162, 28

van der Marel, N., Williams, J. P., Ansdell, M., et al. 2018a, , 854, 177

van der Marel, N., Williams, J. P., & Bruderer, S. 2018b, , 867, L14

van der Plas, G., Ménard, F., Canovas, H., et al. 2017, , 607, A55

Van Eylen, V., Astudillo-Defru, N., Bonfils, X., et al. 2021, , 507, 2154

van Terwisga, S. E., Hacar, A., van Dishoeck, E. F., Oonk, R., & Portegies Zwart, S. 2022, arXiv e-prints, arXiv:2202.11057

van Terwisga, S. E., van Dishoeck, E. F., Ansdell, M., et al. 2018, , 616, A88

Vazan, A., Helled, R., & Guillot, T. 2018, , 610, L14

Venturini, J., Alibert, Y., & Benz, W. 2016, , 596, A90

Venturini, J., Guilera, O. M., Haldemann, J., Ronco, M. P., & Mordasini, C. 2020a, arXiv e-prints, arXiv:2008.05513

Venturini, J., Guilera, O. M., Ronco, M. P., & Mordasini, C. 2020b, arXiv e-prints, arXiv:2008.05497

Venturini, J., Guilera, O. M., Ronco, M. P., & Mordasini, C. 2020c, , 644, A174

Villenave, M., Ménard, F., Dent, W. R. F., et al. 2021, , 653, A46

Villenave, M., Ménard, F., Dent, W. R. F., et al. 2020, , 642, A164

Voelkel, O., Deienno, R., Kretke, K., & Klahr, H. 2021, , 645, A131

Voelkel, O., Klahr, H., Mordasini, C., & Emsenhuber, A. 2022, , 666, A90

Voelkel, O., Klahr, H., Mordasini, C., Emsenhuber, A., & Lenz, C. 2020, , 642, A75

Vorobyov, E. I., Regaly, Z., Guedel, M., & Lin, D. N. C. 2016, , 587, A146

Wada, K., Tanaka, H., Suyama, T., Kimura, H., & Yamamoto, T. 2009, , 702, 1490

Wadhwa, M., McCoy, T. J., & Schrader, D. L. 2020, Annual Review of Earth and Planetary Sciences, 48, 233

Wahl, S. M., Hubbard, W. B., Militzer, B., et al. 2017, , 44, 4649

Walker, G. A. H., Bohlender, D. A., Walker, A. R., et al. 1992, , 396, L91

Warren, P. H. 2011, Earth and Planetary Science Letters, 311, 93–100, citation Key: WARREN201193

Warren, S. G. & Brandt, R. E. 2008a, Journal of Geophysical Research (Atmospheres), 113, D14220

Warren, S. G. & Brandt, R. E. 2008b, Journal of Geophysical Research (Atmospheres), 113, D14220

Weidenschilling, S. J. 1977a, , 180, 57

Weidenschilling, S. J. 1977b, , 180, 57

Weidenschilling, S. J. 1977c,

Weidenschilling, S. J. 1980a, , 44, 172

Weidenschilling, S. J. 1980b, , 44, 172

Weidenschilling, S. J. 1984a, , 60, 553

Weidenschilling, S. J. 1984b, , 60, 553

Weiss, L. M., Isaacson, H. T., Marcy, G. W., et al. 2018, , 156, 254

Whipple, F. L. 1972, in From Plasma to Planet, ed. A. Elvius, 211

Williams, D. R. & Wetherill, G. W. 1994, , 107, 117

Williams, J. P. & Cieza, L. A. 2011, , 49, 67

Windmark, F., Birnstiel, T., Ormel, C. W., & Dullemond, C. P. 2012, , 544, L16

Winn, J. N. & Fabrycky, D. C. 2015, , 53, 409

Winn, J. N., Sanchis-Ojeda, R., & Rappaport, S. 2018, , 83, 37

Wittenmyer, R. A., Butler, R. P., Tinney, C. G., et al. 2016, , 819, 28

Wolszczan, A. & Frail, D. A. 1992, , 355, 145

Woolfson, M. M. 1993, Quarterly Journal of the Royal Astronomical Society, 34, 1

Wright, J. T., Marcy, G. W., Howard, A. W., et al. 2012, The Astrophysical Journal, 753, 160

Wu, Y. 2019, , 874, 91

Wurm, G., Paraskov, G., & Krauss, O. 2005, , 178, 253

Xin, Z., Espaillat, C. C., Rilinger, A. M., Ribas, Á., & Macías, E. 2023, , 942, 4

Xu, W. & Armitage, P. J. 2023, arXiv e-prints, arXiv:2302.04711

Yang, C.-C., Johansen, A., & Carrera, D. 2017, , 606, A80

Yoshida, S., Grunblatt, S., & Price-Whelan, A. M. 2022, , 164, 119

Youdin, A. & Johansen, A. 2007, , 662, 613

Youdin, A. N. & Goodman, J. 2005, , 620, 459

Zeng, L., Jacobsen, S. B., Sasselov, D. D., et al. 2019, Proceedings of the National Academy of Science, 116, 9723

Zhang, K., Bergin, E. A., Blake, G. A., Cleeves, L. I., & Schwarz, K. R. 2017, Nature Astronomy, 1, 0130

Zhang, K., Blake, G. A., & Bergin, E. A. 2015, , 806, L7

Zhang, S., Zhu, Z., Huang, J., et al. 2018a, , 869, L47

Zhang, S., Zhu, Z., Huang, J., et al. 2018b, , 869, L47

Zhu, W. & Dong, S. 2021, , 59, 291

Zhu, W., Petrovich, C., Wu, Y., Dong, S., & Xie, J. 2018, , 860, 101

Zhu, Z., Zhang, S., Jiang, Y.-F., et al. 2019, , 877, L18

Zsom, A., Ormel, C. W., Dullemond, C. P., & Henning, T. 2011a, , 534, A73

Zsom, A., Ormel, C. W., Dullemond, C. P., & Henning, T. 2011b, , 534, A73

Zsom, A., Ormel, C. W., Güttler, C., Blum, J., & Dullemond, C. P. 2010a, , 513, A57

Zsom, A., Ormel, C. W., Güttler, C., Blum, J., & Dullemond, C. P. 2010b, , 513, A57

Öberg, K. I., Guzmán, V. V., Walsh, C., et al. 2021, The Astrophysical Journal Supplement Series, 257, 1

Öberg, K. I., Murray-Clay, R., & Bergin, E. A. 2011, The Astrophysical Journal Letters, 743, L16

Acknowledgements

A PhD is not only a long (and at times painful) process, but also one that shapes us as scientists and human beings as well. First and foremost, I would like to sincerely thank my supervisor and mentor, Dr. Bertram Bitsch, who has shaped my life and who I am as a person and researcher through our collaboration and gave me the opportunity to fulfill my dreams, while always being supportive and motivating me to try my best.

In regards to this thesis, I would like to thank Dr. Bertram Bitsch, Dr. Camille Bergez-Casalou, Dr. Linn Eriksson and Dr. Dominique Segura-Cox for sharing their figures with me to include here and Julia Lienert for editing the german version of the abstract. I am deeply thankful to Prof. Dr. Cornelis Dullemond who took the time to read and evaluate this thesis and be an integral part of my defense committee. On this note, I would also like to thank Prof. Dr. Henrik Beuther and Prof. Dr. Luca Amendola for their time as examiners in my thesis defense.

During my studies, I was fortunate to welcome my son and start navigating the worlds of parenthood and research in parallel. Such a monumental and life-changing experience can unfortunately make things much harder for anyone without adequate support, especially when we face the dilemma of who we are outside of parenthood, but also understand how detrimental a child's first years are and how intertwined their well-being is with the connection with their caregivers. I am thankful for working with such an understanding supervisor and in such a working environment, as is the MPIA and the people I have met there, that motivated me and supported the occasional unexpected changes of schedule.

I would like to acknowledge all the working parents, especially the solo/single parents and the ones without a "village", who jungle too many glass balls with two bare hands and make it through the days, the weeks and months not only surviving but also thriving. I see you, I admire you, and I wish society will (re)form some better solutions for us in the future. At this point, I would like to thank the teachers (and others) in my son's KiTa for being there for him when "Mama arbeitet" (as he says) but I would like to not thank at all the various illnesses he has contracted at times, especially the last one that made our whole family very sick the last week before I hand in this thesis!

I was very fortunate to have the best PhD buddy by my side during this season of life, my fellow student Dr. Camille Bergez-Casalou and even though I am happy that she fulfills her goals and moves on in life, I was sad to miss her the final months of my PhD (and as I am writing this and I am sick while she is in Heidelberg). She really made the experience at least twice more enjoyable than it would have been. I might even be underestimating this... I would also like to thank our "best PhD

support group" for the enjoyable nights playing Werewolf and other games, among others, Dr. Lizxandra Flores-Rivera, Dr. Marcelo Barraza Alfaro, Nicolas Kurtovic, Timmy Delage and Riccardo Franceschi as well as the past and current members of our group for our lunches or outings, digging me out of my office.

I have never written an anknowledgements section before in a thesis, so here I am unleashing all of the gratitude I never gave to the people in my life. Whoever is still reading, bare with me... My friends and family back in Greece who never forget about me, despite all the years I've been away and all the messages I've left unreplied for too long. Χρύσα Σακαδάκη, Κώστα Σακαδάκη, Δημήτρη Σακαδάκη, Στεφανία Νικάκη, Σταυρούλα Σαπλαμίδου και Μάρα Βάλαρη... Σας αγαπώ όλους και σας ευχαριστώ για όσα έχουμε ζήσει μαζί και για την υποστήριξή σας πάντα... My awesome parents and brother, the most integral factors of how I was shaped as a person, who guided me at the same time to find myself on my own and feel invincible, knowing that I can always lean on them if I need it. Μαμά, Μπαμπά και Μπάμπη... Σας αγαπώ και σας ευχαριστώ απ'τα βάθη τις καρδιάς μου για το ποιοί είστε...!

I would like to thank my husband for his support throughout the years and for the endless discussions about life, science, politics and anything imaginable. In particular, for preparing me for my thesis defense with his ruthless astrophysical questions that always make me realize that I know more than I think and less than I think at the same time. Θα είμαι δίπλα σου όσο με θες και τα καλύτερα θα έρθουν. Ψυχή βαθειά...!

Finally but most importantly, I would like to acknowledge and thank from the depths of my heart my sweet son, who shared part of this journey with me, supported me in his tiny ways and helped me put life into perspective. And for his intense will to help me write my thesis (evidence in Fig. B.3).

There is a phrase that I have mentioned a few times in this thesis and I would like to acknowledge that it is paraphrased from a John Green book that has nothing to do with this thesis, planet formation or even science per se. However, I would like to stress how important science lovers can be in giving us perspective and how at times we, as active researchers, can get entangled in the technical details of our work but forget who we are (in the Universe) and what motivates us to do what we do. I am especially one to forget to convey such information to the more general audience but I believe that science can only move forward if we... pause, take a look at the bigger picture, see how things look from other people's eyes and then decide what our next steps will be and why...

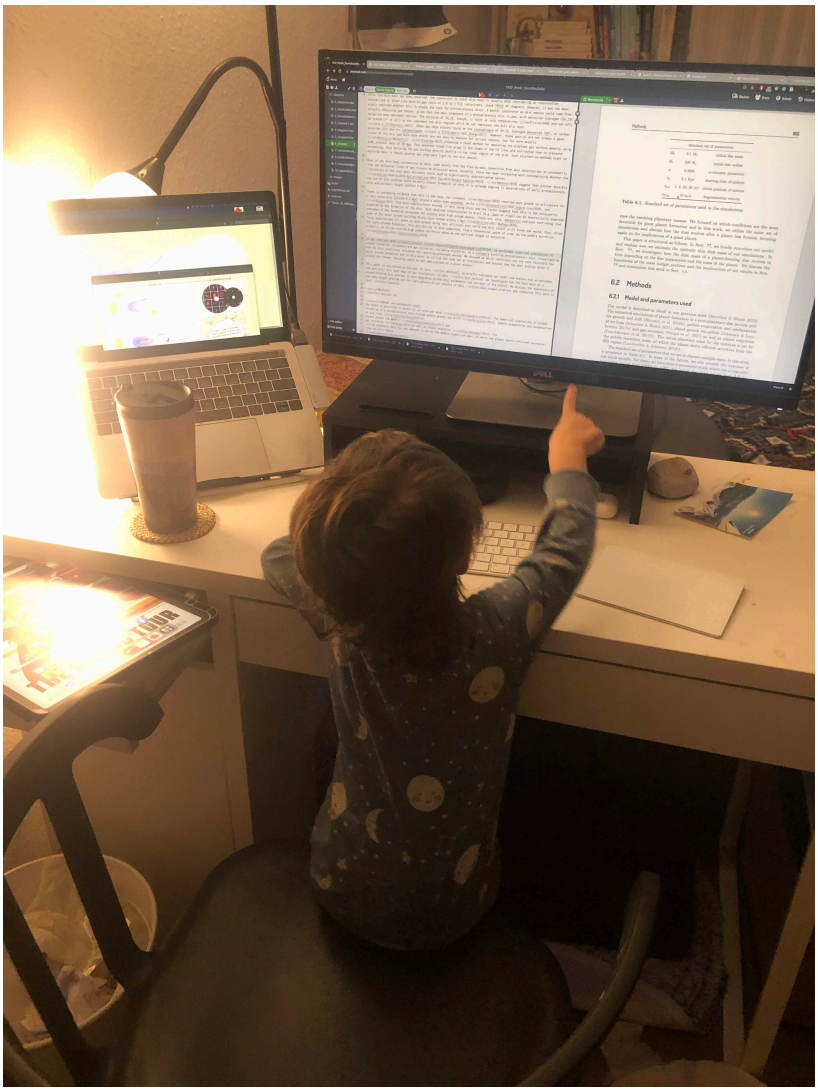

Figure B.3. My little helper!